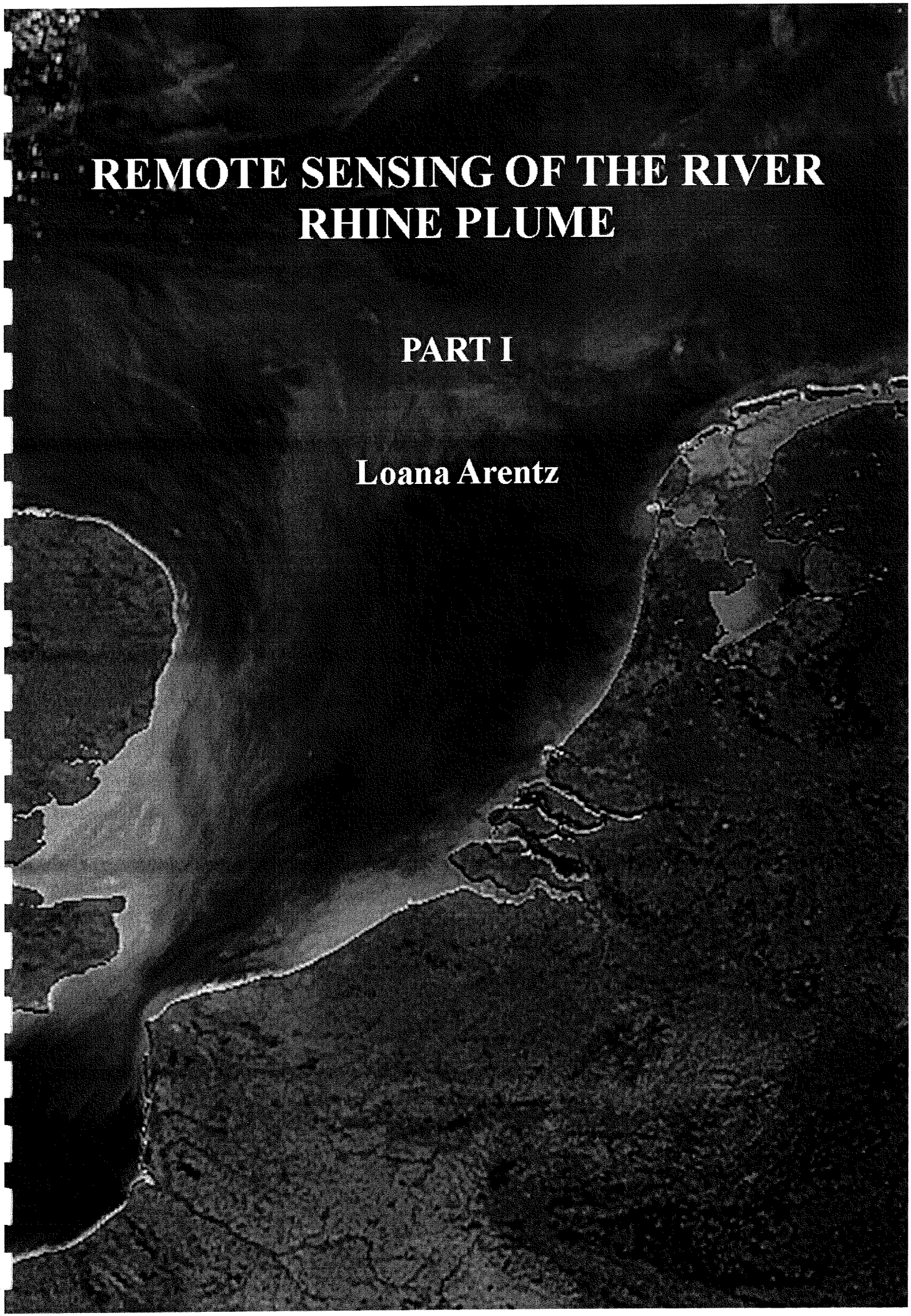

REMOTE SENSING OF THE RIVER RHINE PLUME

PART I

Loana Arentz

REMOTE SENSING OF THE RIVER RHINE PLUME

PART I

M.Sc. thesis of Loana Arentz

Delft University of Technology
Faculty of Civil Engineering and Geosciences
Department of Hydraulic and Geotechnical Engineering
Section of Environmental Fluid Mechanics

December, 2004

Supervisors:
Prof.dr.ir. G. S. Stelling (TUD)
Dr. J. D. Pietrzak (TUD)
Ir. G. J. de Boer (TUD/WL|DH)
Drs. S. Tatman (WL|DH)
Dr.ir. J.C. Winterwerp (TUD/WL|DH)
Dr.ir. J. A. Roelvink (TUD/WL|DH)

Preface

This thesis presents the final instalment of my Master of Science studies at the Faculty of Civil Engineering and Geosciences, Delft University of Technology (the Netherlands). The thesis consists of two parts; part I is the thesis itself and part II consists of appendices which support the text in part I. Due to the large level of detail in the majority of the images it is recommended to view the images in both parts I and II in colour.

I would like to thank my supervisors, prof.dr.ir. G. S. Stelling, dr. J. D. Pietrzak, ir. G. J. de Boer, drs. S. Tatman, dr.ir. J.C. Winterwerp and dr.ir. J. A. Roelvink for their support and advice during the realization of this thesis. In particular I would like to thank Julie Pietrzak and Gerben de Boer for their daily supervision and unlimited help. Another thank you goes out to Gerben who developed a satellite data processing system that allowed me to produce the composite images presented in this thesis. Furthermore I would like to thank J. de Kok for sharing his views on SST imagery with respect to tracing the River Rhine plume.

The biggest thank you of all goes out to my parents for the freedom and support they gave me.

Loana Arentz
(Den Haag 2004)

Abstract

The data content of remote sensing (RS) images of sea surface temperature (SST) and normalized water-leaving radiance (nLw), for the year 1998, with respect to the River Rhine plume, is investigated. Questions that this study tries to answer are: is it possible to identify the plume from the available RS images, and under which conditions is this possible? How much information on the plumes behaviour can be derived from these images? Does or can this information contribute to our general knowledge of the plume?

The images provide a spatial resolution of 1 km^2 and a temporal resolution of 1 or 2 images per day per sensor for nLw and SST, respectively (in the case of a cloudless atmosphere). In the presence of clouds, no signal is detected for the area of surface water underneath the clouds.

Two hypotheses are set up to explain how the RS images can be used to trace the plume. In the hypotheses links are established between salinity gradients that delimit the plume and SST and nLw respectively. The results are based on these hypotheses.

From the available images, 9 SST images in spring provide detailed information on the stratified plume and allow for derivation of indirect information on sub-surface processes. In winter the temperature gradients as visible on SST imagery seem to indicate the broad plume patterns. From the nLw images it was not possible to identify the boundaries of the plume. However it is expected that the nLw images are an excellent source for monitoring suspended particulate matter (SPM) in the North Sea.

The general conclusion of this study is that the RS data used in this project provide a valuable source of information, with respect to the Dutch coastal zone, in addition to the currently available measurement techniques and computer models. The SST imagery turns out to be particularly useful for tracing stratification, whereas nLw imagery seems to be an excellent source for monitoring SPM in the North Sea. For detailed monitoring of the DCZ and the plume, increased spatial and temporal resolutions are required.

Contents

Preface i

Abstract ii

Contents iii

Glossary v

CHAPTER 1 1

INTRODUCTION 1
1.1 General 1
1.2 Proposal 3
1.3 Problem description and Objectives 4
1.4 Framework 5
1.5 Significance 6
1.6 Set-up of this study 6

CHAPTER 2 7

RHINE PLUME DYNAMICS 7
2.1 Introduction 7
2.2 Baroclinic effects 9
2.3 The tidal wave 13
2.4 Wind 15
2.5 Pulsating discharge 16

CHAPTER 3 18

METHOD 18
3.1 Introduction 18
3.2 Hypotheses 18
3.2.1 Hypothesis 1: Sea surface temperature 19
3.2.2 Hypothesis 2: Normalized water-leaving radiance 22
3.3 Remote sensing images: Display and composition variants 24

CHAPTER 4 27

RESULTS 27
4.1 Introduction 27
4.2 Cloud cover 27
4.3 Analysis of the 156 SST images 30
4.4 Analysis of the 163 nLw images 38
4.5 Cross-correlation? 41
4.6 Analysis of the stratified plume 43

CHAPTER 5 ..... **50**

DISCUSSION **50**
5.1 Summary 50
5.2 Conclusions 51
5.3 Recommendations 52

Acknowledgments **53**

References **54**

Glossary

AVHRR	Advanced Very High Resolution Radiometer, a thermal satellite sensor
CDOM	Coloured Dissolved Organic Matter
DAAC	Distributed Active Archive Centre, provide earth observation data and services for global change research (NASA)
DCZ	Dutch Coastal Zone
GAC	Global Area Coverage, data format satellite sensor data
GMT	Greenwich Mean Time
GSFC	Goddard Space Flight Centre, provide earth observation data and services for global change research (NASA)
HRPT	High-Resolution Picture Transmission
KNMI	Koninklijk Nederlands Meteorologisch Instituut, Royal Netherlands Meteorological Institute
LAC	Local Area Coverage, data format satellite sensor data
LOICZ	Land-Ocean Interactions in the Coastal Zone, a project of the International Geosphere-Biosphere Programme
Lw	Water-leaving radiance
MERIS	MEdium Resolution Imaging Spectrometer Instrument, an ocean colour satellite sensor
MODIS	Moderate Resolution Imaging Spectroradiometer, an ocean colour satellite sensor
MUMM	The Management Unit of the North Sea Mathematical Models, a department of the Royal Belgian Institute of Natural Sciences
NASA	National Aeronautics and Space Administration, United States
NIOZ	Royal Netherlands Institute for Sea Research
nLw	normalized water-leaving radiance
NOAA	National Oceanic and Atmospheric Administration
NWO-ALW	Nederlandse organisatie voor Wetenschappelijk Onderzoek – Aard- en Levenswetenschappen (Netherlands Organisation for Scientific Research – Earth and Life Sciences)
PI	Principal Investigator
POES	Polar Orbiting Environmental Satellites
PSU	Practical Salinity Units
RIKZ	Rijksinstituut voor Kust en Zee, National institute for Coast and Sea
RIZA	Rijksinstituut voor Integraal Zoetwaterbeheer en Afvalwaterbehandeling, Institute for Inland Water Management and Waste Water Treatment.
ROFI	Region Of Freshwater Influence
RS	Remote Sensing
SeaDAS	SeaWIFS Data Analysis System

SeaWIFS	Sea-viewing WIde-Field-of-View-Sensor, an ocean colour satellite sensor
SPM	Suspended Particulate Matter
SST	Sea Surface Temperature
TSM	Total Suspended Matter
UTM	Universe Transverse Mercator

Chapter 1

INTRODUCTION

1.1 General

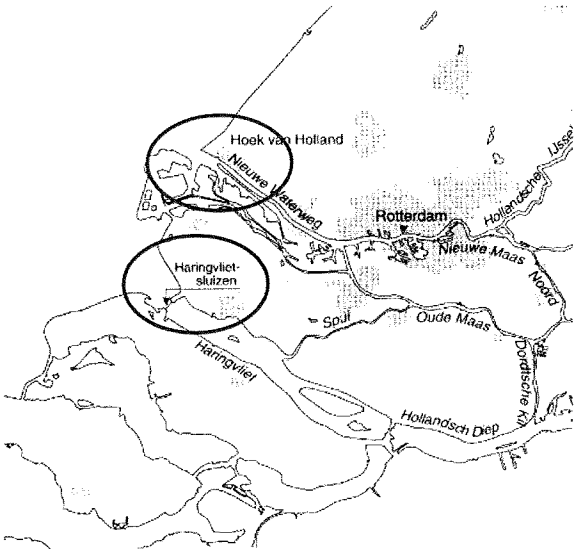

Fig. 1. 1
Rotterdam Waterway (Nieuwe Waterweg) and Haringvliet sluices. Image: www.haringvlietsluizen.nl.

River plumes are formed by river outflows discharging into coastal seas. The River Rhine plume is formed by the discharge of water from the rivers Rhine, Muese and Scheldt. The yearly average discharges of the river Muese and Scheldt, of 320 m^3s^{-1} and 120 m^3s^{-1} respectively, form only a limited contribution to the overall buoyancy compared with the average discharge of 2200 m^3s^{-1} of Rhine water[1]. The discharges of both the rivers Rhine and Muese into the North Sea are divided between the Rotterdam Waterway (New Waterway) and the Haringvliet sluices (see Fig 1.1).

As the buoyant inflow encounters the more dense sea water, and if mixing is limited, a bulge of freshwater is formed in front of the outlet. A density front separates the buoyant water from the North Sea water (see Fig. 1.2). The Coriolis force deflects the freshwater to the right, forming a narrow coastal current. Freshwater and land-derived materials are transported in this coastal current. River plumes can maintain their structure for hundreds of kilometres (e.g. Visser et al., 1994; Kourafalou et al. 1996, Pietrzak et al., 2002)

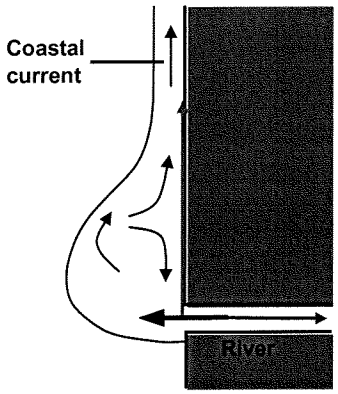

Fig. 1. 2
Top view of a river plume (Northern Hemisphere). y-axis is positive to the north and x is positive to the east. Image: Jacobs (2004).

[1] Source discharges: http://www.haringvlietsluizen.nl

In this thesis the different types of river plume response are classified as stratified, partially mixed or well-mixed (see Fig 1.3). Stratified implies the case of a well defined vertical density gradient at a given offshore location, whereas well-mixed implies the other extreme of a homogeneous water column at any given position within the plume, in which the density gradient increases in the offshore direction. The density in a well-mixed plume is still lower than the density of the offshore sea water, which results in a clear offshore boundary, and hence delineation of the plume. Partially mixed implies all transitional appearances between a stratified and a well-mixed plume.

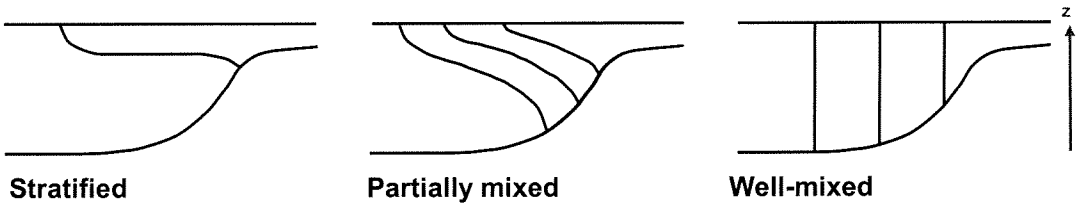

Fig. 1. 3
River plume appearances in the vertical (forms of stratification). The *z*-axis is positive in the upward direction.

When mixing energies are low, the lighter freshwater overlies the denser salt North Sea water resulting in a stratified plume. The breakdown of the stratification resulting in a well-mixed plume can be caused by turbulence generated at the surface (wind) and bottom boundaries (tidal currents), or at the density interface (Kelvin Helmholtz-instabilities) (Lewis 1997).

Tides and winds provide the main sources of energy for breaking down the stratification of the plume in the shallow Dutch coastal zone (DCZ). Still, the density field in the DCZ is dominated by some degree of stratification (Simpson et al., 1993). The appearance of the plume and the flow in the plume are the result of a continuous competition between the stratifying influence of buoyancy input (river run-off) and the net mixing effect of wind and tides.

The River Rhine plume has a significant impact on the currents in the DCZ and is extremely important in determining the transfer of matter and pollutants in coastal seas. It is of considerable interest to improve the understanding of the temporal and spatial structure of the Rhine plume, because of its influence on the circulation in the southern North Sea, and therefore its influence in relation to the ecosystem and environmental problems.

1.2 Proposal

At present, the available information on the Rhine plume is not sufficient to fully understand the physics responsible for its behaviour. The use of remote sensing (RS) images in addition to the currently available field measurements and computer models has high potential in this respect (see section 1.5). This project investigates if RS data can be used in a shallow coastal environment such as the North Sea. **Is it possible to identify the River Rhine plume from RS images, and under which conditions is this possible? Can RS images contribute to our general understanding of the plume behaviour?**

The main advantage of RS images is that they provide a synoptic view (RS data cover the entire North Sea), enabling the user to detect certain surface features which cannot be detected with point or transect field measurements. For example, think of the spatial variability seen in a classic image of the Gulf Stream, see Fig. 1.4.

Fig. 1. 4
Ocean colour image of the Gulf Stream
Image: http://rst.gsfc.nasa.gov/Sect14/gulf_stream_modis.jpg.

If we want to use the images to help us gain a better understanding of the plume, we first need to determine under what conditions the plume can be traced with RS images. Two data sources are available to us: thermal and optical RS data. The thermal RS data used in this project provide Sea Surface Temperature (SST) images, which are measured with the Advanced Very High Resolution Radiometer (AVHRR) on the National Oceanic and Atmospheric Administration's (NOAA) Polar Orbiting Environmental Satellites (POES) satellites. The optical RS data provide images of normalized water-leaving radiance (nLw), which are measured with the Sea-viewing-WIde-Field-of-View-Sensor (SeaWIFS) onboard Orbimage's SeaStar satellite. Both have a data history of several years: AVHRR: 1990 - today and SeaWIFS: September 1997 - today.

Both data sources provide a spatial resolution of approximately 1 km^2. Since the baroclinic (internal) Rossby radius of deformation (Ro_i) is in the order of twenty kilometres (see section 2.2), it is expected that 1 km^2 resolution is just sufficient to detect the spatial variability of the plume. The temporal resolution of at least one image per day per instrument may or may not be sufficient to assess the development of the plume. Cloud cover influences this number; in the presence of clouds, no signal is detected for the area of surface water underneath the

clouds. This often results in one image per instrument per two or three days only (see section 4.2). See Table 1.1 for an overview.

Table 1. 1 Overview: in the case of cloudless atmosphere in an average situation

Sensor	**AVHRR**	**SeaWIFS**
Measures	SST	nLw
Measures at	Day & night	Day
Revisit time	1/12hrs	1/12hrs
Measures from	2 satellites	1 satellite
Nr of images/day	4	1
Spatial resolution	1 km^2	1 km^2

1.3 Problem description and Objectives

Description of the problem investigated: There is a need to understand the data content of RS images. Under what conditions is it possible to trace the plume patterns from optical and thermal RS images? How much information on the plumes behaviour can be derived from these images? Can this information contribute to our general knowledge of the plume?

Objectives: The main objective of this M.Sc. project is to identify conditions under which the plume can be traced, and then to quantify and explain the behaviour of the River Rhine plume from thermal and optical RS images for the year 1998[2].

The parameters describing the behaviour of the Rhine plume that need to be quantified under certain conditions are:

1. Width (offshore extent) of the plume.
2. The northward progression of the plume.
3. If possible the thickness of the plume (determined indirectly).
4. The meandering of the plume (along-shelf wavelengths) and scale of eddies if any present.

Also the variability of the parameters will be assessed:

5. The time scales over which these variations take place.
6. Correlation with meteorological events such as wind speed and direction and the river runoff. Compare time scales of meteorological events to time scales of plume changes (upwelling, downwelling, mixing).
7. Artificial variability: the spatial and temporal coverage of the RS images, on which the numbers are based as well as the effects of cloud cover.

[2] 1998 is selected, because it corresponds with previous analyses of the SeaWIFS data carried out by WL|Delft Hydraulics.

1.4 Framework

This M.Sc. project takes place in the framework of the NWO-ALW funded project 'The transport of fine sediment in the Dutch coastal zone' (PI Dr. Ridderinkhof, NIOZ).

Main motivation for the study: Recent studies[3] suggest, that the transport of suspended particulate matter[4] (SPM) in the DCZ towards the Wadden Sea in general, and through the Marsdiep inlet in particular, is in the order of 10-15 Mton/yr. This is an order of magnitude larger than previous studies suggest. The transport and nature of these sediments not only affect water quality, turbidity levels, pollutant transport and hence the ecology and health of the coastal environment, but also the morphological evolution of our coastline.

The research programme involves a post-doc (NIOZ) and a Ph.D. student (TU Delft). Two M.Sc. projects form sub-themes of the Ph.D. project.

Objective Ph.D. project: The main objective of the Ph.D. project is to gain quantitative knowledge, on the conditions controlling the behaviour of the River Rhine Plume, and the transport of SPM in the DCZ, on the time scale of months and length scales of tens of kilometres.

Approach: Since Simpson et al., (1993) and De Kok (1992) showed that the transport of SPM in the DCZ takes place primarily in the River Rhine plume along the coast, the current (initial) phase (09/2003 – 12/2004) of the Ph.D. project focuses on the hydrodynamics of the Rhine plume (without SPM).

In one M.Sc. project, W. Jacobs has set up an idealised numerical model of the DCZ in order to gain insight into the basic plume behaviour (see Jacobs 2004). This project is the second M.Sc. project

In future work the SPM fluxes will be modelled by the Ph.D. student (G. de Boer) with the ZUNO[5] model (developed by WL | Delft Hydraulics). Because the model results will be validated qualitatively with RS images (patterns), it is important that we understand the data content of the RS images.

---

[3] data analysis by Ridderinkhof et al, 2002: ongoing ferry observations in the Marsdiep tidal inlet to the Wadden Sea

[4] In this thesis Suspended Particulate Matter (SPM) is defined as all matter that stays on a 0.7 μm pore size filter.

[5] ZUNO: ZUidelijke NOordzee (southern North Sea)

1.5 Significance

RS images offer the potential to study and describe the spatial patterns of the plume. If it is possible to quantify and explain the plumes spatial patterns from RS images then:

1. the physical processes responsible for the advection and mixing of the Rhine plume may be better understood, and
2. computer models cannot only be validated, but the RS images can also be used in a data assimilation system, hence improving the predictive powers of models such as the ZUNO model.

1.6 Set-up of this study

Interpreting RS images that only provide information on the sea surface, requires knowledge of both the physical processes responsible for the advection and mixing of the fresher plume water, and RS techniques. In Chapter 2 some basic concepts of river plume dynamics are described. Chapter 3 describes the method used to reach the objectives. In this chapter two hypotheses are developed on which the results, which are presented in Chapter 4, are based. Chapter 4 starts with an analysis of both sequences of images (SST and nLw), which are available to us. In this analysis all the images are selected on which (according to the hypotheses) the Rhine plume is expected to be visible. Once the images showing the plume are selected, the spatial patterns are quantified using the parameters as outlined in section 1.3. In Chapter 5 a summary of the study together with the conclusions and recommendations are presented. Background information on RS (e.g. theoretical background, data acquisition and processing) can be found in Appendix 1.

Chapter 2

RHINE PLUME DYNAMICS

2.1 Introduction

The physical regime of the River Rhine plume is radically different from the deeper parts of the North Sea, where heating and cooling through the water surface constitute the predominant exchange of buoyancy (Simpson et al., 1993). River plume dynamics are initiated by the buoyancy input from the rivers and are for the most part baroclinically mediated (Visser et al., 1994). In Fig. 2.1 the density is plotted as a function of varying salinity and temperature. Water density is determined by salinity, temperature and pressure. But in shallow coastal areas such as the Rhine plume area, pressure effects can be neglected. The dominant influence of salinity differences over temperature differences on density is clearly visible, indicating that in the River Rhine plume, which is also characterised by large differences in salinity, the density field is mainly salinity controlled.

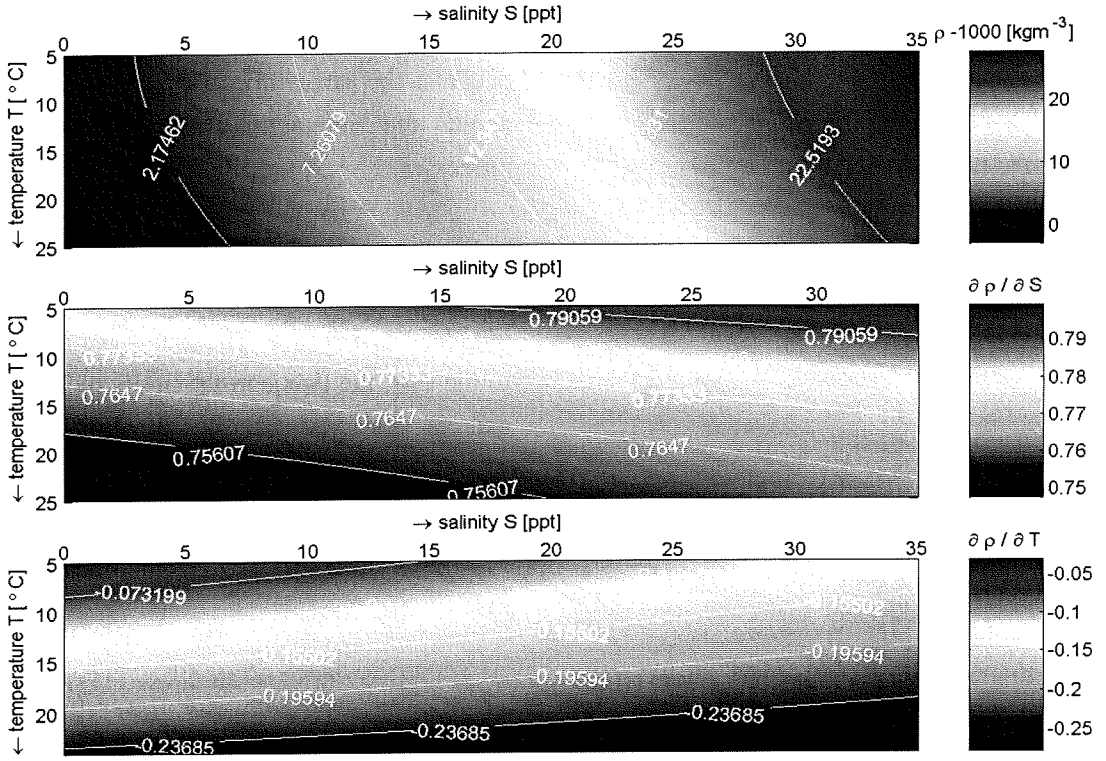

Fig. 2. 1
The equation of state is plotted showing the density of water as a function of temperature and salinity (assuming constant pressure). Delft3D manual March 2003 equations (9.35) and (9.36).

Due to the shallowness of the southern North Sea, mixing energies are often too high to allow for a stratified plume. Instead of the comparatively regular pattern of seasonal stratification, which can be observed in the deeper parts of the North Sea, the Rhine plume experiences a continuous alternation between stratified and well-mixed conditions. This alternation occurs on relatively short time-scales, in response to changes in stratifying freshwater outflow, and the mixing influence of stirring by tidal flow, wind and waves, respectively (Simpson et al., 1993). The **stratification-mixing competition** is relatively difficult to predict because many random components, such as variability of run-off, wind- and wave stirring, as well as up- and downwelling events (Münchow and Garvine, 1993) show an irregular variation in mixing and straining (stratifying) of the density field.

In order to gain knowledge on the hydrodynamic behaviour of the Rhine plume, from RS images, a description of the dominant physical processes responsible for the advection and mixing (horizontal and vertical) of the freshwater will be given. The effects of wave-induced currents are neglected in this project. Because the complex dynamics of the River Rhine plume are for the most part controlled by salinity, a description of the effects of density gradients will be given first in section 2.2. Section 2.3 describes the physical processes initiated by the tidal wave. The tidal wave exerts both a barotropic and baroclinic influence. Section 2.4 describes the effects of wind. The last section, section 2.5, describes the physical mechanism of a pulsating discharge. It should be noted that many of the processes responsible for the advection and mixing of the plume occur at the same time and little is known about the interaction of the separate processes.

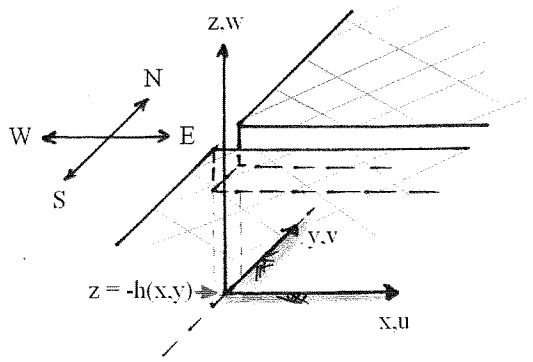

Fig. 2. 2
Cartesian co-ordinate system used in this project.

In the following description a Cartesian co-ordinate system (x, y, z) is used such as indicated in Fig. 2.2. The x-axis is directed to the east, the y-axis to the north and the z-axis is positive in the upward direction, with $z = -h(x, y)$ at the bed and $z = \eta(x, y)$ at the free surface. At the free surface $h = 0$.

2.2 Baroclinic effects

Gravitational (baroclinic) circulation: The average discharge of 2200 m^3s^{-1} of fresh Rhine water in the shallow North Sea generates a cross-shore density gradient, which has a major implication for the water column structure and dynamics in the plume. In the absence of rotation and stirring, the riverine input forms a growing bulge of freshwater near the estuary mouth. The resulting pressure gradient, tends to induce stratification through a gravitational (or estuarine) circulation, in the direction of the horizontal (cross-shore) density gradient (see Fig. 2.3).

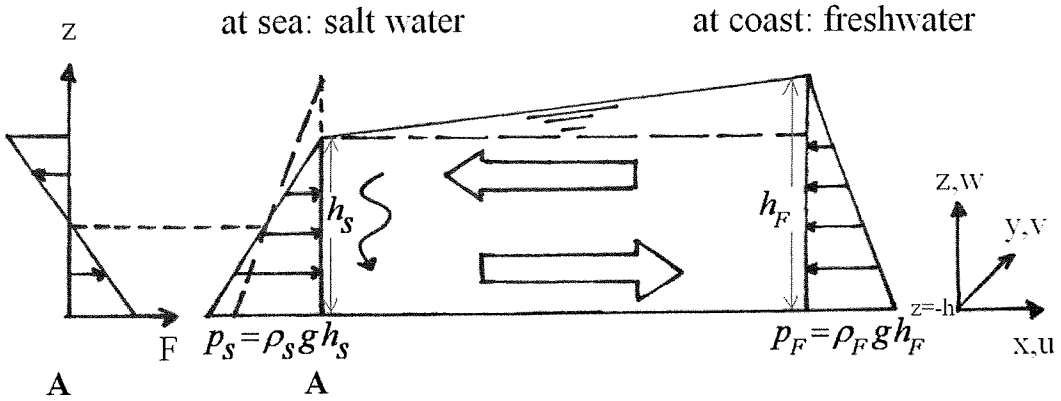

Fig. 2. 3
In the absence of rotation and stirring: cross-shore gravitational circulation due to baroclinic pressure gradient: net surface seaward flow and bottom landward flow. Where p_s and p_F denote the pressure at the bottom due to salt- and freshwater respectively (N). ρ_s And ρ_F denote the salt- and freshwater density respectively (kg m^{-3}), and h the water depth (m).

Coriolis: At the scale of the Rhine plume, the influence of the earth's rotation cannot be neglected. The span where the influence of Coriolis cannot be neglected is indicated by a Rossby radius of deformation (*Ro*), which is a length scale indicating the relation between wave speed and the Coriolis parameter (see equation (1)).

$$\mathrm{Ro} = \frac{c}{f}\ [m] \qquad (1)$$

where c is the wave speed (m s^{-1}) and f is the Coriolis parameter (s^{-1}).

Because the Coriolis parameter is assumed to be constant over the Rhine plume area, the size of this length scale is determined by the wave speed (c). The largest length scale appears for the largest wave speed; the (external) shallow water gravity wave speed for homogeneous waters (c_0), and is referred to as the external or barotropic Rossby radius of deformation (Ro_e).

Assuming a water depth of h = 25 m, f = 1.15x10^{-4} s^{-1} and g = 9.81 m s^{-2}; gives a wave speed of $c_0 = \sqrt{g\,h} = 15.66\,\mathrm{m\,s^{-1}}$ and a barotropic Rossby radius of deformation of $\mathrm{Ro_e} = \mathrm{O}(140\ \mathrm{km})$.

In the case of 2-layered stratified waters, the (internal) wave speed (c_i) decreases due to the reduced gravity effect (g'), where $g' = g \cdot (\rho_s - \rho_f)/\rho_f$. Assuming a density difference in the range of 10-30 kg m^{-3} gives a g' ranging between: 0.10 - 0.29 m s^{-2}; c_i ranging between: $c_i = \sqrt{g'\,h} = 1.57 - 2.71$ m s^{-1} and an internal or baroclinic Rossby radius of deformation in the order of: $\mathrm{Ro_i} = \mathrm{O}(14 - 20\ \mathrm{km})$. This number indicates that the influence of the earth's rotation cannot be neglected in the Rhine plume.

Thermal wind balance: The earth's rotation limits the cross-shore movement of the density currents. The offshore spreading surface flow, in the low salinity bulge, achieves equilibrium when the baroclinic pressure gradient (produced by the cross-shore buoyancy fluxes) is balanced by the Coriolis force. I.e. thermal wind balance is achieved, and a narrow, northward flowing, baroclinic coastal current is formed with the coast to its right (see Fig.1.2 section 1.1).

To explain this, consider a geostrophic flow. The equations of motions reduce to two horizontal geostrophic equations (see equations (2) and (3)) and the hydrostatic relationship, where the Boussinesq approximation has been made (see equation (4)).

$$\frac{1}{\rho_0}\frac{\partial p}{\partial x} = f\,v \qquad (2)$$

$$\frac{1}{\rho_0}\frac{\partial p}{\partial y} = -f\,u \qquad (3)$$

$$\frac{\partial p}{\partial z} = -\rho\,g \qquad (4)$$

where ρ_0 is a reference density which could be the freshwater density ρ_F (kg m^{-3}), p is the pressure (N), u is the cross-shore velocity (m s^{-1}) and v is the alongshore velocity (m s^{-1}).

Differentiation of the geostrophic equations with respect to z, and substitution of the hydrostatic relationship, leads to the thermal wind relation given by equation (5). Here only the x-direction equation is given.

$$\rho_0 f\frac{\partial v}{\partial z} = -g\frac{\partial \rho}{\partial x} \qquad (5)$$

where ρ is the density of the water (kg m^{-3}).

This simple balance in equation (5) tells us, that an alongshore vertical shear will balance the cross-shore density gradient. It also tells us that, when looking in the direction of the flow, the lighter water will be located on the right hand side. Basically, the cross-shore gravitational circulation, such as illustrated in Fig 2.3, is influenced by the earth's rotation to produce a thermal wind balance as illustrated in Fig 2.4 (see also video representations at http://paoc.mit.edu) and Pietrzak (2004).

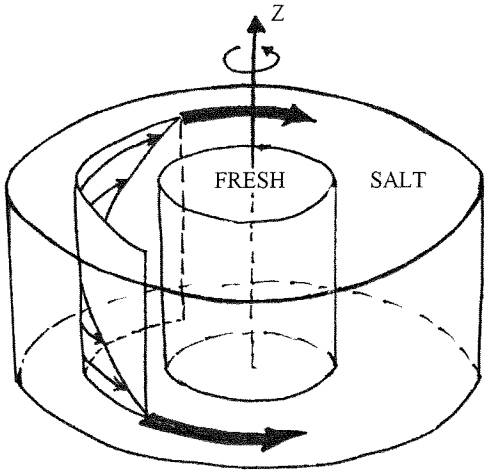

Fig. 2. 4
Thermal wind balance (rotating frame with z=-h at the bottom). Image redrawn from: http://paoc.mit.edu.

With the exclusion of all external forcing except river discharge, Chao and Boicourt (1986) indicate, that the width of the right-bounded coastal current, is comparable to the scale of the baroclinic Rossby radius of deformation (Ro_i).

Coastal trapping: Because the thermal wind balance only prescribes an alongshore velocity gradient in the vertical ($\partial v/\partial z$) and no zero point, the zero point is assumed to be at the bottom because bottom currents are generally retarded by bottom friction and are much smaller than surface currents. The net result of this thermal wind balance is a jet along the freshwater front, with highest velocities normal to the highest cross-shore density gradients. This is illustrated in Fig. 2.5: the cross-shore gradient of alongshore velocities cause coastal trapping of freshwater. It should be noted that the alongshore velocities generated by the cross-shore density gradient (~0.1-0.2 m s^{-1}), are on average an order of magnitude smaller than the alongshore tidal near surface current velocities (~1 m s^{-1}) (De Ruijter 1997). The tidal residual northward alongshore flow is in the order of ~ 0.10 m s^{-1} (Simpson 1997).

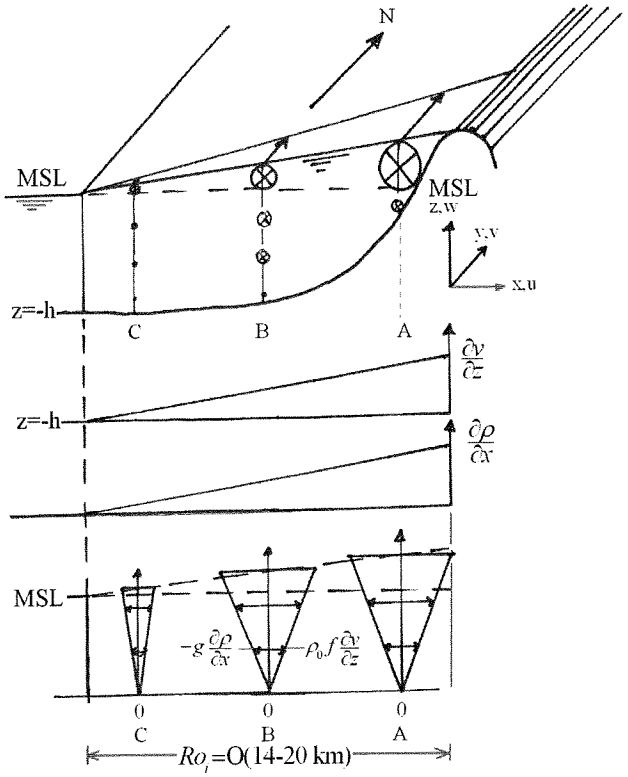

Fig. 2. 5
Thermal wind balance and coastal trapping: the alongshore shear in the vertical balances the horizontal density gradient. (Co-ordinate system : z = -h at the bottom)

Close to the outflow point the alongshore freshwater front is very sharp (Ruddick et al., 1994) and becomes wider more to the north, where it is located at distances of 20-50 km from the coast (De Ruijter et al., 1997). The plume of freshwater gradually mixes with ambient sea water, which erodes the buoyancy difference.

The above-described thermal wind situation represents a first order geostrophic flow. In reality non-linear terms and friction also play a role. Especially the role of bottom friction in the shallow Rhine ROFI cannot be neglected and results in a situation where the prescribed $\partial v/\partial z$ will not fully develop.

Damping at the pycnocline: The density stratification causes very strong damping of vertical turbulent exchange of mass, heat and salinity at the pycnocline (Lewis 1997). This leads to vertical distributions of SPM with relatively high near-bottom concentrations. This important baroclinic effect should be kept in mind when interpreting ocean colour (nLw) RS images. **Sediments, which are trapped below the pycnocline, do not appear on RS images of ocean colour.** The stronger the degree of stratification: the greater the tendency for vertical turbulent motions to be damped at the pycnocline. This damping at the pycnocline is suggested to have important consequences for tidal dynamics. This is explained in section 2.3 (tidal straining).

Baroclinic instability: One important mixing mechanism appears to be due to baroclinic instability. The buoyancy driven baroclinic flow itself may or may not be stable. When the vertical velocity gradient (shear) in stratified waters exceeds a certain threshold, baroclinic instability arises, see Pedlosky (2003) and references therein. Fig. 2.6 highlights the variable and energetic nature of these flows. Typically meandering and eddy formation are observed. The meandering and eddy formation may cause transport and mixing across the density front, resulting in an increase of the average width of the front. Cross-frontal mixing enhances the exchange between the coastal zone and the sea, which would otherwise be blocked by coastal trapping. Only persistent and strong offshore and on-shore winds have a comparable effect (De Kok 1994a). Typical wavelengths of 10-30 km can be expected in the Rhine plume (De Kok 1994a).

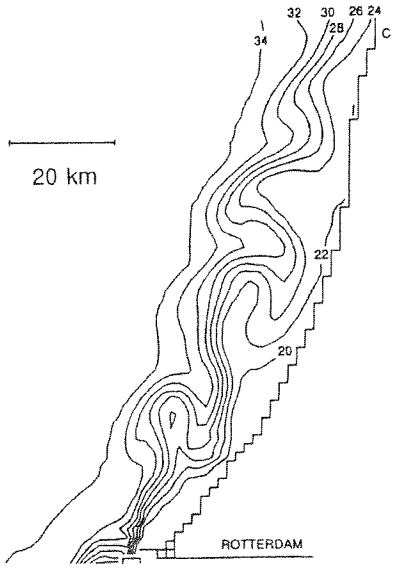

Fig. 2. 6
Numerical simulation with a 2-layer model showing meandering of the Dutch coastal current due to baroclinic instabilities. The grid spacing of 1600 m limits the reproduction of wavelengths smaller than 10 km. Image: De Kok (1994a).

2.3 The tidal wave

The tidal wave enters the North Sea from the north and runs down the English coast to the right, meets another wave entering the North Sea through the Channel, and then runs up along the Dutch coast (see Fig. 2.7). The tidal wave generates an alongshore-reversing tidal current. A small net residual tidal flow is directed northward in the order of 0.1 m s^{-1} (Simpson 1997). Tidal motions play an important role in the generation of turbulence in the shallow River Rhine plume, and are therefore often responsible for the breakdown or onset of stratification. The tide exerts a low and high frequency forcing. The low frequency tidal forcing is expected to induce a regular variation in mixing and straining of the density field over the spring-neap tidal cycle, whereas the high frequency tidal forcing can be observed at neap tide and is often referred to as tidal straining.

Fig. 2. 7
The tidal wave. Image: redrawn from www.rootshell.be.

Spring-neap cycle: As the tidal wave propagates along the Dutch coast, bottom friction absorbs energy, which causes the amplitude to decrease as the wave propagates northward. As a result, a phase difference between horizontal and vertical tide (30-60 minutes in the DCZ) is generated. The tidal wave deforms and generates 'shallow water tides'. The shallow water tides in the southern North Sea are dominated by semi-diurnal constituents, principally the M2 tide but with a significant S2 contribution, which results in a spring-neap cycle (see Fig. 2.8). The level of turbulence, modulated by the low frequency spring-neap tidal forcing, varies over the tidal cycle and exerts a mixing influence on the plume (Simpson 1997).

The ratio of spring- to neap- tidal currents in the DCZ is typically ~2. Since the amount of mixing is proportional to (tidal current amplitude)^3, the energy available for mixing during spring tide is a factor ~8 (2^3) larger than during neaps (Simpson 1997). Typically, by the time of spring there is vertical homogeneity, which persists until mixing diminishes before the next neap period. This spring-neap tidal forcing is relatively well predictable since it occurs at well-defined astronomic periods. When wind stress is low, this variation tends to impose a 14.5-day variation on the stability in the Rhine plume (see Fig. 2.8).

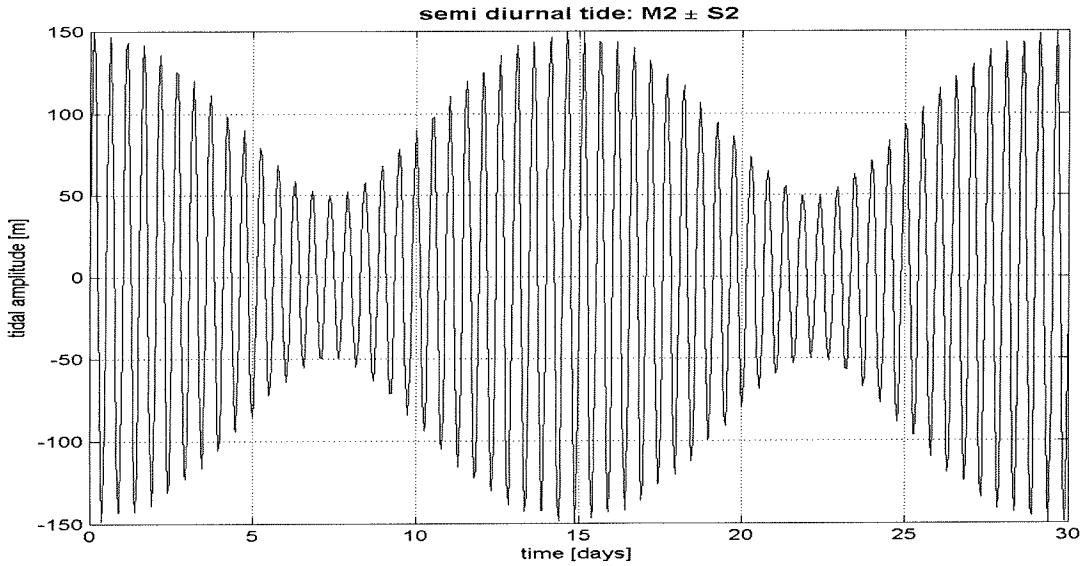

Fig. 2. 8
Tidal forcing from M2 and S2 semi-diurnal tidal constituents results in 14.5 day spring-neap cycle.

Kelvin wave: When assuming that the depth-averaged cross-shore tidal velocities ($\bar{u} = 0$) are zero, the shallow water tidal wave propagating along the Dutch coast can be approximated by a Kelvin wave. A Kelvin wave is a coastally trapped (non-dispersive) wave motion. The wave propagates parallel to the shore with the speed of shallow water gravity waves (c_0). The water level profile, perpendicular to shore, decays exponentially seaward (Northern Hemisphere). The decay scale is limited by the earth's rotation, and the amplitude of the Kelvin wave becomes zero at approximately three times the barotropic (external) Rossby radius of deformation (Ro_e is in the order of 140 km; see section 2.2). The dynamics of a Kelvin wave are such that it is exactly a linearized shallow water gravity wave in the alongshore direction, and exactly geostrophic in the cross-shore direction.

Tidal straining: In the case of stratification, which generally occurs during neap tide, the vertical structure of the plume is observed to oscillate with a semi-diurnal frequency between stratified and well-mixed conditions (Simpson et al., 1993, Simpson and Souza, 1995, Souza and Simpson, 1996). Tidal straining results in a semi-diurnal oscillation of the offshore extent of the plume (at the sea surface). This high frequency cross-shore tidal straining is the result of the interaction between cross-shore shear in the tidal current and the cross-shore horizontal density gradient.

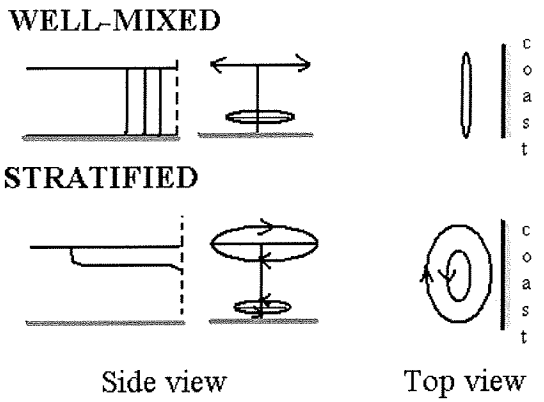

Fig. 2. 9
Tidal current ellipses in case of a well-mixed or stratified plume. Image: redrawn from and Souza and Simpson 1996 and Simpson 1997.

According to Visser et al (1994), the cross-shore component of shear comes from a semi-diurnal change in the form of the tidal current ellipses. The vertical structures of these tidal ellipses are observed to be significantly different for stratified and well-mixed conditions. In particular, during well-mixed conditions, tidal currents are essentially rectilinear and directed parallel to the coast (cross-shore tidal velocities are zero). With the onset of stratification, significant cross-shore components reaching 40% of the magnitude of the alongshore components appear. These components are 180° out of phase from near-surface to near-bottom with surface currents rotating clockwise, and bottom currents anti-clockwise. This is illustrated in Fig. 2.9.

Visser et al., (1994) suggest that tidal currents depend not only on tidal forcing at well-defined astronomic periods, but also on the less regular and more unpredictable stratifying and mixing processes that take place here. The strong cross-shore tidal currents during the neap/stratified period can only develop due to a decoupling of the upper and lower portions of the water column due to reduced viscosity within the pycnocline. Visser et al., (1994) suggest that, as a result of this viscous decoupling between the layers, water column response to the same periodic barotropic forcing may be significantly different from time to time during stratified appearances of the plume, depending on the degree of viscous decoupling.

2.4 Wind

Another main source of energy for mixing in the Rhine plume, apart from the tides, is provided by wind. The DCZ is too shallow to apply Ekman wind dynamics in which the wind friction is primarily balanced by the Coriolis force. Ekman wind dynamics is the process whereby surface wind stress drives a relatively shallow upper ocean flow that transports water to the right of the wind direction (in the Northern Hemisphere). Again the role of bottom friction cannot be neglected in the shallow Rhine plume area and therefore, in contrast to deeper 'bottom-frictionless-Ekman waters', the wind stress is primarily balanced by bottom friction. The possible interactions between wind stress and river plumes (wind-induced advection) are not yet fully understood. Observations (Münchow and Garvine 1993) as well as numerical simulations (Kourafalou et al., 1996b) of river plumes consistently show that steady alongshore winds act to advect the plume either on- or offshore in a manner consistent with Ekman dynamics (Fong 1998). Upwelling winds on the Northern Hemisphere tend to spread the plume offshore, diminishing the strength of the right-bounded coastal current (see Fig. 2.10). In contrast, downwelling winds strengthen the down coast transport of freshwater by enhancing cross-shore density gradients, and hence, the baroclinic coastal current (Fong 1998). This is illustrated in Fig. 2.11. The isopycnals tend to tilt to the vertical and the alongshore velocities increase. North-easterly winds along the Dutch coast exert an upwelling influence, while south-westerly winds exert a downwelling influence (De Kok, 1994a).

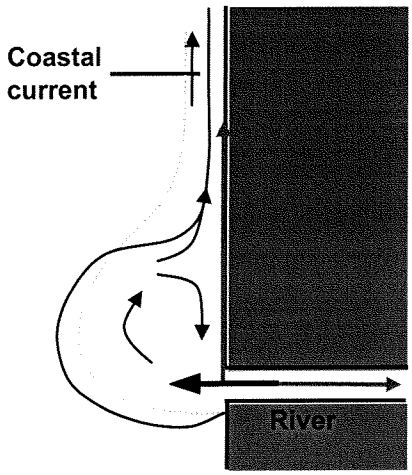

Fig. 2. 10
North-easterly winds: upwelling at coast
Image: redrawn from Jacobs (2004).

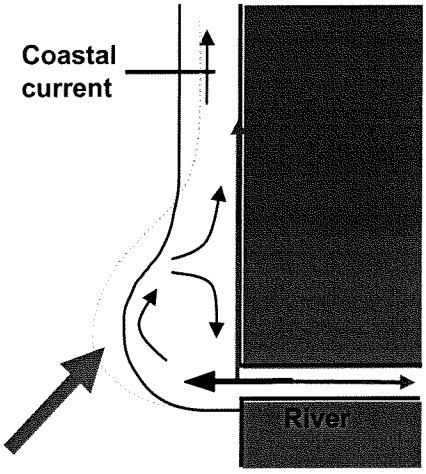

Fig. 2. 11
South-westerly winds: downwelling at coast
Image: redrawn from Jacobs (2004).

It should be noted that the influence of wind forcing can be two-fold. In the case of upwelling (north-easterly) winds the plume is not only advected offshore thereby enhancing stratification; it can also lead to the mixing of plume waters. The thin fresh upper layer has a large 'surface area per unit of buoyancy' exposed to wind stress, which requires little energy to mix up.

2.5 Pulsating discharge

The discharge of the water from the rivers Rhine and Muese is modulated by the tidal wave propagating along the Dutch coast. Dependent on the tidal current velocities upstream of the river mouth (in the case of the Rotterdam Waterway), larger or smaller amounts of freshwater are released into the North Sea. In particular, during periods of flood, the freshwater discharge is partly (and sometimes completely) blocked due to salt sea water which is entering the estuary, whereas during ebb, when the water level is low, large amounts of freshwater are discharged freely. The offshore spreading of the discharged 'pulses' of freshwater strongly depend on the ratio between advection and mixing rates. When the net discharge is halted at some point during the tidal cycle, the river water discharged over the previous tidal cycle is pinched off at the river mouth and exits on to the shelf as an isolated blob (De Ruijter et al., 1997). It is expected that a pulsating discharge may result in a meandering appearance of the plume (see Fig. 2.12), which should not be confused with the meandering due to baroclinic instabilities (see section 2.2).

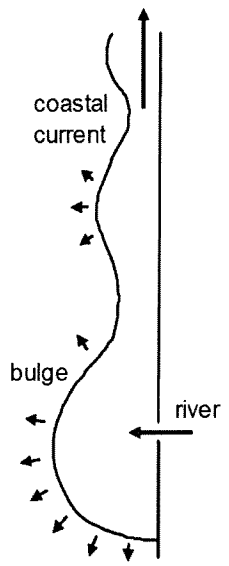

Fig. 2. 12
Meandering appearance of the plume due to pulsating discharge (Image: G. de Boer).

Another aspect to keep in mind, when interpreting RS images, is that the discharge of water from both the Rhine and the Muese is divided between the Rotterdam Waterway and the Haringvliet sluices. In order to minimise the salt intrusion into the Rotterdam Waterway estuary, the freshwater outflow is regulated by the Haringvliet sluices. The ebb opening of the sluices is therefore coupled with the Rhine discharge at Lobith. If the discharge is too low, the sluices are kept closed. This may result in a stagnation of discharge through the sluices in summer when discharges are generally low (see Fig. 2.13). The 1998-year-averaged Rhine/Muese discharge through the Rotterdam Waterway is measured to be approximately 1065 m^3 s^{-1}, and the discharge through the Haringvliet was 685 m^3 s^{-1} only (www.waterbase.nl).

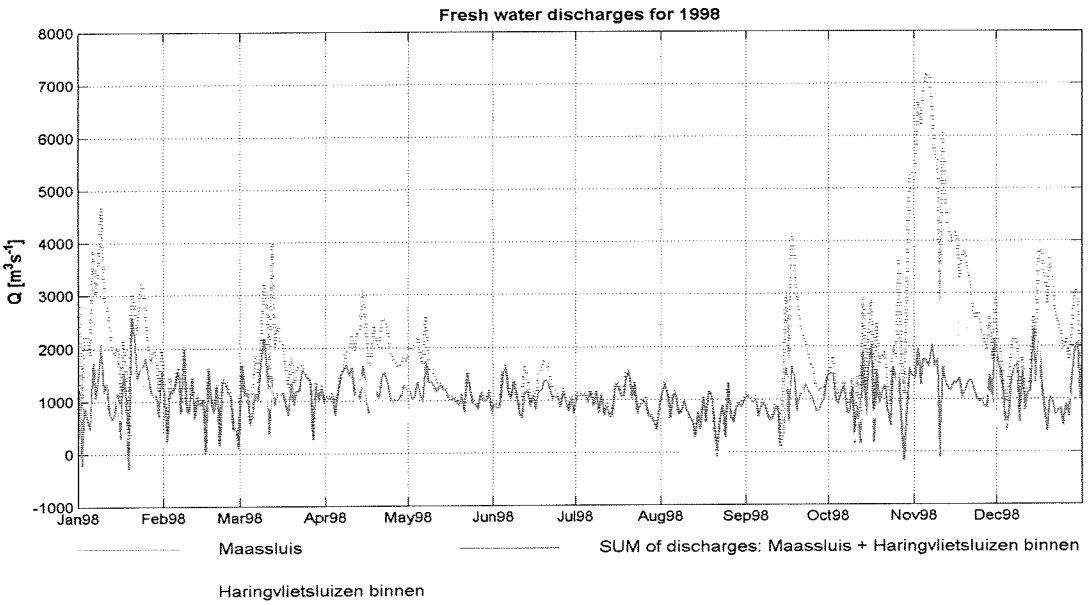

Fig. 2. 13
1998 Discharges: Maassluis (Rotterdam Waterway) & Haringvliet sluices (www.waterbase.nl).

Chapter 3

METHOD

3.1 Introduction

This chapter describes the method applied to reach the objectives. First, in section 3.2, two hypotheses are set up to explain how the available RS images can be used to trace the spatial patterns of the plume (see Fig. 3.1). A description is given of what to look for when analysing the images together with the assumptions that preceded this description. Then, section 3.3 explains how meteorological data, which are largely responsible for the plumes behaviour (see Chapter 2), can be combined with the RS images to produce various composite images allowing for optimal analysis of the images. Moreover, displaying the RS images in several representations is also dealt with. The hypotheses are tested in Chapter 4. Appendix 1 gives detailed background information on RS data, processing and satellites involved.

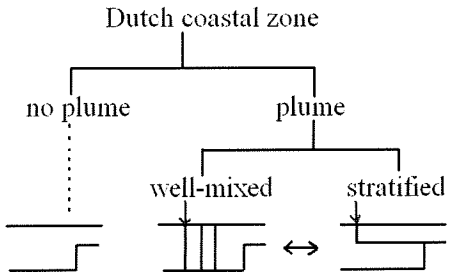

Fig. 3. 1
Schematization of the Dutch coastal zone.

3.2 Hypotheses

The hypotheses described in this section explain how the plume can be traced from RS images of sea surface temperature (SST) and normalized-water leaving radiance (nLw), which only provide information on the sea surface.

3.2.1 Hypothesis 1: Sea surface temperature

SST images provide the temperature of the sea surface. How can SST be related to the plume, which is governed by salinity differences? The hypothesis set up in this section makes a link between salinity and SST. This hypothesis is based on "salinity and temperature stratification in the Rhine plume" by De Kok et al., (2001).

Temperature differences between river and sea water can be used to trace the plume. In winter, the plume is generally colder than the surrounding sea water and in summer, vice versa. These temperature differences tend to fade away with time/distance from the river mouth as the river water mixes with the sea water.

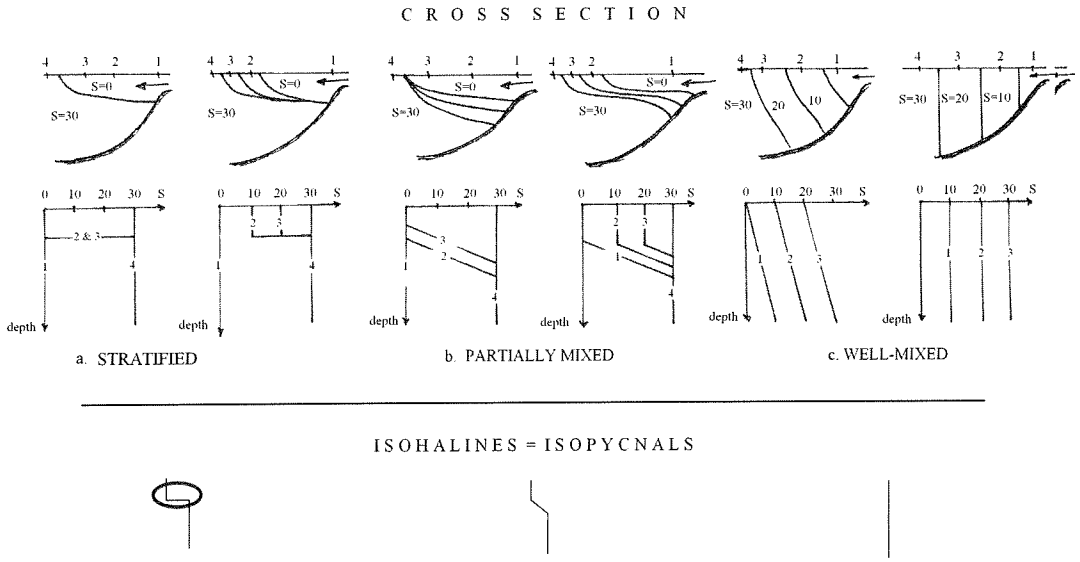

Fig. 3. 2
Top: different forms of stratification. Bottom: accompanying isolines.

In the case of a stratified plume the temperature difference between river and sea water is maintained due to damping of vertical turbulent exchange of mass, heat and salinity at the pycnocline (see circle in Fig 3.2). **The result is that temperature gradients as visible on SST imagery often coincide with salinity gradients that mark the stratified plume.** The degree of stratification determines the degree to which the temperature differences are maintained. Maximum damping occurs in the case of a stratified plume (case "a" in Fig. 3.2), which can be considered as an ideal case, which is unlikely to appear in nature. In the case of a well-mixed plume (case "c" in Fig. 3.2) no pronounced temperature gradients are expected to be visible on SST imagery as the relatively 'small' temperature difference is instantaneously mixed over the whole water column (no net temperature in/decrease in large volume expected). Often a more transitional appearance exists between the surface layer and the lower layers (case b in Fig. 3.2 partially mixed), which shows up as a more gradual temperature gradient on SST imagery. The initial temperature difference between river and sea water determines to what extent the river water can still be discerned on SST imagery.

Generally maximum temperature differences occur in late spring and early summer when the sea water is still cold and the shallow river water is warming up more rapidly. The temperature difference can be more than 10 °C and sea areas containing 20 % river water can still be discerned by their temperature contrast (De Kok et al., 2001). In winter the temperature difference is much less pronounced.

In the case of a partially mixed plume, the fresh surface layer as observed in the DCZ has a typical depth of 2-5 m and because of its shallowness the changes in temperature as a result of surface heat fluxes take place relatively quickly and can be quite substantial (same energy in- or output in smaller volume) (De Kok et al., 2001). These SST sinks and sources make SST a non-conservative tracer. We assume that the non-conservative nature of SST doesn't matter for our purpose, since we are not interested in exact numbers.

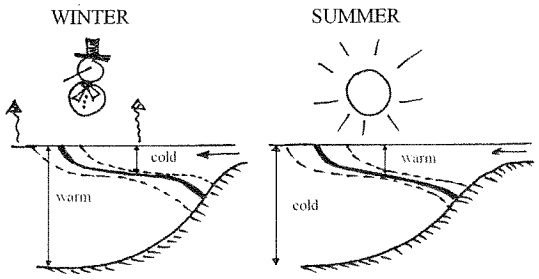

Fig. 3. 3
Extra temperature contrast between fresh- and saltwater due to surface cooling and heating.

Surface heat fluxes generally result in an extra temperature contrast between river and sea water which makes it easier to trace the stratified plume by its temperature contrast and to assess the degree of stratification. In winter, the shallow colder surface layer cools faster than the deeper surrounding waters and in summer, vice versa (see Fig. 3.3). The largest temperature gradients due to surface heat fluxes appear on sunny days in early summer, when the surface layer temperature difference between day and night can exceed 3 °C (De Kok et al., (2001)). It is to be expected that in these stratified areas the halocline coincides with the most important vertical temperature gradient, which can be seen as the thermocline. According to De Kok et al., (2001) temperature stratification can only develop in spring and summer in areas where salinity stratification exists, with low turbulence levels and small vertical mixing.

In order to get a rough indication of the temperature increase of a relatively thin fresh surface layer compared with the deeper surrounding salt layer, a simple equation (6) has been set up:

$$\Delta T = \frac{E}{\rho \cdot h \cdot C_d} \qquad (6)$$

where E is the energy in/output (J m^{-2}); h is the thickness of the surface water layer (m); ρ is the density of the surface layer water (kg m^{-3}); C_d is the specific heat of the surface layer water (J kg^{-1} K^{-1}) and ΔT is the temperature in/decrease of the surface water layer (°C).

Appendix 2 shows the daily solar irradiation data for 1998 measured in Den Helder. It can be seen that in spring and summer the daily irradiation is on average 2000 J cm^{-2} day^{-1}, with a peak in mid May of 2750 J cm^{-2} day^{-1}. Graphs based on equation (6), showing the temperature

increase due to a certain solar energy input with varying thicknesses of a fresh- or salt water layer, are also given in Appendix 2. It can be seen that for water depths greater than 8 meters a maximum solar irradiation does not result in a temperature increase of more than 1 °C (according to this simple theory). Note that, in the case of a very thin surface layer, the effect of wind will result in more pronounced cooling than in the case of thicker layers.

Table 3.1 presents some examples of the temperature increase of a fresh surface layer of a certain depth for an energy input of 2000 J cm^{-2} day^{-1}.

Table 3. 1 Temperature increase of fresh surface layer of varying thickness for an energy of 2000 J cm^{-2} day^{-1}.

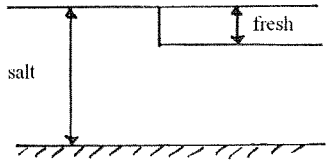

Thickness fresh layer [m]	***ΔT* fresh layer/day**
5	1
2	2.5
1	4.5
0.5	9
0.2	22

It is expected that the stratified plume can be best discerned on sunny days in spring and summer. In this period, the initial temperature difference between river-and sea water, as well as the extra temperature contrast due to daily surface heating, are maximised, which results in maximum temperature gradients. **It has to be studied however, to what extent temperature gradients visible on satellite SST imagery, coincide with the salinity gradients marking the boundary of the plume.**

Surface heat fluxes: Seasonal surface heating and cooling, which are responsible for the extra temperature gradients in the shallow stratified plume, also affect the temperature of the deeper waters. It is expected that these temperature gradients follow the depth contours. E.g. in very shallow waters the response to surface heat fluxes can be very quick, especially when the water is vertically mixed.

Hot spots: In periods of low winds, the thin surface layer mixes very slowly with the lower layers, and a significant vertical temperature gradient can develop in the upper few cm of the water column, independent of the vertical salinity gradient. In summer, this is called a hot spot. Because SST imagery only provides information on the very thin upper layer of the water column, SST images are less reliable on unclouded sunny days in spring and summer because of the possible development of hot spots. Hot spots are never visible on night and morning images (due to the effect of wind).

3.2.2 Hypothesis 2: Normalized water-leaving radiance

SeaWIFS uses the optical properties of the sea to derive water-leaving radiance (Lw). Water-leaving radiance is solar irradiation (light) which, after interaction (absorption and/or scattering) with the substances present in the upper part of the water column, is back-scattered to the sensor thereby providing information on the relative concentrations of the substances present (see Appendix 1). Normalisation is the analytical step that transforms the intensity of light measured by the SeaWIFS sensor, into the radiance that would be measured exiting the surface of the ocean with the sun at zenith (directly overhead).

This hypothesis is based on the assumptions that:

1. nLw is a tracer of the plume, and
2. nLw is monotonically correlated to SPM concentrations in the upper part of the water column

Assumption 1 is based on the findings of Simpson et al., (1993) and De Kok (1992), who showed that the transport of SPM in the DCZ takes place primarily in the River Rhine plume along the coast (see also section 1.4). By measuring relative surface SPM concentrations it is expected that this signal is representative of the surface patterns of the plume. This SPM signal can be measured by measuring green light intensities. In the green wavelength range the amount of light back-scattered off SPM dominates the signal detected by the SeaWIFS sensor (see Appendix 1). An increase in the measured green light intensity is assumed to indicate a similar (monotone) increase in SPM concentrations in the upper part of the water column. These assumptions do not hold during periods of storm when increased SPM concentrations can be observed over the whole southern North Sea.

The majority of SPM in the DCZ is supplied through the English Channel originating from the Dover Straits. The remainder of the SPM supply mainly originates from erosion and re-suspension of bottom sediment. The SPM supply through fluvial input forms only a very small contribution to the overall yearly amount of SPM transported in the DCZ (WL|Delft Hydraulics 2001). Since we are only interested in tracing the plume patterns, it does not matter where the SPM originates from (we are not interested in exact numbers).

In contrast to SST, the net result is that nLw imagery can only be used to trace plume waters which are mixed to some degree (thus not stratified). This is illustrated in Fig. 3.4. In the case of a stratified plume, the SPM remains trapped below the pycnocline hence inhibiting the SeaWIFS sensor to receive a signal (river water is low in SPM). In the case of a well-mixed or partially mixed water column, the sediments are distributed over the water column hence allowing the SeaWIFS sensor to receive a signal (SPM patterns are visible along the coast). Fig. 3.4 gives an idealised representation. In reality the observed SPM patterns are modified by plume dynamics.

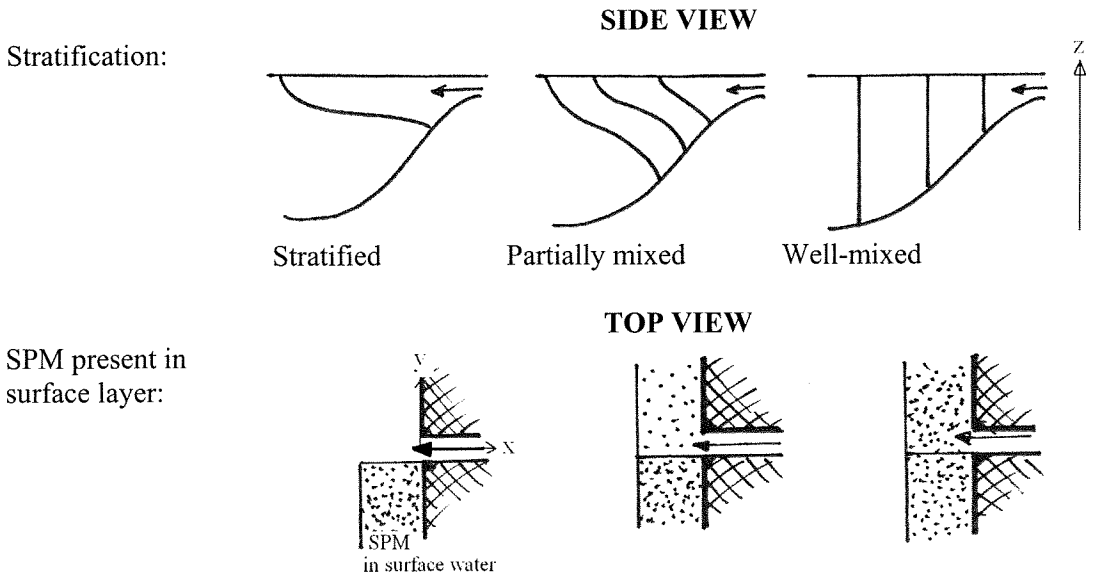

Fig. 3. 4
Idealised representation of surface SPM concentrations in different cases of stratification.

There are a few aspects which can interfere with the assumptions made, and which should be kept in mind when analysing the images:

At first, a more ideal parameter for tracing increased SPM patterns would have been a parameter expressing the ratio of water-leaving radiance (Lw) to downwelling irradiance (light) just above the surface (Kirk 1996). The water-leaving radiance is the amount of light that is backscattered by the constituents present in the upper layer of the water-column. The downwelling irradiance is the amount of light entering the sea surface (amount of solar light that is transmitted through the atmosphere: sun-to-sea). An increase in this ratio indicates an increase of SPM concentration in the upper part of the water column. By measuring water-leaving radiances (Lw) only, no information is provided on the amount of downwelling irradiance. If the amount of light that entered the water is unknown, little can be said about the actual fraction of the light that is backscattered or absorbed by the water constituents. E.g. an increase in the Lw signal can be due to increased SPM signals, but also as a result of a particularly non-transmissive atmosphere (little light is transmitted from sun to sea).

The assumption of a monotone correlation between nLw and SPM concentrations is only valid if the downwelling irradiance is constant. But the downwelling irradiance is largely dependent of atmospheric effects and the solar zenith angle (see Fig. 3.5). E.g. when the solar zenith angle is large, only a small amount of the light reaches the sea surface (small downwelling irradiance) because a large part of the light is scattered and absorbed in the atmosphere (the path of the light from the sun through the atmosphere to the sea is longer). By normalizing the water-leaving radiance

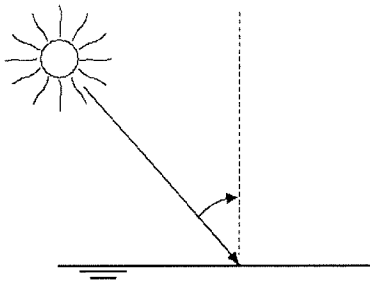

Fig. 3. 5
Solar zenith angle.

(nLw), and thus assuming that the radiance (Lw) is exiting from a flat sea surface with the sun at zenith (directly overhead) and the atmosphere is absent, the variation to the nLw due to variations in downwelling irradiance (sun to sea transmittance) is neglected. However, in this project the SeaStar satellite makes its pass at approximately the same time every day (around noon), so the solar angle only gradually changes in time as the solar elevation changes with the seasons. For this reason it can be safely assumed that downwelling irradiance is constant. The atmospheric effects are less constant in space and time. Especially the distribution of aerosols responsible for scattering of light on its way to the sea surface can be highly variable (see Appendix 1). The extent of the error in assuming constant downwelling irradiance caused by variable aerosol scattering is unknown.

Secondly, the signal measured by the SeaWIFS sensor does not only comprise SPM; it also contains coloured dissolved organic matter (CDOM) and chlorophyll from algae. Because most of the suspended matter present in the North Sea is inorganic (SPM), an increase in the backscatter signal is assumed to be indicative of an increased SPM concentration. It should be noted that when high concentrations of algae (chlorophyll) are present, the uncertainty with the data increases. From May to June and September to October increased nLw signals should be considered with more care because in these periods a higher nLw signal may be due to increased algae concentrations rather than increased SPM concentrations (WL|Delft Hydraulics, 2002). Algal blooms are relatively easily recognized as often discrete patches. See Appendix 1 for more details.

3.3 Remote sensing images: Display and composition variants

In order to allow for optimal interpretation of the images, G. de Boer wrote numerous scripts which enable to produce various representations of the RS images and the addition of consistent meteorological data. Most of the options the scripts offer were exploited to produce a large number of sequences of the 1998 RS images for use in this project (see CD).

With the scripts the colour scaling of the RS images can be adjusted to maximum contrast per image ("locally scaled"), or to scaling between a manually set minimum and maximum value of SST or nLw ("globally scaled") which makes it easy to compare sequences of images. Also the cut-out of the RS image can be specified allowing to zoom in on the DCZ or to zoom out for an overview (to some extent). The digital RS images used in this project are displayed in the Universe Transverse Mercator (UTM 31) map projection. Lines of latitude and longitude and depth contours can be added to the satellite image.

Because the lateral spreading and mixing of the plume is largely determined by meteorological events (see Chapter 2), graphs with wind speed and direction, water level and freshwater discharges over a specified number of days before the satellite observation can be included. The meteorological data are obtained from measurement stations located at several

positions in the North Sea. Every measurement station is assigned a colour. The co-ordinates of the location and the colour of the measurement stations are shown in Table 3.2. The data in the meteorological graphs are plotted in the colour of the measurements station from which the data originate. In all RS images the location of the measurement stations can be plotted as a dot in the colour assigned to the measurement station. These coloured dots should not be confused with the colour bar on the right of the satellite image, indicating the value of either nLw or SST.

Table 3. 2 Co-ordinates and colour of the measurement stations

Co-ordinates	°N	°E	Color
Europlatform	52.00	3.28	red
Haringvliet 10	51.87	3.87	orange
Haringvlietsluizen binnen	51.83	4.03	yellow
K13	53.22	3.22	green
Meetpost Noordwijk	52.27	4.30	blue
Maassluis	51.92	4.27	grey
Den Helder	52.97	4.75	black

Fig. 3.6 is an example of a typical presentation of the RS data. Hourly potential wind speeds[6] and wind directions obtained from the "Europlatform", "Meetpost Noordwijk" and "K13" measuring stations (KNMI) and a wind rose are plotted. In order to get an idea of the decrease in tidal amplitude as the tidal wave propagates northward along the Dutch coast, 10-minute water level data obtained from three measuring stations: "Haringvliet", "Meetpost Noordwijk" and "Den Helder" are plotted (RIKZ/RIZA). The daily amounts of freshwater discharges released through the Rotterdam Waterway and the Haringvliet sluices into the North Sea are obtained from the "Maassluis" and "Haringvlietsluizen binnen" measurement stations, respectively (RIKZ/RIZA) and are plotted. Typically these time series span a period of 4 days prior to the given RS image (satellite pass). The vertical red line in Fig 3.6 indicates the time at which the satellite image was taken.

Because of the important role of solar heating effects when interpreting SST imagery, solar irradiation data can also be added to the SST maps. Daily solar irradiation data were obtained from the "Den Helder" measuring station (KNMI).

[6] Potential wind speed: means corrected to the wind speed at 10 m height over open water with a roughness length 0.002m (http://www.knmi.nl/samenw/hydra/faq/upot.htm)

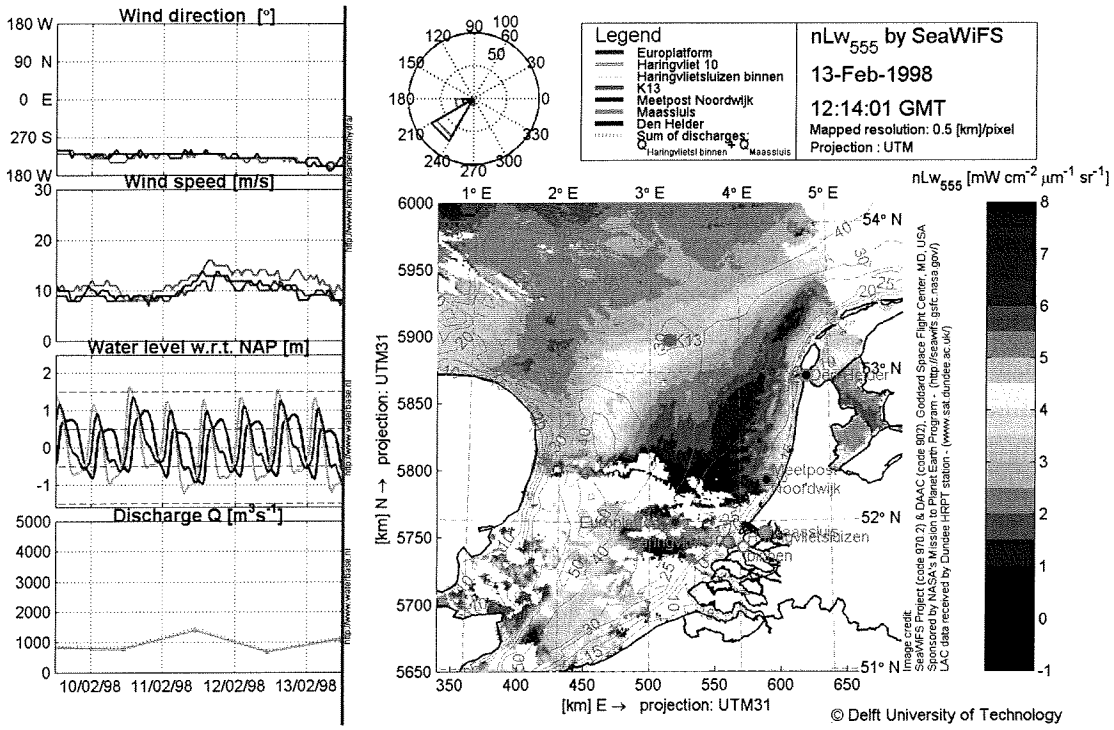

Fig. 3. 6
Example: SeaWIFS image of nLw measured in band 5 centred at 555 nm. Large cut-out (350 km x 350 km); scaled to show maximum contrast; additional meteorological data over 4 days prior to satellite pass.

Acknowledgements for meteorological and satellite data are also included in the images. The SeaWIFS data are supplied by NASA, the meteorological data are supplied by KNMI and RIZA/RIKZ (see acknowledgements).

Chapter 4

RESULTS

4.1 Introduction

This chapter presents the results of this study. In the next section, section 4.2 the spatial and temporal distribution of a selection of the available 1998 images of SST and nLw are treated. The selection is based on the amount of cloud cover of the DCZ. Then, in sections 4.3 and 4.4 the results of an analysis of the selected SST and nLw images respectively are presented. Monthly and seasonal averages were composed and analysed followed by an analysis of the individual images. All images on which the Rhine plume is visible are selected for further analysis. The selection is based on the hypotheses, which were set up in the previous chapter (section 3.2). Section 4.5 explores the cross-correlation between the observed plume patterns on the SST and nLw imagery (as far as this is possible with this limited number of images). Finally, the images on which the plume is visible are further analysed in section 4.6. The information on the plumes behaviour that can be derived from these images is presented in this section.

4.2 Cloud cover

156 Readily processed **images of Sea Surface Temperature** were obtained from KNMI. All images show a large part of the DCZ because only these images are archived by KNMI. Raw Level 1A High-Resolution Picture Transmission (HRPT) data for a first selection of 244 SeaWIFS images covering the southern North Sea were obtained from NASA. This first selection was based on the amount of cloud cover of the DCZ. The data were processed to produce Level 2 images of normalized water-leaving radiance by using the SeaWIFS Data Analysis System (SeaDAS) with MUMM's turbid water extended atmospheric correction algorithm. From these images a second selection of **163 images of nLw** was made in which a significant part of the DCZ was visible (not covered by clouds). Both KNMI images and Level 1A HRPT data were obtained free of charge. Details on RS data levels, data acquisition and data processing can be found in Appendix 1.

Spatial coverage: To give an indication of the spatial coverage of the selected images, for every pixel in the image it is determined how many times this pixel is not flagged off. This has been determined for both selections of RS images. The results are plotted in Figs. 4.1 and 4.2.

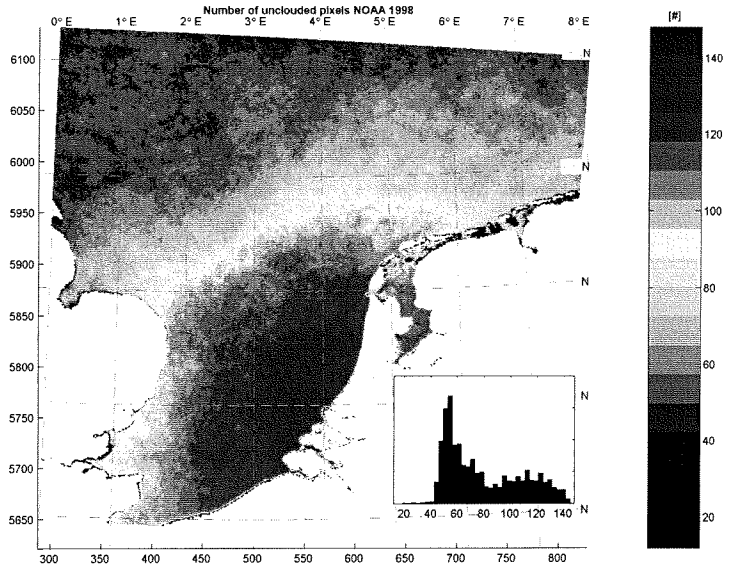

Fig. 4. 1
SST: Number of unclouded pixels per 156 pixels (number of unclouded samples per grid cell).

It can be seen that in more than 140 out of 156 SST images clouds do not cover the Rhine plume area. The reason for this is that KNMI only archives images on which a significant part of the DCZ is visible. The excellent coverage of the Rhine plume area make SST a very attractive data source for monitoring the Rhine plume

For nLw the criteria of selection clearly judged cloud cover less severe. Out of the 163 nLw images, the central North Sea is covered only about 80 times. The narrow strip along the coast, the Rhine plume area, is covered even less due to geo-referencing inaccuracies and beach blinding (see Appendix 1).

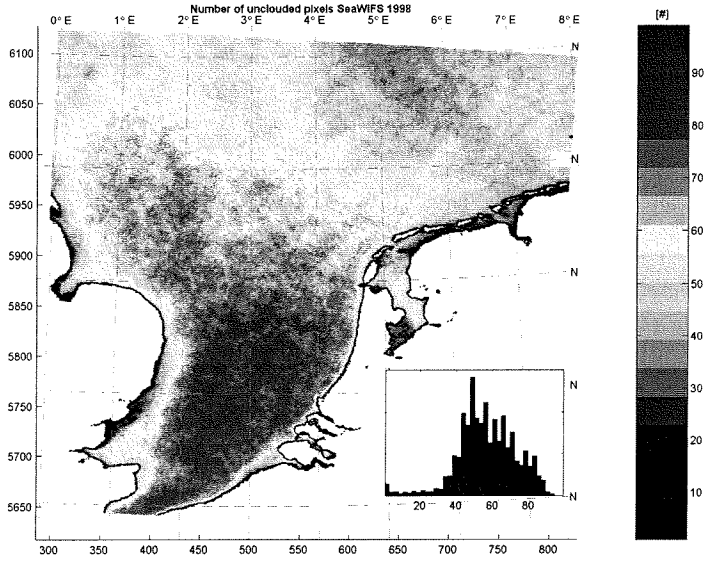

Fig. 4. 2
nLw: Number of unclouded pixels per 163 pixels.

The much better spatial coverage of the SST images can be explained by the fact that measurement of SST generally occurs from two satellites, which each cross the North Sea twice every day (24 hours). One satellite crosses the North Sea in the morning and evening, while the other satellite makes its pass in the afternoon and at night. In May 1998 a third satellite was launched in a morning/evening orbit. The nLw images were measured from only one satellite, which crosses the North Sea around noon and at night (see Table 4.1). In addition, nLw can be measured only during the day whereas SST can be measured both day and night. The contribution of each satellite to the selection of images is shown in Table 4.1.

Table 4. 1 Time span in which each satellite passes the North Sea (for selection of images)

What	When	Satellites	Operational in '98	Time span of satellite pass (GMT):	
SST	Day & night	3 satellites:			
		NOAA 12	All of 98	Morning	05:30-07:27
				Evening	16:07-18:05
		NOAA 14	All of 98	Afternoon	12:43-14:19
				Night	02:16-04-26
		NOAA 15	From 31-Aug '98	Morning	07:25-08:44
				Evening	17:40-19:20
nLw	Day	1 satellite:			
		SeaSTAR	All of '98	Noon	11:19-13:38

Temporal distribution: Fig. 4.3 shows the number of available images per month. The largest amount of available SST images appears in May, August and September. In these periods the plume is expected to be best discernible by its temperature contrast (see section 3.2.1). In contrast to the favourable temporal distribution of the SST imagery, the availability of nLw imagery in winter is minimal. This introduces the paradox: the main processes which drive the dominant SPM supply are active in winter when extensive cloud cover spoils a large portion of the images.

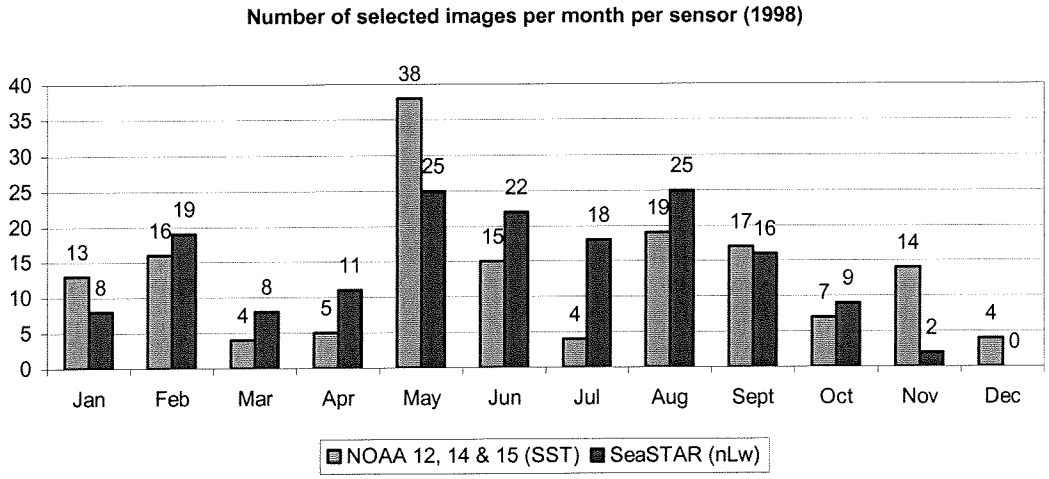

Fig. 4. 3
Temporal distribution of the 156 SST and 163 nLw images per month.

Fig. 4.4 shows the distribution in time of the 156 SST and 163 nLw images. It can be seen that the available images are strongly clustered, indicating that there was less cloud cover in these periods.

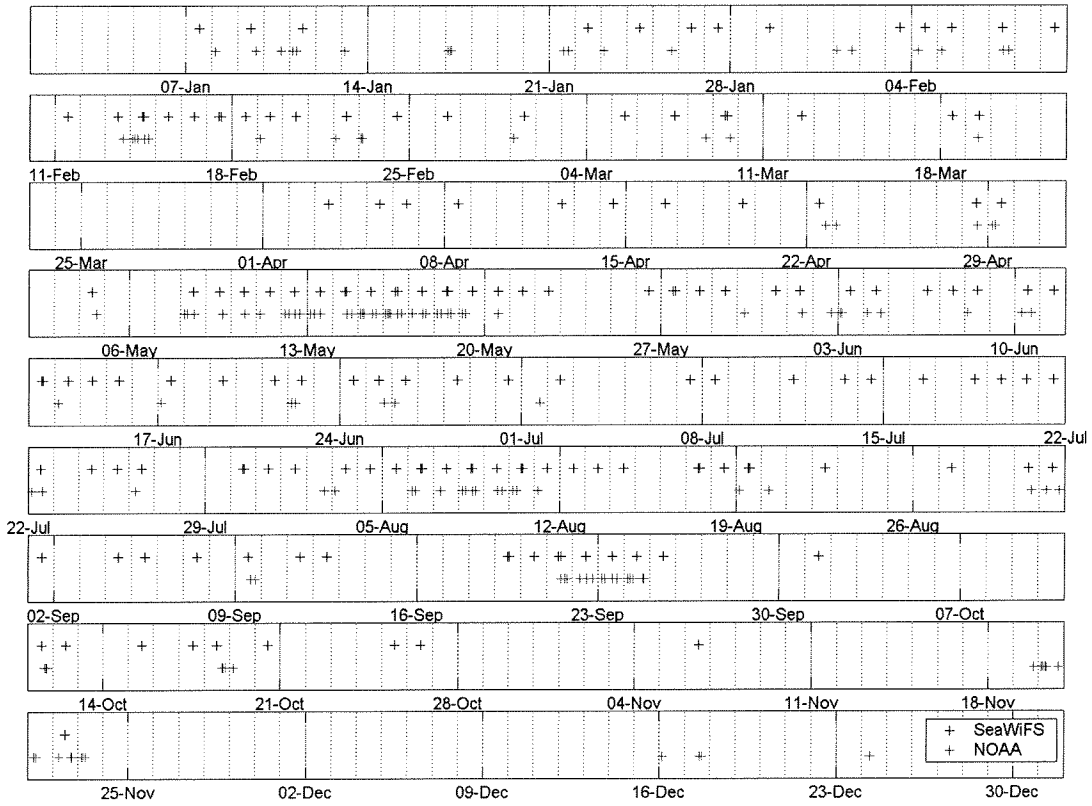

Fig. 4. 4
Temporal distribution of the 156 available SST and 163 available nLw images for 1998.

4.3 Analysis of the 156 SST images

The hypothesis in section 3.2.1 states that the **stratified plume** (see Fig.1.3) can be discerned by its temperature contrast. But not all temperature gradients as visible on SST imagery coincide with the salinity gradients marking the plume. **This section presents the results of an analysis of 156 SST images in which it is determined to what extent temperature gradients, as visible on SST imagery, coincide with the real plume front as delineated by salinity.**

Throughout most of the year, clearly visible temperature gradients are found in a strip of varying width along the Dutch coast. Also the southward extent of the strip is quite variable. The yearly averaged standard deviation (based on unclouded pixels of 156 images as presented in Fig. 4.1) demonstrates the variability of the coastal strip (see Fig. 4.5). Also note the variability of the East Anglian plume.

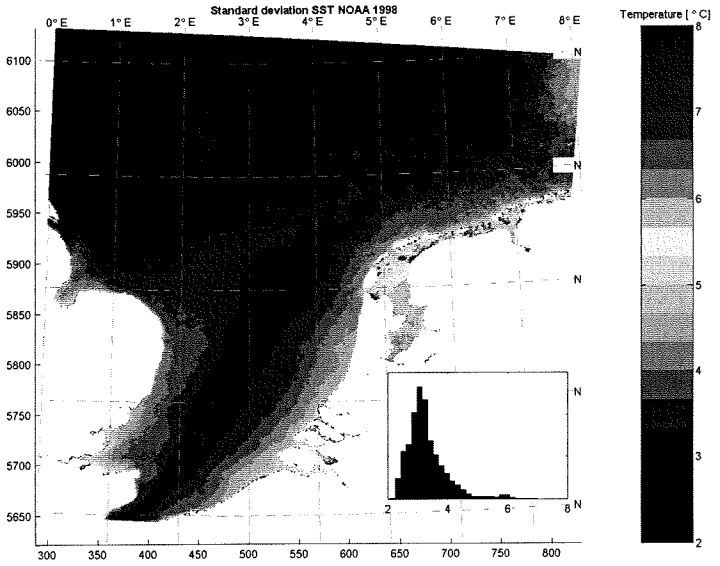

Fig. 4. 5
Yearly standard deviation per pixel for 156 SST images for 1998.

Although the hypothesis states that only the stratified plume can be discerned by its temperature contrast, the yearly averaged standard deviation pattern seems to illustrate the broad plume patterns. Is this possible? Can the plume extend this far southward? To further analyse this point, seasonal and monthly averages of SST were composed and analysed.

Seasonal mean SST patterns: Figs. 4.6-4.9 show that, in spring and summer, the coastal strip is on average warmer and, in fall and winter, colder than the North Sea water. The colour bars indicate the SST in °C. What causes these temperature differences and when is there a transition from warmer to colder and/or vice versa?

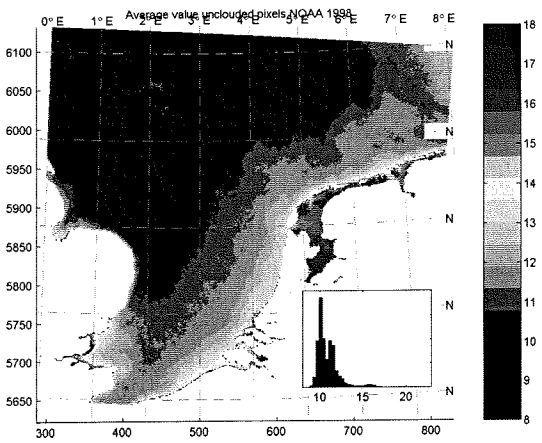

Fig. 4. 6
Mean SST spring 1998 based on 54 images.

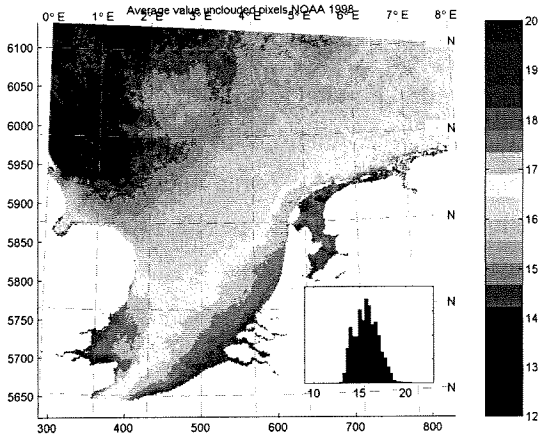

Fig. 4. 7
Mean SST summer 1998 based on 32 images.

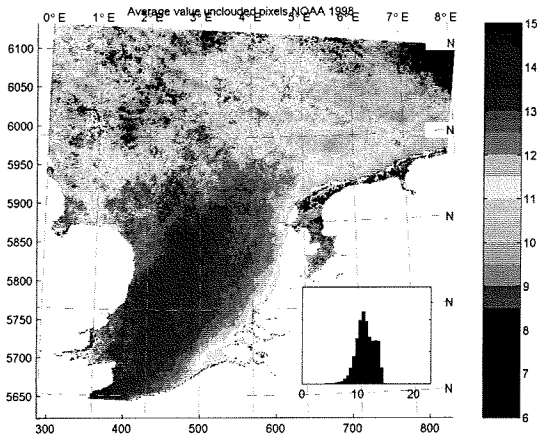

Fig. 4. 8
Mean SST fall 1998 based on 28 images.

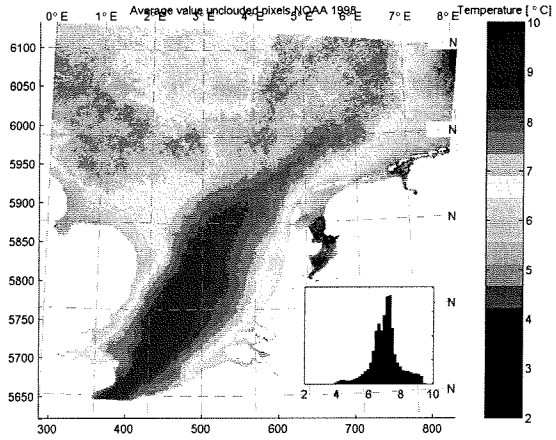

Fig. 4. 9
Mean SST winter 1998 based on 42 images.

The observed patterns of temperature gradients can be due to temperature differences between river- and sea water thereby indicating the plume, or due to local effects which are not indicative of the plume. Local effects can be the result of seasonal surface heating and cooling of the North Sea water and are strongly correlated to depth. In shallower waters surface heat fluxes generally result in larger temperature fluctuations than in deeper waters (same energy input in smaller volume). The net result is that the shallower Dutch coastal strip is generally colder in winter and warmer in summer than the central North Sea or Channel waters (see for example Fig. 3.3 section 3.2.1). In addition, water masses coming from the deep Atlantic entering the North Sea through the English Channel may also affect the overall pattern of temperature gradients. In winter, the Atlantic waters are expected to be warmer than the relatively shallow "cooled" North Sea waters. In summer, the Atlantic waters are expected to be colder than the shallower "heated" North Sea waters. It should be noted that, especially in winter when winds are high and consistently from south-westerly direction, the Atlantic waters are forced into the North Sea.

In situ measurements of SST at 1 m below the sea surface, illustrating the net result of all temperature effects for 1998 are shown in the Fig. 4.10. It can be seen that the largest temperature fluctuations between summer and winter appear in the shallow Dutch coastal strip. In the deeper parts, these temperature fluctuations are relatively constant and the temperatures in the 'deepest K13 measurement station' are on average 1 °C colder than the measurements in the somewhat 'shallower Europlatform measurement station'. What causes these extra pronounced temperature fluctuations in the shallow Dutch coastal strip? Is this due to surface heat fluxes or due to the plume or due to a combination of both?

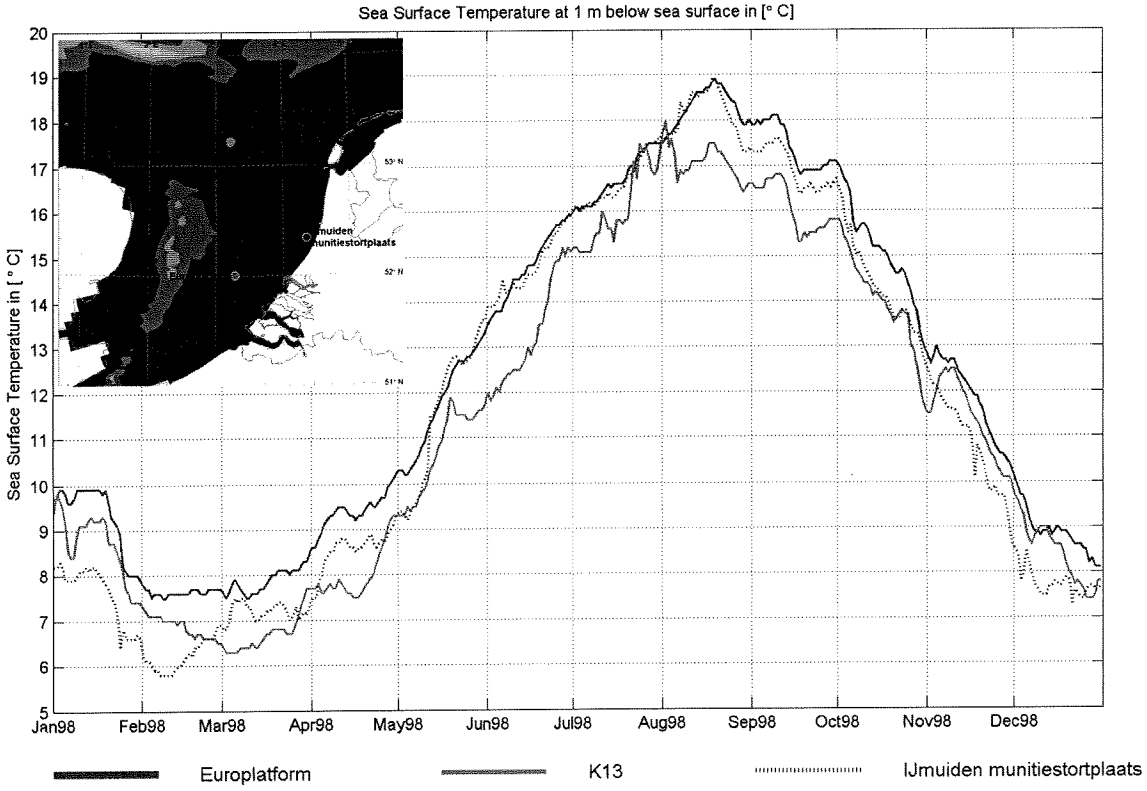

Fig. 4. 10
'Sea Surface Temperature' at 1 m below surface for 1998 (www.waterbase.nl) for three locations: Europlatform, K13 and IJmuiden munitiestortplaats. The locations are plotted in the bathymetry map on top left.

Validation: The seasonal average SST's, at 1 m below the sea surface, have been computed (see Table 4.2). When comparing the seasonal mean surface SST data measured by the AVHRR satellite sensor with the in-situ measurements at 1 m below the sea surface (measurement buoy), it can be seen that the seasonal averages for Europlatform and K13 match. The average for the shallower measurement station of IJmuiden munitiestortplaats differs to some extent.

Table 4. 2 Seasonal mean SST in °C at 1 m below surface (www.waterbase.nl)

Measurement station	Spring	Summer	Fall	Winter
K13	9.8	16.3	12.1	7.5
Europlatform	11.1	17.3	12.8	8.3
IJmuiden munitiestortplaats	10.6	17.1	11.9	7.1

The seasonal mean SST patterns in spring and summer seem to largely follow the bathymetry (see Figs. 4.11-4.13). It is suggested that these observed temperature gradients along the Dutch coast are the result of local effects (surface heat fluxes). This argument is supported by the fact that the freshwater discharges in these seasons were very low (on average 1000 $m^3 s^{-1}$: see Appendix 3) and thus do not allow the development of such a wide plume (large offshore extent).

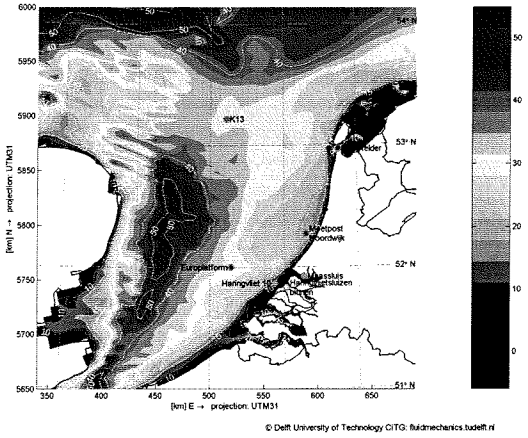

Fig. 4. 11
Bathymetry (from ZUNO) of southern North Sea (depth in m). The colour bar indicates the depth in m.

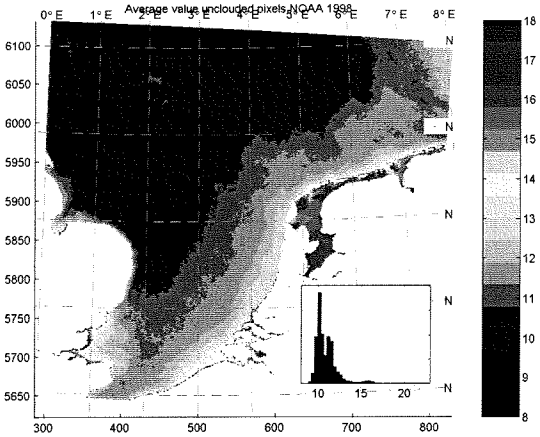

Fig. 4. 12
Mean SST spring 1998 (54 images). The colour bars indicate the SST in °C.

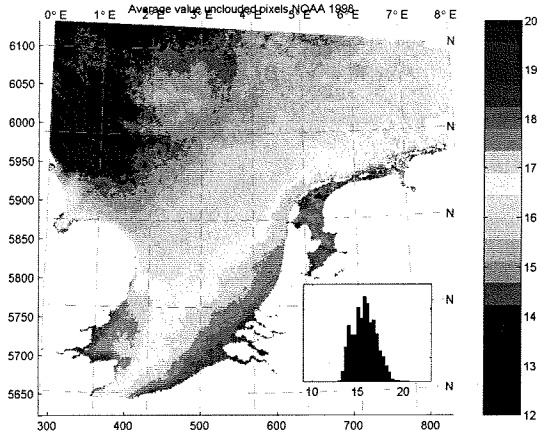

Fig. 4. 13
Mean SST summer 1998 (32 images). The colour bars indicate the SST in °C.

How about the observed mean SST patterns in fall and winter? Do these perhaps illustrate water masses or the plumes patterns?

Monthly mean SST patterns: When analyzing the monthly mean patterns of SST for 1998 (see Appendix 4), it can be seen that in March and April the temperature gradient patterns have vanished. In May, the shallower coastal strip starts to heat up again. By the time of August 1998, the temperature gradients follow almost exactly the bathymetry indicating the local surface heating effects. In September, the temperature gradients have vanished again. Between October and February, when air temperatures are decreasing and freshwater discharges are increasing, a temperature gradient pattern starts to develop which largely coincides with the continental water pattern found in winter by Eleveld et al., (2004) (see Fig. 4.14). A simplified numerical simulation by Pietrzak (2002) also calculated a salinity pattern, which is similar to the observed SST patterns in winter (see Fig. 4.15). This simulation was carried out primarily to assess the transit time of freshwater from the Rhine to Denmark following the huge river discharges of January 1995. The model was run with tides and

synoptic wind forcing, however a simple constant initial salinity field of 32 PSU was specified. The river discharge of ~ 11000 m^3 s^{-1} from the Rhine quickly led to the formation of a well-mixed plume. The resulting salinity pattern resembled the surface patterns observed in AVHHR channel 1 reflectance data (see Fig. 4.16). Especially the mean SST pattern as observed in January (see Fig. 4.17) shows a large resemblance.

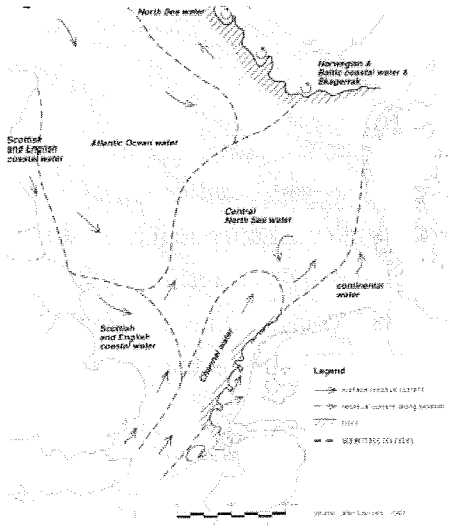

Fig. 4. 14
Residual currents in winter 2001, in which the current has been corrected for tidal movements. Eleveld et al., (2004).

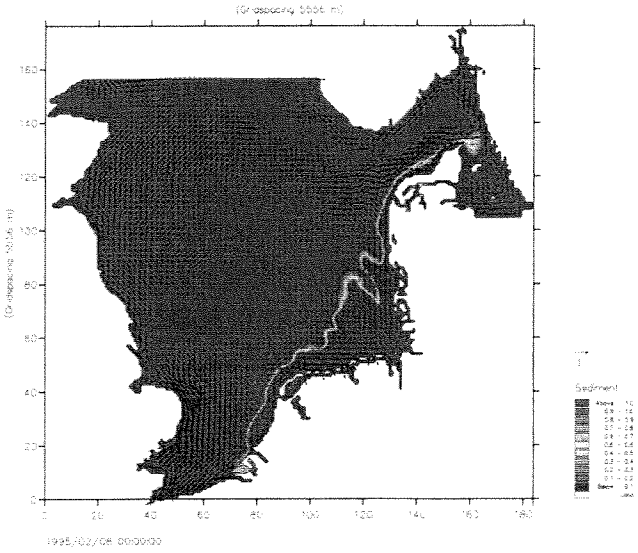

Fig. 4. 15
Numerical results showing the surface velocity field and sediment concentration on the 8th Feb. 1995. Image: Pietrzak (2002).

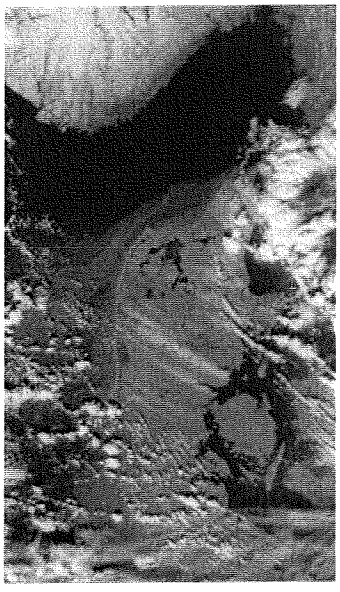

Fig. 4. 16
AVHRR NOAA reflectance satellite image from Feb. 8th 1995. Image: Pietrzak (2002).

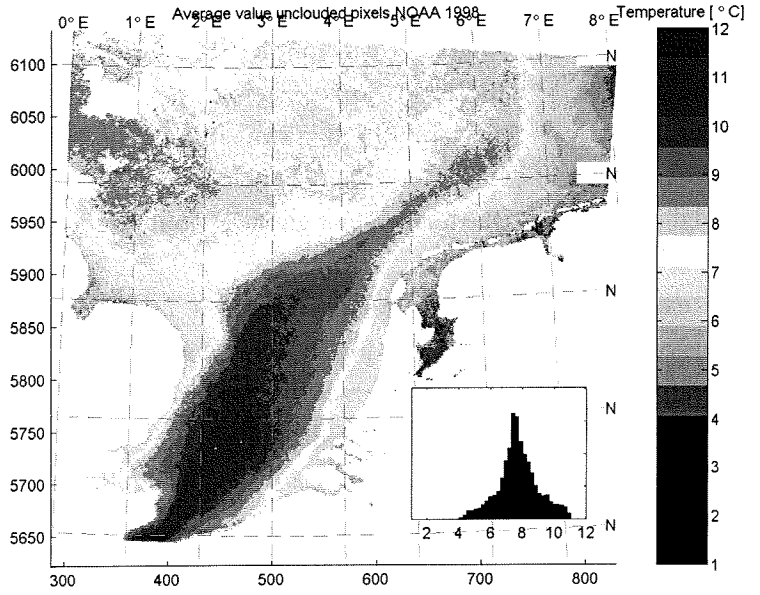

Fig. 4. 17
Monthly mean SST January (based on 13 images).

November 1998 is marked by extremely high discharges (peak of 7000 m^3 s^{-1} see Appendix 3). January/February/December were marked by dominant south-westerly winds and January and December by relatively high discharges (~ 3000 m^3 s^{-1} on average: see Appendix 3). Warm Atlantic waters are pushed through the English Channel and seem to delineate the plume. The patterns shown in January/ February/November/December suggest the plume, yet nothing can be proven yet. To continue the speculation a little further, the next section tries to explain the short-term variability of the suggested plume patterns in terms of plume dynamics (Chapter 2).

Short term variability of the suggested plume patterns: On the individual images for January/February/November/December, large fluctuations in the suggested plume patterns can be observed within a few hours. Also "sharper" and more gradual temperature gradients appear. The direct reason for these fluctuating patterns is often difficult to give. In the shallow North Sea, the most convenient path for the water to follow (least resistance) is not always the one that follows the deeper isobaths. Wind-, tide- and density effects plus the shape of the bathymetry contours can also play an important role in determining the pattern certain water masses tend to follow. A few interesting examples, which highlight these fluctuating patterns, are given in Appendix 5.

Example 1-6 for 8-13 January is dominated by south-westerly winds. South-westerly winds would force a plume of freshwater towards the coast (downwelling). This sequence of images clearly shows that within a few hours the width, the temperature gradient and the southward extent of the "plume" can vary considerably. South-westerly winds push the warmer Atlantic waters through the English Channel which delineate the "plume". The suggested plume patterns seem to be largely influenced by the stage of the tide. During low water (LW), the suggested cold water plume extends further southward than during high water. Also the width of the suggested plume seems to be wider and the temperature gradient is less pronounced during low water than during high water. These effects were best visible on 11-Jan 03:39 (HW>LW) and 11-Jan 06:30 (LW) (example 4 → 5). The coastal strip widens, the southward extend increases and the temperature gradient decreases.

The example images for February, examples 7-15, clearly show an increased southward intrusion of the coastal pattern. Is this Rhine water or is there another freshwater source? The Scheldt discharges (yearly average of 120 m^3 s^{-1}) are generally much lower than the Rhine/Muese discharges (2200 + 320 m^3 s^{-1}: see Appendix 3: discharges). Is it possible to observe Rhine waters this far southward? Typically, the Coriolis would force the freshwater to the right after entering the North Sea; however local experience (J. de Kok and H. Winterwerp) shows that wind can force the fresh Rhine water in southward direction. Also see the numerical simulations made by Lacroix et al., 2004.

Notice the development of a westwards pointing bulb of higher temperature water just off Hoek van Holland on February 14th (example 9-13). On February 23rd (ex 14-15), this bulge

has grown and came onshore. Why? If these patterns indicate the plume, how are these unusual patterns explained in terms of plume dynamics?

Similar patterns (see Fig. 4.18) were found on 19-20 November (example 16-21). November was marked by very high discharges (peak of 7000 $m^3 s^{-1}$). Distinct bulges of colder coastal waters travel northward along the Dutch coast. Do these bulges indicate the plume? The fact that these images were taken 1 day after spring tide (see Appendix 6) and the fact that this period is marked by huge discharges and very low wind speeds (Appendix 3) make it even more confusing. If these bulges indicate the plume, can we expect the plume to be well-mixed or stratified? Why does the plume come onshore? Is this because of the bathymetry pattern, which it seems to follow to some extent? This needs clarification.

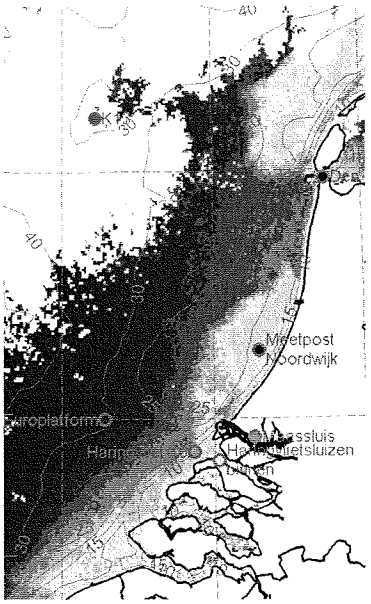

Fig. 4. 18
Cut-out of SST image for 20-Nov 1998 06:37.

The question remains: do the SST patterns in winter indicate the plume patterns? This argument needs further investigation (probably with a computer model).

Stratified plume: Further analysis of the individual daily images showed some distinct patches of warmer waters propagating along the Dutch coast in April and May. According to the hypothesis (hypothesis 1), it is expected that these patches indicate the stratified plume unless hot spots have developed. Hot spots show as pronounced temperature gradients and should not be mistaken for the plumes patterns (see section 3.2.1).

Hot spots tend to develop on unclouded sunny days in spring and summer. Some examples of hot spot development are given in Appendix 7. The temperature gradients shown in example 2, 4 and 7 are hot spots. Also note the often explosive temperature increase of the shallow (average of 4 m) Lake IJssel on these images indicating a high input of energy. The same quick response to surface heat fluxes can be observed in a narrow coastal strip (depths < 10 m). From these images it seems that the development of hot spots generally occurs around noon, when the sun is directly overhead. The hours prior to the time of satellite pass of the images on which hot spots are discernible are often marked by very low wind speeds (see Examples 8-10). When wind speeds pick up, the very thin layer is quickly mixed and the temperature gradient vanishes. The remainder of the observed patches of warmer water is expected to represent the stratified plume. These images are presented in Appendix 8.

It seems that only in April and May the plume can be discerned by its temperature contrast (see Appendix 4). This seems to agree with the De Kok et al., (2001), where it is hypothesised that, only on hot unclouded days in spring and summer, the temperature contrast is

pronounced enough to discern the stratified plume. In some cases, several pixels in the temperature gradient marking the edge of the plume are flagged off, because the atmospheric correction algorithm (see Appendix 1) confuses very large temperature gradients with clouds.

Out of all 156 images provided by KNMI, the plume is distinct on 9 images only. These images were taken in April and May and show the stratified plume. The large temperature increase of the freshwater layer during the day suggests a thin upper layer. The SST patterns shown on the images taken from January/February/November/December only suggest the plume patterns, but this argument needs further investigation. The 9 selected images (see Table 4.3) allow for detailed analysis and are further analysed in section 4.6 results.

Table 4. 3 Selected SST images showing the stratified plume

1.	22-Apr	17:37
2.	12-May	03:02
3.	12-May	07:09
4.	12-May	16:57
5.	13-May	02:51
6.	13-May	06:47
7.	13-May	12:43
8.	14-May	14:13
9.	14-May	17:53

4.4 Analysis of the 163 nLw images

The hypothesis in section 3.2.2 states that SPM patterns along the Dutch coast are indicative of a plume which is mixed to some degree (partially or well-mixed). Images taken during periods of storm should be considered less reliable. From May to June and September to October, increased nLw signals should be considered with more care because in these periods a higher nLw signal may be due to increased algae concentrations rather than increased SPM concentrations. **The results of an analysis of the 163 nLw images in which it is determined which images can be used to trace the plumes patterns are presented in this section.**

Seasonal and monthly mean nLw patterns: When analyzing the seasonal and monthly mean images (see Appendix 4), it can be seen that the North Sea is characterized by persistent high SPM concentrations (in the upper part of the water column) near the Flemish Banks, near the Humber estuary and in the Greater Thames Estuary at the head of the East Anglian Plume (see Fig. 4.19). In fall and winter, a band of increased SPM concentrations along the Dutch coast is clearly discernible. These observations agree very well with the observations made by Eleveld et al., (2004). The observed patterns are also shown in the yearly averaged standard deviation (based on unclouded pixels of 163 images) (see Fig. 4.20).

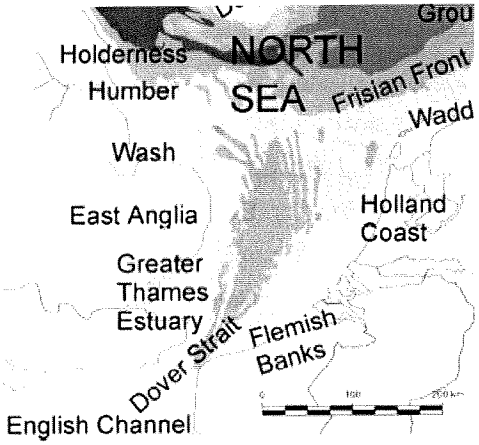

Fig. 4. 19

Research area. Image: Eleveld et al., (2004).

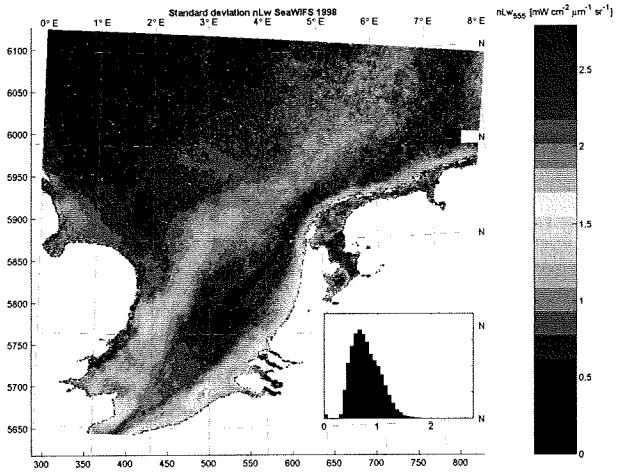

Fig. 4. 20

Yearly standard deviation per pixel for 163 nLw images for 1998.

The majority of the SPM transport in the DCZ occurred in winter when also the largest supply through the English Channel occurred. The remainder of the year the SPM concentrations were much lower. Another peak of increased SPM concentrations in the DCZ occurred in October 1998. In Appendix 3, it can be seen that October 1998 was marked by high wind speeds, which presumably eroded and/or re-suspended bottom sediments, resulting in the observed increased SPM signal. In general, during periods of high winds, increased SPM concentrations were observed at the Flemish Banks. Towards the end of the summer almost all SPM in the DCZ has vanished.

KNMI reported a (south) westerly storm of wind force 10 (~26 m s^{-1}) with strong gusts of wind on 4 Jan 1998. Unfortunately, clouds covered the SeaWIFS images during this period.

Analysis of the individual daily images: On 8 May, some discrete patches of increased nLw values suddenly appeared in the DCZ (see Fig. 4.21). These increased nLw values were presumably due to algae. In Fig. 4.22 and in Appendix 7 it can be seen that these patches coincide with the hot spots on the SST image of this day. In hot spots where nutrients and light are abundant, explosive algae growth can be triggered.

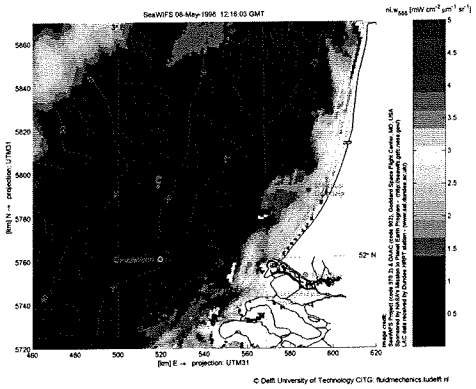

Fig. 4. 21

nLw 08-May 12:16

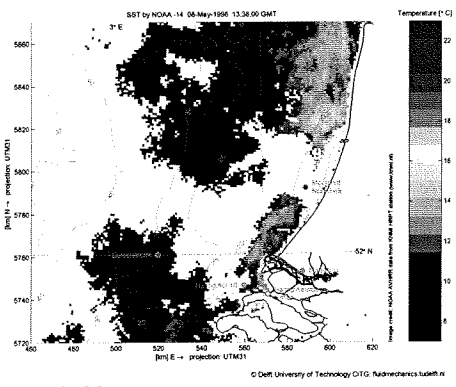

Fig. 4. 22

SST 08-May 13:38

The result of an analysis of the 163 nLw images is that the SPM patterns shown along the Dutch coast (mainly in winter) do not allow for quantification of the plume patterns, because there remains a lot of uncertainty with respect to the exact position of the boundary of the plume. What can be identified from the nLw images is some kind of wavelength development (see Figs. 4.23-24). These patterns may suggest baroclinic instabilities. De Kok (1996; 1997) suggested in a simple two-layer model in which he imposed tidal forcing, wind forcing and buoyancy forcing, that in case of weak north-easterly to south-westerly winds, frontal meanders can develop with wavelengths between 10 and 30 km (see section 2.2). The wavelengths shown here seem to coincide with the wavelengths found by De Kok, but with these coarse spatial and temporal scales this argument needs further investigation.

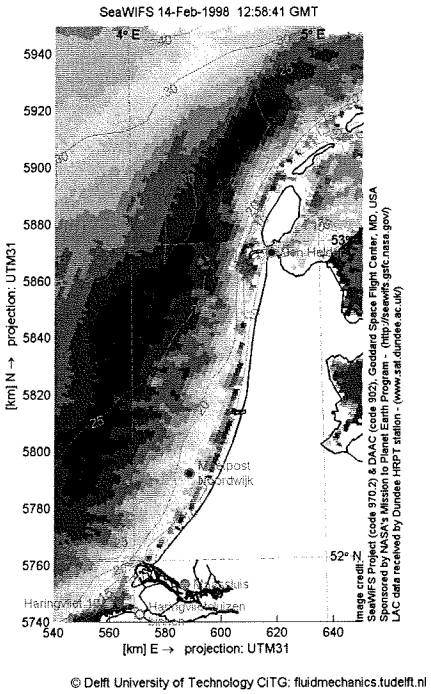

Fig. 4. 23
nLw 14-Feb 12:58.

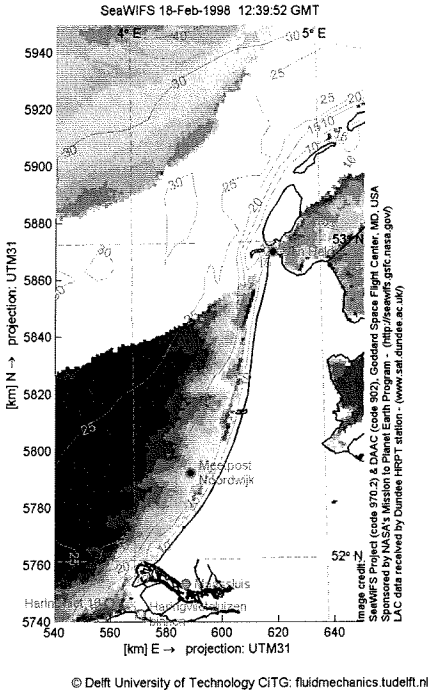

Fig. 4. 24
nLw 18-Feb 12:39.

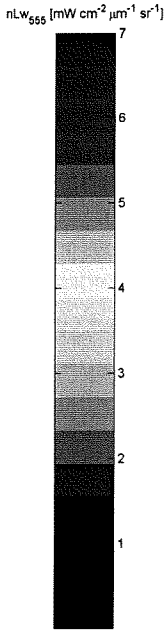

Meandering of the SPM patterns along the Dutch coast during weak south-westerly winds

Figs. 4.23-24 also show the difficulty with respect to determining the exact boundary of the plume. More examples can be found on the accompanying CD which contains all RS images for 1998 used in this project.

It turns out that nLw imagery is not such a good tracer of the plume. Nevertheless, it is expected that the nLw images are an excellent source for monitoring SPM in the North Sea (see Framework: section 1.4).

4.5 Cross-correlation?

Since the SST images from January/February/November and December seem to indicate the broad plume patterns, this section investigates whether there is any cross-correlation between the suggested plume patterns by the SST images, and the available nLw imagery for this period (for as far as possible with the limited number of nLw images in this period). Cross-correlating images showing or suggesting the plumes patterns with a time difference of more than 6 hours are not considered. It should be kept in mind that the (suggested) plume patterns can vary within a few hours (see section 4.3 short term variability of the suggested plume patterns).

For January, when the SST patterns best match the continental water pattern found by Eleveld et al., (2004), there is only one 'cross-correlating' image available (note the time difference of 6 hours). See Figs. 4.25 and 4.26.

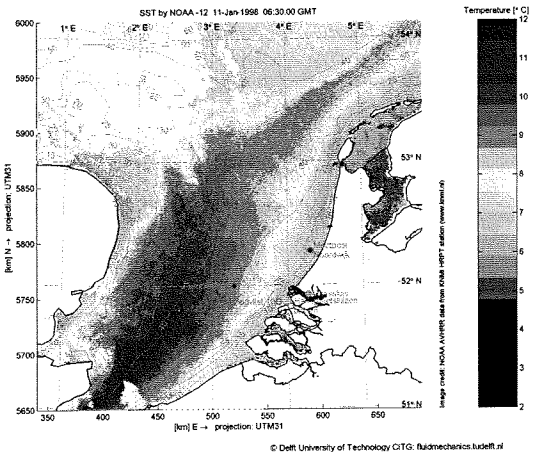

Fig. 4. 25
SST 11-Jan 06:30.

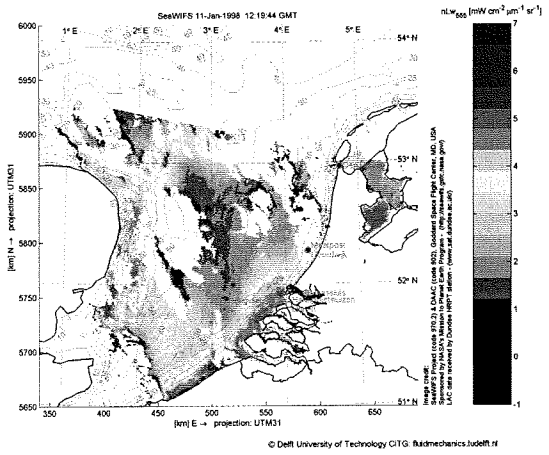

Fig. 4. 26
nLw 11-Jan 12:19.

The SST and nLw patterns observed in Figs. 4.25 and 4.26 seem to match to a large extent. According to Fig. 3.4 (section 3.2.2), the sudden decrease in SPM concentrations north of the outflow point suggests a stratified plume. This argument is supported by a freshwater discharge of 3000 $m^3 s^{-1}$. The stratified plume prohibits the SeaWIFS sensor to receive a SPM signal because all SPM remains trapped below the pycnocline. Unfortunately, this prohibits comparison of plume patterns for January.

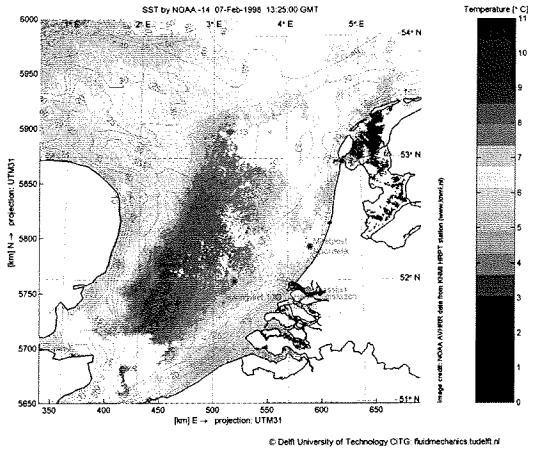

Fig. 4. 27
SST 07-Feb 13:25.

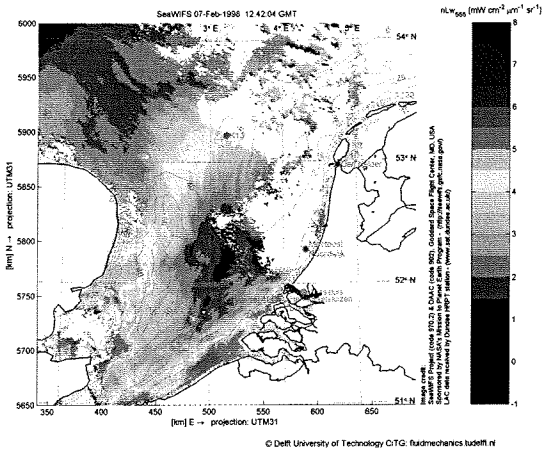

Fig. 4. 28
nLw 07-Feb 12:42.

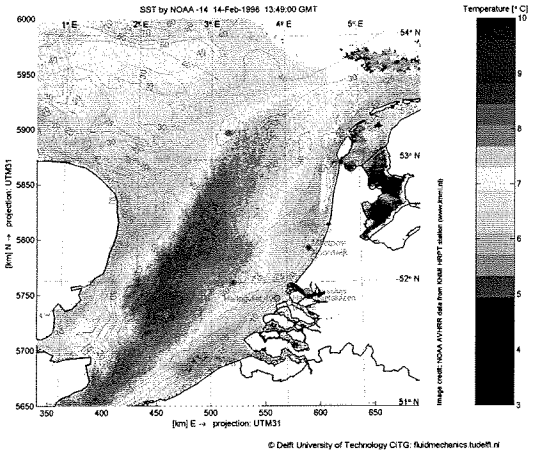

Fig. 4. 29
SST 14-Feb 13:49.

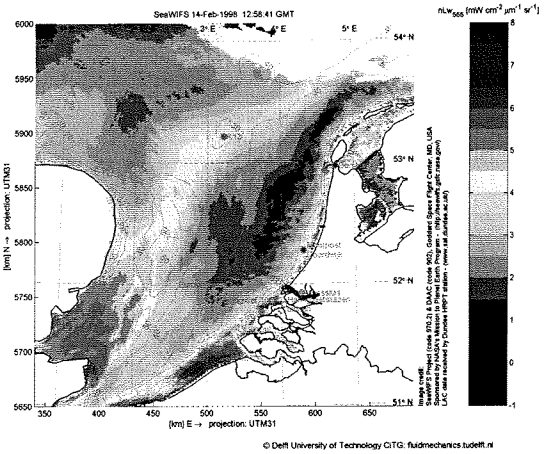

Fig. 4. 30
nLw 14-Feb 12:58.

In the remainder of the cross-correlating images available to us (Figs. 4.27-4.30), the SST patterns in winter suggest that the continental or plume waters are somewhere in the coastal band, which globally follows the bathymetry. The only difficulty lies within tracing the exact border. The bands of increased SPM values along the Dutch coast are much narrower than the band shown in the SST images. Can these patterns be explained by the difference between physics of water masses and physics of SPM? What do these patterns indicate? Do the SPM patterns perhaps indicate the minimal plume width, whereas the SST patterns may be representative of the maximum plume width? These remain open questions. **A lot of uncertainty remains with respect to the exact position of the boundary of the plume in this period.**

4.6 Analysis of the stratified plume

In this section, the information on the plumes behaviour that can be derived from the limited number of images on which the plume is visible is presented. The behaviour, as stated in the objectives, is described by the following parameters: the offshore extent, the northward progression, the meandering and scale of eddies (if present) and the thickness of the plume. **Out of all available RS images of SST and nLw for 1998, only 9 SST images showed the (stratified) plume. The nLw images turned out not be a very good delimiter of the plume.** The 9 SST images together with consistent meteorological data are presented in Appendix 8. These 9 images will now be further analysed (see Table 4.4).

Table 4. 4 SST images showing the stratified plume.

1.	22-Apr	17:37
2.	12-May	03:02
3.	12-May	07:09
4.	12-May	16:57
5.	13-May	02:51
6.	13-May	06:47
7.	13-May	12:43
8.	14-May	14:13
9.	14-May	17:53

On April 22nd, a relatively large freshwater discharge of ~2500 $m^3 s^{-1}$ was discharged through both the Haringvliet sluices and the Rotterdam Waterway. On the 8 images taken in May, the freshwater outflow was very low (~1200 $m^3 s^{-1}$) and freshwater was only discharged through the Rotterdam Waterway. On April 22nd, the solar irradiation was ~2000 J cm^{-2} day^{-1}, whereas the daily solar irradiation on 12-14 May peaked with 2400-2800 J cm^{-2} day^{-1}. May 12-14 was marked by relatively low north-easterly winds.

The 8 images in May were taken in a time span of 63 hours. This sequence of images in May allows for derivation of information on the evolution of the stratified plume in space and time. Fig. 4.31 gives a "summary" of the May sequence of SST images showing the plume together with the accompanying meteorological data.

Tidal beat and coastal upwelling: The tidal beat in releasing patches of freshwater when water levels are low is clearly discernible. As the patches of freshwater travel further northward, the bulges tend to stretch out in alongshore direction and eventually blend together. Appendix 9 shows how the varying alongshore tidal currents move the fresher waters north- and southward. Coastal upwelling (see section 2.4), as a result of periods of predominant (north-) easterly winds, is clearly visible on all images taken in May.

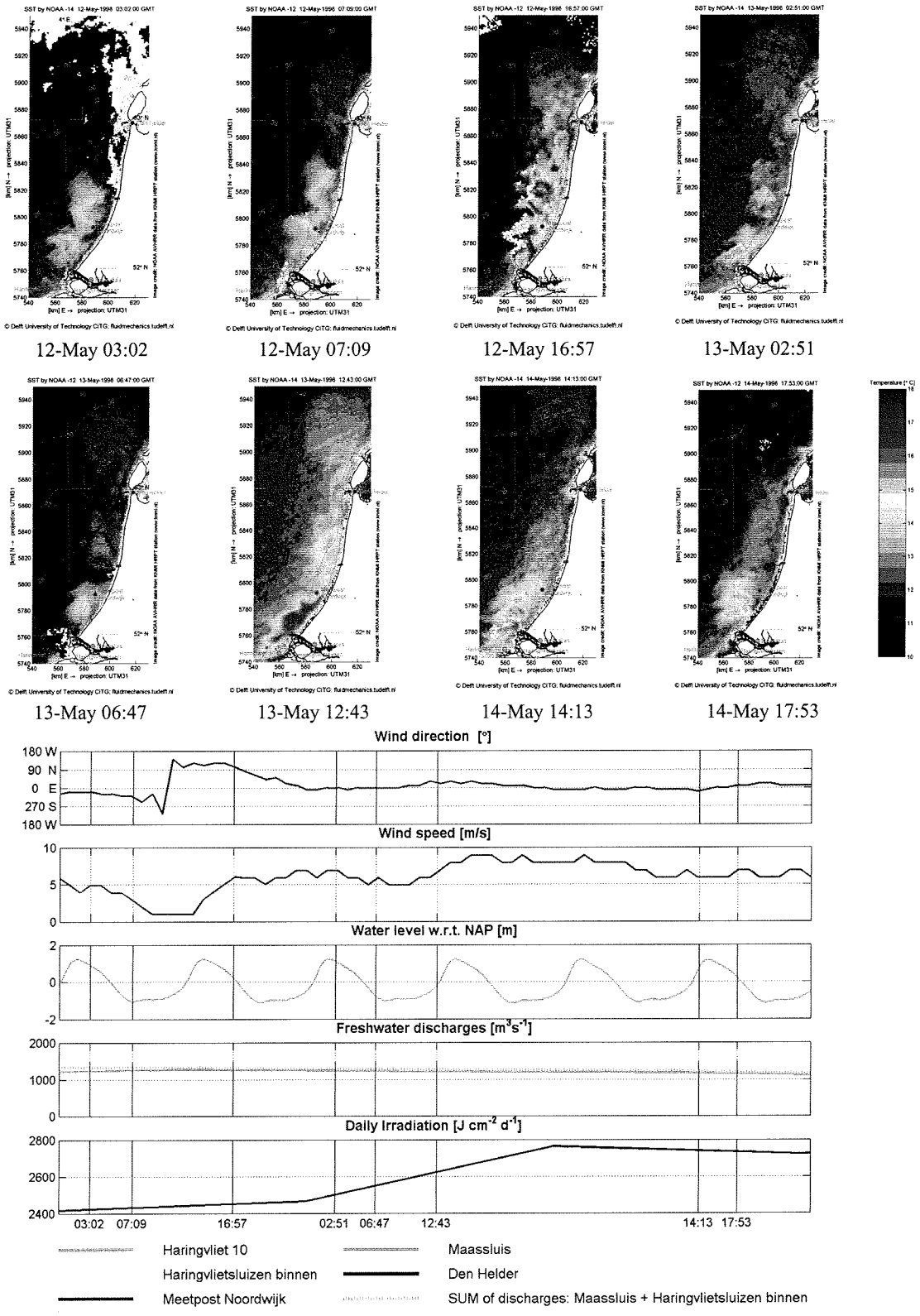

Fig. 4. 31
Overview of the 8 SST images taken in May together with the accompanying meteorological data.

Stratified plume at spring tide: It is very striking that, when looking at the temporal spreading of the available images with respect to the low frequency spring-neap tidal forcing, it shows that the May sequence of images was taken during spring tide (see Appendix 6). This is contrary to the classic observations of Visser et al., (1994), Simpson (1990; 1993; 1995; 1997), Souza (1996; 1997), who typically observe a stratified plume during neap tide and a well-mixed plume during spring tide. Particularly, because the stratifying influence of the discharge was very low on 12-14 May ($Q \approx 1200$ m^3 s^{-1}), one would expect the mixing influence of the spring tidal forcing to dominate the stratifying influence of the freshwater discharge, resulting in a well-mixed plume. However, the period of 12-14 May was marked by (north-) easterly winds, which are expected to enhance the development of a stratified plume. Because the wind speeds were very low (< 10 m s^{-1}), it would be expected that the mixing effect of the spring tide would dominate. **Apparently, stratification can occur at spring tide.**

Tidal straining at spring tide: When observing stratification at spring tide, can we also observe the effect of tidal straining which is generally observed in case of a stratified plume at neap tide (see section 2.3 tidal straining)? Tidal straining is expected to show a semi-diurnal oscillating cross-shore movement of the width (offshore extent) of the plume as a result of the semi-diurnal change of the tidal current ellipses (generating cross-shore velocities in the case of stratification). Unfortunately, the temporal resolution of the 8 images taken in May is not sufficient to identify the tidal straining effect.

Offshore extent and northward progression of the stratified plume: Another "summary" of all SST images showing the plume (Appendix 8) is given in Fig. 4.32. Every individual image is scaled to achieve maximum contrast allowing for optimal quantification of the plumes patterns. In this representation the temperature gradients are best discernable (images cannot be compared directly). Fig. 4.33 shows that the northward progression of the plume cannot be quantified from these SST images. As the stratified plume travels northward along the Dutch coast, the vertical stratification gradually breaks down and results in a more mixed appearance of the plume, which can no longer be discerned by its temperature contrast. The white horizontal lines in the images mark the maximum northward progression at which the plume can still be (vaguely) discerned by its temperature contrast. The black lines in the cross-shore direction indicate the offshore extent of the stratified patches, and the numbers indicate the width in kilometres. The SST image taken on 12 May 12:54 is not added to this sequence because this image is considered less reliable due hot spot development (see Appendix 7). Close to the outflow point, the alongshore freshwater front is very sharp (indicating a stratified plume) and becomes wider more to the north, where it is located at distances of ~20-50 km from the coast. These numbers coincide with previous studies performed by Ruddick et al., (1994), De Ruijter et al., (1997).

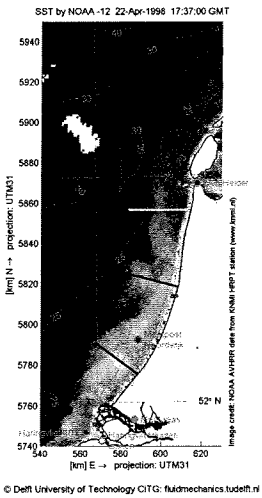

22-Apr 17:37
24

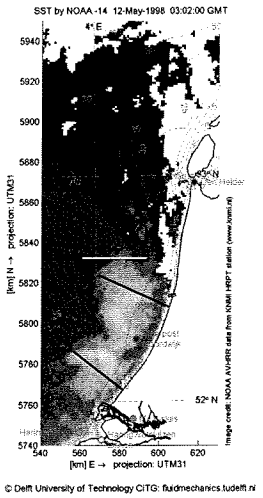

12-May 03:02
28-33

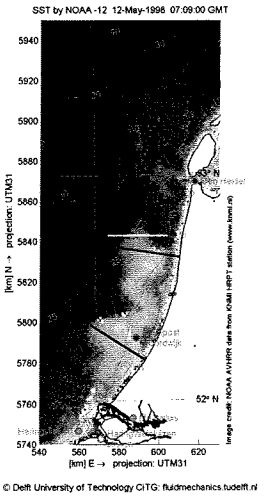

12-May 07:09
25-28

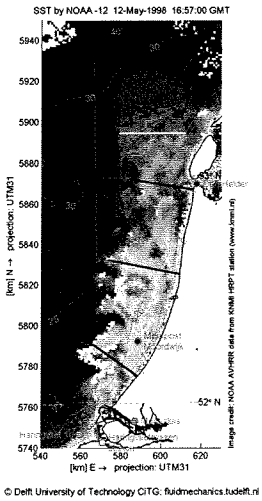

12-May 16:57
24-31

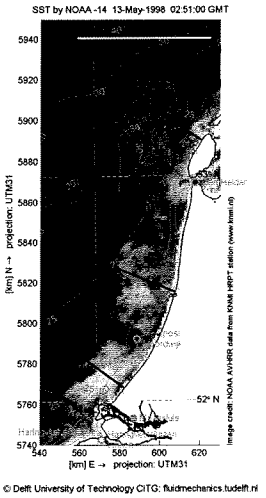

13-May 02:51
19-28-52

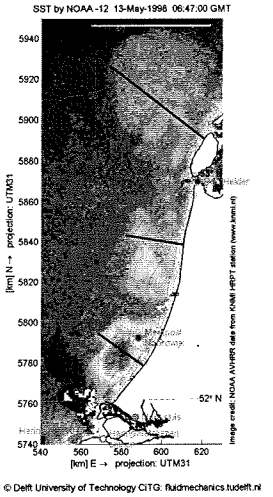

13-May 06:47
24-24-52

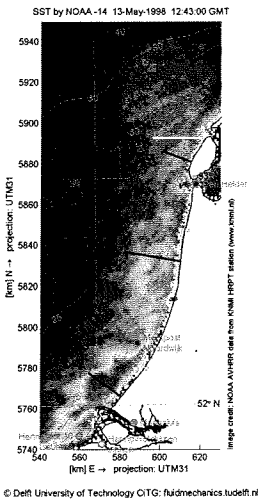

13-May 12:43
24-19-11

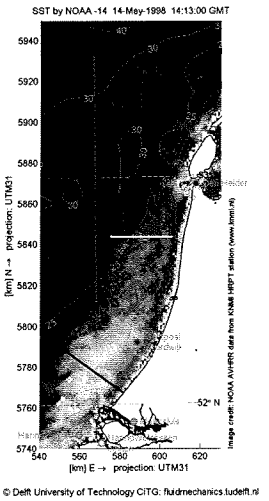

14-May 14:13
28

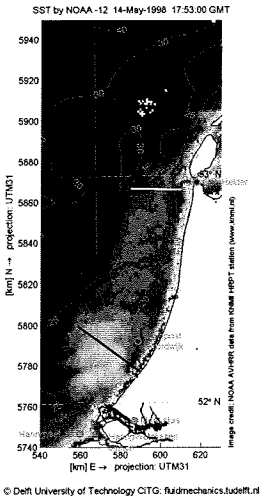

14-May 17:53
33

Fig. 4. 32
Summary of all SST images showing the stratified plume (numbers indicate offshore extent of plume in km)

Thickness of the stratified plume: The thickness of the plume can be estimated by using equation (6) (section 3.2.1) and Appendix 2: if the temperature increase (ΔT) and the energy input (E) responsible for this temperature increase are known, the thickness of the stratified plume (h) can be estimated with equation (6) (section 3.2.1) and Appendix 2..

In order to give an indication of the relative temperature differences and temperature gradients from image to image, the May sequence of SST images is now scaled between 10 and 18 °C, which allows for direct comparison between the images (see Fig 4.33).

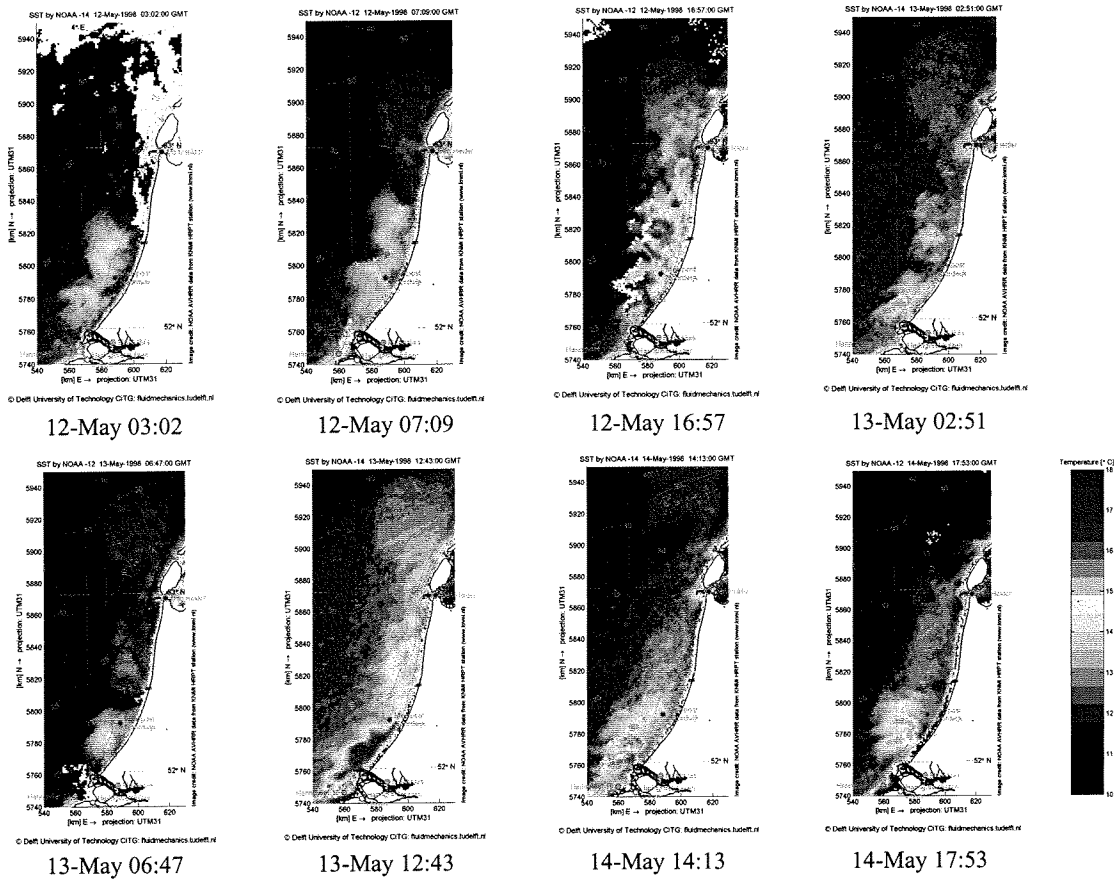

Fig. 4. 33
Summary of all SST images showing the stratified plume (all images scaled between 10-18 °C).

The images taken on 13 May 06:47 and 13 May 12:43 clearly show an increase in temperature as a result of solar heating. The images taken on 12 May (07:09 and 16:57) show something similar but are considered less reliable because of the hot spot, which developed at 12 May 12:54. For this reason, only the images taken on 13 May allow for estimation of the thickness of the plume. In Fig 4.34 these images are each scaled to achieve maximum contrast.

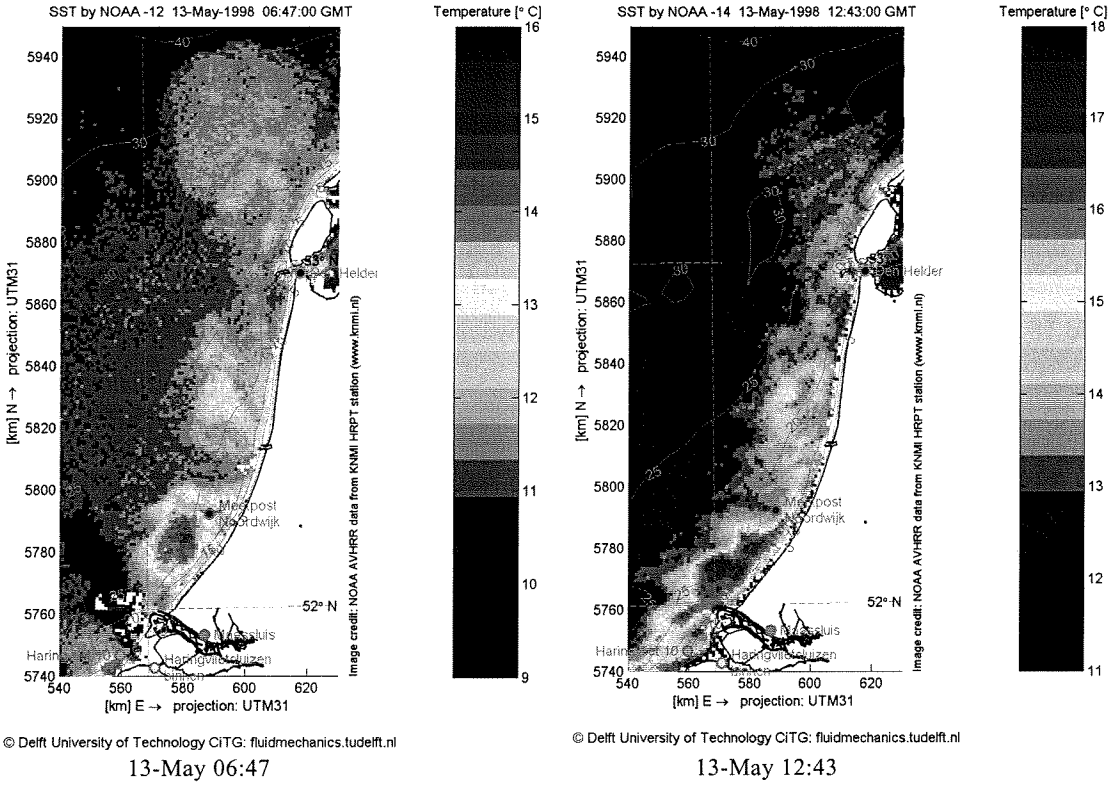

Fig. 4. 34
SST images used to estimate the thickness of the stratified plume.

The temperature increase on May 13th (ΔT) between 06:47 and 12:43 is ≈ 3 °C. The solar irradiation on 13 May 1998 was 2464 J cm^{-2} day^{-1} (KNMI). When assuming that the variation of the solar irradiation over the day is of the form:

$$y = -(a \cdot x - b)^2 + c \qquad (7)$$

The sun rose at 04:23 GMT and sunset was at 19:28 GMT (http://iamest.jrc.it). Then a, b and c can be calculated with a calculation program such as Matlab by computing:

$\int_{04:23}^{19:28} \left(-(a \cdot x - b)^2 + c\right) \cdot dt = 2464$ J cm^{-2}day^{-1}. Resulting in a = 5.63e-004; b = 1.01 and c = 1.03. With these data the net amount of energy responsible for heating the stratified layer with 3 °C can be estimated by calculating the surface area of the parabola (Fig 4.35):

$\int_{06:47}^{12:43} \left(-(a \cdot x - b)^2 + c\right) \cdot dt \approx 1200$ J cm^{-2}.

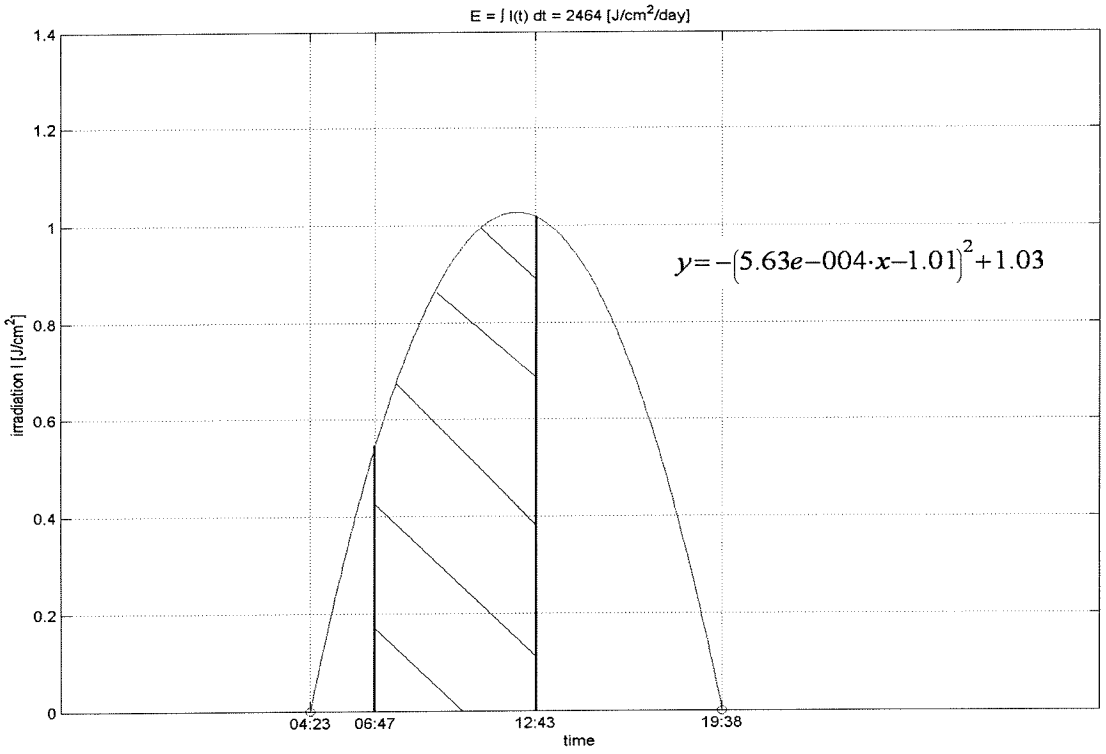

Fig. 4. 35
May 13th: daily solar irradiation = 2464 J cm^{-2} (KNMI). Sunrise: 04:23; Sunset: 19:38 (http://iamest.jrc.it).

Appendix 2 shows that for E = 1200 J cm^{-2} and ΔT = 3 °C the thickness of the plume h is less than 1 meter.

Summary: Contrary to previous measurements it appears that stratification can occur during spring tide. How can this be explained? As Visser et al., (1994) suggest, the water column response, to the same barotropic forcing, may be significantly different, depending on the degree of viscous decoupling between the layers as a result of tidal straining. Any data source indicating stratification is therefore considered as an important data source.

The sequence of 8 images taken in May allows for derivation of information on the evolution of the stratified plume in space and time. Unfortunately, the temporal resolution of these images was not sufficient to identify the occurrence of tidal straining. Also the tidal beat in releasing patches of freshwater and the coastal upwelling effect were clearly discernible. Furthermore, the temperature increase in the fresh surface layer, as a result of surface heat fluxes, allowed for estimation of the thickness of the freshwater layer.

In spite of the surface limitation of information, the SST data used in this project have proven to be a valuable data source with respect to the Rhine plume. This section has shown that besides sea surface temperature the images provide indirect information on the sub-surface processes.

Chapter 5

DISCUSSION

5.1 Summary

The data content of remote sensing (RS) images of sea surface temperature (SST) and normalized-water leaving radiance (nLw), for the year 1998, with respect to the River Rhine plume, is investigated. Questions that this study tries to answer are: is it possible to identify the plume from the available RS images, and under which conditions is this possible? How much information on the plumes behaviour can be derived from these images and does or can this information contribute to our general knowledge of the plume?

The images provide a spatial resolution of 1 km^2 and a temporal resolution of 1 or 2 images per day per sensor for nLw and SST, respectively (in the case of a cloudless atmosphere). In the presence of clouds, no signal is detected for the area of surface water underneath the clouds. The SST images provide a better temporal coverage than the nLw images because SST can be measured during the day and at night and generally data is available from two satellites, whereas nLw can only be measured during the day and only one satellite is used.

Two hypotheses were set up to explain how the RS images of SST and nLw can be used to trace the plume. In the hypotheses, links are established between the salinity gradient which delimits the plume and SST and nLw, respectively. **The first hypothesis** states that temperature differences between river and sea water can be used to trace the stratified plume. Only in the case of a stratified plume, the temperature front coincides with the salinity front that marks the plume, because temperature differences between river- and sea water are maintained due to damping of vertical turbulent exchange of mass, heat and salinity at the pycnocline. Surface heat fluxes play an advantageous role because they generally result in an extra temperature contrast between river- and sea water (especially in spring and summer). **The second hypothesis** is based on the assumption that the transport of SPM in the Dutch coastal zone takes place primarily in the Rhine plume. The hypothesis states that measurements of relative SPM concentrations (i.e. intensity of green light) in the upper part of the water column can be used to trace the plumes patterns. By assuming a monotone correlation between nLw and SPM concentrations, an error is made because this argument indirectly assumes that the atmospheric effects are constant in space and time. The extent of the error is unknown. In contrast to SST, nLw imagery can only be used to trace plume waters which are mixed to some degree (partially or well-mixed). In the case of a stratified plume, the SPM remains trapped below the pycnocline, hence inhibiting the SeaWIFS sensor to receive a signal.

156 Readily processed **images of SST** were obtained from KNMI and 244 raw nLw data files were obtained from NASA. Both data were free of charge. The raw nLw data were processed to produce nLw images. From these **nLw images** a selection of **163** was made, based on the amount of cloud cover in the plume area.

The 156 SST and 163 nLw images were analysed in accordance with the hypotheses, and all images allowing for quantification of the plume patterns were selected. The result of this analysis:

- 9 SST images in spring allow for identification and quantification of the stratified plume patterns.
- Stratification can develop during spring tide.
- SST images in January seem to indicate plume patterns (though at present not definite).
- The nLw images do not allow for quantification of the plume patterns because there remains a lot of uncertainty with respect to the exact position of the boundary of the plume.

5.2 Conclusions

- The RS data used in this project provide a valuable source of information with respect to the Dutch coastal zone in addition to the currently available measurement techniques and computer models. From the images which were available to us it can be concluded that:
  - The SST images can provide detailed information on the stratified plume and allow for derivation of indirect information on sub-surface processes.
  - nLw Imagery is not such a good tracer of the plume. Nevertheless, it is expected that the nLw images are an excellent source for monitoring SPM in the North Sea
- For correct interpretation of the RS data, which only provide information on the sea surface, knowledge of both plume dynamics and RS technology are required.
- For detailed monitoring of dynamic plume behaviour, increased spatial and temporal resolutions are required (when using polar orbiting satellites there is always a resolution trade-off between spatial and temporal resolution. At present the launch of multiple satellites (such as NOAA) could provide a solution).

5.3 Recommendations

- For a better understanding of plume behaviour, available data sources should be combined. For example:
  - By combining satellite data and numerical model results in a data assimilation system (Data Model Integration) it can be investigated whether, for example, the broad SST patterns in winter do illustrate plume patterns.
  - AVHRR reflectance data (band 1) can provide additional information to the SeaWIFS reflectance data[7].
  - It is expected that by combining HF RADAR data, which provide information on surface currents, with RS data we can learn more about sub-surface processes such as tidal straining.
- If 3D numerical models are validated with RS images of SST, the effects of surface heat fluxes should be included in the calculation.
- For a better analysis of the River Rhine plume, the images should be expanded further south. In doing so, the origin of SPM and warmer or colder waters through the English Channel can be investigated.
- An alternative way to trace the River Rhine plume could be to look for dissolved components. Tracking SPM (solids) has the disadvantage that solids tend to sink and so the signal decreases with time/distance from the river mouth. Temperature differences have the same drawbacks; they also fade away with time/distance. Dissolved components keep their signal strength until complete mixing of the river water with the sea water has occurred.
- Investigate the application of the high-resolution modes of MERIS[8] (300 m instead of 1.1 km) in addition to SeaWIFS.

For further application of SeaWIFS data:

- Investigate the extent of the error made by normalizing the water-leaving radiance, thereby assuming that the atmospheric effects are constant in space and time.

[7] Note that AVHRR measures ratio of water-leaving radiance (Lw) to downwelling irradiance (light) just above the surface. This is a better indicator of SPM concentrations present in surface layer than just normalized water-leaving radiance measured by SeaWIFS (see section 3.2.2).

[8] Medium Resolution Imaging Spectrometer onboard ESA's Envisat satellite

Acknowledgments

The author would like to thank the SeaWIFS Project (Code 970.2) for the production and the Goddard Distributed Active Archive Centre (Code 902) at the Goddard Space Flight Centre, Greenbelt, MD 20771 and the HRPT station of Dundee University, for the distribution of SeaWIFS ocean colour data. NASA's Mission to Planet Earth Program sponsors these activities. NASA also provided the SeaDAS processing software, and MUMM kindly provided the MUMM atmospheric correction extension.

The Royal Netherlands Meteorological Institute (KNMI) is acknowledged for the production and distribution of NOAA-AVHRR SST data and the meteorological wind data (KNMI HYDRA Project: Wind climate assessment of the Netherlands: www.knmi.nl/samenw/hydra).

The National Institute for Coastal and Marine Management (RIKZ) and the Institute for Inland Water Management and Waste Water Treatment (RIZA) are acknowledged for providing the remainder of the meteorological data used in this project (waterbase: http://www.waterbase.nl).

References

Canada Centre for Remote Sensing, 2004. Fundamentals of Remote Sensing Tutorial. http://www.ccrs.nrcan.gc.ca/ccrs/learn/tutorials/fundam/download_e.html

Chao, S.-Y., & Boicourt, W.C. 1986. Onset of estuarine plumes. Journal of Physical Oceanography, 16, 2137-2149.

De Kok, J.M. 1992. A three-dimensional finite difference model for computation of near- and far-field transport of suspended matter near a river mouth. Continental Shelf Research, 12, no5/6, 625-642.

De Kok, J.M. 1994a. Numerical modelling of transport processes in coastal waters. Ph.D. thesis, University of Utrecht.

De Kok, J.M. 1996. A two-layer model of the Rhine plume. Journal of marine systems, 8, 269-284.

De Kok, J.M. 1997. Baroclinic eddy formation in a Rhine plume model. Journal of marine systems, 12, 35-52.

De Kok, J.M., De Valk, C., Van Kester, J.H.Th. M., De Goede, E., & Uittenbogaard, R.E. 2001. Salinity and temperature stratification in the Rhine plume. Estuarine, coastal and shelf science, 53, 467-475.

De Ruijter, W.P.M., Visser, A.W., & Bos, W.G. 1997. The Rhine outflow: A prototypical pulsed plume in a high energy shallow sea. Journal of marine systems, 12, 263-276.

Eleveld, M.A., Pasterkamp, R., & Van der Woerd, H.J., 2004. A survey of total suspended matter in the southern North Sea based on the 2001 SeaWIFS data. EARSel eProceedings, Vol 3, No 2, 166-178.

Fong, D.A. 1998. Dynamics of freshwater plumes: observations and numerical modelling of the wind-forced response and alongshore transport. Ph.D. thesis, Massachusetts Institute of Technology / Woods Hole Oceanography Institution joint program in oceanography, Massachusetts, USA.

Garvine, R. W. 1999. Penetration of buoyant coastal discharge onto the continental shelf. Journal of physical oceanography, 29, 1892-1909.

Garvine, R.W. 2001. The impact of model configuration in studies of buoyant coastal discharge. Journal of marine research, 59, 193-225.

Gerritsen, H., Vos, R.J., Van der Kaaij, Th., Lane, A., & Boon, J.G. 2000. Suspended sediment modelling in a shelf sea (North Sea). Coastal engineering, 41(1-3), 317-352.

Gerritsen, H., Boon, J.G., Van der Kaaij, T., & Vos, R.J. 2001. Integrated modelling of suspended matter in the North Sea. Estuarine, coastal and shelf science, 53(4), 581-594.

Hickey, B.M., Pietrafesa, L.J., Jay, D.A., & Boicourt, W.C. 1998. The Columbia river plume: sub tidal variability in the velocity and salinity fields. Journal of geophysical research, 103(C5), 10339-10368.

Hoogenboom, H.J., Peters, S.W.M., Dekker, A.D., Hakvoort, J.H.M., & Pasterkamp, R. 1999a. The current status of the new generation ocean colour sensors for monitoring dutch waters. Technical report. UPS-2 report 99-28, project 2.1/DE-01. BCRS (BeleidsCommissie Remote Sensing, the Netherlands remote Sensing Board); Programme Bureau; Rijkswaterstaat Survey Department, P.O. Box 5023;2600 GA Delft; The Netherlands.

Hoogenboom, H.J. (Ed.). 2001. Noordzee-atlas voor zwevende stof; een overzicht op basis van SeaWIFS satellietbeelden uit 1999 (North Sea atlas for suspended matter; an overview based on SeaWIFS images in 1999). Tech. rept. RIKZ/IT/2001.013. National Institute for Coastal and Marine Management/RIKZ, Kortenaerkade 1; P.O. Box 20970; 2500 EX The Hague. 41 pp.

Jacobs, W. 2004. Modelling the Rhine River Plume. M.Sc. thesis. TUDelft, June 30th.

Kirk, J.T.O. 1996. Light and Photosynthesis in Aquatic Ecosystems (2nd Ed.), Cambridge University Press, Cambridge.

Kourafalou, V. H., Lee, T.N., Oey, L.-Y., & Wang, J.D. 1996a. The fate of river discharge on the continental shelf. 1. Modelling the river plume and the inner shelf coastal current. Journal of geophysical research, 101(C2), 3415-3434.

Kourafalou, V. H., Lee, T.N., Oey, L.-Y., & Wang, J.D. 1996b. The fate of river discharge on the continental shelf. 2. Transport of coastal low salinity waters under realistic wind and tidal forcing. Journal of geophysical research, 101(C2), 3435-3455.

Lacroix, G., Ruddick, K., Ozer, J. & Lancelot, C. 2004. Modelling the impact of the Scheldt and Rhine/Muese plumes on the salinity distribution in Belgian waters (southern North Sea). Journal of Sea Research. 52(3): 149-163

Lewis, R., 1997. Dispersion in Estuaries and Coastal Waters.

Marshal, J., & Plumb, A. 2003. Lecture notes: 'Physics of atmospheres and oceans'. http://www-paoc.mit.edu/labweb/notes.

Munchow, A., & Garvine, R.W. 1993. Dynamical properties of a buoyancy driven coastal current. Journal of geophysical research, 98(C11), 20063-20077.

Pasterkamp, R., & Van Drunen (Eds.), M. 2002. Noordzee-atlas voor zwevend stof op basis van satellietbeelden in 2000 (atlas of suspended sediment transport for the North Sea:

based on satellite imagery of 2000). Tech. rept. RIKZ/IT/2002.102. National Institute for Coastal and Marine Management/RIKZ, Kortenaerkade 1; P.O. Box 20970; 2500 EX The Hague. available via http://www.watermarkt.nl.

Pasterkamp, R., Esveld, M., Van der Woerd, H., & Van Drunen, M. 2003. Noordzee-atlas voor zwevend stof op basis van satellietbeelden in 2001 (atlas of suspended sediment transport for the North Sea: based on satellite imagery of 2001). Tech. rept. AGI-GAR-2003-38. RijkswaterstaatAdvies dienst geo-informatie (AGI), Postbox 5023; 2600 GA Delft.

Pedlosky, J. (2003) Baroclinic instability of time dependent currents. Journal of Fluid Mechanics, 490, 189-215.

Ridderinkhof, H., Van Haren, H., Eijgenraam, F., & Hillebrand, T. 2002. Ferry observations on temperature, salinity and currents in the Marsdiep tidal inlet between the North Sea and Wadden Sea. In N.C. Flemming et al. (eds). Operational oceanography: implementation at the European and regional scales. Proc. 2nd Intl. conf. on EuroGOOS, Elsevier, Amsterdam, 139-147.

Pietrzak, J.D. 2002. A three-dimensional hydrostatic model for coastal and ocean modelling using a generalised topography following co-ordinate system. Ocean modelling, 4, 173-205.

Pietrzak, J.D. 2004. Draft lecture notes 'CT 5317 Physical Oceanography', TU Delft.

Roozekrans, J.N. A ten-year NOAA-AVHRR SST database of the North Sea. http://www.knmi.nl/onderzk/applied/sd/en/sd_NOAA_AVHRR_KNMI.html

Roozekrans, J.N. & Prangsma, G.J. 1992. Observatie van het aard-atmosfeersysteem door de NOAA-satellieten (ontvangst, productie, toepassing en gebruik van de NOAA-data), BCRS-rapport 92-02, PB-BCRS, Delft.

Ruddick, K.G., Deleersnijder, E., De Mulder, T. & Luyten, P.J. 1994. A model study of the Rhine discharge front and downwelling circulation. Tellus 46A(2): 149-159.

Ruddick, K.G., Ovidio, F., & Rijkeboer, M. 2000. Atmospheric correction of SeaWIFS imagery for turbid and inland waters. Applied optics, 39(6), 897-912.

Simpson, J.H., Brown, J., Matthews, J., & Allen, G. 1990. Tidal straining, density currents, and stirring in the control of estuarine stratification. Estuaries, 13(2), 125-132.

Simpson, J.H., Bos, W.G., Schirmer, F., Souza, A.J., Rippeth, T.P., Jones, S.E., & Hydes, D. 1993. Periodic stratification in the Rhine ROFI in the North Sea. Oceanologica acta, 16(1), 23-32.

Simpson, J.H., & Souza, A.J. 1995. Semidiurnal switching of stratification in the region of freshwater influence of the Rhine. Journal of geophysical research, 100(C4), 7037-7044.

Simpson, J.H. 1997. Physical processes in the ROFI regime. Journal of marine systems, 12, 3-15.

Souza, A.J., & Simpson, J.H. 1996. The modification of tidal ellipses by stratification in the Rhine ROFI. Continental shelf research, 16(8), 997-1007.

Souza, A.J., & Simpson, J.H. 1997. Controls on stratification in the Rhine ROFI system. Journal of marine systems, 12, 311-323.

SRON, 2004. Project proposal: 'Improved understanding of the fate and transport of Suspended Particulate Matter in the Dutch Coastal Zone using satellite data'.

Stewart, R.H. 2002. Introduction to physical oceanography. USA: Texas A&M University.

Turner, M.R.J. 2002. Remote sensing and numerical modelling of suspended sediment. M.Sc. thesis, WL| Delft Hydraulics and IHE Delft.

Van der Woerd, H., & Pasterkamp, R. 2004. Mapping of the North Sea turbid coastal waters using SeaWIFS data. Canadian Journal Remote Sensing, 30(1): 44-53.

Van Raaphorst, W., Philippart, C.J.M., Smit, J.P.C., Dijkstra, F.J., & Malschaert, J.F.P. 1998. Distribution of suspended particulate matter in the North Sea as inferred from NOAA/AVHRR reactance images and in situ observation. Journal of sea research, 39: 197-215.

Visser, A.W., Souza, A.S., Hessner, K., & Simpson, J.H. 1994. The effect of stratification on tidal current profiles in a region of freshwater influence. Oceanologica acta, 17(4), 369-381.

Walker, N.D. 1996. Satellite assessment of the Mississippi river plume variability: causes and predictability. Remote sensing of environment, 21-35.

WL| Delft Hydraulics. 2003. Delft3D-FLOW, user manual. Delft: WL Delft Hydraulics.

WL|Delft Hydraulics. 2002. Data Model Integration and Total Suspended Matter. Delft: WL|Delft Hydraulics.

WL|Delft Hydraulics. 2001. Description and model representation T_0 situation. Part 1: The transport of fine-grained sediments in the southern North Sea. Delft: WL|Delft Hydraulics.

Yankovsky, A.E., & Chapman, D.C. 1997. A simple theory for the fate of buoyant coastal discharges. Journal of physical oceanography, 27, 1386-1401.

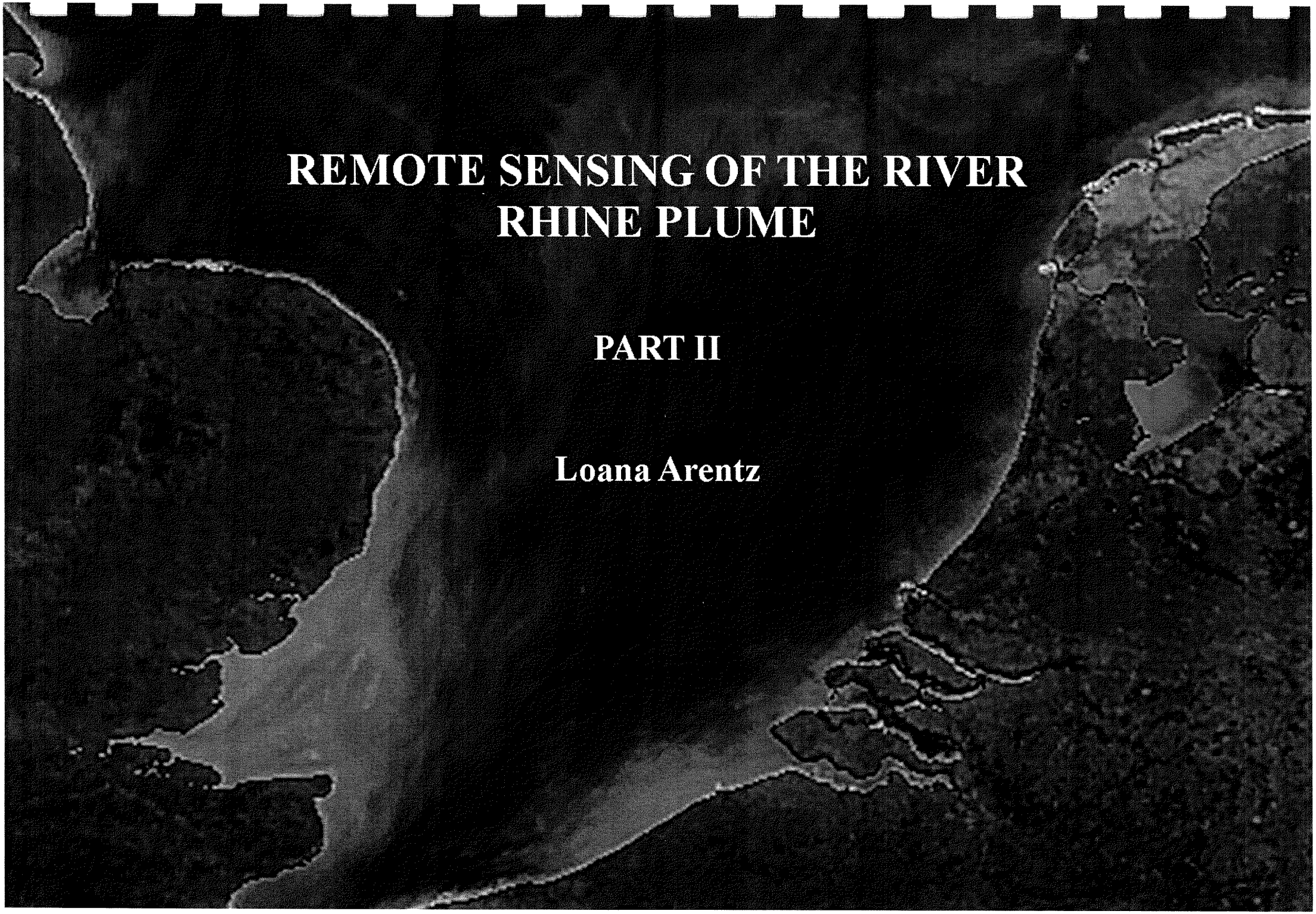

REMOTE SENSING OF THE RIVER RHINE PLUME

PART II

Loana Arentz

Contents

Contents i

APPENDIX 1 1

TECHNOLOGY - RS Methodology 1
A.1.1 Introduction 2
A.1.2 Theory of thermal and optical RS 2
A.1.3 Sensors 7
A.1.4 Data processing 12

APPENDIX 2 16

E–h-ΔT diagram 16

APPENDIX 3 19

METEOROLOGICAL DATA 1998 19

APPENDIX 4 23

SEASONAL AND MONTHLY MEANS 1998 23

APPENDIX 5 27

PLUME VARIABILITY? 27

APPENDIX 6 49

PHASES OF THE MOON 49

APPENDIX 7 51

HOT SPOTS 51

APPENDIX 8 62

RESULTS SST 62

APPENDIX 9 72

TIDAL PULSING 72

Appendix 1

TECHNOLOGY - RS Methodology

A.1.1 Introduction

Thermal and optical remote sensing (RS) systems are designed to detect terrestrial and solar radiation respectively. Terrestrial radiation is a measure of sea surface temperature and can be detected with the Advanced Very High Resolution Radiometer (AVHRR) both day and night. The Sea-viewing-Wide-Field-of-View-Sensor (SeaWIFS) detects solar radiation which has interacted with the constituents present in the upper part of the water column thereby providing information on their relative concentrations. Solar radiation can only be detected during the day.

A.1.2 Theory of thermal and optical RS

Radiometric quantities: Satellite sensors detect electromagnetic radiation (energy) Electromagnetic radiation (EMR) of energy travels (radiates) like harmonic sinusoidal waves at the speed of light. Unlike other wave types which require a carrier (e.g. water waves), energy waves can transmit through a vacuum (such as space). All energy levels (of EM radiation) are ordered according to their wavelength in a spectrum called the EM spectrum (see Fig. A.1.1). High energy levels travel in short EM waves, whereas low energy levels travel in long EM waves. RS systems operate in one or several portions of the EM spectrum.

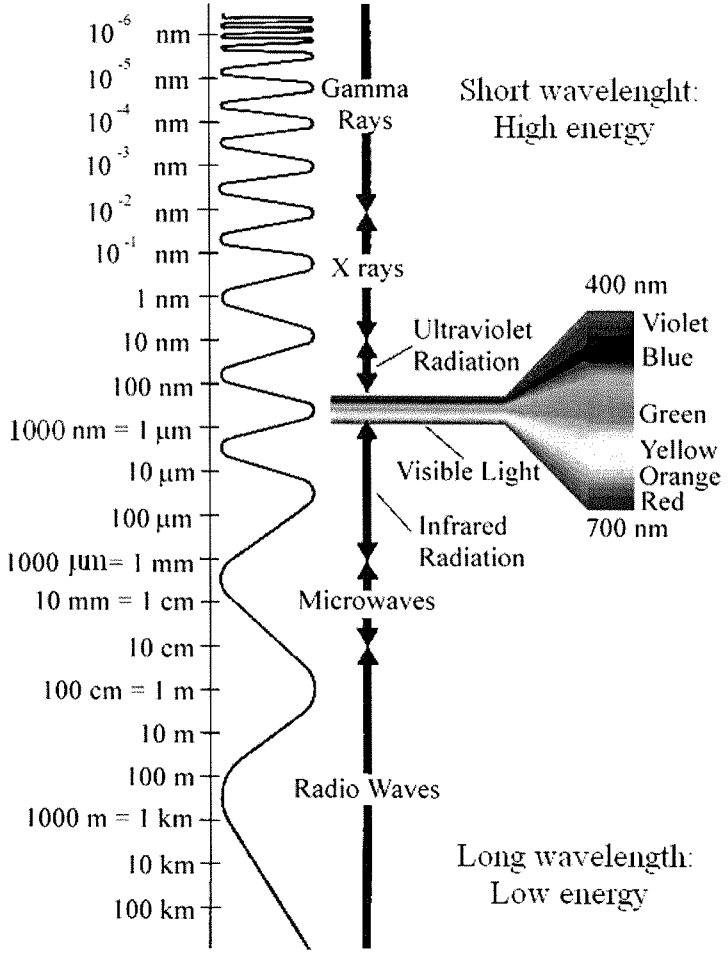

Fig.A.1. 1

EM spectrum. Visible range: 400-700 nm and the thermal IR: 3- 100µm.
Image: http://ethel.as.arizona.edu

The human eye, our "remote sensor(s)", can detect EMR at the visible light wavelengths of the EM spectrum, ranging from 400 to 700 nm (1 nm = 10^{-9} m). Our eyes perceive this "visible" EMR or (visible) light as colour. The longest visible wavelength (to our eyes) is perceived as red, and the shortest as violet (see Fig. A.1.1). Note how small the visible portion of EM radiation is relative to the rest of the spectrum.

SeaWIFS, the "optical sensor" used in this project measures energy in the visible light range of the EM spectrum. The AVHRR, the "thermal sensor" measures in the (thermal) infrared range of the spectrum which ranges from 3 to 100μm (1 μm = 10^{-6} m).

Energy sources: The primary source of energy (EMR) is the sun. The sun illuminates the earth. Solar irradiation (incoming/incident EMR) arrives at the earth at wavelengths which are determined by the energy output level of the sun. Approximately 41% of the total solar radiation arrives at the earth's surface at the visible wavelength range and is often referred to as light (see Fig. A.1.2).

As EMR travels through the earth's atmosphere, atmospheric gasses, suspended particulates (aerosols) and clouds present in the atmosphere absorb or scatter a fraction of the EMR. The remainder, only a very small part of the EMR, is transmitted in a straight-line path (see Fig. A.1.3). Once the transmitted EMR has reached the sea surface (air-sea interface), a fraction part will penetrate into the upper layer while some will be reflected off the sea surface back into the atmosphere (sun glint). The EMR that penetrates into the upper layer of the water column is now absorbed and scattered by the water molecules and water constituents present in the surface layer. There are four main types of substances that can interact with EMR: pure seawater, phytoplankton (and associated degradation products), suspended particulate matter (i.e. non-chlorophyllous inorganic matter) and yellow substance (coloured dissolved organic matter) (Kirk 1996). In the water column, both absorption and scattering can occur with pure water and phytoplankton, whereas sediment particles (SPM) and yellow substance only cause scattering and absorption respectively (Kirk 1996).

The portion of the EMR which is absorbed is later re-emitted as thermal radiation at longer wavelengths (invisible to human eye). This EMR is often referred to as thermal- or terrestrial radiation or heat. All bodies whose temperature is above absolute zero Kelvin (-273.2 °C) emit EMR over a range of wavelengths within the thermal infrared portion of the EM spectrum (3 - 100μm). This **thermal radiation is the energy source for thermal RS** and can be measured during day and night.

The amount of EMR which after penetration into the water column is not absorbed but scattered back up into the atmosphere contains information about the underwater compositions of the various constituents (in the upper penetrated layer). This so called **"water-leaving radiance" is the parameter of interest for optical RS**. The water-leaving radiance can be seen as light which is reflected off the optically active substances present in the upper part of the water column. Optical RS is often referred to as measurement of this reflected light. Note that water-leaving radiance is not the same as the surface-reflected solar beam (sun glint) which does not penetrate the water column and does not contain information about the underwater light field. The water-leaving radiance is only a small percentage of the EMR that enters the water because most of the EMR at different wavelengths are absorbed by the substances present in the upper part of the water column

Fig. A.1.2 shows the actual solar and terrestrial radiation. The light yellow shape shows that the EMR radiation leaving the surface of the sun (energy output of the sun) travels at relatively short wavelengths. The dark yellow shape shows the solar irradiation, which after interaction with the atmosphere, arrives at the earth's surface. Approximately 41 percent of the total solar irradiation falls within the visible wavelength range (0.4 to 0.7 μm), with a maximum radiation intensity at 0.48 μm. The broken green shape shows how the solar irradiation is absorbed and re-radiated as heat at longer wavelengths, with a maximum emission at 9.7 μm. The earth radiates ~160.000 times less than the sun (www.udel.edu).

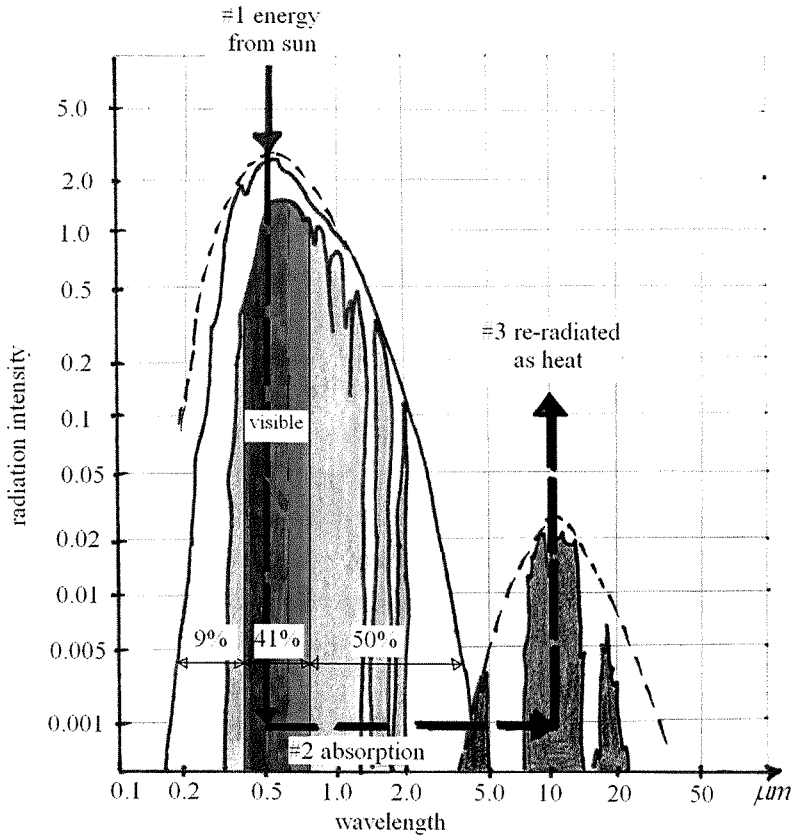

Fig.A.1. 2

Actual solar and terrestrial radiation. Note the log scales.

Atmospheric interaction: The processes of atmospheric interaction, absorbance and scattering, are shown in Fig. A.1.3. Scattering in the atmosphere occurs when radiant energy interacts with gaseous molecules, particulates (aerosols) and clouds, which cause the radiant energy to diverge from its original path. Divergence can either cause the incident radiation to bounce off the particles' surface in a single predictable direction (often referred to as reflection), or it can result in dispersion of the incident radiation in many unpredictable directions. Scattering often results in a change of velocity or wavelength. In the presence of clouds, the scattering of shortwave radiation can be very strong, hence inhibiting the sensor to receive a signal from the sea surface.

Absorption of EMR is wavelength selective. The most significant atmospheric absorbers of EMR are gasses: ozone (O_3), carbon dioxide (CO_2), water vapour (H_2O) and oxygen (O_2). Absorbed EM radiation is usually re-reradiated at longer wavelengths. Certain wavelengths of EMR pass relatively unimpeded through the atmosphere, whereas others are partially or totally absorbed. The spectral regions (wavelength ranges/bands) of the EM spectrum that are particularly transmissive of EMR are often referred to as atmospheric windows or transmission bands. The wavelength ranges where absorption by atmospheric gasses occurs directly are called atmospheric blinds or absorption bands. RS data acquisition of surface features is limited to the "atmospheric windows" of the EM spectrum. **None of the windows transmit 100 %.**

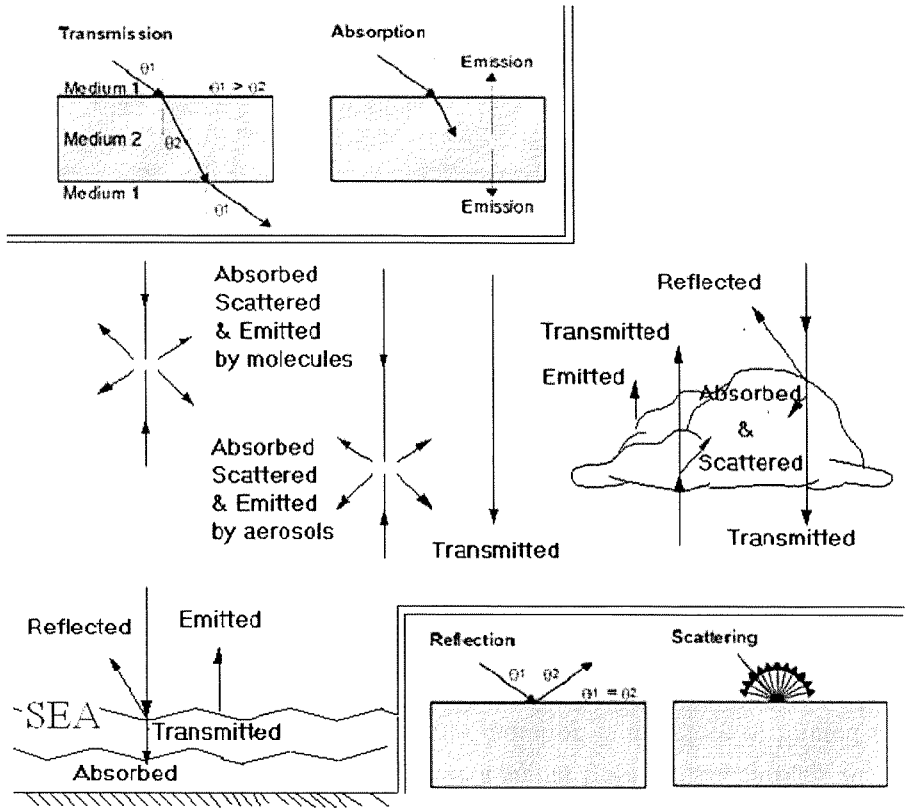

Fig.A.1. 3

Atmospheric interactions. Image: http://rst.gsfc.nasa.gov & http://orbit-net.nesdis.noaa.gov

Fig. A.1.4 shows the absorption-transmission of EMR by atmospheric gasses as a function of wavelength in case of a cloud-free atmosphere. The visible region of the EM spectrum resides within an atmospheric window in the wavelength range of about 0.3 to 0.9 μm, while emitted energy from the earth's surface (thermal radiation) is sensed through windows at 3 to 5 μm and 8 to 14 μm. Atmospheric windows become less transparent/transmissive when air is moist (high humidity). Clouds (water vapour H_2O) absorb most of the long wave radiation emitted from the earth's surface. The degree to which these processes of atmospheric interaction affect the radiation along the path through the atmosphere depends on the path length, the presence of particulates and absorbing gases and the wavelengths involved.

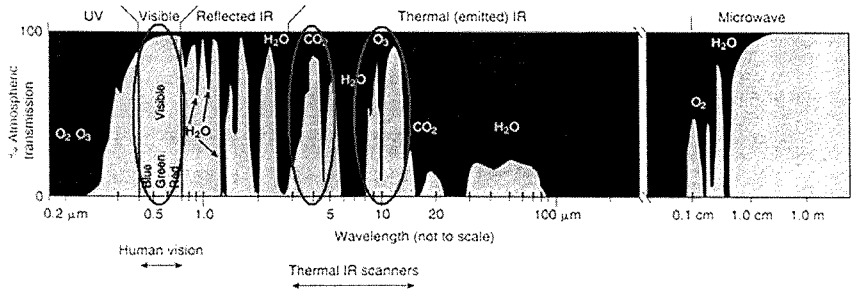

Fig.A.1. 4

Absorption-transmission characteristics of a cloud-free atmosphere. Black zones mark minimal passage of radiation, whereas, grey areas denote atmospheric windows, in which absorption of radiation by atmospheric gasses is minimized. Image: www.udel.edu

Fig. A.1.5 gives an indication of the average ratios of EMR which are reflected, scattered, absorbed and transmitted. The message to derive from this picture is that from the total signal detected by the satellite sensor, only a fraction is the signal of interest. **Even when measuring EMR in atmospheric windows, only about 4-5% of the total radiation detected by the satellite sensors is the signal of interest. The other 95 % of the signal is due to atmospheric effects.**

In the presence of clouds, the scattering of shortwave radiation (light) and absorption of long wave radiation (terrestrial radiation) can be very strong, hence inhibiting the sensor to receive a signal from the sea surface. RS of water-leaving radiance and terrestrial radiation is therefore of limited use in such cases. The net result is that both optical and thermal RS are very sensitive to cloud cover.

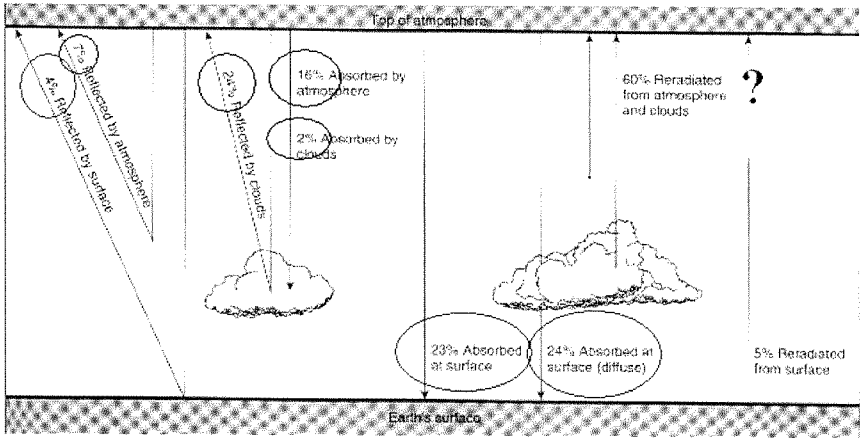

Fig.A.1. 5

Radiation balance: net result of the atmospheric interactions of absorption and scattering when measuring in atmospheric window. Image: www.udel.edu

Corrections must be applied to the measured data to account for this atmospheric radiance, allowing accurate measurement of the intensity and the wavelength of the radiance exiting the water surface. These corrections are part of the data processing (see section A.1.4 data processing).

Spectral response (signature): All matter/substances absorb and radiate varying energy levels over a range of wavelengths in their own characteristic way depending on their chemical composition and physical state. The variation in radiation intensity with wavelength is called the spectral response or spectral signature. The radiation intensity is not only dependant on the type of material (vegetation, water etc) but also on the concentration thereof. Various kinds of material in the surface layer can be recognized and distinguished from each other by their spectral signature. The shape of spectral signatures has a major influence on the choice of wavelength region (band) in which RS data are acquired for a particular application. Features and their different conditions must show enough variation to allow for individual identification. For example: water and vegetation may radiate somewhat similarly in the 2-5 μm wavelengths but are easily separated when measuring in the 0.8-2 μm wavelength range (see Fig. A.1.6).

A.1.3 Sensors

Both the AVHRR and the SeaWIFS sensors measure in multiple spectral bands. The choice of the location of the bands is determined by the purpose of the satellite. By combining measurements from one band with measurements from different bands or with other datasets, it is possible to acquire information on land- or sea surface and to detect clouds.

Advanced Very High Resolution Radiometer (AVHRR): The AVHRR has three bands in the thermal IR region of the EM spectrum which are specifically designed to measure the temperature of the sea surface (see Table A.1.1). Combining measurements made in these three bands (3, 4 and 5) allows for a relatively accurate atmospheric correction, resulting in a relatively accurate SST signal.

Table A.1. 1 Spectral characteristics AVHRR

Band	Wavelength (μm)		Bandwidth (μm)	Design purpose
1	0.58 - 0.68	VIS: Red	0.10	Cloud, snow and ice monitoring
2	0.725 - 1.1	Near IR	0.375	Water, vegetation and agriculture
3	3.55 -3.93	Thermal IR	0.38	Sea surface temperature
4	10.3 - 11.3	Thermal IR	1.00	Sea surface temperature
5	11.5 - 12.5	Thermal IR	1.00	Sea surface temperature

Sea-viewing WIde Field-of-view Sensor: The SeaWIFS mission is a public-private partnership between NASA and Orbimage Inc. The SeaStar satellite which carries the SeaWIFS sensor was launched in August 1997 and was specifically designed for monitoring phytoplankton (chlorophyll) concentrations in "Case 1" waters. The term "Case 1" (and also "Case 2") refers to water "type" defined by optical characteristics. Case 1 water is clear, open-ocean water, with low inorganic suspended particulate matter concentrations (SPM). Chlorophyll (phytoplankton) are the primary optically active material in Case 1 water. Other substances that can interact with the solar irradiation like SPM and coloured dissolved organic matter (CDOM) (see section A.1.2 energy interactions) are not considered here due to their very low attribution (low concentrations). However, in this project, we are interested in the Dutch coastal zone, which is more typical of Case 2 waters, characterized by high inorganic suspended matter resulting in a higher optical complexity. This specification has direct implications for the application of SeaWIFS data for analysis of the Rhine plume.

Table A.1. 2 Spectral characteristics SeaWIFS (Source: NASA 1994, the living ocean – observing ocean color from space, NASA pub code PAM-554). Because SeaWIFS is primarily designed for Case 1 waters, these spectral characteristics also hold for Case 1 waters

Band	Wavelength (nm)		(nm)	Design purpose (**Case 1**)
1	402 - 422	VIS: Violet	20	Dissolved organic matter absorption
2	433 - 453	VIS: Blue	20	Chlorophyll absorption
3	480 - 500	VIS: Blue-green	20	"
4	500 - 520	VIS: Blue-green	20	"
5	545 - 565	VIS: Green	20	"
6	660 - 680	VIS: Red	20	Atmospheric aerosols
7	745 - 785	Reflective IR	40	"
8	845 - 885	Reflective IR	40	"

SeaWIFS measures in eight spectral bands of very narrow wavelength ranges (see Table A.1.2) tailored for specific detection of phytoplankton (chlorophyll) concentrations in oceanic Case 1 waters. Bands 7 and 8 in the reflective infrared are necessary for the retrieval of aerosol related properties at the visible wavelengths for atmospheric correction purposes.

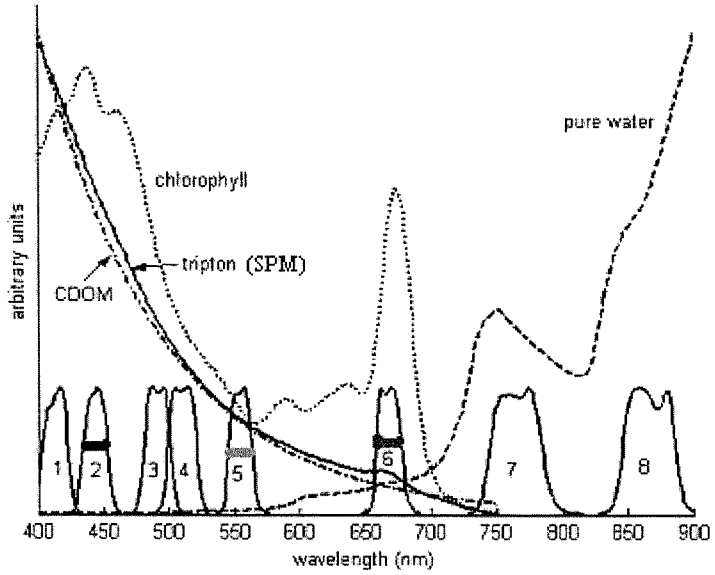

Fig.A.1. 6

Typical spectral absorption curves (spectral signatures) for chlorophyll, SPM, CDOM and water in Case 2 water. Image: van der Woerd et al., 2004

Although SeaWIFS is primarily designed for detection of chlorophyll concentrations in Case 1 waters, this project aims to use SeaWIFS images for the detection of sediments (SPM) in turbid Case 2 water. SPM is hypothesised to be a tracer of the plume. The location of the six visible wavelength bands is determined by a dominant spectral chlorophyll signal in Case 1 water bodies. For the purpose of this project, it would be ideal to have a bandwidth with maximal sensitivity for sediments (SPM) and minimal sensitivity to the other constituents present in the upper layer of the water column. Also the sensitivity to inaccuracies in atmospheric correction should be minimized. Fig. A.1.6 shows the location of the eight SeaWIFS bands in relation to typical absorption curves (spectral signatures) of chlorophyll, SPM, CDOM and water in Case 2 waters. Because the spectral signatures do not show enough variation to allow for individual identification of SPM, such an ideal band for tracing SPM does not exist.

Studies by WL|Delft Hydraulics, 2002 and van der Woerd et al., (2004) have shown that band 5 turns out to be the most appropriate SeaWIFS band for tracing SPM in the turbid North Sea. This argument assumes that the backscatter due to seawater is constant and that the ratio between SPM-, chlorophyll- and CDOM backscatter is constant. Because most of the suspended matter present in the North Sea is inorganic, an increase in the backscatter signal is assumed to be indicative of an increased SPM concentration. It should be noted that when high concentrations of algae (chlorophyll) are present, the uncertainty with the data increases. Generally the highest concentrations of algae in the North Sea are found close to the coast in May/June and September/October (Peperzak et al., 1998). On the other hand, algal blooms are relatively easily recognized as (often) discrete patches of increased chlorophyll concentration. However, SeaWIFS images from these months should be considered more uncertain..

Data formats: Both sensors (SeaWIFS and AVHRR) produce scientific data of two spatial resolutions: high, Local Area Coverage (LAC), 1 km^2 resolution data, and low, Global Area Coverage (GAC), 4 km^2 resolution data. Because there is a limit to the amount of recording storage onboard the spacecraft, only GAC data are recorded. For this study the 1 km^2 resolution data are needed, because the width of the Rhine plume is in the order of the internal Rossby radius of deformation (4km). The satellites broadcast the full resolution LAC data in real-time. Various High Resolution Picture Transmission (HRPT) ground stations all over the world pick up this signal. Due to the finite reception area of the HRPT stations, the HRPT LAC data are inherently regional in spatial coverage. HRPT data (= non-recorded, continuously broadcasted, LAC data) is lost unless it is received by a ground station. The 1 km^2 resolution HRPT data are available for the North Sea because of the presence of HRPT ground stations (Dundee in Scotland for SeaWIFS and AVHRR data and KNMI in the Netherlands for AVHRR data only).

Data levels: For RS data to be useful, RS data is usually processed through several "levels" ranging from raw data up to Level 4 data (see Table A.1.3). In general, at higher levels, the data have been converted into more usable parameters and formats that are of interest to specific users. At Level 4, RS products are refined through the use of mathematical models and combinations with other measurements. **In this project the data are processed up to Level 2.** The definitions of the data levels were agreed upon by the National Academy of Sciences Committee on Data Management (CODMAC) and are applicable to all types of RS data.

Table A.1. 3 Data levels RS data

Level 0	Before there has been any data processing, the raw electronic counts from all bands is termed Level 0 data. Raw data simply consist of the electronic signal that is produced when photons of light are detected by the instrument (satellite sensor). The signals are assigned to picture elements (pixels) which are the basic pieces of a remote sensing image. The electronic signal has not yet been converted to measured radiances. This is the data format the HRPT stations receive.
Level 1A	The electronic level 0 signal from the detector (satellite sensor) is converted into radiances measured at the satellite sensor, and ancillary information (meteorological and ozone), including radiometric and geometric calibration coefficients and geo location parameters are added/assigned to the data. The SeaWIFS project provides Level 1A data to the community.
Level 1B	The Level 1A data have been modified using the sensor calibration (not all instruments will have a level 1B equivalent).
Level 2	Level 2 products are derived geophysical variables at the same resolution and location as the Level 1 source data. The conversion from L1 data to L2 products applies atmospheric corrections to calculate *Earth surface radiances* from the radiances measured at the satellite. KNMI provides L2 data to the community.
Level 3	Level 3 data products are variables mapped on uniform space-time grid scales, usually with some completeness and consistency.
Level 4	Level 4 data products are model output or results from analyses of lower level data, e.g. variables derived from multiple measurements.
Source: http://observer.gsfc.nasa.gov/sec3/ProductLevels.html	

AVHRR data acquisition: Dundee in Scotland and KNMI in the Netherlands receive NOAA Level 0 satellite data for the North Sea. Dundee records both raw Level 0 HRPT data and processed (up tot various levels) data, whereas KNMI only provides Level 2 products. The NOAA data used in this project were acquired from the KNMI HRPT station. The reason why KNMI only archives Level 2 data is to save recording space. KNMI developed a fully automated processing system which automatically processes the Level 0 data to Level 2 data. In case of Level 2 data of sea surface temperature the HRPT scene is automatically cropped to the region as shown is Fig. A.1.7.

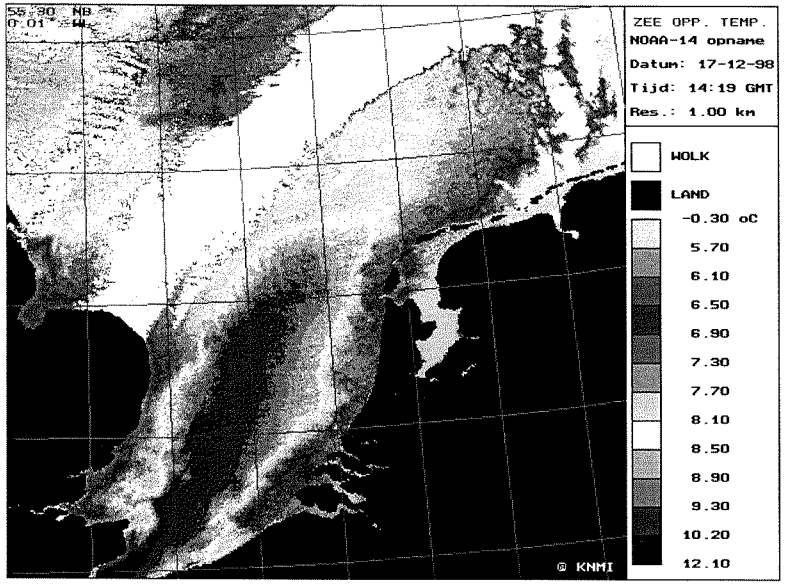

Fig.A.1. 7

KNMIs region of interest for SST imagery.

Only SST images in which a large part of the North Sea is visible (not blocked by clouds) are archived in binary format. The data in the archive are accessible for public and can be obtained via the archive manager (H. Roozekrans). KNMI charges costs for the man hours required to get the requested data from the archive (Roozekrans en Prangsma, 1992). **For this project, all 156 Level 2 images of SST available for the year 1998 were obtained from KNMI.**

SeaWIFS data acquisition: The main archive for all SeaWIFS data is the Goddard Space Flight Centre (GSFC) Distributed Active Archive Centre (DAAC). Various approved HRPT ground stations all over the world downlink and store real-time high resolution LAC data and are under contract with Goddard DAAC to distribute the data. The GSFC DAAC remains the proprietor of the data. Each HRPT pass will be kept as one data file. For this reason HRPT scenes can range from very short (if satellite is at the horizon of the station) to very long (several minutes). One of the HRPT ground stations that cover the North Sea is in Dundee in Scotland (however there are more).

The procedure for ordering SeaWIFS data from the Goddard DAAC is straightforward and can be done quite easily via internet. After specifying a HRPT station and time period, the available images ("thumbnails") can be viewed with a browser. The desired images can be selected and ordered.

Access to SeaWIFS data is restricted to authorized users strictly for research and educational purposes only. A free authorized user status can be obtained from NASA by registering with the SeaWIFS project. A contract must be signed, promising that the data will not be used commercially. An acknowledgement to the Goddard DAAC has to be included in any report where SeaWIFS data is used (see acknowledgements of this report). **For this project G. de Boer obtained a SeaWIFS authorized user-license from NASA and 244 HRPT scenes in 1998 which showed a significant of the North Sea were obtained from DAAC.**

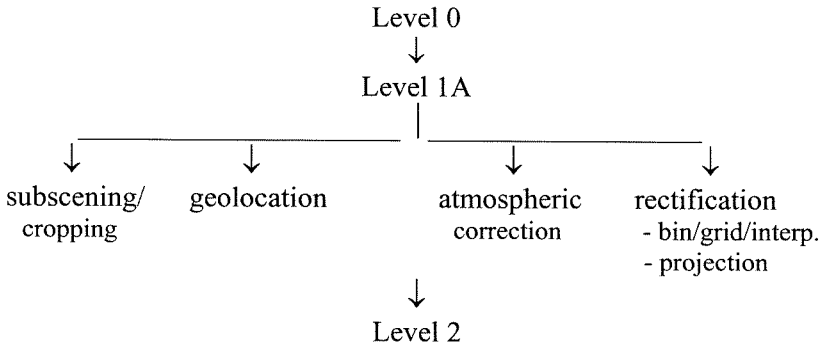

Fig.A.1. 8

Data processing chart

A.1.4 Data processing

Data processing in general: Some of the basic steps in processing of raw sensor data into an end product are illustrated in Fig. A.1.8. To ensure a reduction in processing time the images are first "subscened" (cropped) to the region of interest. Then, the RS signal is "geolocated", i.e. the measured pixels are manually (by hand: image per image) assigned a spatial location on the earth's surface (resulting in an image). Note that this is not possible if the coastline is covered by clouds. After geolocation the data are rectified (binned/gridded and interpolated) to a grid which is equidistant in some map projection in order to allow for statistical analysis and image-by-image comparison (see Fig. A.1.9).

This introduces a small loss of information for images with high spatial resolution (centre of swath) or doubling of pixels in images with low spatial resolution (side of swath). One of the last and most important steps in processing comprises the atmospheric correction. The radiance measured at the satellite sensor (the so-called Top Of Atmosphere, or TOA signal) is corrected for atmospheric effects translating the measured signal to surface albedo (a measure of temperature) and subsurface reflectance in the case of AVHRR and SeaWIFS respectively. The image is then masked with flags for land and for clouds and ice to indicate non-usable pixels.

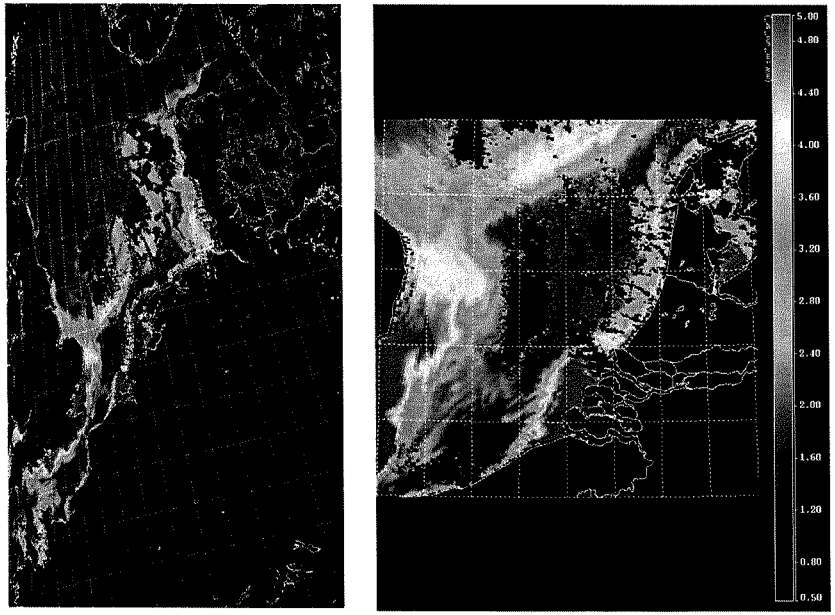

Before rectification After rectification

Fig.A.1. 9

SeaWIFS 9-Mar 1998 12:00

Data processing AVHRR: The RS data from the AVHRR have already been automatically processed up to Level 2 data to produce images of Sea Surface Temperature (see A.1.3: AVHRR data acquisition). The geolocation of the pixel values in KNMIs processing system is performed after polar stereographic projection of the raw data (Roozekrans and Prangsma, 1992). This can be recognized for instance, by a distorted coastline. For best results geolocation should be performed before projection. If this is not done the result is that distorted images do not coincide with the drawn coastline over the whole coastline. With the data processing system developed by Gerben de Boer (section 3.3 of Part I) the polar stereographic projection of the SST images can be transformed to a UTM 31 projection.

Data processing SeaWIFS: The raw Level 1A SeaWIFS data were processed with the SeaWIFS Data Analysis System (SeaDAS) to produce normalized water-leaving radiance. "Normalized water-leaving radiance" is the radiance that would be measured exiting a flat surface of the ocean with the Sun at zenith (directly overhead) and the atmosphere absent (Kirk, 1996). Because SeaWIFS was developed from a perspective of global ocean monitoring, the science teams responsible for the development of SeaDAS have concentrated on processing algorithms based on clear, open-ocean, Case 1 waters. The use of the standard SeaDAS processing software in coastal regions causes anomalies, because the atmospheric correction algorithm implemented in SeaDAS encountered problems for turbid waters. The Management Unit of the North Sea Mathematical Models (MUMM); a department of the Royal Belgian Institute of Natural Sciences have adapted the standard processing method and developed an extension for the SeaDAS software with respect to SeaWIFS atmospheric correction over turbid waters (Ruddick et al., 2000). This MUMM software was used for the atmospheric correction of SeaWIFS' turbid water in this project.

A first level of geo-corrections is already included in the Level 1A data (see data levels). A geolocation manual refinement processing step can be done using SeaDAS, but is very time consuming because every image has to be adjusted by hand. Because the first level geo-correction is quite accurate already, the images were not manually geolocated. Still the image and the drawn coastline may not always coincide. All images have been subscened to (60 °N, 48 °N, 4 °W, 12 °E).

Validation impasse: Absolute validation of RS data is difficult to achieve, because it is hard to get in situ sample information that temporally and spatially coincides with the satellite image. Exact matches will be very sparse. Even in case of an exact match, RS information can never be properly linked to in-situ measurements because RS information is averaged over a 1 km^2 area. This validation impasse is however not much of a problem for the objectives of this study since SST and nLw are only used as a tracer (i.e. qualitative measure), leaving actual (i.e. quantitative) values irrelevant.

Table A.1. 4 Sensor & satellite details

	AVHRR (http://www.oso.noaa.gov/poesstatus/)	**SeaWIFS**
Name	Advanced Very High Resolution Radiometer	Sea-viewing WIde-Field-of-View-Sensor
Operational on satellites	NOAA's Polar Orbiting Environmental Satellites: - NOAA-12 : launched 14-May 1991 - NOAA-14: launched 30-Dec 1994 - NOAA-15: launched 13-May 1998	Orbimages's SeaStar Aug-1997
Orbit altitude	804/845/808 km	705 km
Orbit type	Polar orbiting, sun-synchronous[1]	Polar orbiting, sun-synchronous
Orbital period	~ 100 min	~ 100 min
	~14 orbits/day	~14 orbits/day
Spectral resolution	5 bands	8 bands
Temporal resolution (Revisit time)	2/day	2/day
Swath width	2700 km 2399km (scan angle 55.4 degr)	2801 km (58.3 deg); 1502 km (45.0 deg)
Spatial resolution (IFOV[2])	Resolution: LAC 1.1 km at nadir GAC 4.4 km at nadir	Resolution 1.13 km LAC at nadir; 4.5 km GAC
Radiometric resolution	10 bit = 2^{10} (1024)	10 bits

[1] Sun-synchronous satellites pass over a point on the Earth at the same time each day. The sun-synchronous environmental satellites are "polar orbiting," meaning that they orbit the Earth from north to south, passing over the North and South Poles during each orbit.
[2] IFOV = Instantaneous Field-of-View

Appendix 2

E–h-ΔT diagram

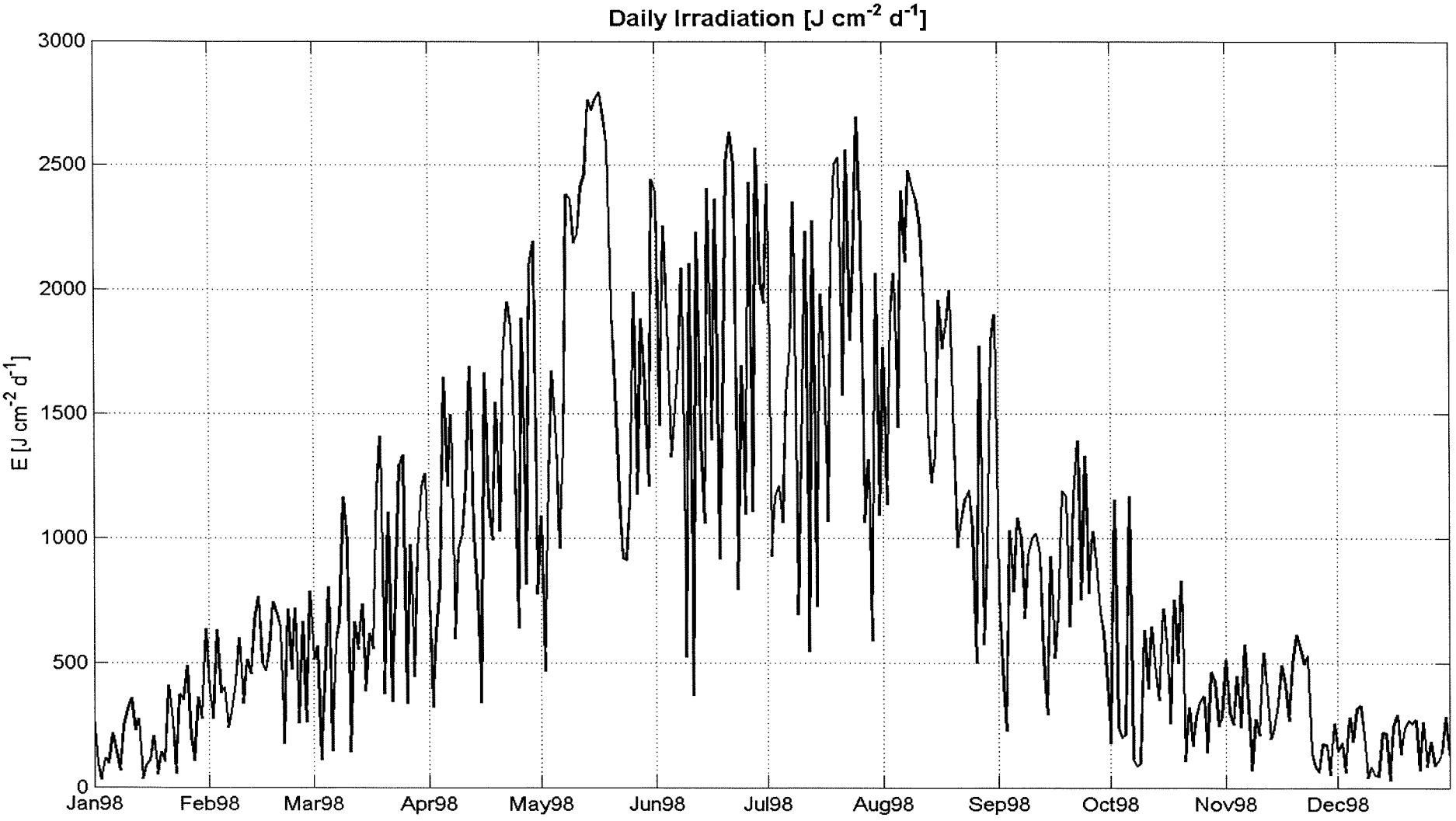

Daily solar irradiation for 1998 from de Kooy Den Helder (KNMI)

$$\Delta T = \frac{E}{\rho \cdot h \cdot C_d}$$

For FRESHwater:

E : energy input [J m^{-2}]

h : thicknes water layer [m]

ρ : 998 [kg m^{-3}]

C_d : 4186 [J $kg^{-1}K^{-1}$]

ΔT : temperature increase freshwater layer

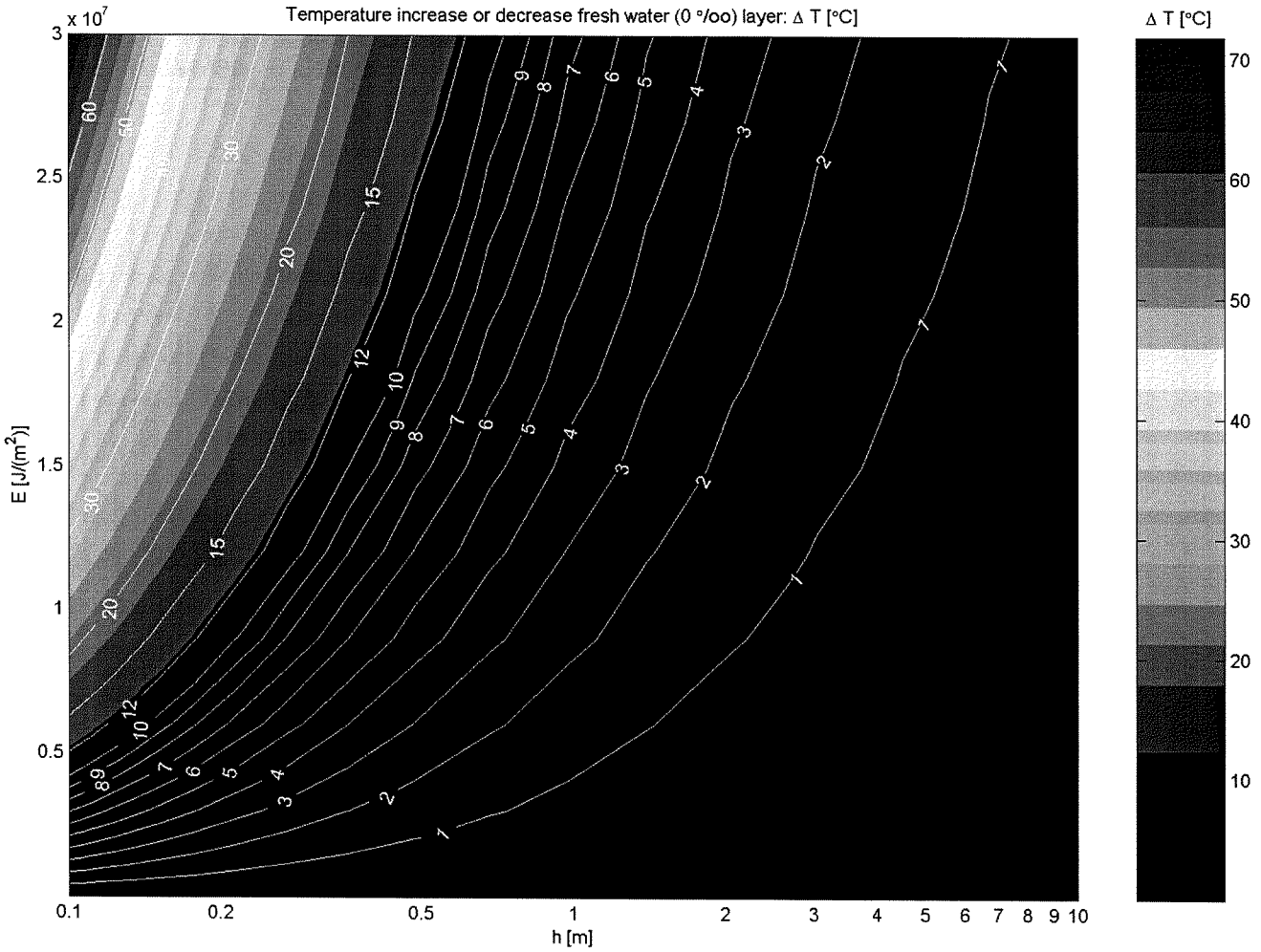

E-h-ΔT diagram for freshwater

Appendix 3

METEOROLOGICAL DATA 1998

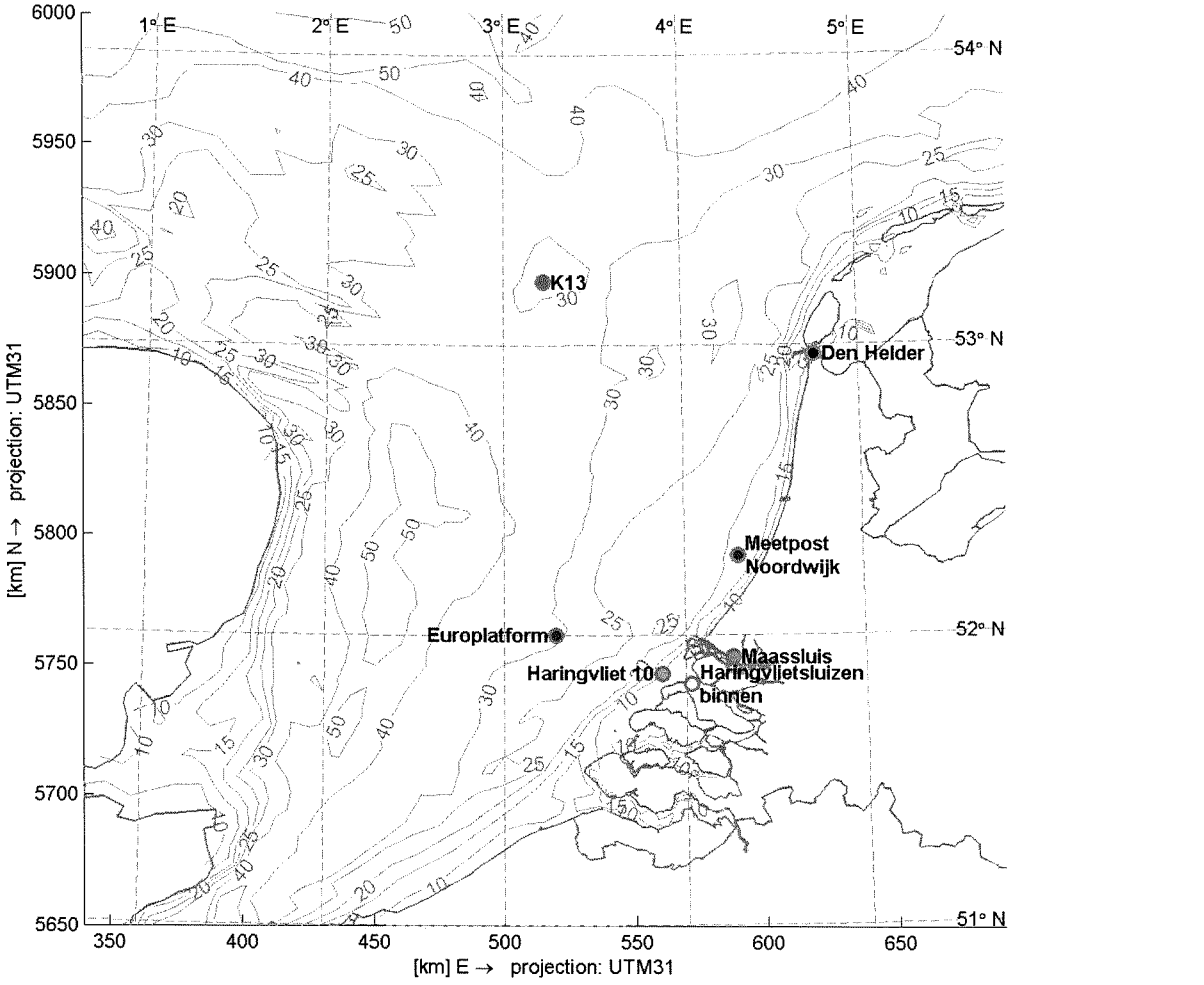

© Delft University of Technology CiTG: fluidmechanics.tudelft.nl

Locations of measuring stations meteorological data and bathymetry (in m).

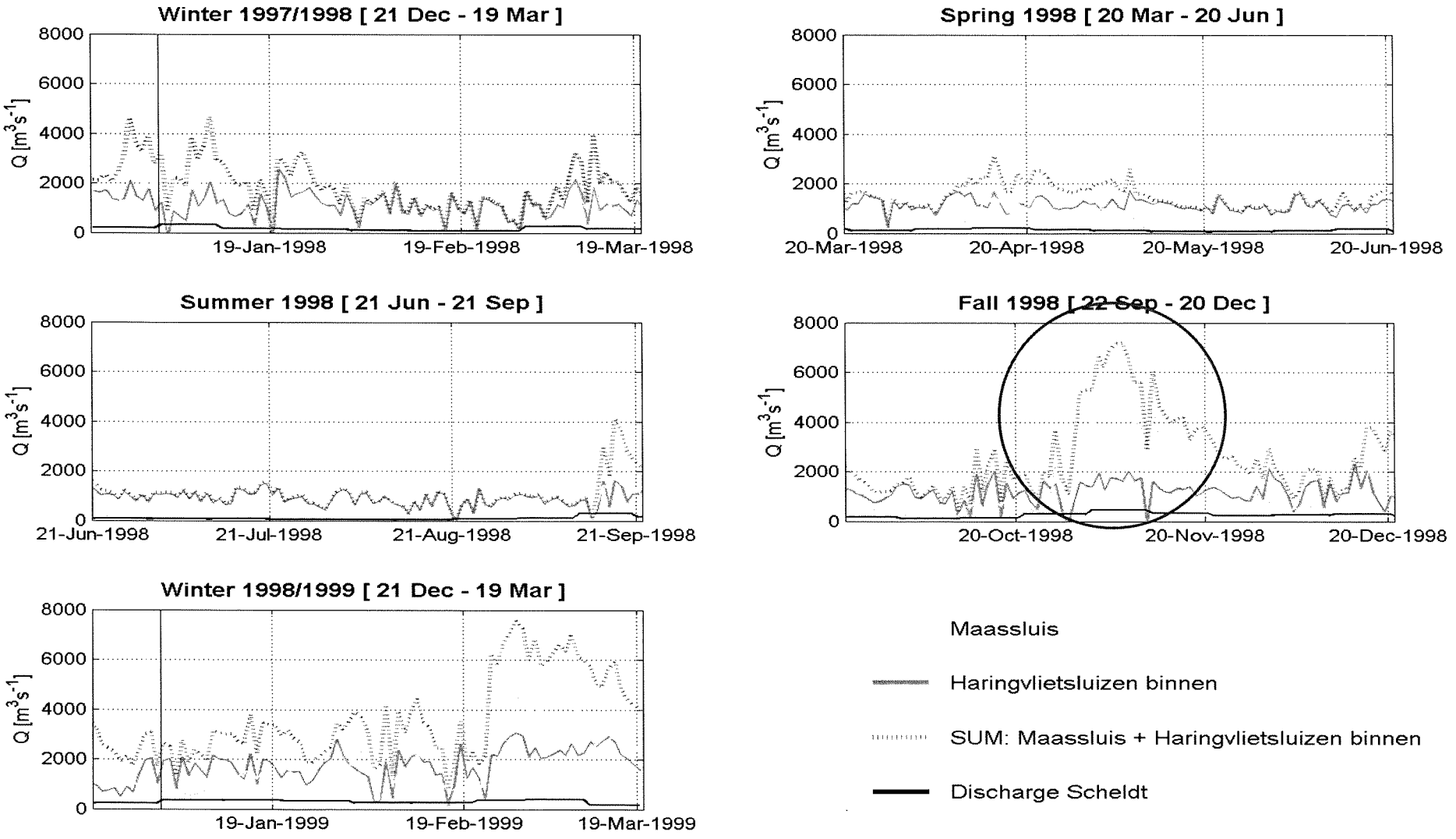

1998 Discharges (RIKZ/RIZA)

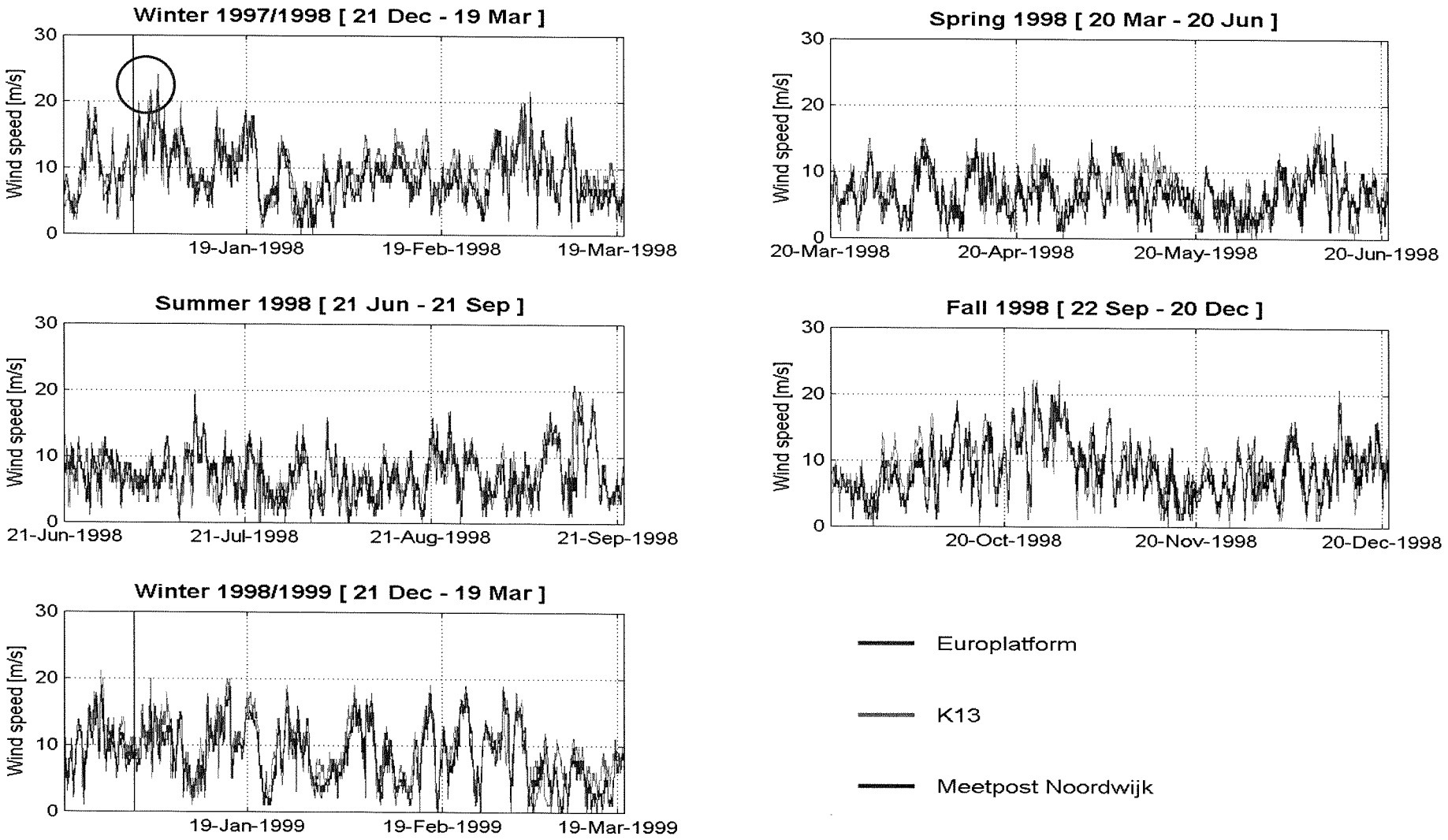

1998 Wind speeds (KNMI)

Appendix 4

SEASONAL AND MONTHLY MEANS 1998

Seasonal means SST 1998 (based on unclouded pixels):

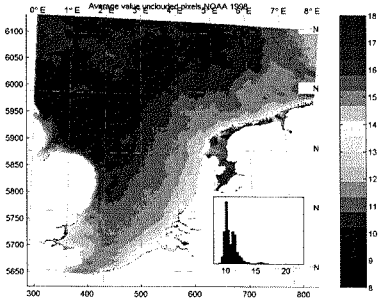

Spring (54)

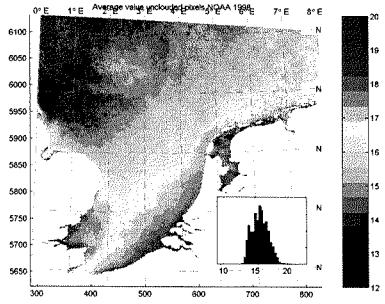

Summer (32)

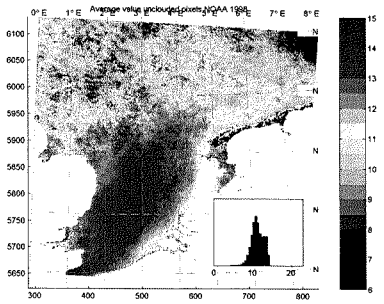

Fall (28)

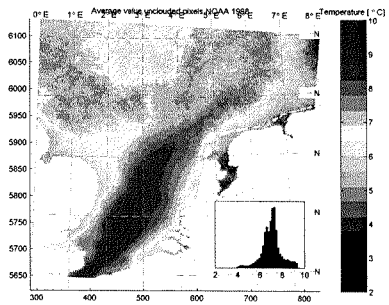

Winter (42)

Seasonal means nLw 1998 (based on unclouded pixels):

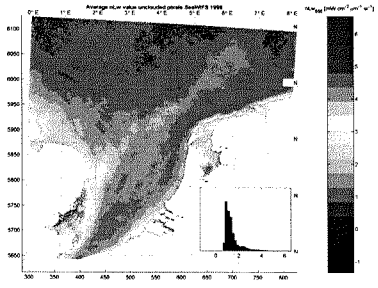

Spring (51)

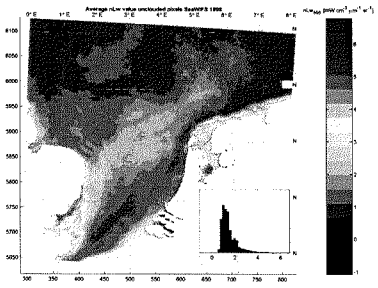

Summer (62)

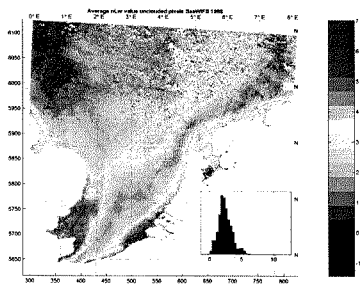

Fall (15)

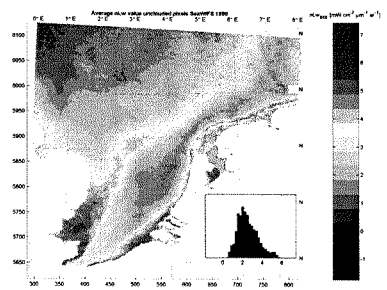

Winter (35)

Note: the numbers indicate the number of images on which the mean is based.

Monthly means SST 1998 (based on unclouded pixels). The numbers indicate the number of available images for that month.

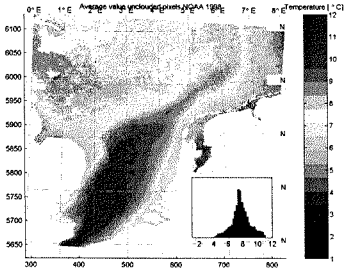

Jan (13)

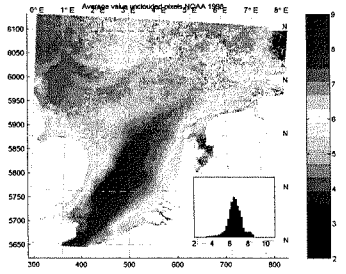

Feb (16)

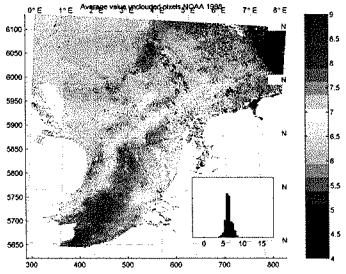

Mar (4)

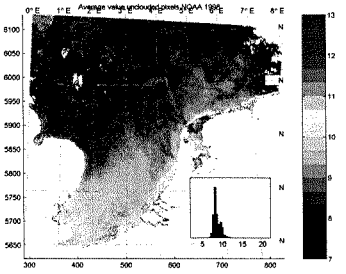

Apr (5)

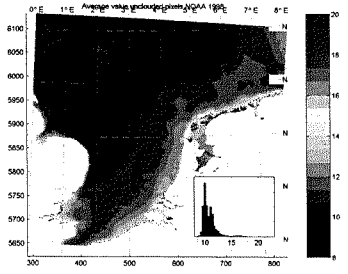

May (38)

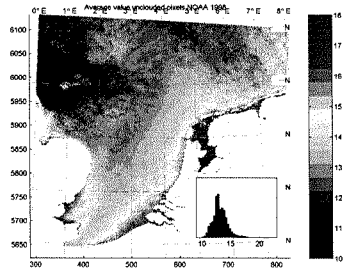

Jun (15)

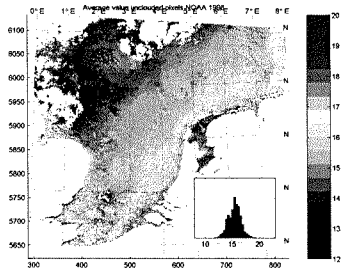

Jul (4)

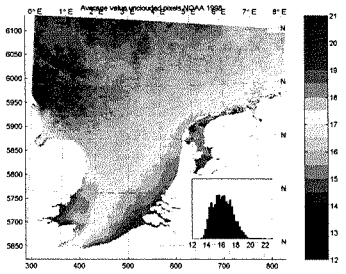

Aug (19)

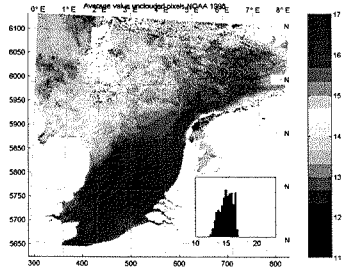

Sep (17)

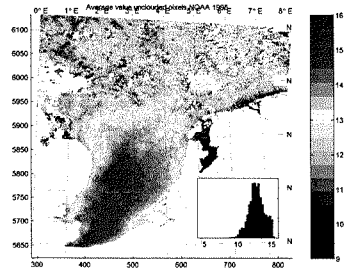

Oct (7)

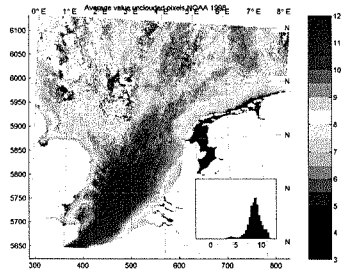

Nov (14)

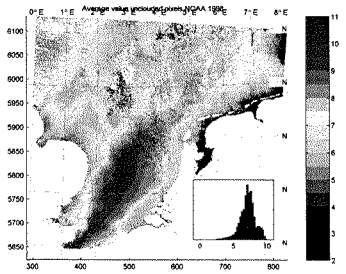

Dec (4)

Monthly means nLw 1998 (based on unclouded pixels). The numbers indicate the number of available images for that month.

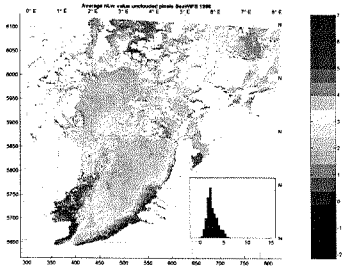

Jan (8)

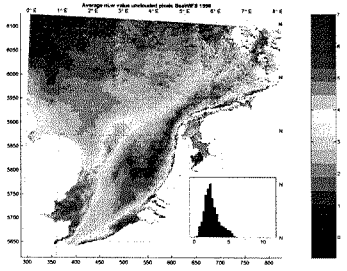

Feb (19)

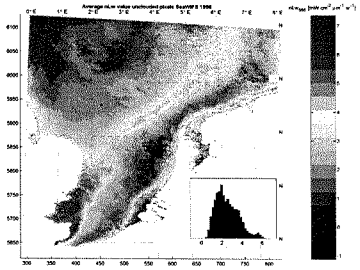

Mar (8)

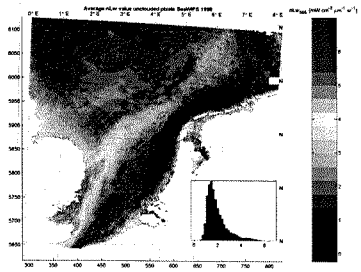

Apr (11)

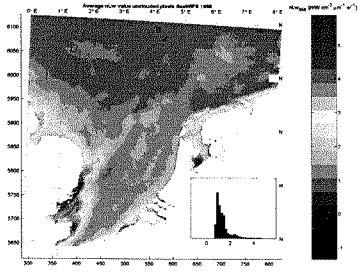

May (25)

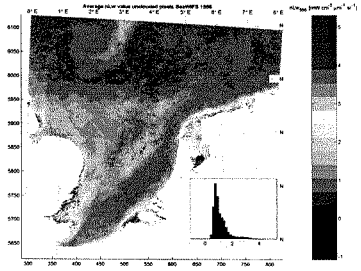

Jun (22)

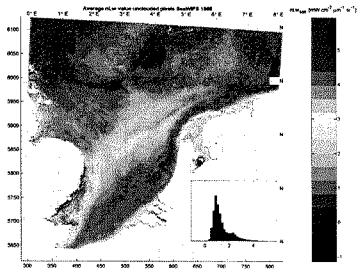

Jul (17)

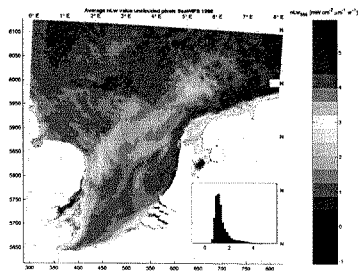

Aug (26)

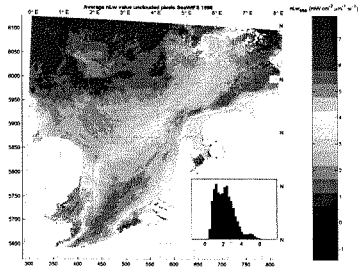

Sep (16)

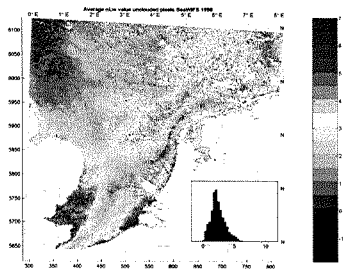

Oct (9)

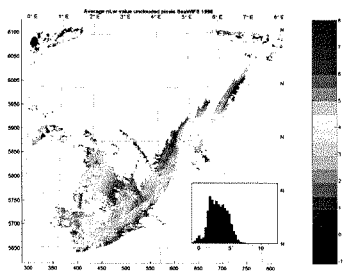

Nov (2)

Dec (0)

Appendix 5

PLUME VARIABILITY?

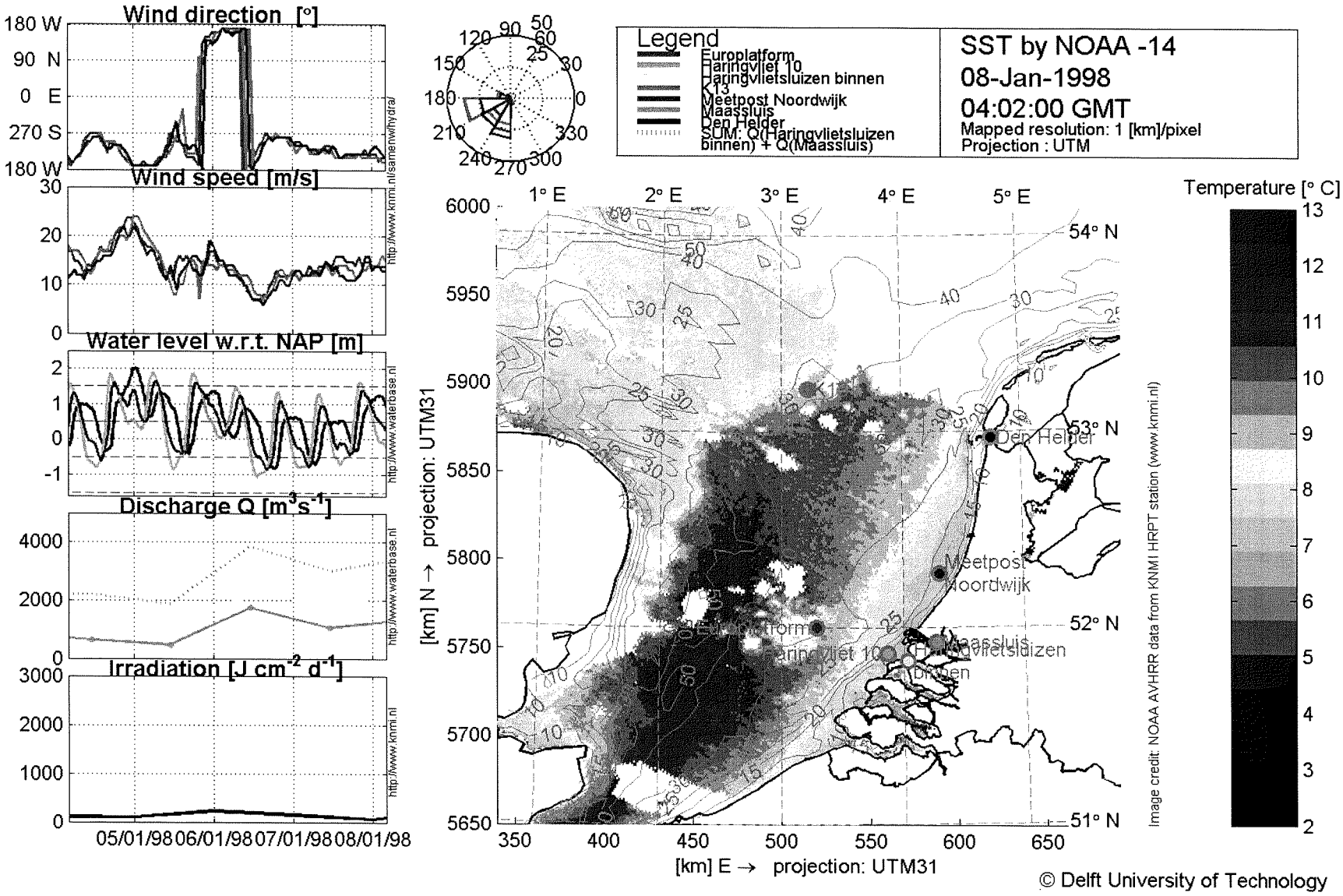
Wind direction [°]
180 W
90 N
0 E
270 S
180 W
Wind speed [m/s]
30
20
10
0
Water level w.r.t. NAP [m]
2
1
0
-1
Discharge Q [m3s-1]
4000
2000
0
Irradiation [J cm-2 d-1]
3000
2000
1000
0
05/01/98 06/01/98 07/01/98 08/01/98
http://www.knmi.nl/samenw/hydra
http://www.waterbase.nl
http://www.knmi.nl
Legend
Europlatform
Haringvliet 10
Haringvlietsluizen binnen
K13
Meetpost Noordwijk
Maassluis
Den Helder
SUM: Q(Haringvlietsluizen binnen) + Q(Maassluis)
SST by NOAA -14
08-Jan-1998
04:02:00 GMT
Mapped resolution: 1 [km]/pixel
Projection : UTM
Temperature [° C]
13
12
11
10
9
8
7
6
5
4
3
2
1° E
2° E
3° E
4° E
5° E
54° N
53° N
52° N
51° N
Den Helder
Meetpost Noordwijk
Maassluis
6000
5950
5900
5850
5800
5750
5700
5650
[km] N → projection: UTM31
350
400
450
500
550
600
650
[km] E → projection: UTM31
Image credit: NOAA AVHRR data from KNMI HRPT station (www.knmi.nl)
© Delft University of Technology

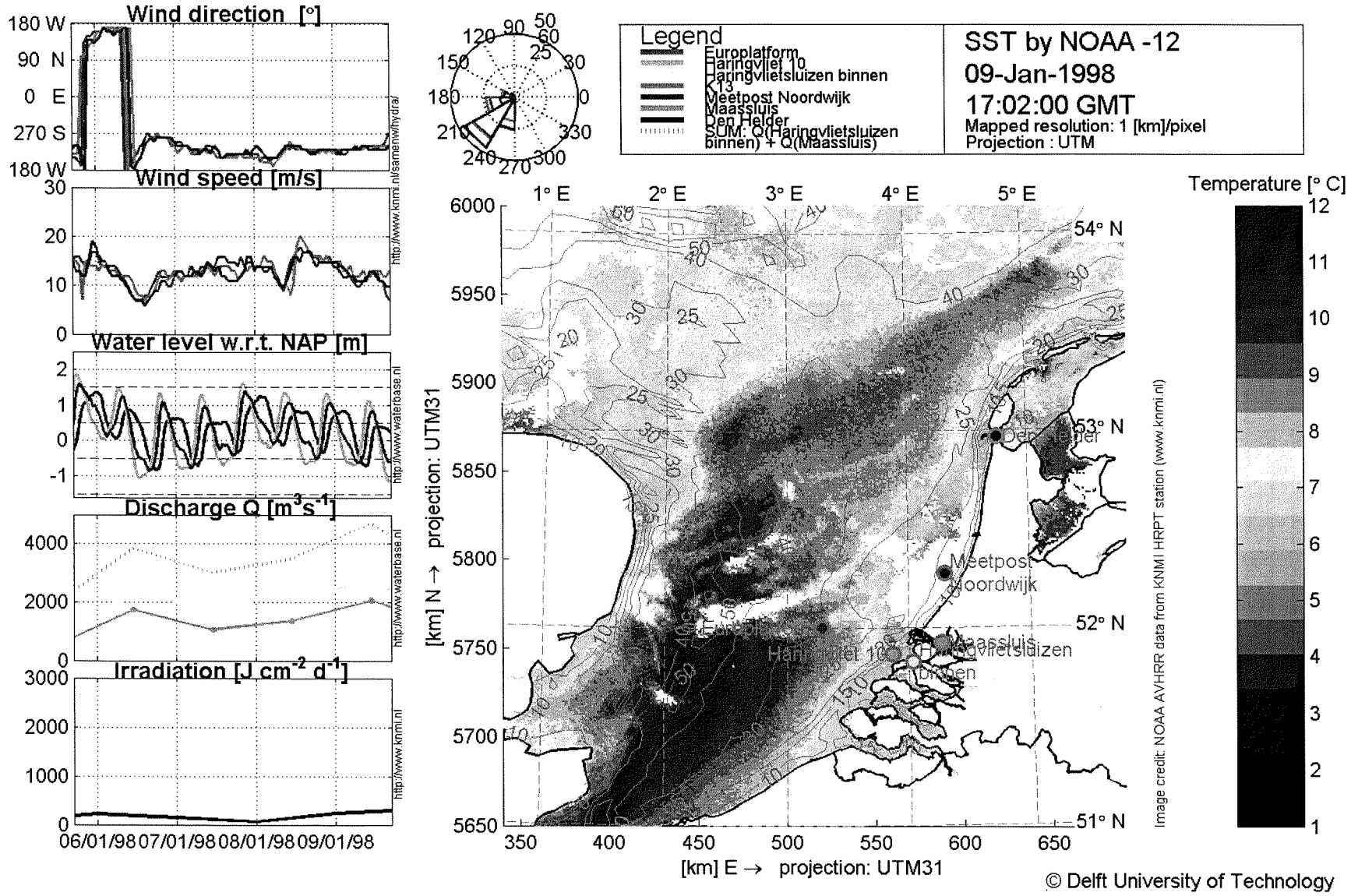
Wind direction [°]
180 W
90 N
0 E
270 S
180 W
Wind speed [m/s]
30
20
10
0
Water level w.r.t. NAP [m]
2
1
0
-1
Discharge Q [m3s-1]
4000
2000
0
Irradiation [J cm-2 d-1]
3000
2000
1000
0
06/01/98 07/01/98 08/01/98 09/01/98
http://www.knmi.nl/samenw/hydra/
http://www.waterbase.nl
http://www.knmi.nl
Legend
Europlatform
Haringvliet 10
Haringvlietsluizen binnen
K13
Meetpost Noordwijk
Maassluis
Den Helder
SUM: Q(Haringvlietsluizen binnen) + Q(Maassluis)
SST by NOAA -12
09-Jan-1998
17:02:00 GMT
Mapped resolution: 1 [km]/pixel
Projection : UTM
Temperature [° C]
12
11
10
9
8
7
6
5
4
3
2
1
1° E
2° E
3° E
4° E
5° E
54° N
53° N
52° N
51° N
6000
5950
5900
5850
5800
5750
5700
5650
350
400
450
500
550
600
650
[km] N → projection: UTM31
[km] E → projection: UTM31
Meetpost Noordwijk
Maassluis
Image credit: NOAA AVHRR data from KNMI HRPT station (www.knmi.nl)
© Delft University of Technology

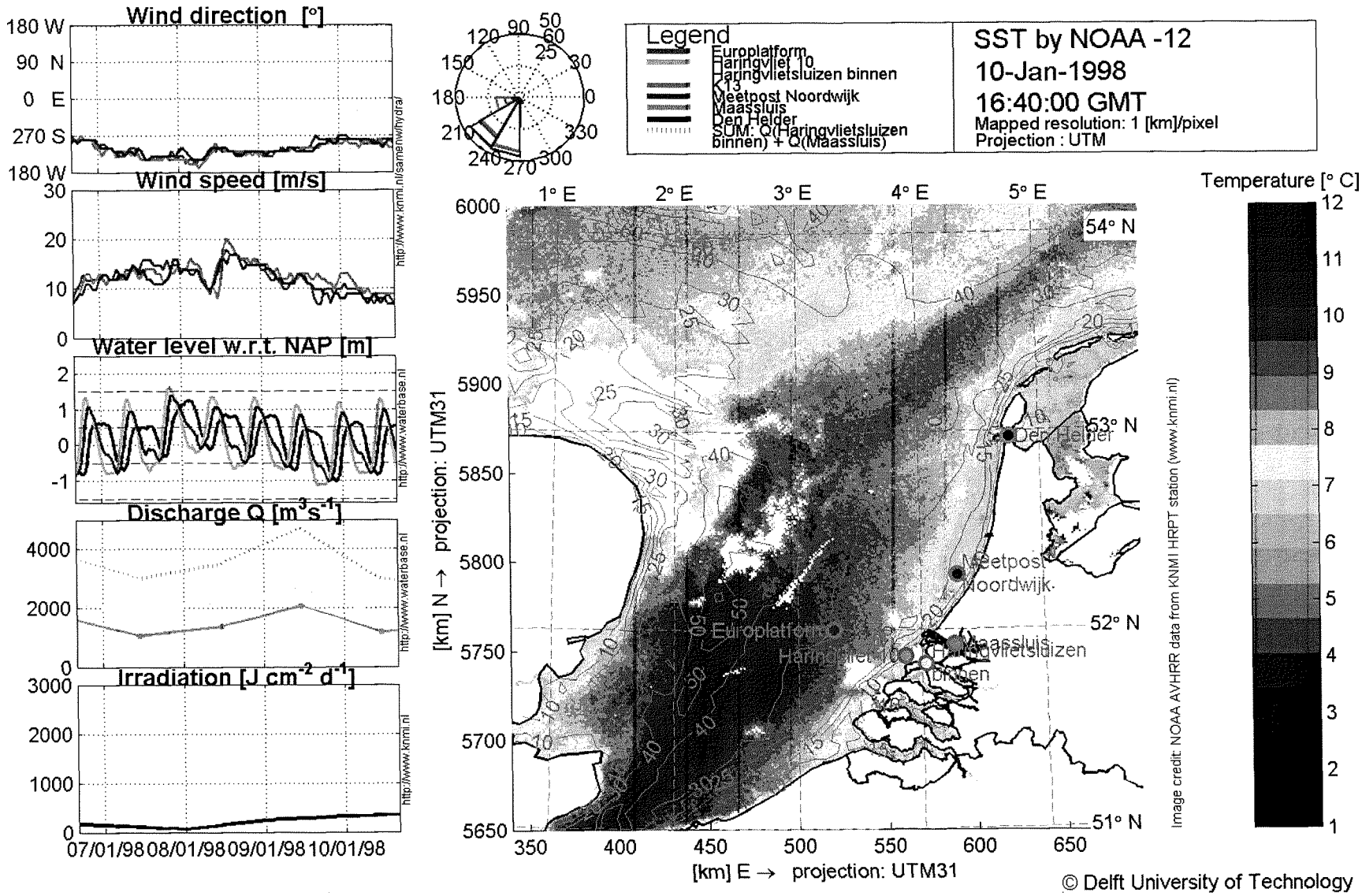
Wind direction [°]
180 W
90 N
0 E
270 S
180 W
Wind speed [m/s]
30
20
10
0
Water level w.r.t. NAP [m]
2
1
0
-1
Discharge Q [m3s-1]
4000
2000
0
Irradiation [J cm-2 d-1]
3000
2000
1000
0
07/01/98 08/01/98 09/01/98 10/01/98
http://www.knmi.nl/samenw/hydra/
http://www.waterbase.nl
http://www.waterbase.nl
http://www.knmi.nl
Legend
Europlatform
Haringvliet 10
Haringvlietsluizen binnen
K13
Meetpost Noordwijk
Maassluis
Den Helder
SUM: Q(Haringvlietsluizen binnen) + Q(Maassluis)
SST by NOAA -12
10-Jan-1998
16:40:00 GMT
Mapped resolution: 1 [km]/pixel
Projection : UTM
Temperature [° C]
12
11
10
9
8
7
6
5
4
3
2
1
1° E
2° E
3° E
4° E
5° E
54° N
53° N
52° N
51° N
6000
5950
5900
5850
5800
5750
5700
5650
[km] N → projection: UTM31
350
400
450
500
550
600
650
[km] E → projection: UTM31
Den Helder
Meetpost Noordwijk
Europlatform
Haringvliet 10
Maassluis
Haringvlietsluizen binnen
Image credit: NOAA AVHRR data from KNMI HRPT station (www.knmi.nl)
© Delft University of Technology

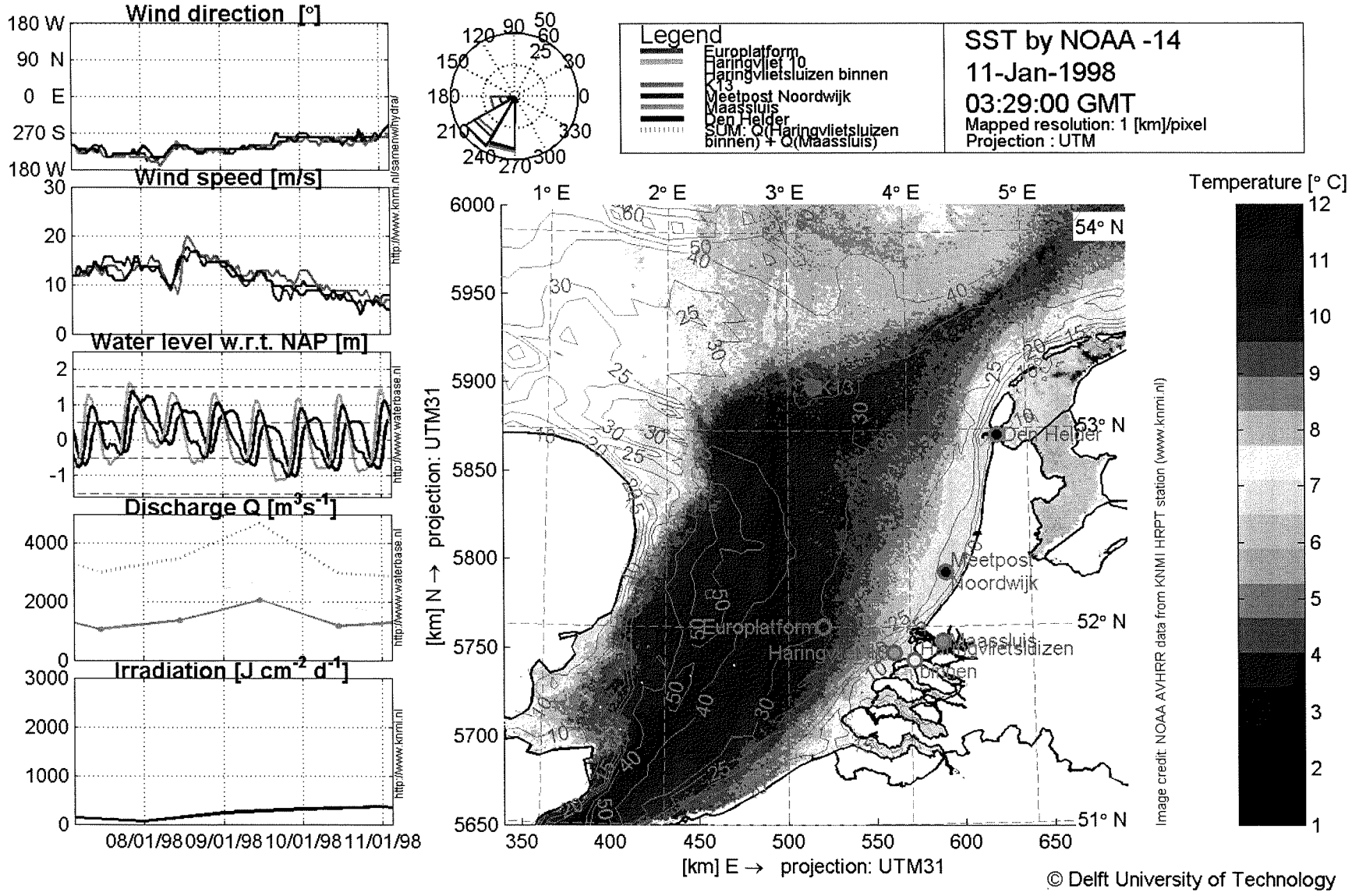
Wind direction [°]
180 W
90 N
0 E
270 S
180 W
Wind speed [m/s]
30
20
10
0
Water level w.r.t. NAP [m]
2
1
0
-1
Discharge Q [m³s⁻¹]
4000
2000
0
Irradiation [J cm⁻² d⁻¹]
3000
2000
1000
0
08/01/98 09/01/98 10/01/98 11/01/98
http://www.knmi.nl/samenw/hydra
http://www.knmi.nl
http://www.waterbase.nl
http://www.waterbase.nl
http://www.knmi.nl
90 50 120 60 150 25 30 180 0 210 330 240 270 300
Legend
Europlatform
Haringvliet 10
Haringvlietsluizen binnen
K13
Meetpost Noordwijk
Maassluis
Den Helder
SUM: Q(Haringvlietsluizen binnen) + Q(Maassluis)
SST by NOAA -14
11-Jan-1998
03:29:00 GMT
Mapped resolution: 1 [km]/pixel
Projection : UTM
1° E
2° E
3° E
4° E
5° E
54° N
53° N
52° N
51° N
6000
5950
5900
5850
5800
5750
5700
5650
[km] N → projection: UTM31
350
400
450
500
550
600
650
[km] E → projection: UTM31
Den Helder
Meetpost Noordwijk
Europlatform
Haringvlietsluizen
Temperature [° C]
12
11
10
9
8
7
6
5
4
3
2
1
Image credit: NOAA AVHRR data from KNMI HRPT station (www.knmi.nl)
© Delft University of Technology

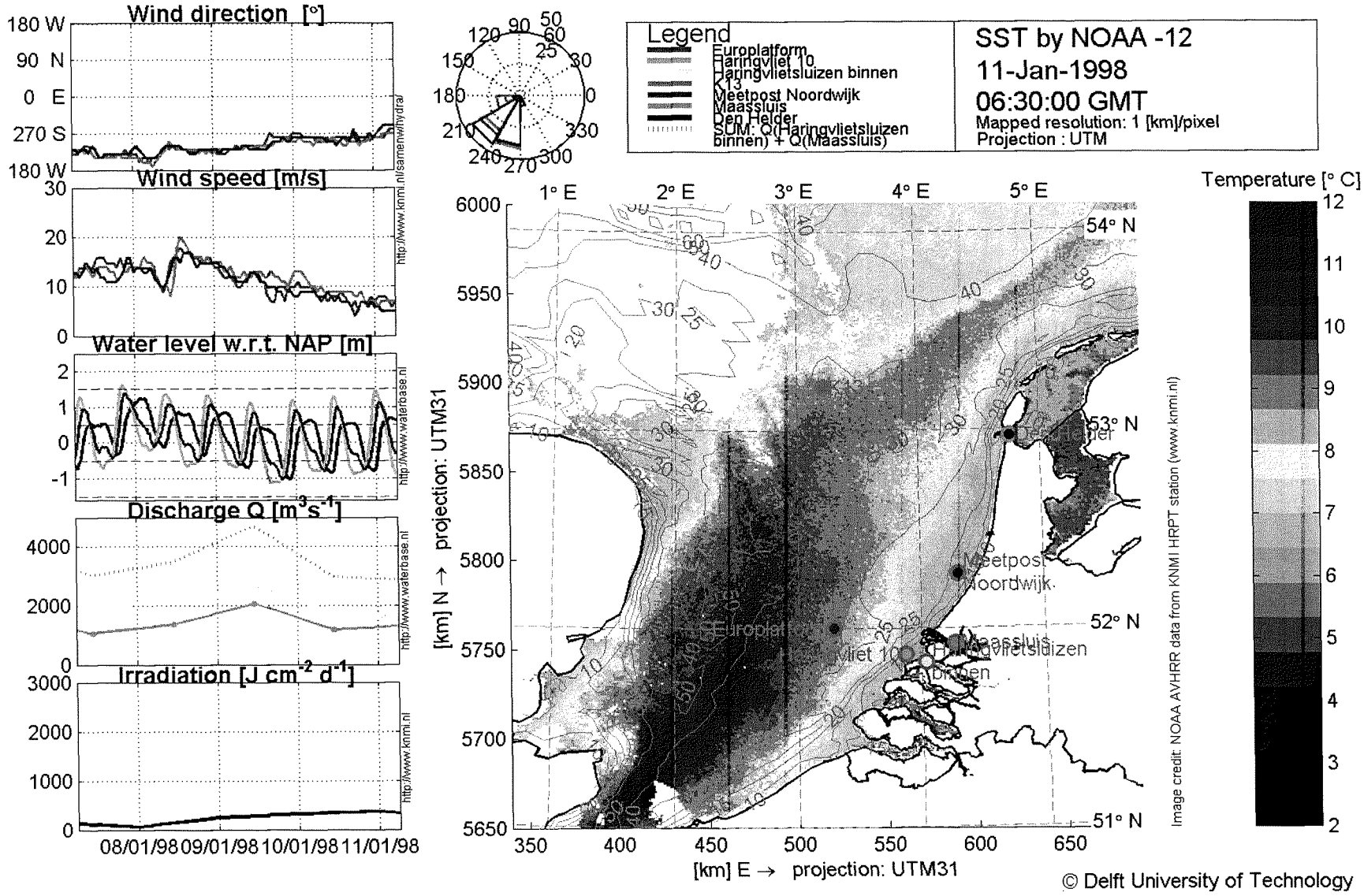
Wind direction [°]
180 W
90 N
0 E
270 S
180 W
Wind speed [m/s]
30
20
10
0
Water level w.r.t. NAP [m]
2
1
0
-1
Discharge Q [m3s-1]
4000
2000
0
Irradiation [J cm-2 d-1]
3000
2000
1000
0
08/01/98 09/01/98 10/01/98 11/01/98
http://www.knmi.nl/samenw/hydra/
http://www.waterbase.nl
http://www.knmi.nl
90 50
120 60
150 25 30
180 0
210 330
240 270 300
Legend
Europlatform
Haringvliet 10
Haringvlietsluizen binnen
K13
Meetpost Noordwijk
Maassluis
Den Helder
SUM: Q(Haringvlietsluizen binnen) + Q(Maassluis)
SST by NOAA -12
11-Jan-1998
06:30:00 GMT
Mapped resolution: 1 [km]/pixel
Projection : UTM
1° E
2° E
3° E
4° E
5° E
54° N
53° N
52° N
51° N
6000
5950
5900
5850
5800
5750
5700
5650
[km] N → projection: UTM31
350
400
450
500
550
600
650
[km] E → projection: UTM31
Meetpost Noordwijk
Europlat
Haringvliet 10
Maassluis
Haringvlietsluizen binnen
Temperature [° C]
12
11
10
9
8
7
6
5
4
3
2
Image credit: NOAA AVHRR data from KNMI HRPT station (www.knmi.nl)
© Delft University of Technology

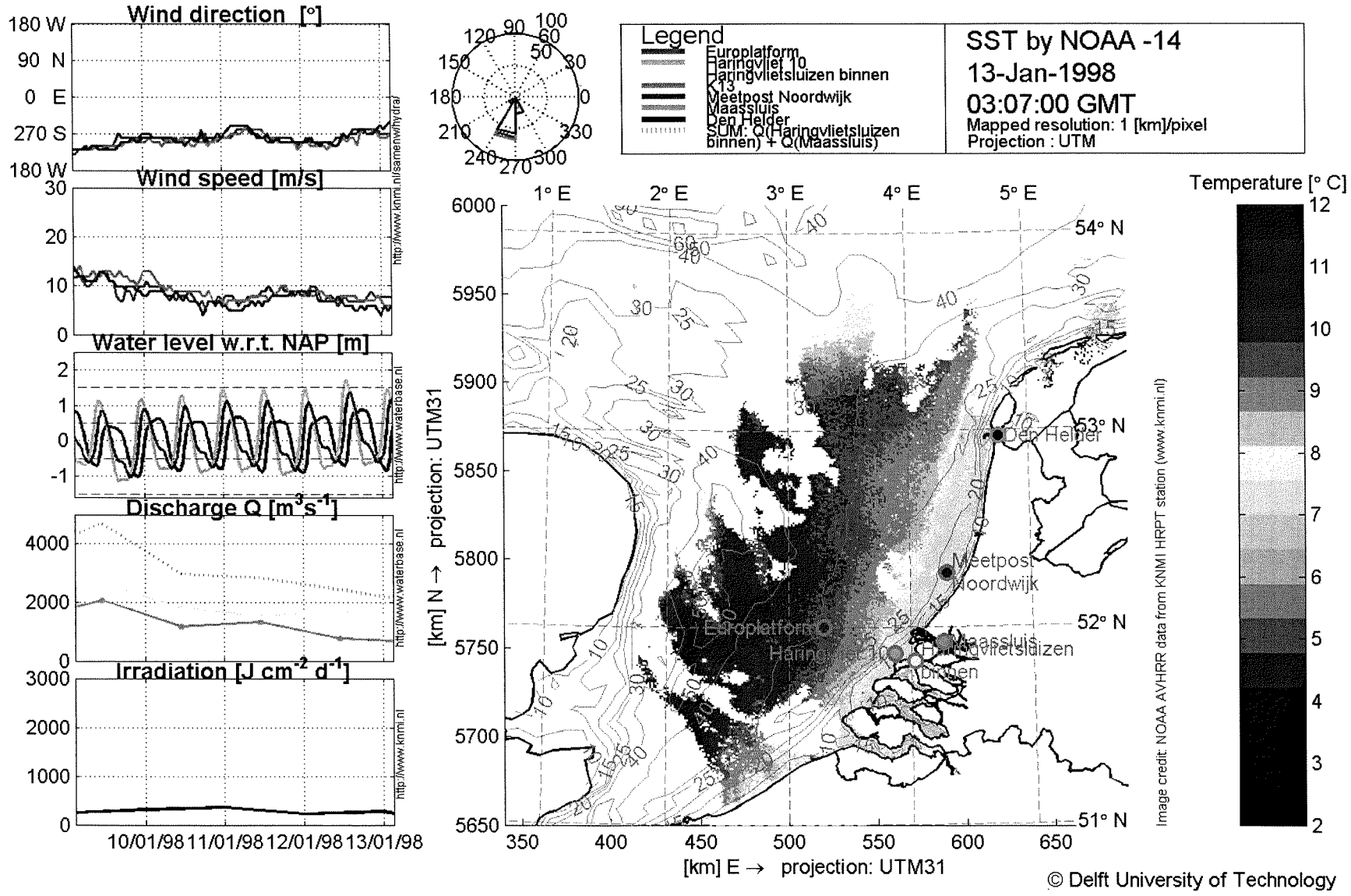
Wind direction [°]
180 W
90 N
0 E
270 S
180 W
Wind speed [m/s]
Water level w.r.t. NAP [m]
Discharge Q [m³s⁻¹]
Irradiation [J cm⁻² d⁻¹]
10/01/98 11/01/98 12/01/98 13/01/98
http://www.knmi.nl/samenw/hydra/
http://www.waterbase.nl
http://www.knmi.nl
Legend
Europlatform
Haringvliet 10
Haringvlietsluizen binnen
K13
Meetpost Noordwijk
Maassluis
Den Helder
SUM: Q(Haringvlietsluizen binnen) + Q(Maassluis)
SST by NOAA -14
13-Jan-1998
03:07:00 GMT
Mapped resolution: 1 [km]/pixel
Projection : UTM
Temperature [° C]
[km] N → projection: UTM31
[km] E → projection: UTM31
Meetpost Noordwijk
Maassluis
Image credit: NOAA AVHRR data from KNMI HRPT station (www.knmi.nl)
© Delft University of Technology

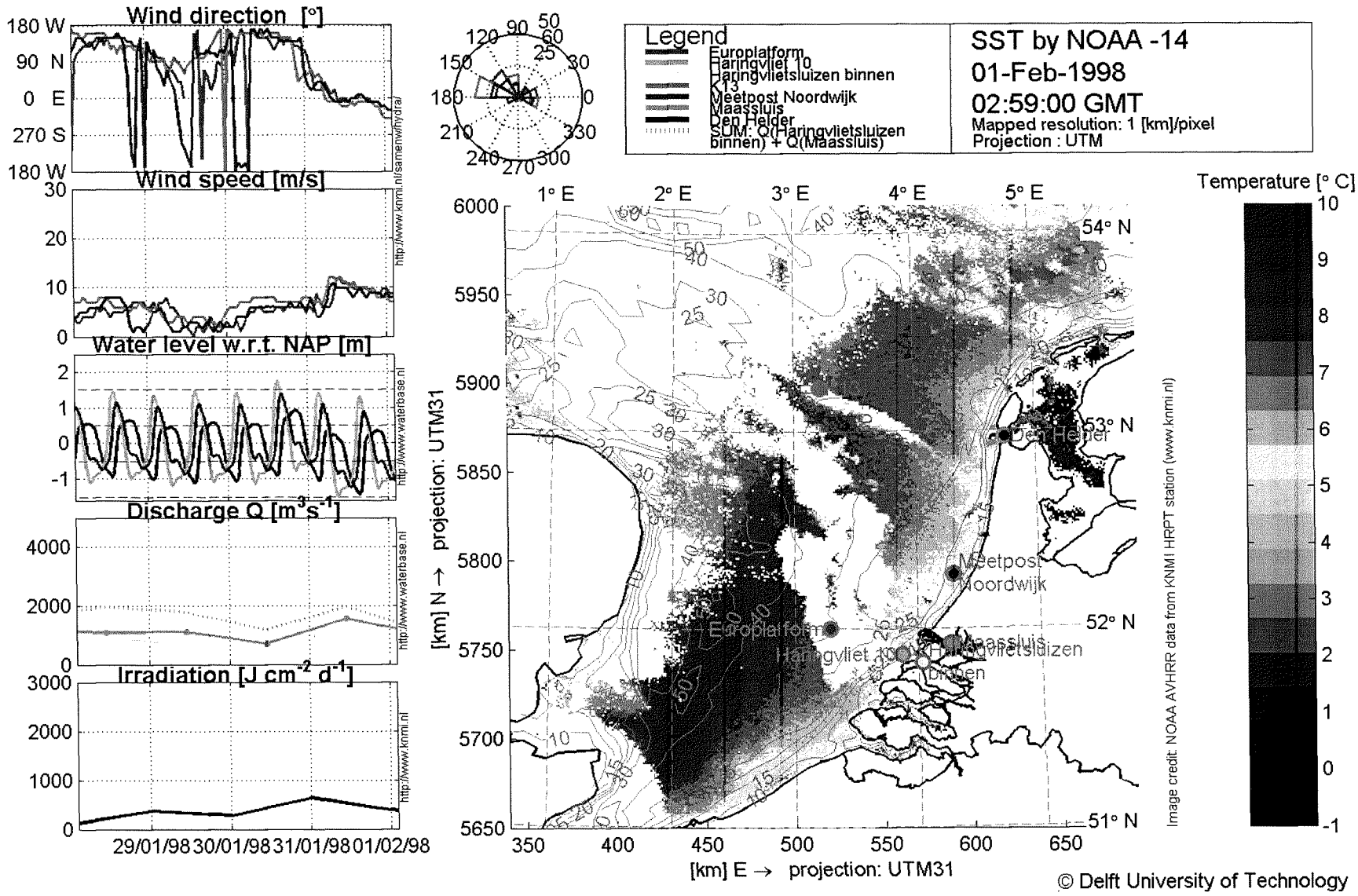
Wind direction [°]
180 W
90 N
0 E
270 S
180 W
Wind speed [m/s]
30
20
10
0
Water level w.r.t. NAP [m]
2
1
0
-1
Discharge Q [m3s-1]
4000
2000
0
Irradiation [J cm-2 d-1]
3000
2000
1000
0
29/01/98 30/01/98 31/01/98 01/02/98
http://www.knmi.nl/samenw/hydra/
http://www.waterbase.nl
http://www.knmi.nl
Legend
Europlatform
Haringvliet 10
Haringvlietsluizen binnen
K13
Meetpost Noordwijk
Maassluis
Den Helder
SUM: Q(Haringvlietsluizen binnen) + Q(Maassluis)
SST by NOAA -14
01-Feb-1998
02:59:00 GMT
Mapped resolution: 1 [km]/pixel
Projection : UTM
Temperature [° C]
10
9
8
7
6
5
4
3
2
1
0
-1
1° E
2° E
3° E
4° E
5° E
54° N
53° N
52° N
51° N
6000
5950
5900
5850
5800
5750
5700
5650
[km] N → projection: UTM31
350
400
450
500
550
600
650
[km] E → projection: UTM31
Den Helder
Meetpost Noordwijk
Europlatform
Haringvliet 10
Maassluis
Haringvlietsluizen binnen
Image credit: NOAA AVHRR data from KNMI HRPT station (www.knmi.nl)
© Delft University of Technology

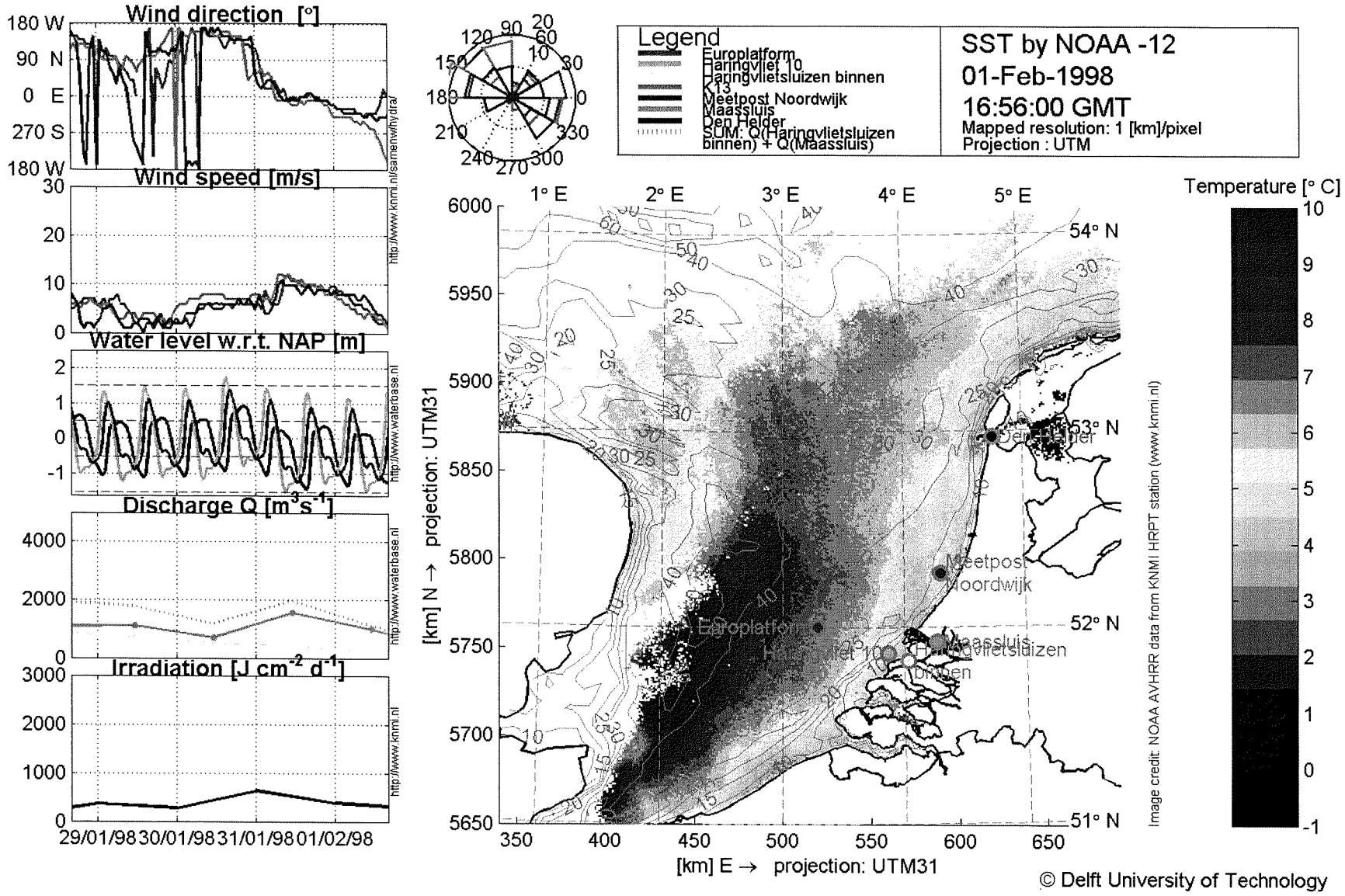
Wind direction [°]
180 W
90 N
0 E
270 S
180 W
Wind speed [m/s]
30
20
10
0
Water level w.r.t. NAP [m]
2
1
0
-1
Discharge Q [m3s-1]
4000
2000
0
Irradiation [J cm-2 d-1]
3000
2000
1000
0
29/01/98 30/01/98 31/01/98 01/02/98
http://www.knmi.nl/samenw/hydra/
http://www.waterbase.nl
http://www.knmi.nl
Legend
Europlatform
Haringvliet 10
Haringvlietsluizen binnen
K13
Meetpost Noordwijk
Maassluis
Den Helder
SUM: Q(Haringvlietsluizen binnen) + Q(Maassluis)
SST by NOAA -12
01-Feb-1998
16:56:00 GMT
Mapped resolution: 1 [km]/pixel
Projection : UTM
1° E
2° E
3° E
4° E
5° E
54° N
53° N
52° N
51° N
6000
5950
5900
5850
5800
5750
5700
5650
[km] N → projection: UTM31
350
400
450
500
550
600
650
[km] E → projection: UTM31
Den Helder
Meetpost Noordwijk
Europlatform
Maassluis
Haringvlietsluizen
Temperature [° C]
10
9
8
7
6
5
4
3
2
1
0
-1
Image credit: NOAA AVHRR data from KNMI HRPT station (www.knmi.nl)
© Delft University of Technology

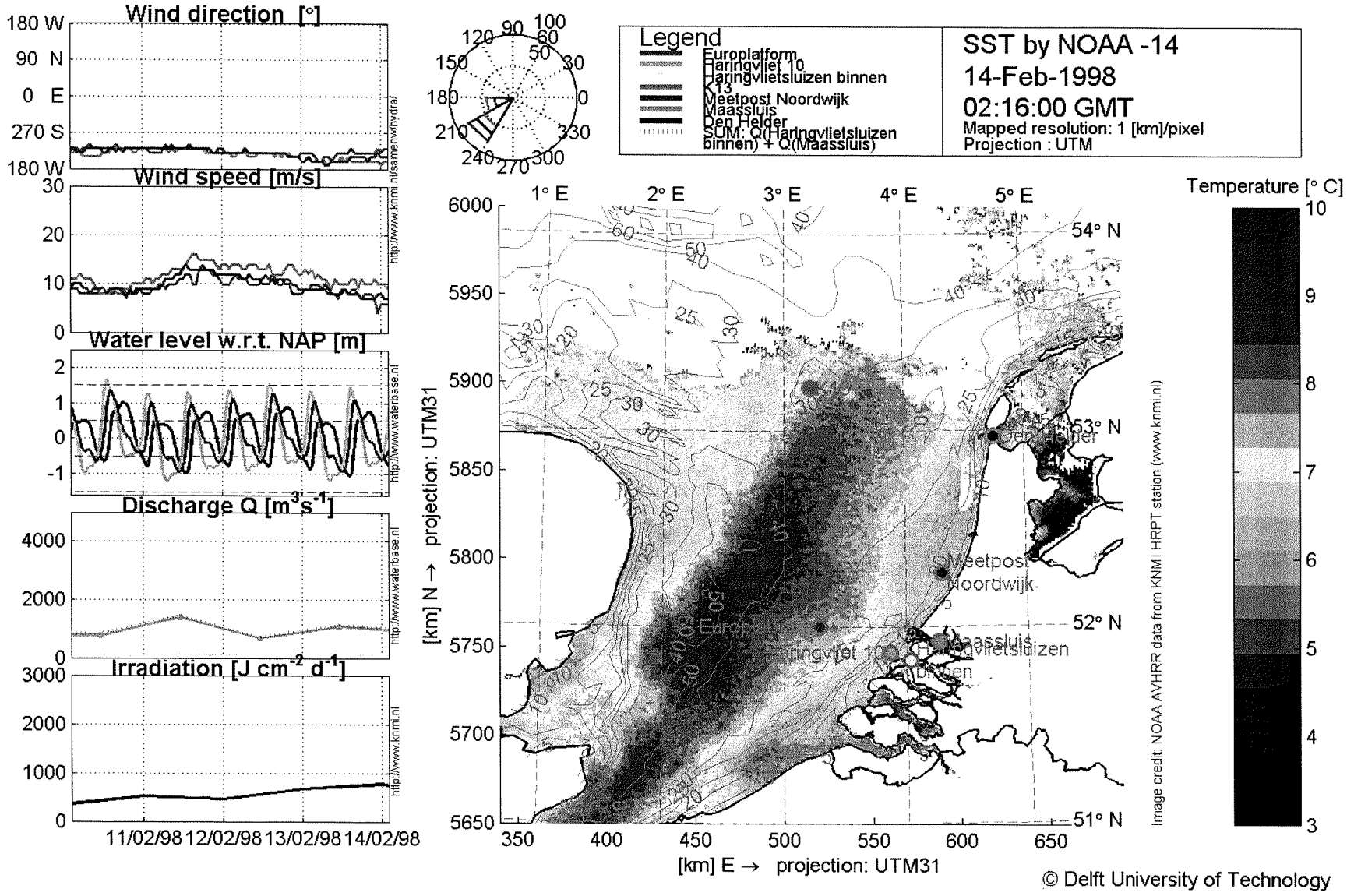
Wind direction [°]
180 W
90 N
0 E
270 S
180 W
Wind speed [m/s]
30
20
10
0
Water level w.r.t. NAP [m]
2
1
0
-1
Discharge Q [m3s-1]
4000
2000
0
Irradiation [J cm-2 d-1]
3000
2000
1000
0
11/02/98 12/02/98 13/02/98 14/02/98
http://www.knmi.nl/samenw/hydra
http://www.waterbase.nl
http://www.knmi.nl
Legend
Europlatform
Haringvliet 10
Haringvlietsluizen binnen
Q13
Meetpost Noordwijk
Maassluis
Den Helder
SUM: Q(Haringvlietsluizen binnen) + Q(Maassluis)
SST by NOAA -14
14-Feb-1998
02:16:00 GMT
Mapped resolution: 1 [km]/pixel
Projection : UTM
Temperature [° C]
10
9
8
7
6
5
4
3
1° E
2° E
3° E
4° E
5° E
54° N
53° N
52° N
51° N
6000
5950
5900
5850
5800
5750
5700
5650
350
400
450
500
550
600
650
[km] N → projection: UTM31
[km] E → projection: UTM31
Meetpost Noordwijk
Maassluis
Image credit: NOAA AVHRR data from KNMI HRPT station (www.knmi.nl)
© Delft University of Technology

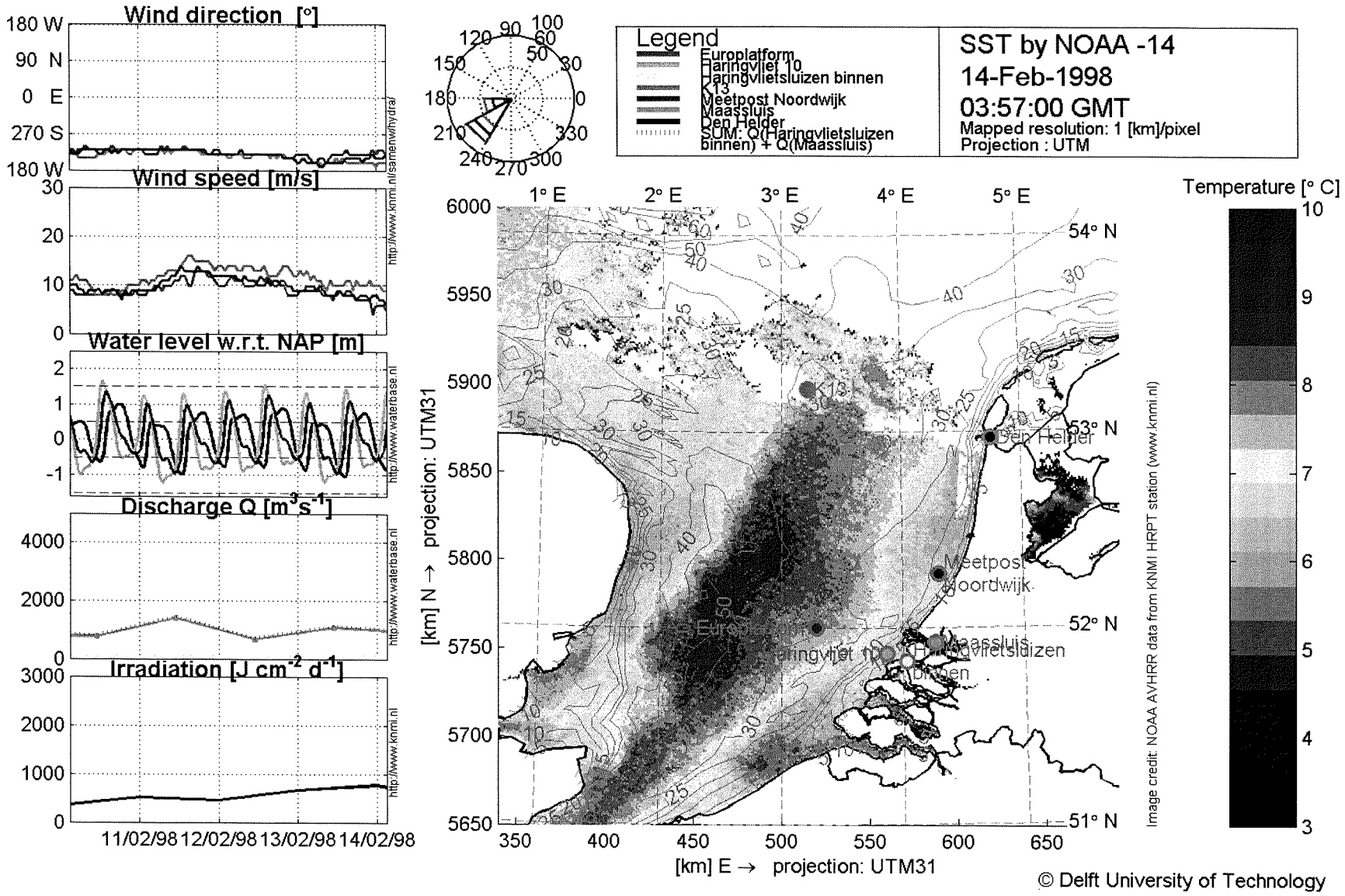
Wind direction [°]
180 W
90 N
0 E
270 S
180 W
Wind speed [m/s]
30
20
10
0
Water level w.r.t. NAP [m]
2
1
0
-1
Discharge Q [m³s⁻¹]
4000
2000
0
Irradiation [J cm⁻² d⁻¹]
3000
2000
1000
0
11/02/98 12/02/98 13/02/98 14/02/98
http://www.knmi.nl/samenw/hydra
http://www.knmi.nl
http://www.waterbase.nl
Legend
Europlatform
Haringvliet 10
Haringvlietsluizen binnen
K13
Meetpost Noordwijk
Maassluis
Den Helder
SUM: Q(Haringvlietsluizen binnen) + Q(Maassluis)
SST by NOAA -14
14-Feb-1998
03:57:00 GMT
Mapped resolution: 1 [km]/pixel
Projection : UTM
1° E
2° E
3° E
4° E
5° E
54° N
53° N
52° N
51° N
6000
5950
5900
5850
5800
5750
5700
5650
[km] N → projection: UTM31
350
400
450
500
550
600
650
[km] E → projection: UTM31
K13
Den Helder
Meetpost Noordwijk
Maassluis
Haringvlietsluizen binnen
Temperature [° C]
10
9
8
7
6
5
4
3
Image credit: NOAA AVHRR data from KNMI HRPT station (www.knmi.nl)
© Delft University of Technology

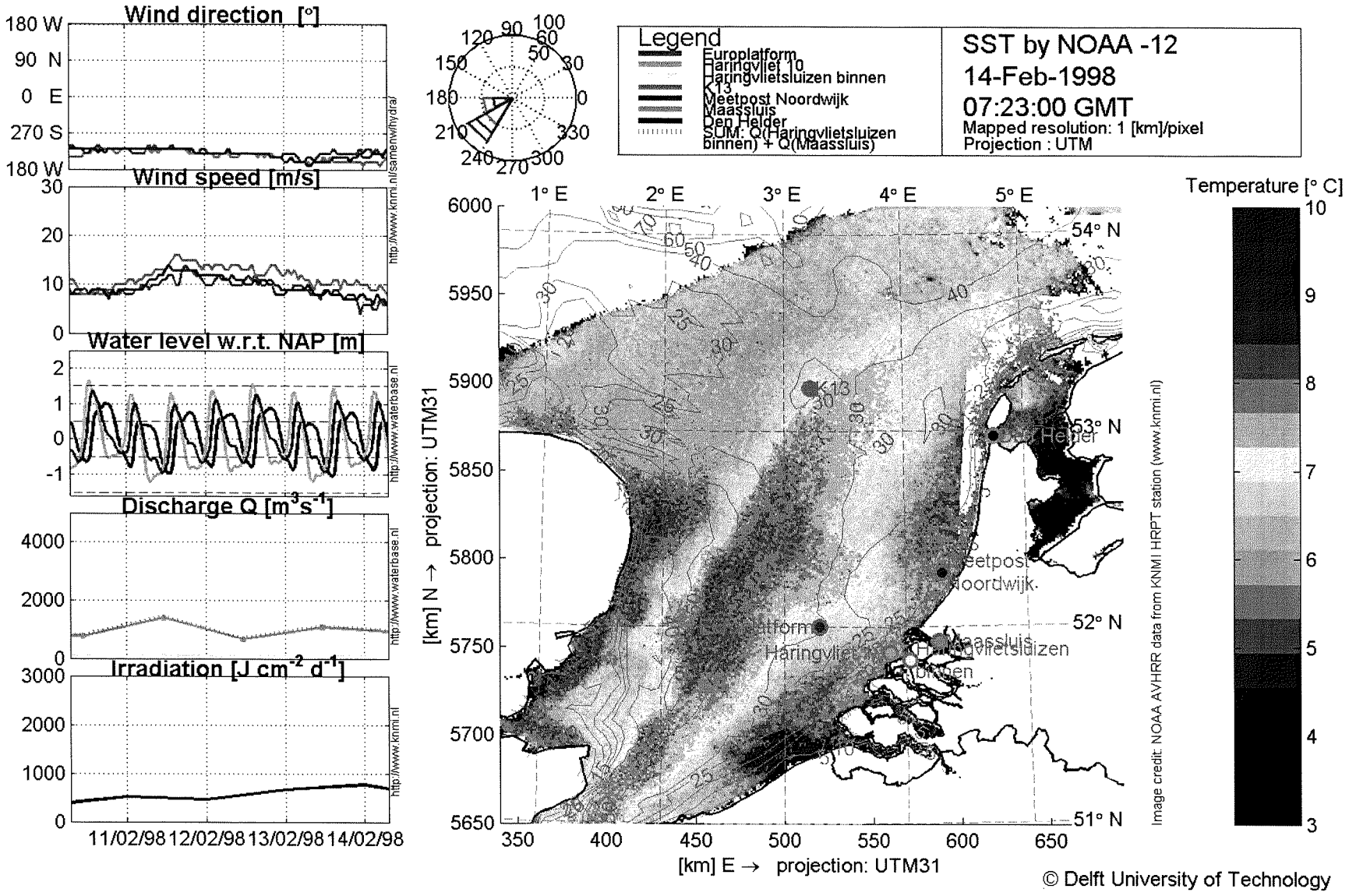
Wind direction [°]
180 W
90 N
0 E
270 S
180 W
Wind speed [m/s]
30
20
10
0
Water level w.r.t. NAP [m]
2
1
0
-1
Discharge Q [m3s-1]
4000
2000
0
Irradiation [J cm-2 d-1]
3000
2000
1000
0
11/02/98 12/02/98 13/02/98 14/02/98
http://www.knmi.nl/samenwerk/hydra/
http://www.waterbase.nl
http://www.knmi.nl
Legend
Europlatform
Haringvliet 10
Haringvlietsluizen binnen
K13
Meetpost Noordwijk
Maassluis
Den Helder
SUM: Q(Haringvlietsluizen binnen) + Q(Maassluis)
SST by NOAA -12
14-Feb-1998
07:23:00 GMT
Mapped resolution: 1 [km]/pixel
Projection : UTM
Temperature [° C]
10
9
8
7
6
5
4
3
1° E
2° E
3° E
4° E
5° E
54° N
53° N
52° N
51° N
6000
5950
5900
5850
5800
5750
5700
5650
[km] N → projection: UTM31
350
400
450
500
550
600
650
[km] E → projection: UTM31
K13
Meetpost Noordwijk
Maassluis
Haringvlietsluizen
Image credit: NOAA AVHRR data from KNMI HRPT station (www.knmi.nl)
© Delft University of Technology

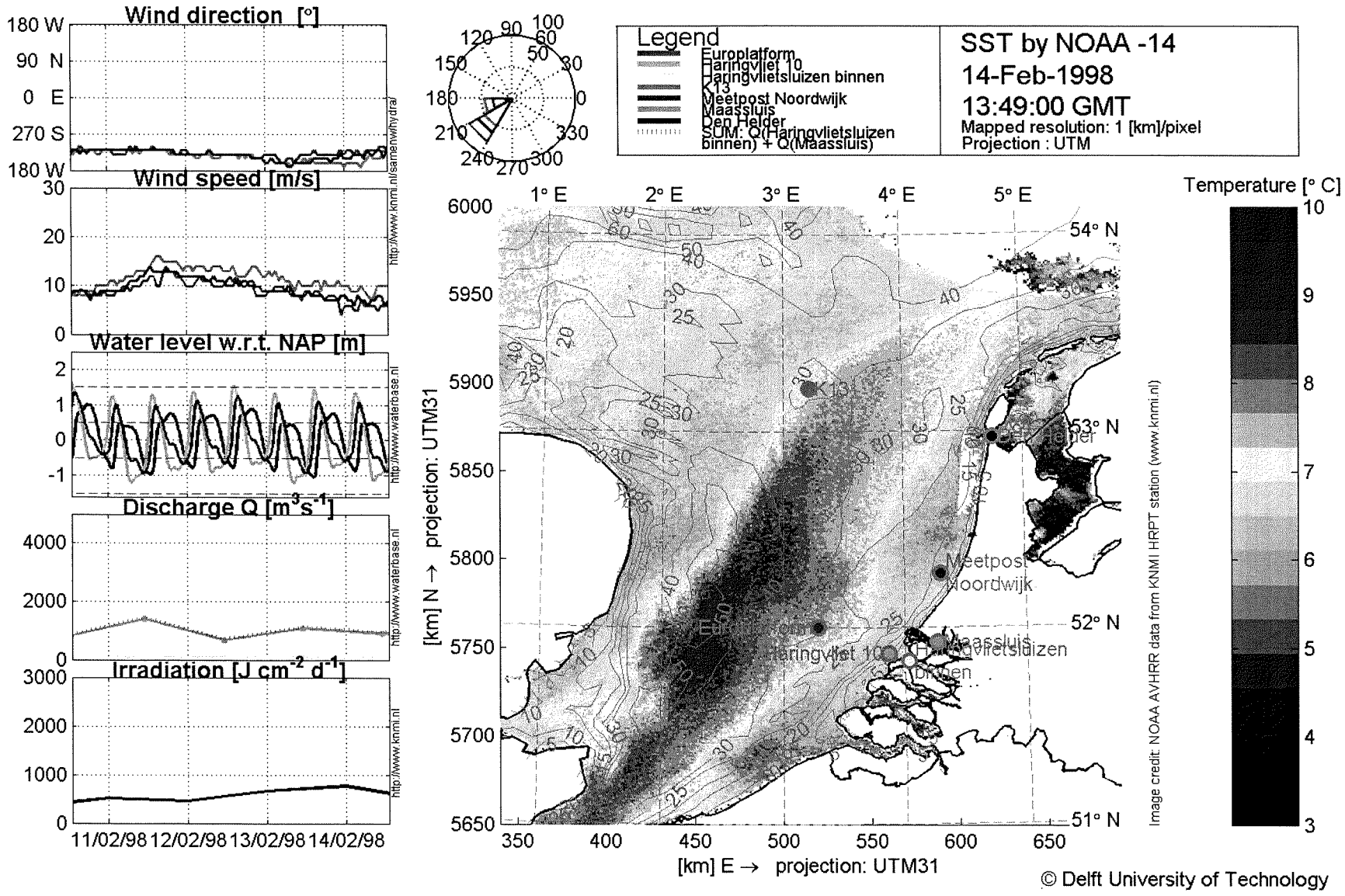
Wind direction [°]
180 W
90 N
0 E
270 S
180 W
Wind speed [m/s]
Water level w.r.t. NAP [m]
Discharge Q [m3s-1]
Irradiation [J cm-2 d-1]
11/02/98 12/02/98 13/02/98 14/02/98
http://www.knmi.nl/samenwhydra/
http://www.waterbase.nl
Legend
Europlatform
Haringvliet 10
Haringvlietsluizen binnen
K13
Meetpost Noordwijk
Maassluis
Den Helder
SUM: Q(Haringvlietsluizen binnen) + Q(Maassluis)
SST by NOAA -14
14-Feb-1998
13:49:00 GMT
Mapped resolution: 1 [km]/pixel
Projection : UTM
Temperature [° C]
[km] N → projection: UTM31
[km] E → projection: UTM31
Image credit: NOAA AVHRR data from KNMI HRPT station (www.knmi.nl)
© Delft University of Technology

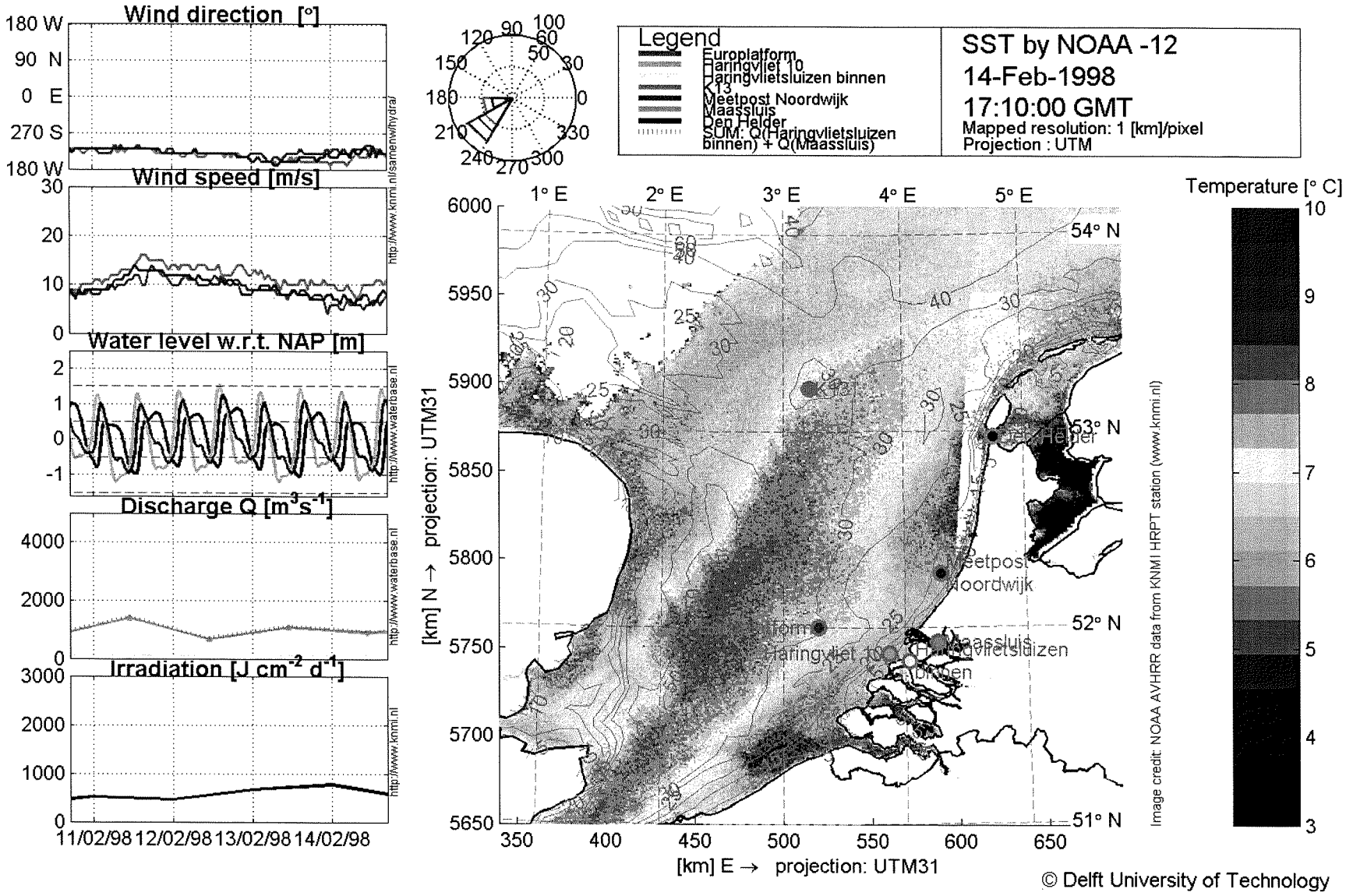
Wind direction [°]
180 W
90 N
0 E
270 S
180 W
Wind speed [m/s]
30
20
10
0
Water level w.r.t. NAP [m]
2
1
0
-1
Discharge Q [m3s-1]
4000
2000
0
Irradiation [J cm-2 d-1]
3000
2000
1000
0
11/02/98 12/02/98 13/02/98 14/02/98
http://www.knmi.nl/samenw/hydra
http://www.waterbase.nl
http://www.waterbase.nl
http://www.knmi.nl
Legend
Europlatform
Haringvliet 10
Haringvlietsluizen binnen
K13
Meetpost Noordwijk
Maassluis
Den Helder
SUM: Q(Haringvlietsluizen binnen) + Q(Maassluis)
SST by NOAA -12
14-Feb-1998
17:10:00 GMT
Mapped resolution: 1 [km]/pixel
Projection : UTM
Temperature [° C]
10
9
8
7
6
5
4
3
1° E
2° E
3° E
4° E
5° E
54° N
53° N
52° N
51° N
6000
5950
5900
5850
5800
5750
5700
5650
[km] N → projection: UTM31
350
400
450
500
550
600
650
[km] E → projection: UTM31
Image credit: NOAA AVHRR data from KNMI HRPT station (www.knmi.nl)
© Delft University of Technology

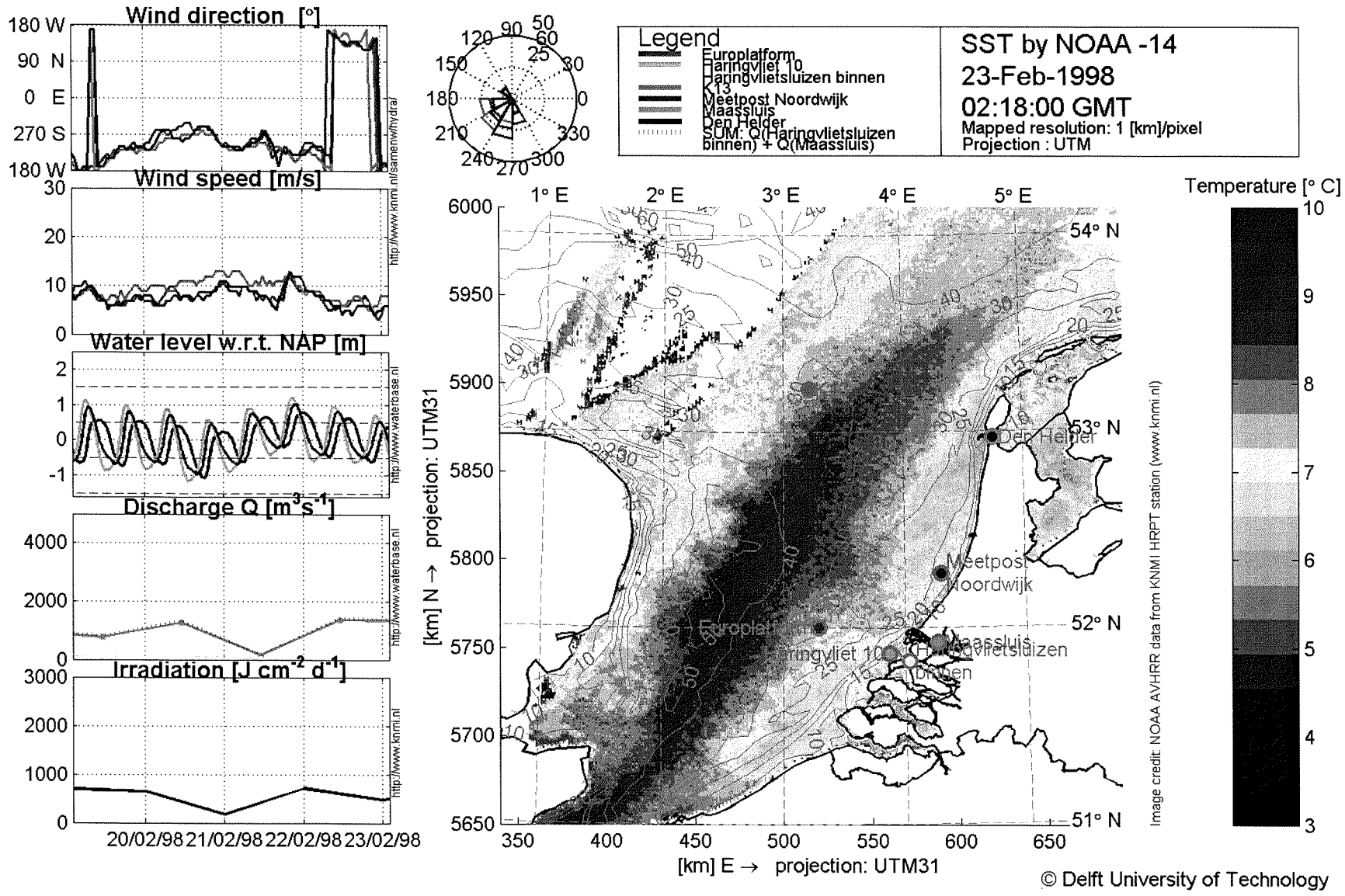
Wind direction [°]
180 W
90 N
0 E
270 S
180 W
Wind speed [m/s]
Water level w.r.t. NAP [m]
Discharge Q [m³s⁻¹]
Irradiation [J cm⁻² d⁻¹]
20/02/98 21/02/98 22/02/98 23/02/98
http://www.knmi.nl/samenw/hydra
http://www.waterbase.nl
http://www.knmi.nl
Legend
Europlatform
Haringvliet 10
Haringvlietsluizen binnen
K13
Meetpost Noordwijk
Maassluis
Den Helder
SUM: Q(Haringvlietsluizen binnen) + Q(Maassluis)
SST by NOAA -14
23-Feb-1998
02:18:00 GMT
Mapped resolution: 1 [km]/pixel
Projection : UTM
Temperature [° C]
1° E
2° E
3° E
4° E
5° E
54° N
53° N
52° N
51° N
Den Helder
Meetpost Noordwijk
Europlatform
Maassluis
Haringvliet 10
Haringvlietsluizen binnen
[km] N → projection: UTM31
[km] E → projection: UTM31
Image credit: NOAA AVHRR data from KNMI HRPT station (www.knmi.nl)
© Delft University of Technology

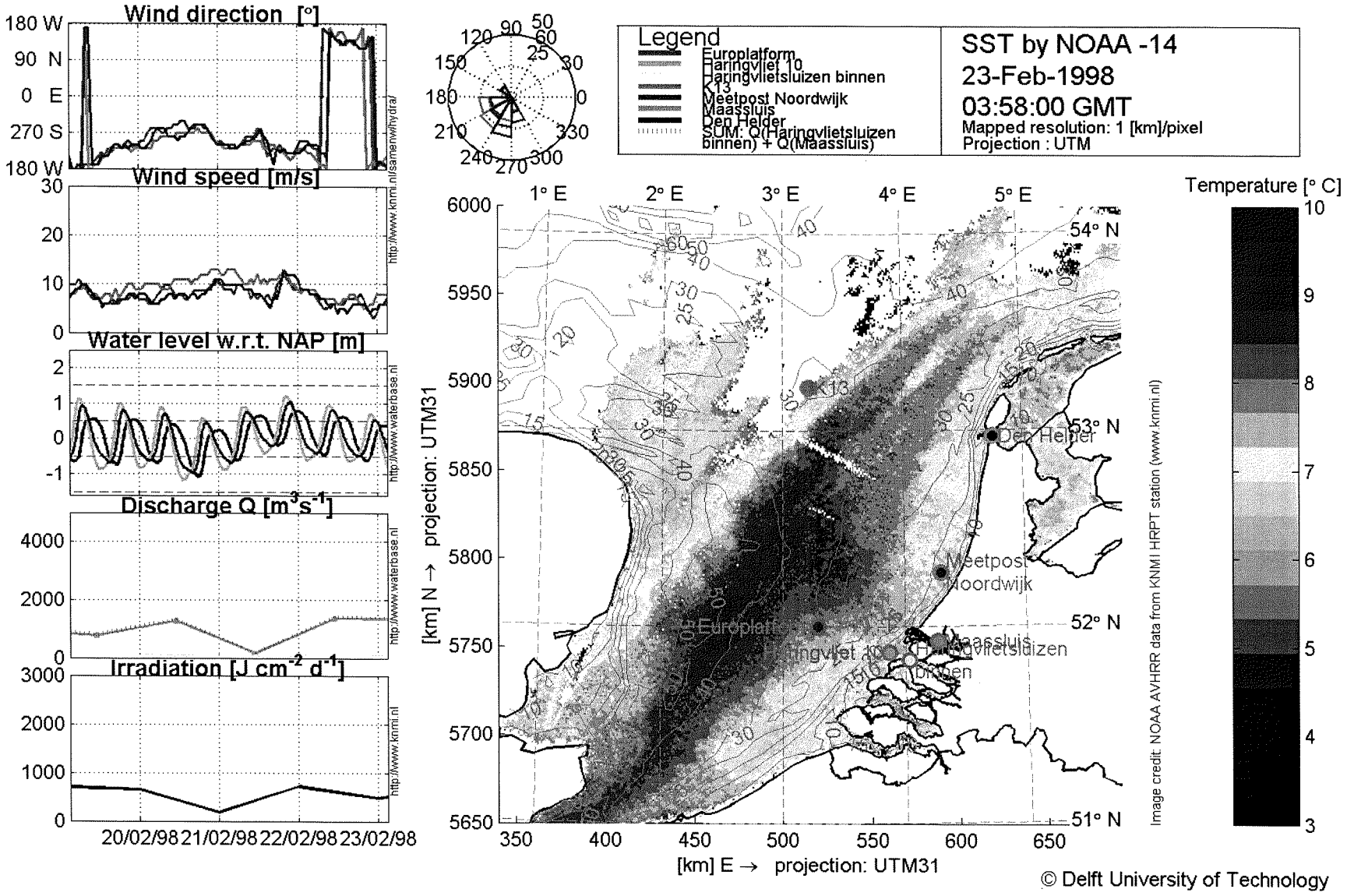
Wind direction [°]
180 W
90 N
0 E
270 S
180 W
Wind speed [m/s]
30
20
10
0
Water level w.r.t. NAP [m]
2
1
0
-1
Discharge Q [m3s-1]
4000
2000
0
Irradiation [J cm-2 d-1]
3000
2000
1000
0
20/02/98 21/02/98 22/02/98 23/02/98
http://www.knmi.nl/samenw/hydra/
http://www.waterbase.nl
http://www.knmi.nl
Legend
Europlatform
Haringvliet 10
Haringvlietsluizen binnen
K13
Meetpost Noordwijk
Maassluis
Den Helder
SUM: Q(Haringvlietsluizen binnen) + Q(Maassluis)
SST by NOAA -14
23-Feb-1998
03:58:00 GMT
Mapped resolution: 1 [km]/pixel
Projection : UTM
Temperature [° C]
10
9
8
7
6
5
4
3
1° E
2° E
3° E
4° E
5° E
54° N
53° N
52° N
51° N
Den Helder
Meetpost Noordwijk
Maassluis
Europlatform
K13
[km] N → projection: UTM31
[km] E → projection: UTM31
6000
5950
5900
5850
5800
5750
5700
5650
350
400
450
500
550
600
650
Image credit: NOAA AVHRR data from KNMI HRPT station (www.knmi.nl)
© Delft University of Technology

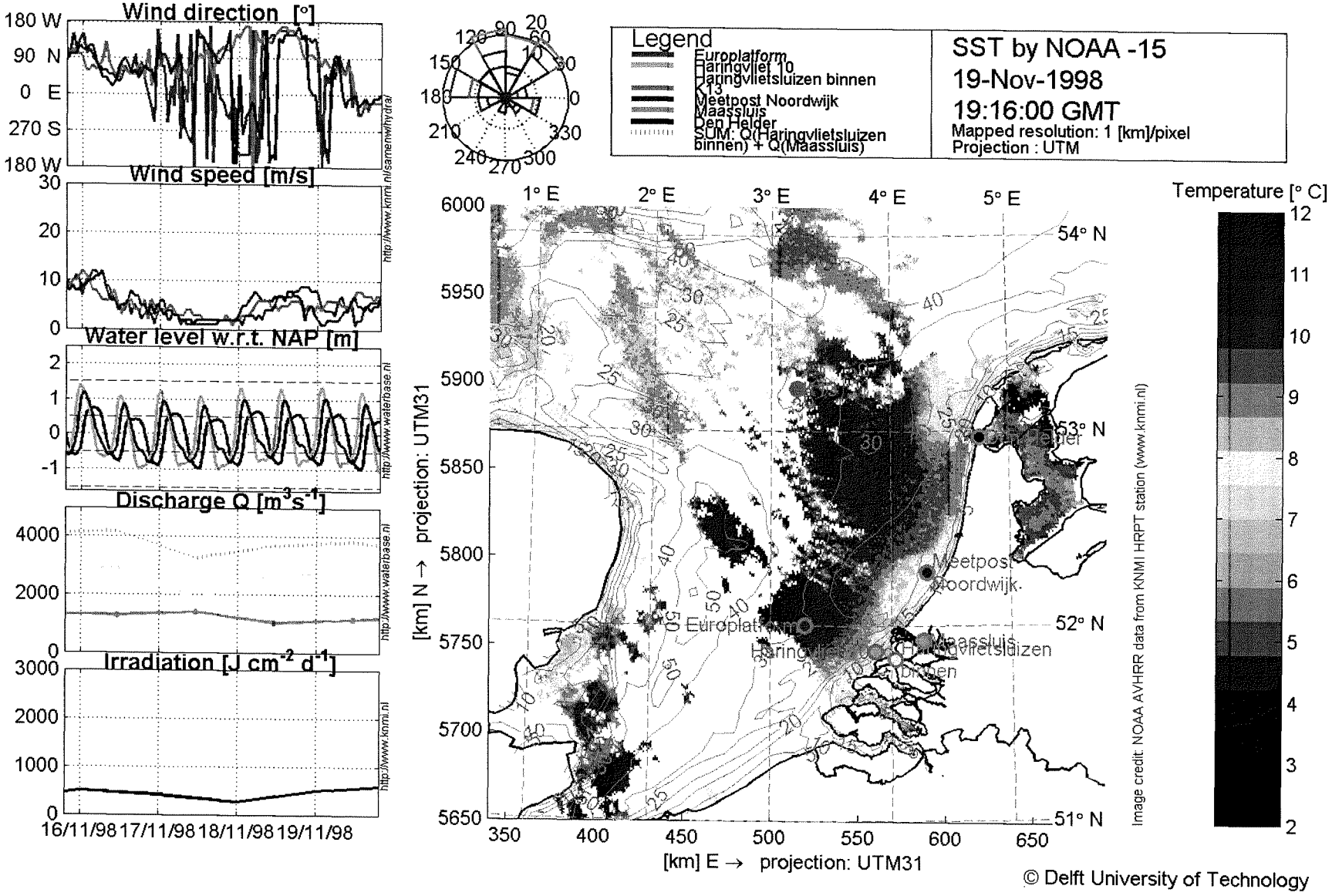
Wind direction [°]
180 W
90 N
0 E
270 S
180 W
Wind speed [m/s]
30
20
10
0
Water level w.r.t. NAP [m]
2
1
0
-1
Discharge Q [m3s-1]
4000
2000
0
Irradiation [J cm-2 d-1]
3000
2000
1000
0
16/11/98 17/11/98 18/11/98 19/11/98
http://www.knmi.nl/samenwhydra/
http://www.waterbase.nl
http://www.knmi.nl
90 20 60 120 150 30 180 0 210 330 240 270 300
Legend
Europlatform
Haringvliet 10
Haringvlietsluizen binnen
K13
Meetpost Noordwijk
Maassluis
Den Helder
SUM: Q(Haringvlietsluizen binnen) + Q(Maassluis)
SST by NOAA -15
19-Nov-1998
19:16:00 GMT
Mapped resolution: 1 [km]/pixel
Projection : UTM
1° E
2° E
3° E
4° E
5° E
54° N
53° N
52° N
51° N
6000
5950
5900
5850
5800
5750
5700
5650
[km] N → projection: UTM31
350
400
450
500
550
600
650
[km] E → projection: UTM31
Meetpost Noordwijk
Europlatform
Haringvlietsluizen
Maassluis
Den Helder
Temperature [° C]
12
11
10
9
8
7
6
5
4
3
2
Image credit: NOAA AVHRR data from KNMI HRPT station (www.knmi.nl)
© Delft University of Technology

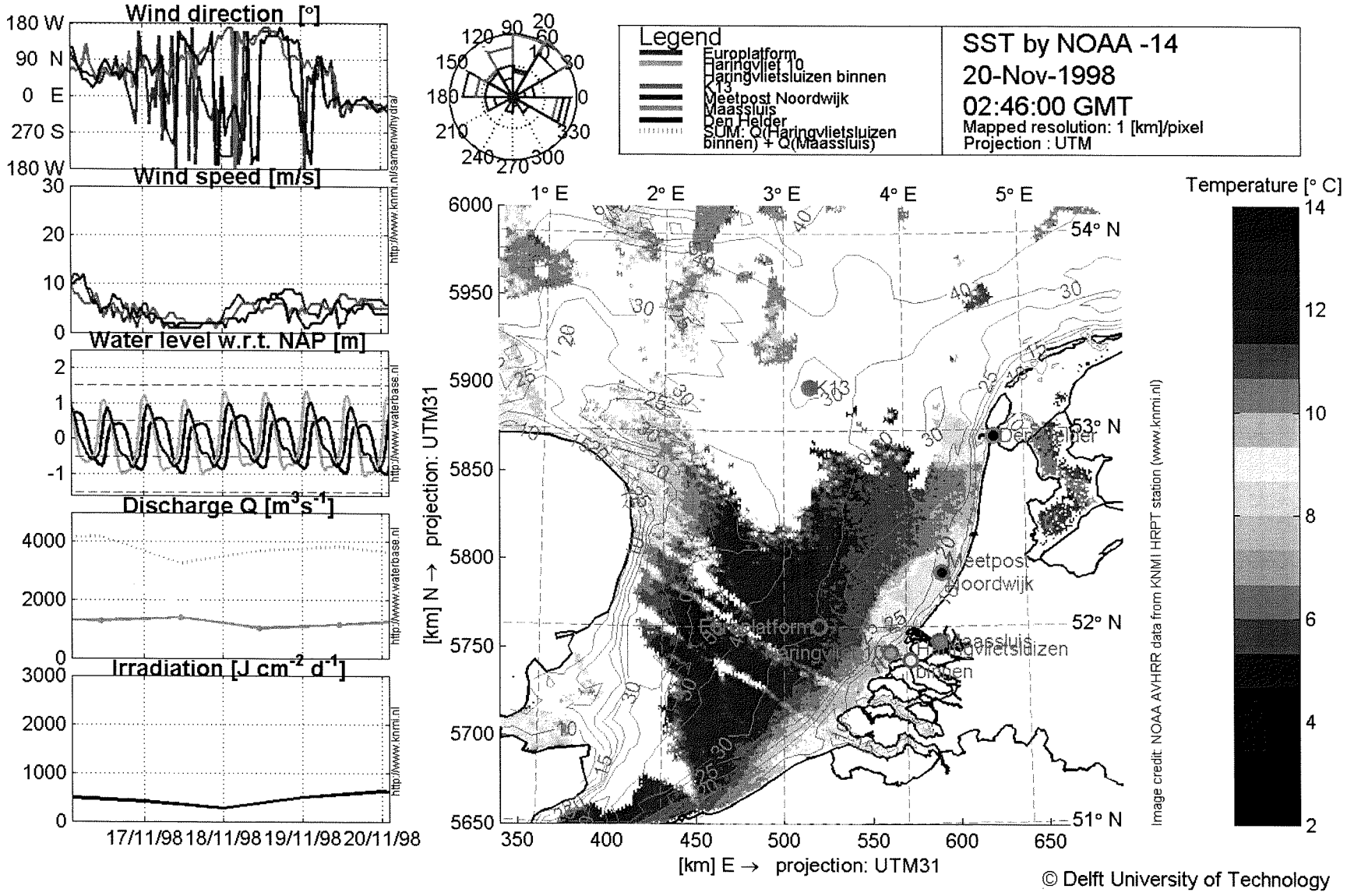
Wind direction [°]
180 W
90 N
0 E
270 S
180 W
Wind speed [m/s]
30
20
10
0
Water level w.r.t. NAP [m]
2
1
0
-1
Discharge Q [m3s-1]
4000
2000
0
Irradiation [J cm-2 d-1]
3000
2000
1000
0
17/11/98 18/11/98 19/11/98 20/11/98
http://www.knmi.nl/samenw/hydra
http://www.waterbase.nl
http://www.knmi.nl
Legend
Europlatform
Haringvliet 10
Haringvlietsluizen binnen
K13
Meetpost Noordwijk
Maassluis
Den Helder
SUM: Q(Haringvlietsluizen binnen) + Q(Maassluis)
SST by NOAA -14
20-Nov-1998
02:46:00 GMT
Mapped resolution: 1 [km]/pixel
Projection : UTM
Temperature [° C]
14
12
10
8
6
4
2
1° E
2° E
3° E
4° E
5° E
54° N
53° N
52° N
51° N
6000
5950
5900
5850
5800
5750
5700
5650
350
400
450
500
550
600
650
[km] N → projection: UTM31
[km] E → projection: UTM31
K13
Meetpost Noordwijk
Maassluis
Image credit: NOAA AVHRR data from KNMI HRPT station (www.knmi.nl)
© Delft University of Technology

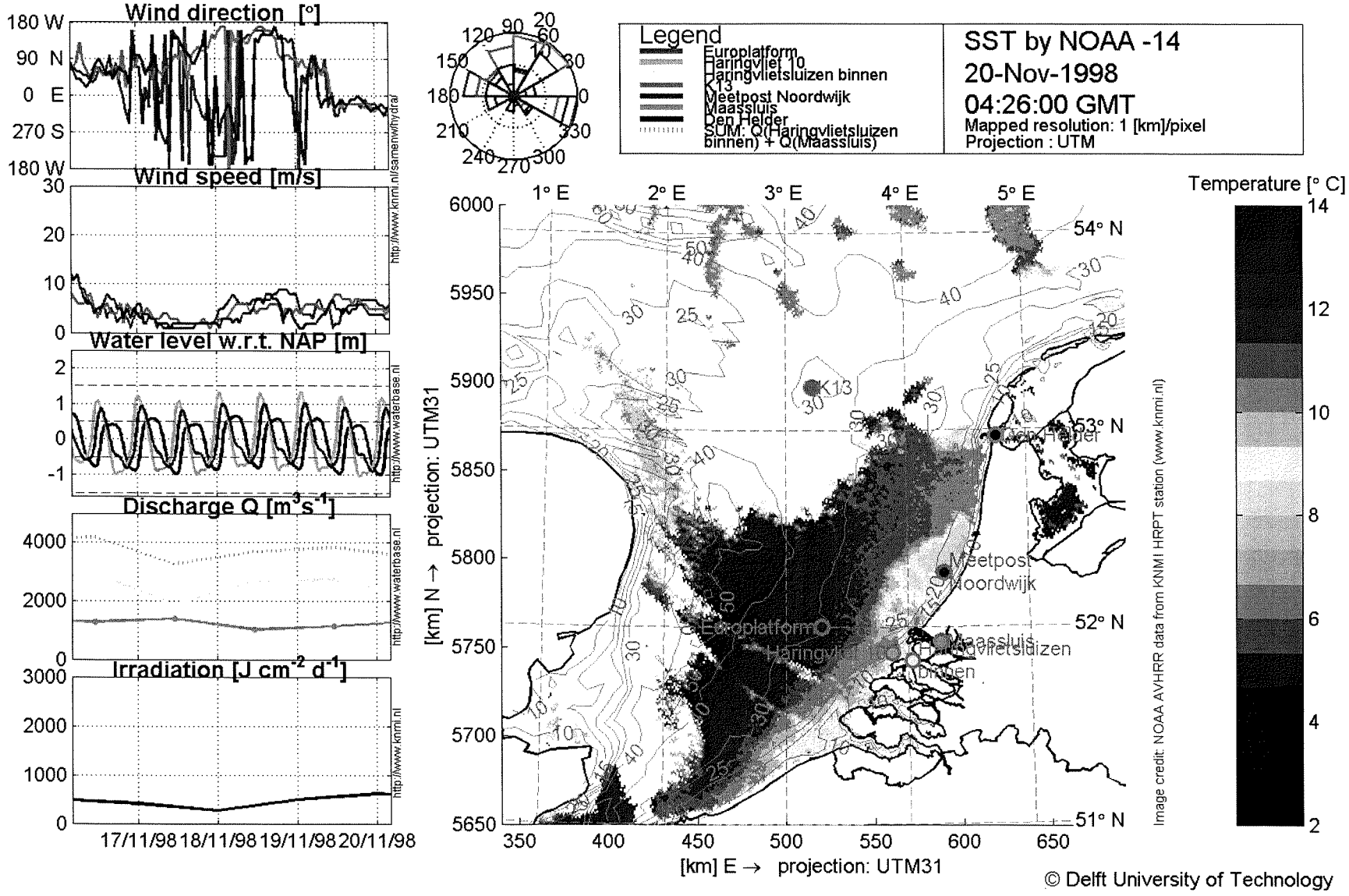
Wind direction [°]
180 W
90 N
0 E
270 S
180 W
Wind speed [m/s]
30
20
10
0
Water level w.r.t. NAP [m]
2
1
0
-1
Discharge Q [m³s⁻¹]
4000
2000
0
Irradiation [J cm⁻² d⁻¹]
3000
2000
1000
0
17/11/98 18/11/98 19/11/98 20/11/98
http://www.knmi.nl/samenw/hydra/
http://www.knmi.nl
http://www.waterbase.nl
Legend
Europlatform
Haringvliet 10
Haringvlietsluizen binnen
K13
Meetpost Noordwijk
Maassluis
Den Helder
SUM: Q(Haringvlietsluizen binnen) + Q(Maassluis)
SST by NOAA -14
20-Nov-1998
04:26:00 GMT
Mapped resolution: 1 [km]/pixel
Projection : UTM
Temperature [° C]
14
12
10
8
6
4
2
1° E
2° E
3° E
4° E
5° E
54° N
53° N
52° N
51° N
K13
Meetpost Noordwijk
Europlatform
Haringvliet
Maassluis
Haringvlietsluizen binnen
6000
5950
5900
5850
5800
5750
5700
5650
[km] N → projection: UTM31
350
400
450
500
550
600
650
[km] E → projection: UTM31
Image credit: NOAA AVHRR data from KNMI HRPT station (www.knmi.nl)
© Delft University of Technology

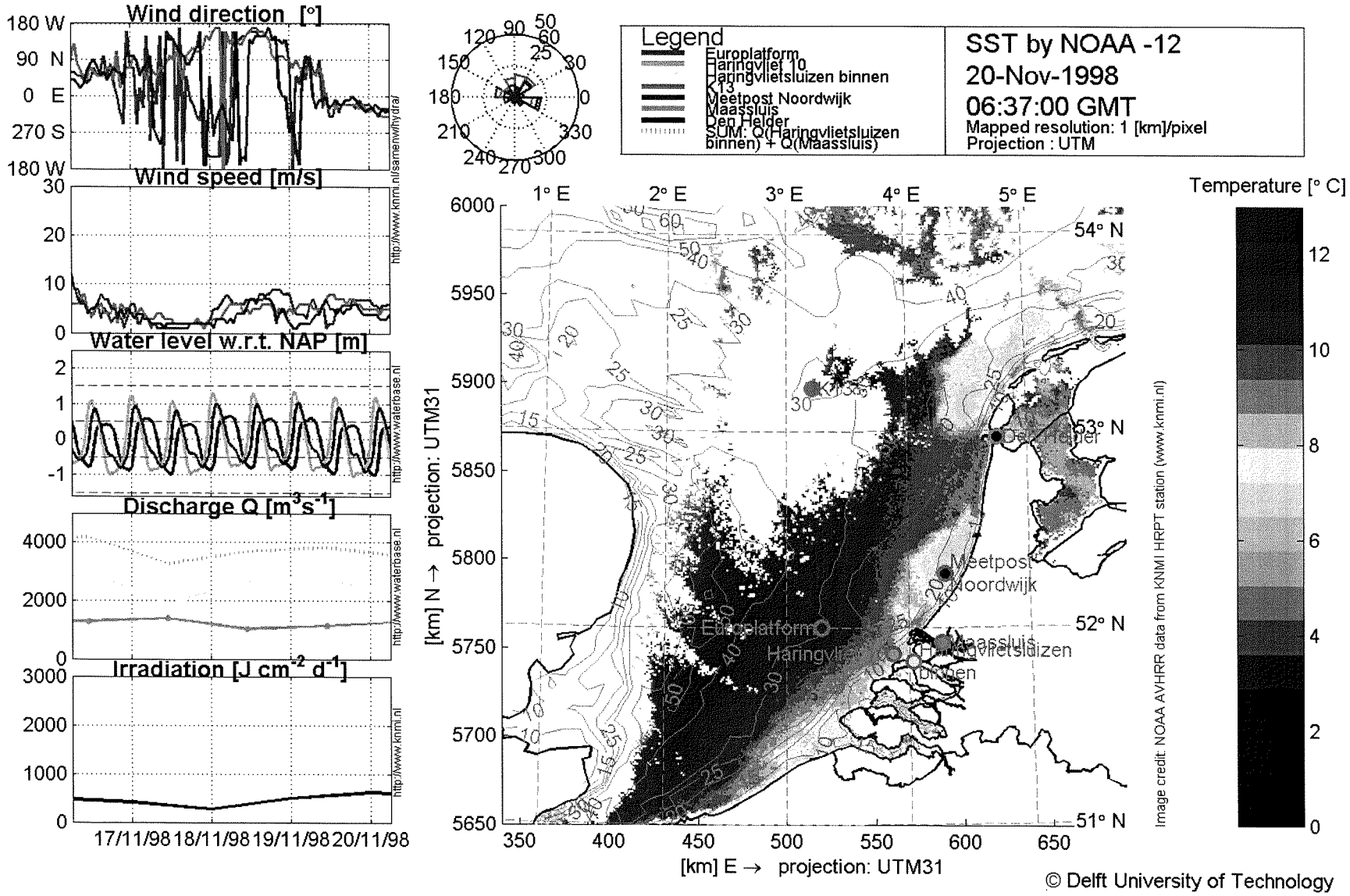
Wind direction [°]
180 W
90 N
0 E
270 S
180 W
Wind speed [m/s]
Water level w.r.t. NAP [m]
Discharge Q [m3s-1]
Irradiation [J cm-2 d-1]
17/11/98 18/11/98 19/11/98 20/11/98
http://www.knmi.nl/samenw/hydra/
http://www.waterbase.nl
http://www.knmi.nl
Legend
Europlatform
Haringvliet 10
Haringvlietsluizen binnen
K13
Meetpost Noordwijk
Maassluis
Den Helder
SUM: Q(Haringvlietsluizen binnen) + Q(Maassluis)
SST by NOAA -12
20-Nov-1998
06:37:00 GMT
Mapped resolution: 1 [km]/pixel
Projection : UTM
Temperature [° C]
1° E
2° E
3° E
4° E
5° E
54° N
53° N
52° N
51° N
[km] N → projection: UTM31
[km] E → projection: UTM31
Meetpost Noordwijk
Europlatform
Maassluis
Image credit: NOAA AVHRR data from KNMI HRPT station (www.knmi.nl)
© Delft University of Technology

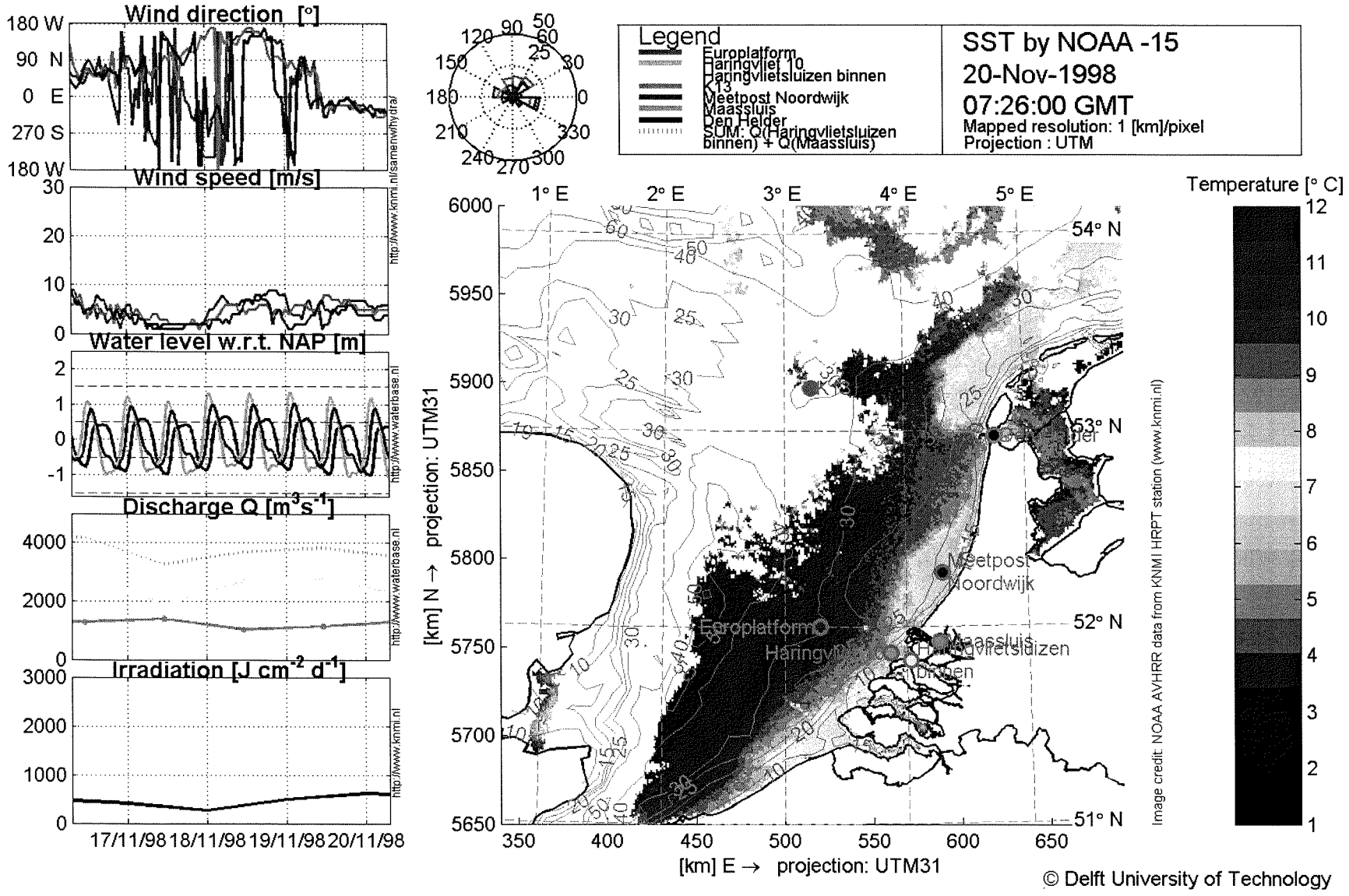
Wind direction [°]
180 W
90 N
0 E
270 S
180 W
Wind speed [m/s]
Water level w.r.t. NAP [m]
Discharge Q [m3s-1]
Irradiation [J cm-2 d-1]
17/11/98 18/11/98 19/11/98 20/11/98
http://www.knmi.nl/samenw/hydra/
http://www.waterbase.nl
http://www.knmi.nl
Legend
Europlatform
Haringvliet 10
Haringvlietsluizen binnen
K13
Meetpost Noordwijk
Maassluis
Den Helder
SUM: Q(Haringvlietsluizen binnen) + Q(Maassluis)
SST by NOAA -15
20-Nov-1998
07:26:00 GMT
Mapped resolution: 1 [km]/pixel
Projection : UTM
Temperature [° C]
1° E
2° E
3° E
4° E
5° E
54° N
53° N
52° N
51° N
[km] N → projection: UTM31
[km] E → projection: UTM31
Meetpost Noordwijk
Europlatform
Haringvl
Maassluis
Image credit: NOAA AVHRR data from KNMI HRPT station (www.knmi.nl)
© Delft University of Technology

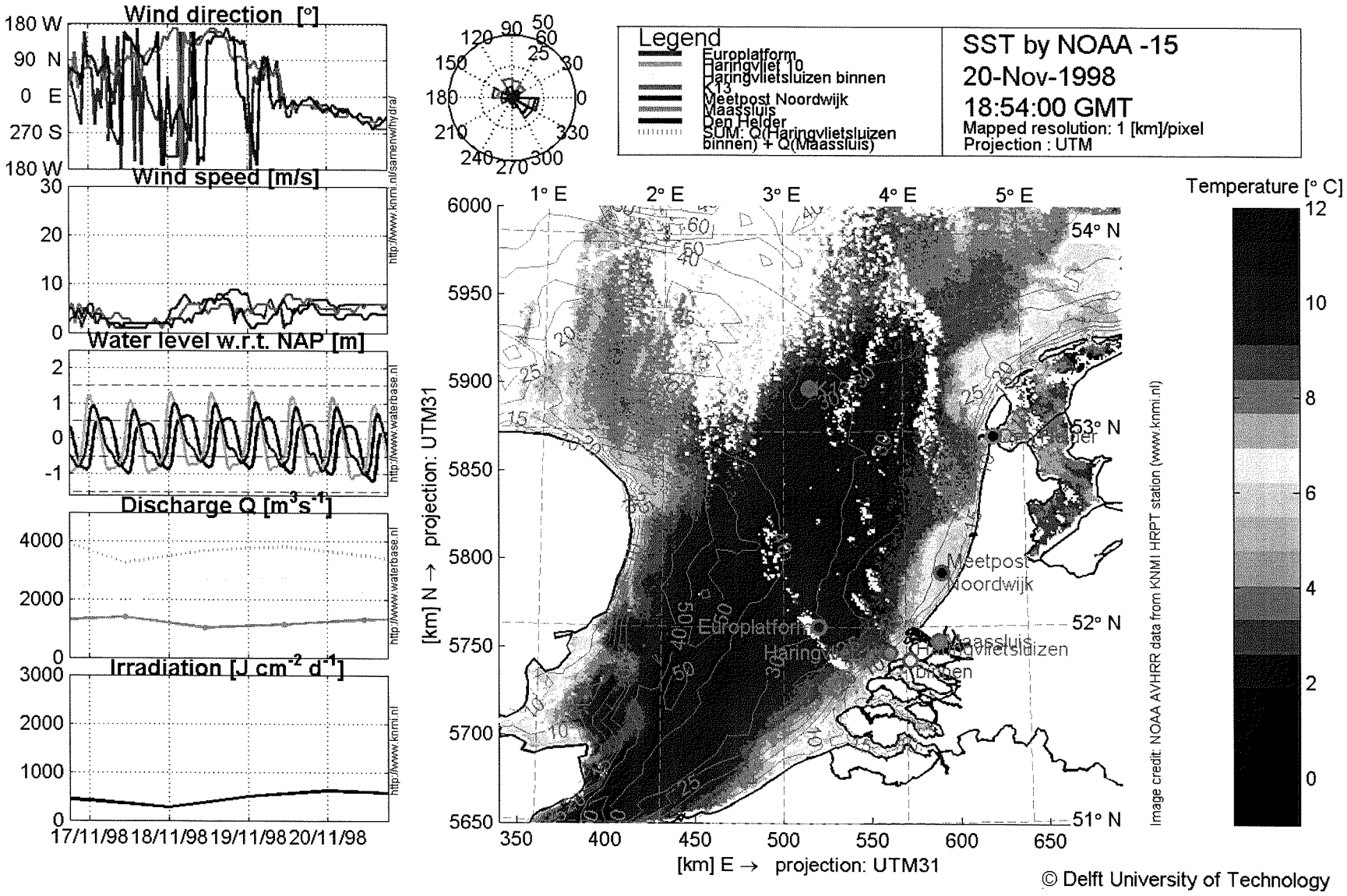
Wind direction [°]
180 W
90 N
0 E
270 S
180 W
Wind speed [m/s]
30
20
10
0
Water level w.r.t. NAP [m]
2
1
0
-1
Discharge Q [m3s-1]
4000
2000
0
Irradiation [J cm-2 d-1]
3000
2000
1000
0
17/11/98 18/11/98 19/11/98 20/11/98
http://www.knmi.nl/samenw/hydra/
http://www.waterbase.nl
http://www.knmi.nl
Legend
Europlatform
Haringvliet 10
Haringvlietsluizen binnen
K13
Meetpost Noordwijk
Maassluis
Den Helder
SUM: Q(Haringvlietsluizen binnen) + Q(Maassluis)
SST by NOAA -15
20-Nov-1998
18:54:00 GMT
Mapped resolution: 1 [km]/pixel
Projection : UTM
Temperature [° C]
12
10
8
6
4
2
0
1° E
2° E
3° E
4° E
5° E
54° N
53° N
52° N
51° N
6000
5950
5900
5850
5800
5750
5700
5650
[km] N → projection: UTM31
350
400
450
500
550
600
650
[km] E → projection: UTM31
Meetpost Noordwijk
Europlatform
Maassluis
Haringvlietsluizen
Image credit: NOAA AVHRR data from KNMI HRPT station (www.knmi.nl)
© Delft University of Technology

Appendix 6

PHASES OF THE MOON

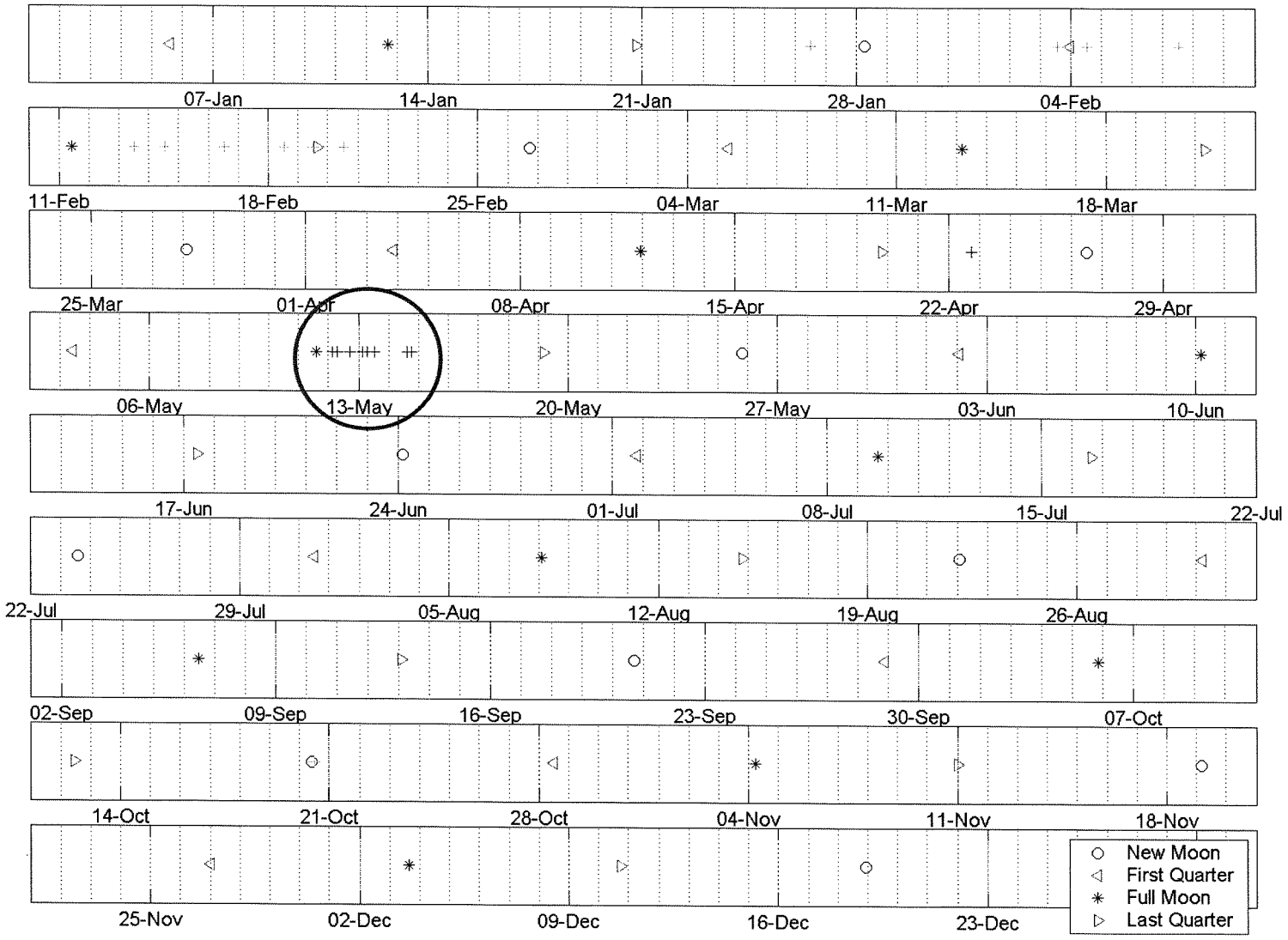

In DCZ spring tide generally occurs 2-2.5 days after new- or full moon. Neap tide occurs 2-2.5 days after first- or last quarter.

+ indicates the position of the selected nLw images w.r.t. the phases of the moon

+ indicates the position of the selected SST images w.r.t. the phases of the moon

Appendix 7

HOT SPOTS

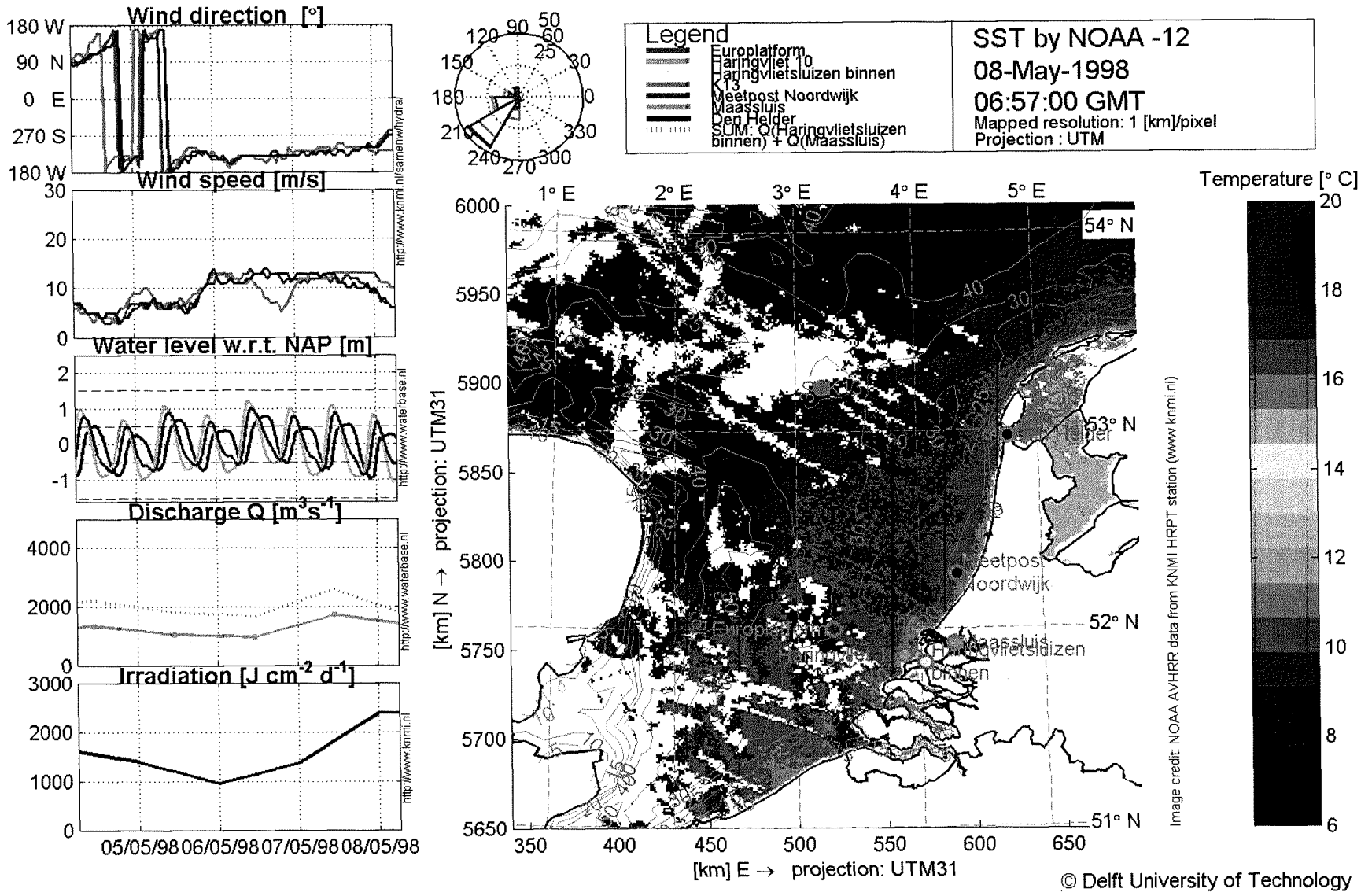
Wind direction [°]
180 W
90 N
0 E
270 S
180 W
Wind speed [m/s]
30
20
10
0
Water level w.r.t. NAP [m]
2
1
0
-1
Discharge Q [m3s-1]
4000
2000
0
Irradiation [J cm-2 d-1]
3000
2000
1000
0
05/05/98 06/05/98 07/05/98 08/05/98
http://www.knmi.nl/samenw/hydra/
http://www.waterbase.nl
http://www.knmi.nl
Legend
Europlatform
Haringvliet 10
Haringvlietsluizen binnen
K13
Meetpost Noordwijk
Maassluis
Den Helder
SUM: Q(Haringvlietsluizen binnen) + Q(Maassluis)
SST by NOAA -12
08-May-1998
06:57:00 GMT
Mapped resolution: 1 [km]/pixel
Projection : UTM
Temperature [° C]
20
18
16
14
12
10
8
6
1° E
2° E
3° E
4° E
5° E
54° N
53° N
52° N
51° N
6000
5950
5900
5850
5800
5750
5700
5650
[km] N → projection: UTM31
350
400
450
500
550
600
650
[km] E → projection: UTM31
Image credit: NOAA AVHRR data from KNMI HRPT station (www.knmi.nl)
© Delft University of Technology

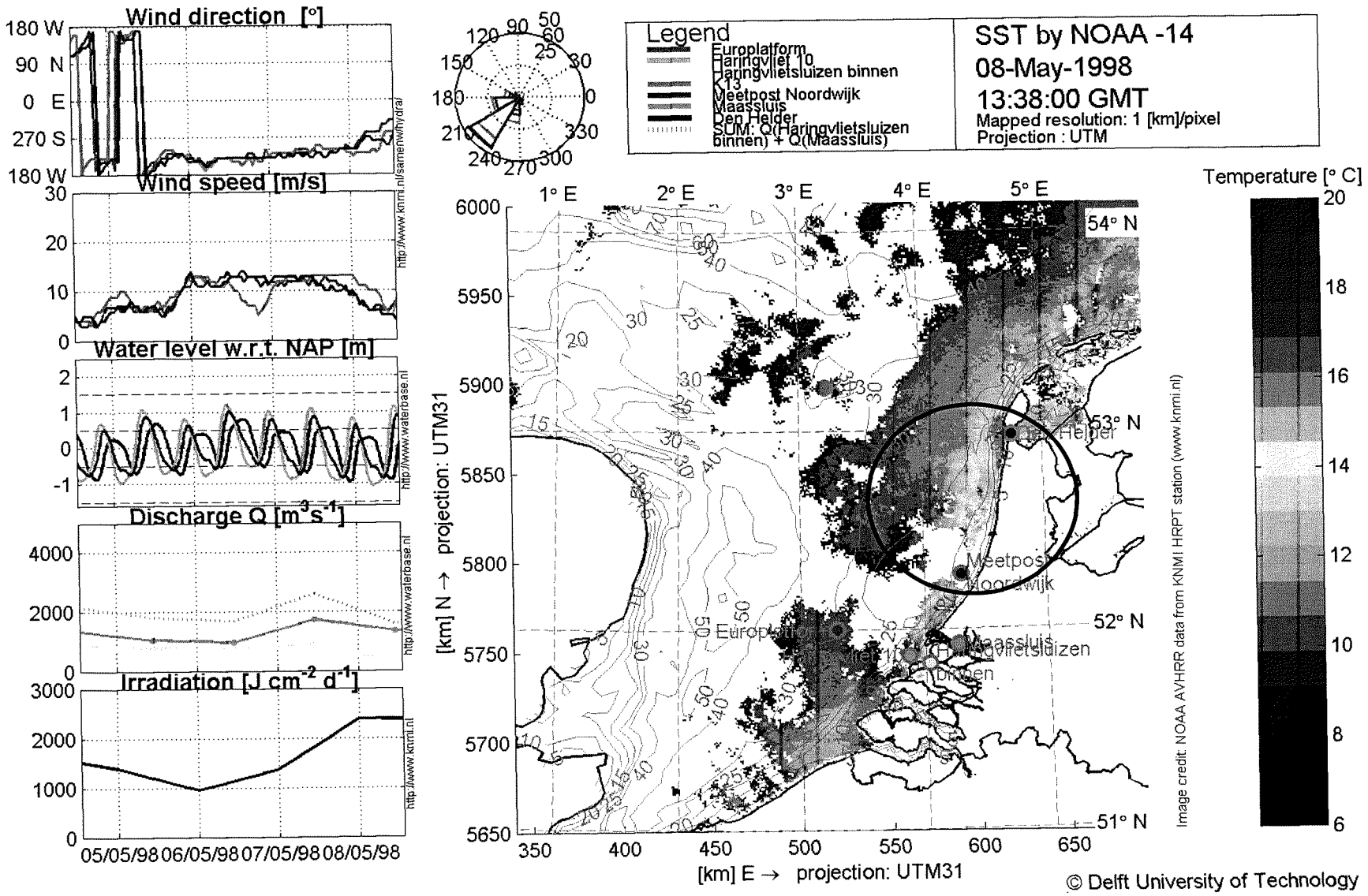
Wind direction [°]
180 W
90 N
0 E
270 S
180 W
Wind speed [m/s]
30
20
10
0
Water level w.r.t. NAP [m]
2
1
0
-1
Discharge Q [m3s-1]
4000
2000
0
Irradiation [J cm-2 d-1]
3000
2000
1000
0
05/05/98 06/05/98 07/05/98 08/05/98
http://www.knmi.nl/samenw/hydra
http://www.waterbase.nl
http://www.knmi.nl
Legend
Europlatform
Haringvliet 10
Haringvlietsluizen binnen
K13
Meetpost Noordwijk
Maassluis
Den Helder
SUM: Q(Haringvlietsluizen binnen) + Q(Maassluis)
SST by NOAA -14
08-May-1998
13:38:00 GMT
Mapped resolution: 1 [km]/pixel
Projection : UTM
Temperature [° C]
20
18
16
14
12
10
8
6
1° E
2° E
3° E
4° E
5° E
54° N
53° N
52° N
51° N
6000
5950
5900
5850
5800
5750
5700
5650
[km] N → projection: UTM31
350
400
450
500
550
600
650
[km] E → projection: UTM31
Meetpost Noordwijk
Maassluis
Image credit: NOAA AVHRR data from KNMI HRPT station (www.knmi.nl)
© Delft University of Technology

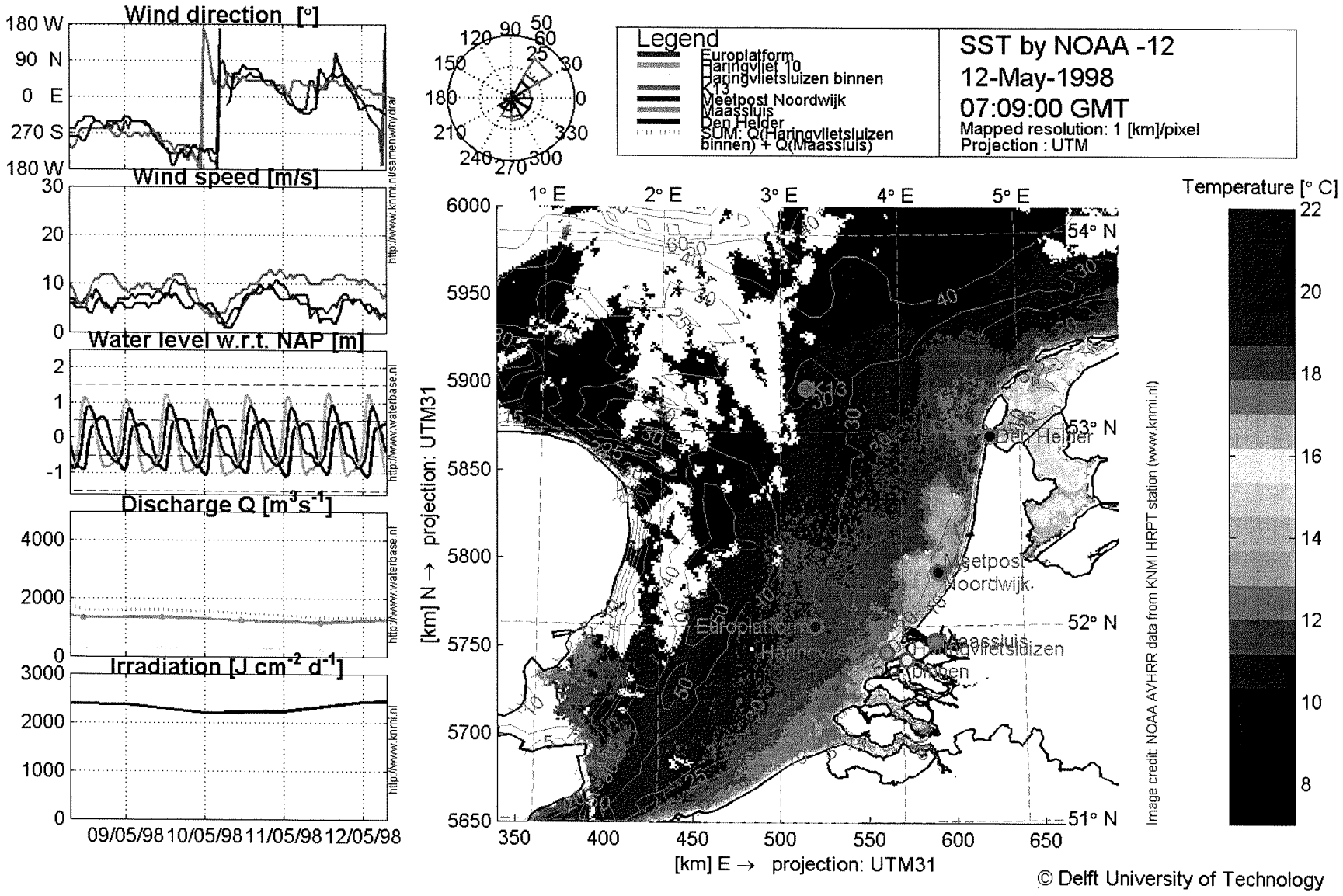
Wind direction [°]
180 W
90 N
0 E
270 S
180 W
Wind speed [m/s]
30
20
10
0
Water level w.r.t. NAP [m]
2
1
0
-1
Discharge Q [m3s-1]
4000
2000
0
Irradiation [J cm-2 d-1]
3000
2000
1000
0
09/05/98 10/05/98 11/05/98 12/05/98
http://www.knmi.nl/samenw/hydra
http://www.waterbase.nl
http://www.knmi.nl
Legend
Europlatform
Haringvliet 10
Haringvlietsluizen binnen
K13
Meetpost Noordwijk
Maassluis
Den Helder
SUM: Q(Haringvlietsluizen binnen) + Q(Maassluis)
SST by NOAA -12
12-May-1998
07:09:00 GMT
Mapped resolution: 1 [km]/pixel
Projection : UTM
Temperature [° C]
22
20
18
16
14
12
10
8
1° E
2° E
3° E
4° E
5° E
54° N
53° N
52° N
51° N
6000
5950
5900
5850
5800
5750
5700
5650
[km] N → projection: UTM31
350
400
450
500
550
600
650
[km] E → projection: UTM31
Den Helder
Meetpost Noordwijk
Europlatform
Maassluis
Image credit: NOAA AVHRR data from KNMI HRPT station (www.knmi.nl)
© Delft University of Technology

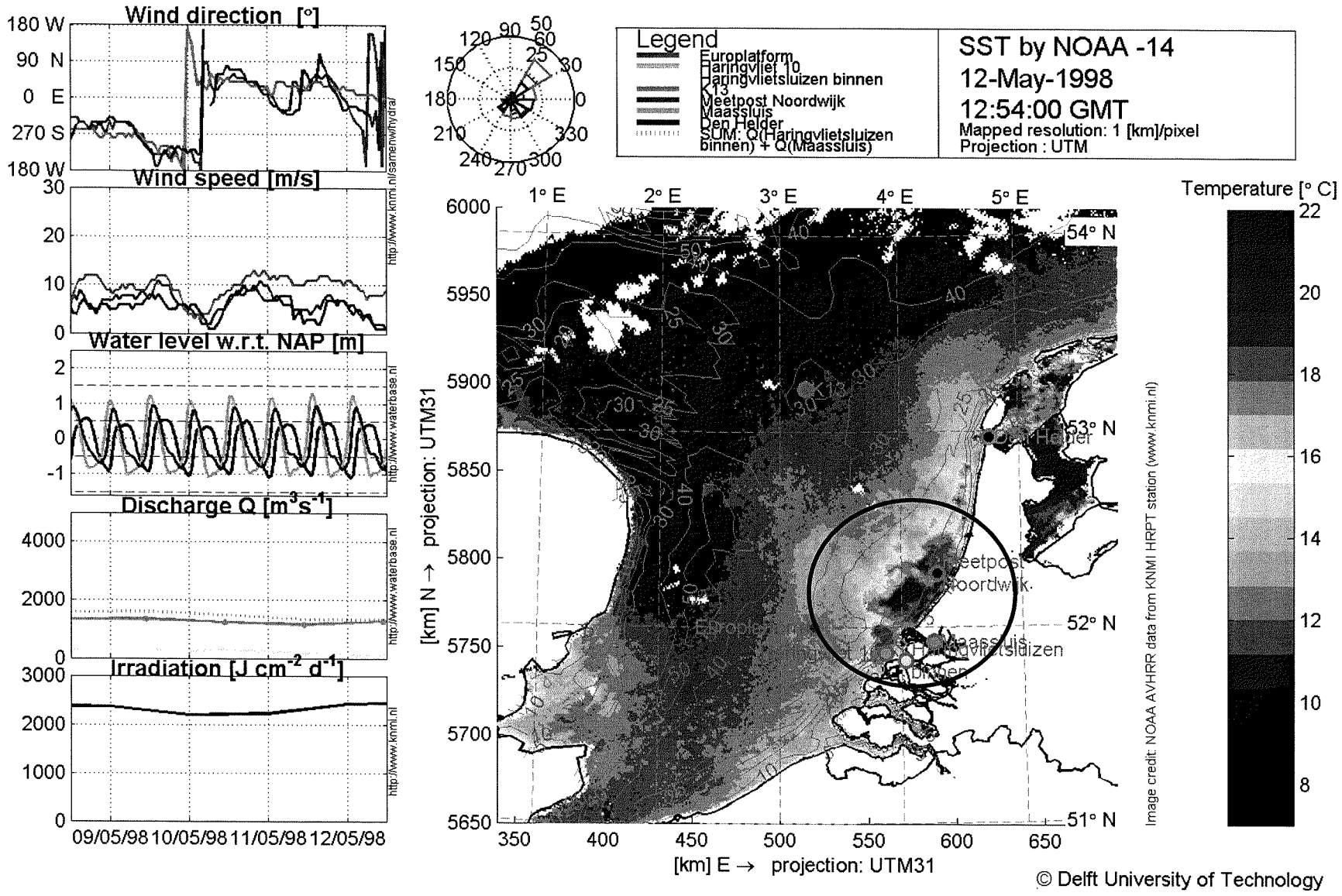
Wind direction [°]
180 W
90 N
0 E
270 S
180 W
Wind speed [m/s]
Water level w.r.t. NAP [m]
Discharge Q [m³s⁻¹]
Irradiation [J cm⁻² d⁻¹]
09/05/98 10/05/98 11/05/98 12/05/98
http://www.knmi.nl/samenwhydra/
http://www.waterbase.nl
http://www.knmi.nl
Legend
Europlatform
Haringvliet 10
Haringvlietsluizen binnen
K13
Meetpost Noordwijk
Maassluis
Den Helder
SUM: Q(Haringvlietsluizen binnen) + Q(Maassluis)
SST by NOAA -14
12-May-1998
12:54:00 GMT
Mapped resolution: 1 [km]/pixel
Projection : UTM
Temperature [° C]
[km] N → projection: UTM31
[km] E → projection: UTM31
Image credit: NOAA AVHRR data from KNMI HRPT station (www.knmi.nl)
© Delft University of Technology

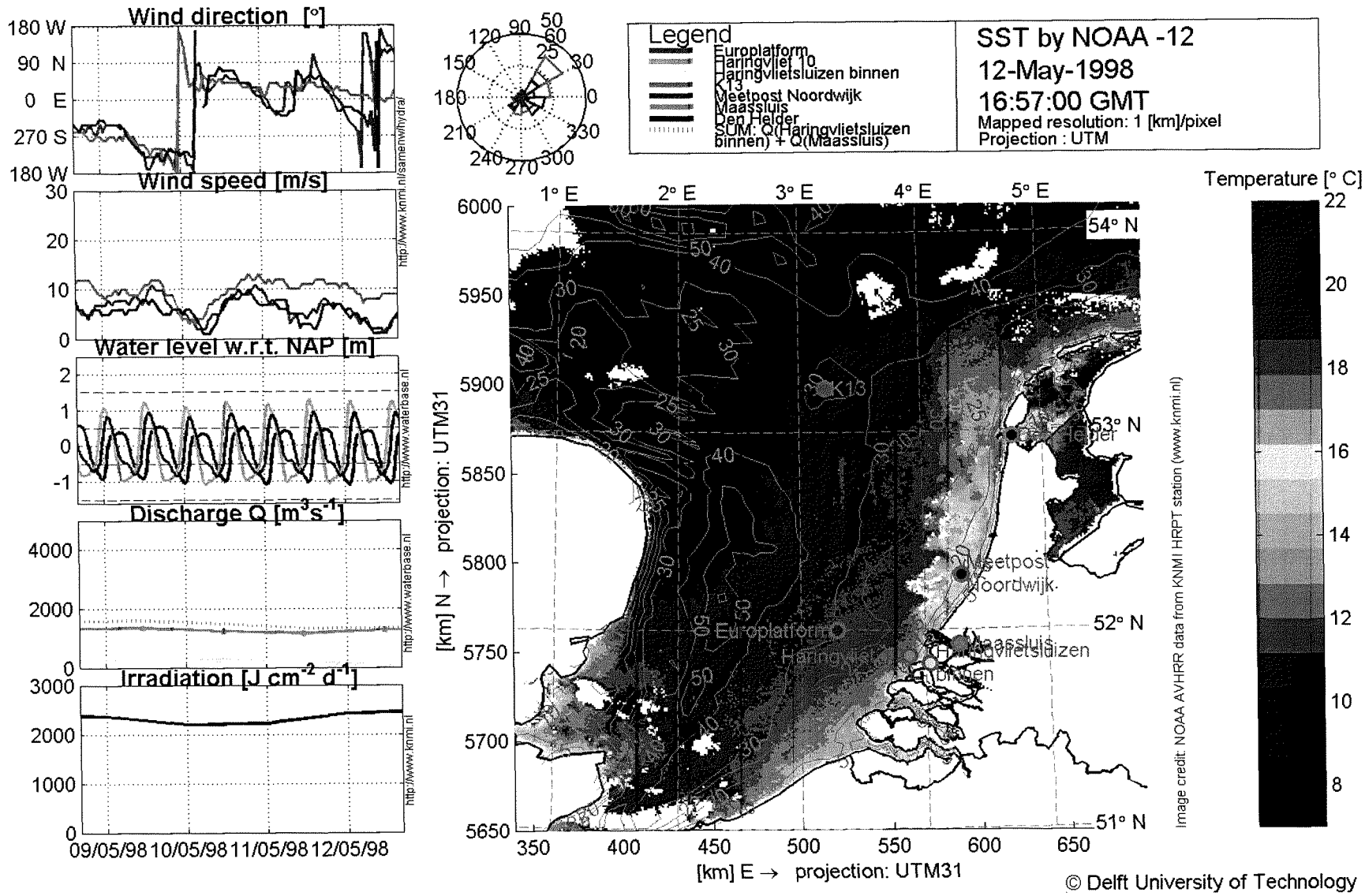
Wind direction [°]
180 W
90 N
0 E
270 S
180 W
Wind speed [m/s]
30
20
10
0
Water level w.r.t. NAP [m]
2
1
0
-1
Discharge Q [m3s-1]
4000
2000
0
Irradiation [J cm-2 d-1]
3000
2000
1000
0
09/05/98 10/05/98 11/05/98 12/05/98
http://www.knmi.nl/samenw/hydra/
http://www.waterbase.nl
http://www.knmi.nl
Legend
Europlatform
Haringvliet 10
Haringvlietsluizen binnen
K13
Meetpost Noordwijk
Maassluis
Den Helder
SUM: Q(Haringvlietsluizen binnen) + Q(Maassluis)
SST by NOAA -12
12-May-1998
16:57:00 GMT
Mapped resolution: 1 [km]/pixel
Projection : UTM
Temperature [° C]
22
20
18
16
14
12
10
8
1° E
2° E
3° E
4° E
5° E
54° N
53° N
52° N
51° N
6000
5950
5900
5850
5800
5750
5700
5650
[km] N → projection: UTM31
350
400
450
500
550
600
650
[km] E → projection: UTM31
Europlatform
K13
Meetpost Noordwijk
Maassluis
Image credit: NOAA AVHRR data from KNMI HRPT station (www.knmi.nl)
© Delft University of Technology

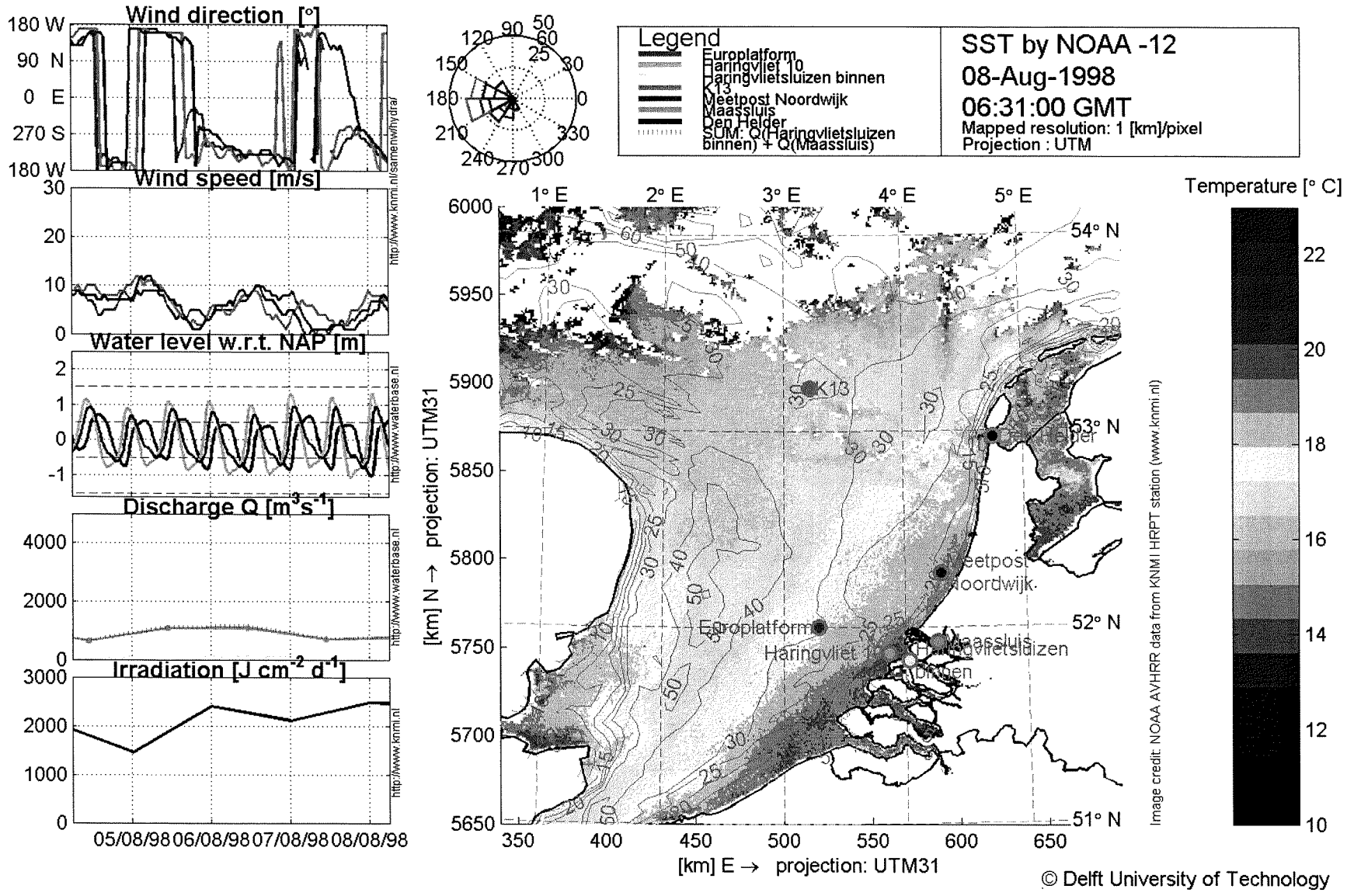
Wind direction [°]
180 W
90 N
0 E
270 S
180 W
Wind speed [m/s]
Water level w.r.t. NAP [m]
Discharge Q [m³s⁻¹]
Irradiation [J cm⁻² d⁻¹]
05/08/98 06/08/98 07/08/98 08/08/98
http://www.knmi.nl/samenwhydra/
http://www.waterbase.nl
http://www.knmi.nl
Legend
Europlatform
Haringvliet 10
Haringvlietsluizen binnen
K13
Meetpost Noordwijk
Maassluis
Den Helder
SUM: Q(Haringvlietsluizen binnen) + Q(Maassluis)
SST by NOAA -12
08-Aug-1998
06:31:00 GMT
Mapped resolution: 1 [km]/pixel
Projection : UTM
Temperature [° C]
[km] N → projection: UTM31
[km] E → projection: UTM31
Image credit: NOAA AVHRR data from KNMI HRPT station (www.knmi.nl)
© Delft University of Technology

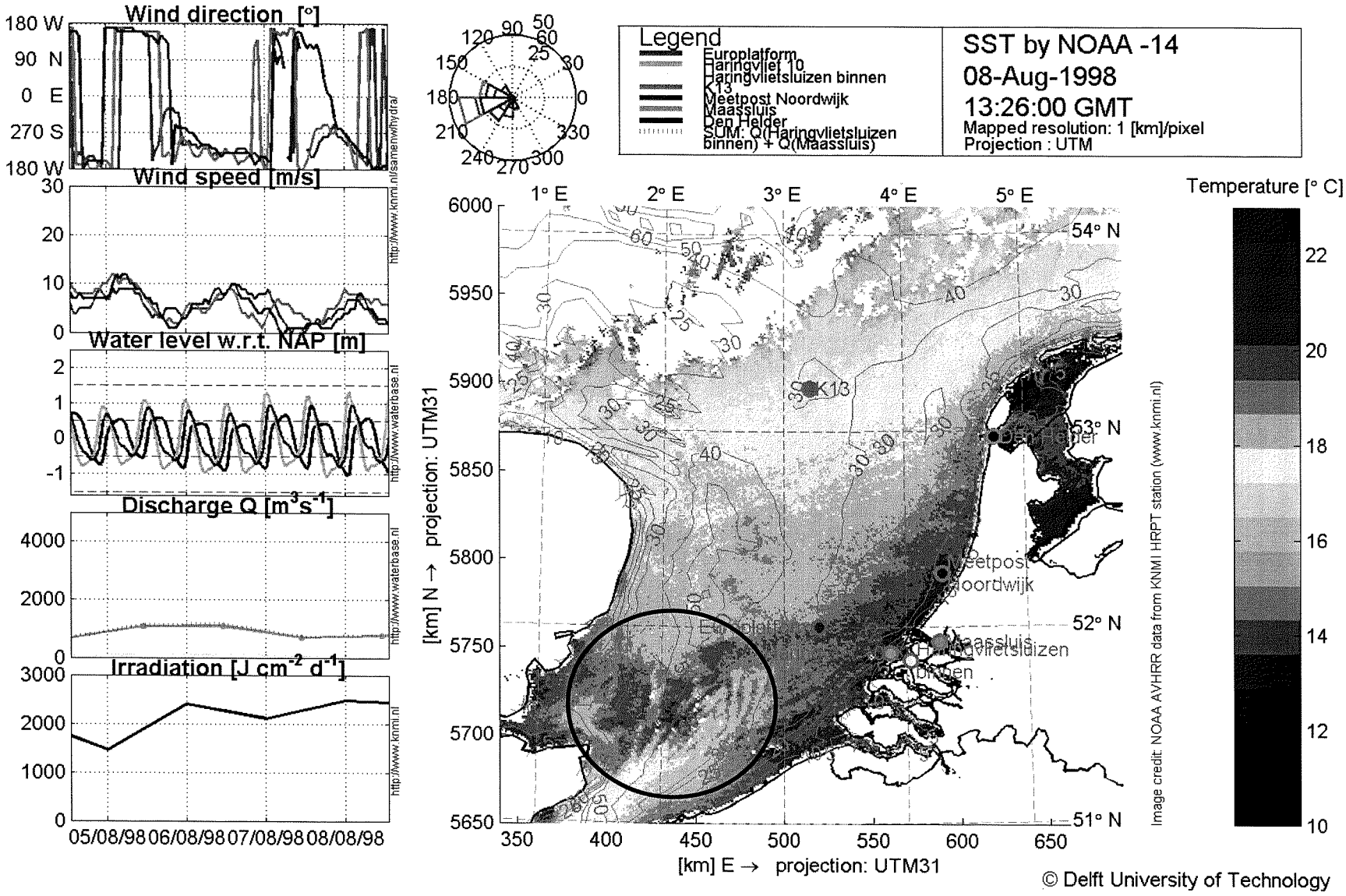
Wind direction [°]
180 W
90 N
0 E
270 S
180 W
Wind speed [m/s]
30
20
10
0
Water level w.r.t. NAP [m]
2
1
0
-1
Discharge Q [m3s-1]
4000
2000
0
Irradiation [J cm-2 d-1]
3000
2000
1000
0
05/08/98 06/08/98 07/08/98 08/08/98
http://www.knmi.nl/samenw/hydra/
http://www.waterbase.nl
http://www.knmi.nl
Legend
Europlatform
Haringvliet 10
Haringvlietsluizen binnen
K13
Meetpost Noordwijk
Maassluis
Den Helder
SUM: Q(Haringvlietsluizen binnen) + Q(Maassluis)
SST by NOAA -14
08-Aug-1998
13:26:00 GMT
Mapped resolution: 1 [km]/pixel
Projection : UTM
1° E
2° E
3° E
4° E
5° E
54° N
53° N
52° N
51° N
6000
5950
5900
5850
5800
5750
5700
5650
[km] N → projection: UTM31
350
400
450
500
550
600
650
[km] E → projection: UTM31
K13
Meetpost Noordwijk
Maassluis
Haringvlietsluizen
Den Helder
Temperature [° C]
22
20
18
16
14
12
10
Image credit: NOAA AVHRR data from KNMI HRPT station (www.knmi.nl)
© Delft University of Technology

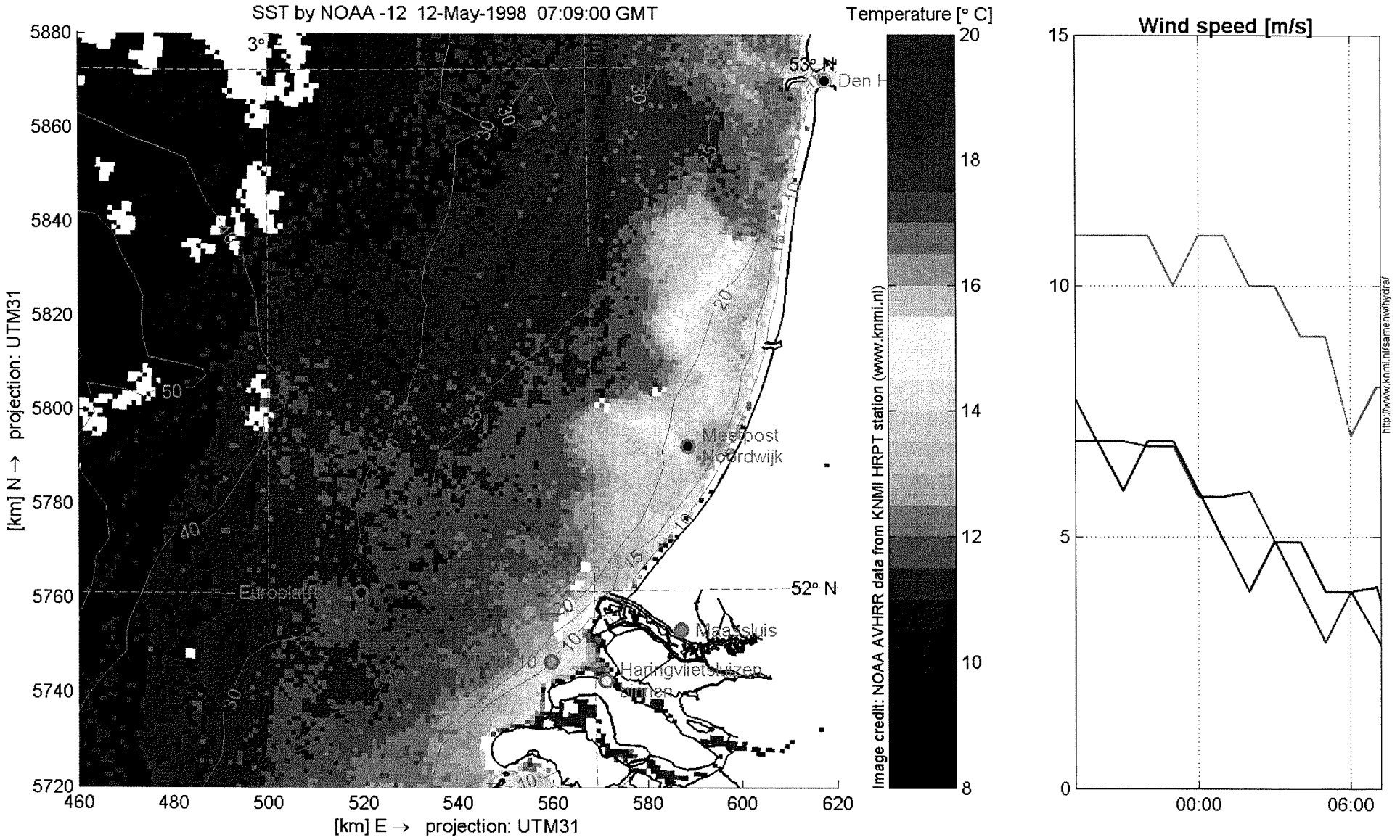
SST by NOAA -12 12-May-1998 07:09:00 GMT
Temperature [° C]
Wind speed [m/s]
[km] N → projection: UTM31
[km] E → projection: UTM31
Meetpost Noordwijk
Europlatform
Maassluis
Haringvlietsluizen
52° N
53° N
Image credit: NOAA AVHRR data from KNMI HRPT station (www.knmi.nl)
http://www.knmi.nl/samenw/hydra/
© Delft University of Technology CiTG: fluidmechanics.tudelft.nl

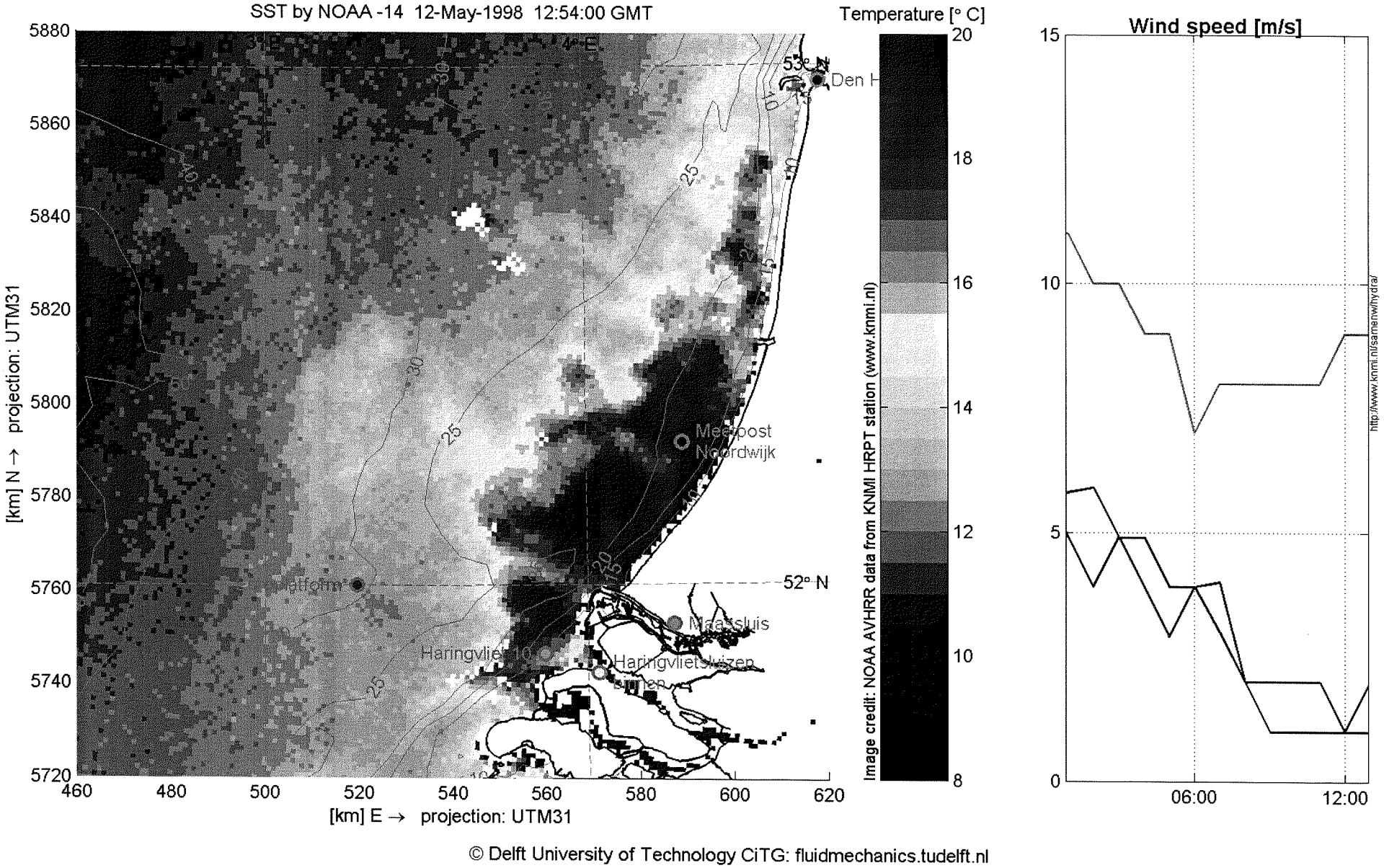

© Delft University of Technology CiTG: fluidmechanics.tudelft.nl

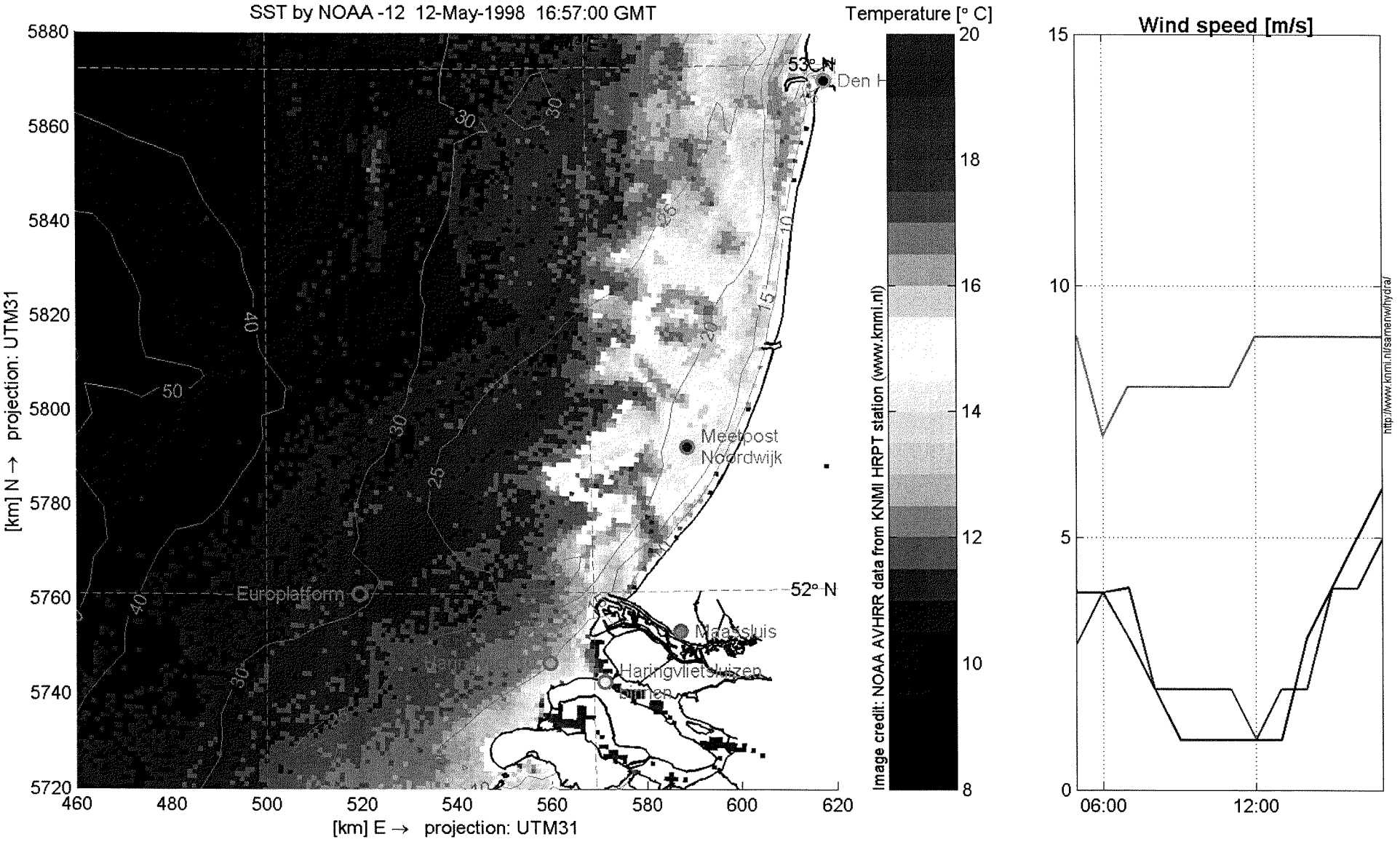
SST by NOAA -12 12-May-1998 16:57:00 GMT
Temperature [° C]
Wind speed [m/s]
[km] N → projection: UTM31
[km] E → projection: UTM31
53° N
52° N
Den H
Meetpost Noordwijk
Europlatform
Maassluis
Haringvlietsluizen
Image credit: NOAA AVHRR data from KNMI HRPT station (www.knmi.nl)
http://www.knmi.nl/samenw/hydra/
© Delft University of Technology CiTG: fluidmechanics.tudelft.nl

Appendix 8

RESULTS SST

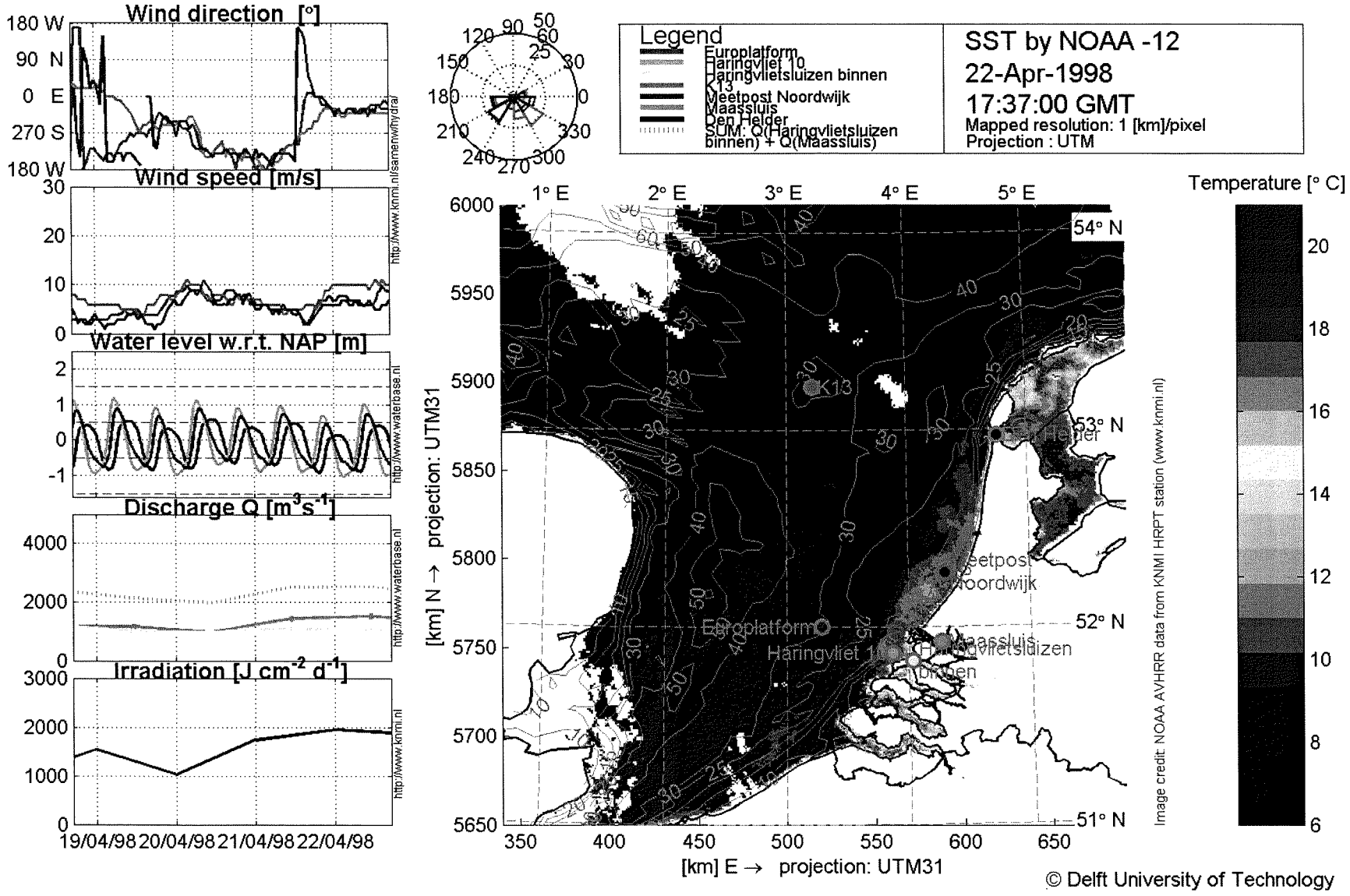
Wind direction [°]
180 W
90 N
0 E
270 S
180 W
Wind speed [m/s]
30
20
10
0
Water level w.r.t. NAP [m]
2
1
0
-1
Discharge Q [m³s⁻¹]
4000
2000
0
Irradiation [J.cm⁻² d⁻¹]
3000
2000
1000
0
19/04/98 20/04/98 21/04/98 22/04/98
http://www.knmi.nl/samenw/hydra/
http://www.waterbase.nl
http://www.knmi.nl
Legend
Europlatform
Haringvliet 10
Haringvlietsluizen binnen
K13
Meetpost Noordwijk
Maassluis
Den Helder
SUM: Q(Haringvlietsluizen binnen) + Q(Maassluis)
SST by NOAA -12
22-Apr-1998
17:37:00 GMT
Mapped resolution: 1 [km]/pixel
Projection : UTM
1° E
2° E
3° E
4° E
5° E
54° N
53° N
52° N
51° N
6000
5950
5900
5850
5800
5750
5700
5650
[km] N → projection: UTM31
350
400
450
500
550
600
650
[km] E → projection: UTM31
K13
Europlatform
Haringvliet 10
Meetpost Noordwijk
Maassluis
Haringvlietsluizen binnen
Image credit: NOAA AVHRR data from KNMI HRPT station (www.knmi.nl)
Temperature [° C]
20
18
16
14
12
10
8
6
© Delft University of Technology

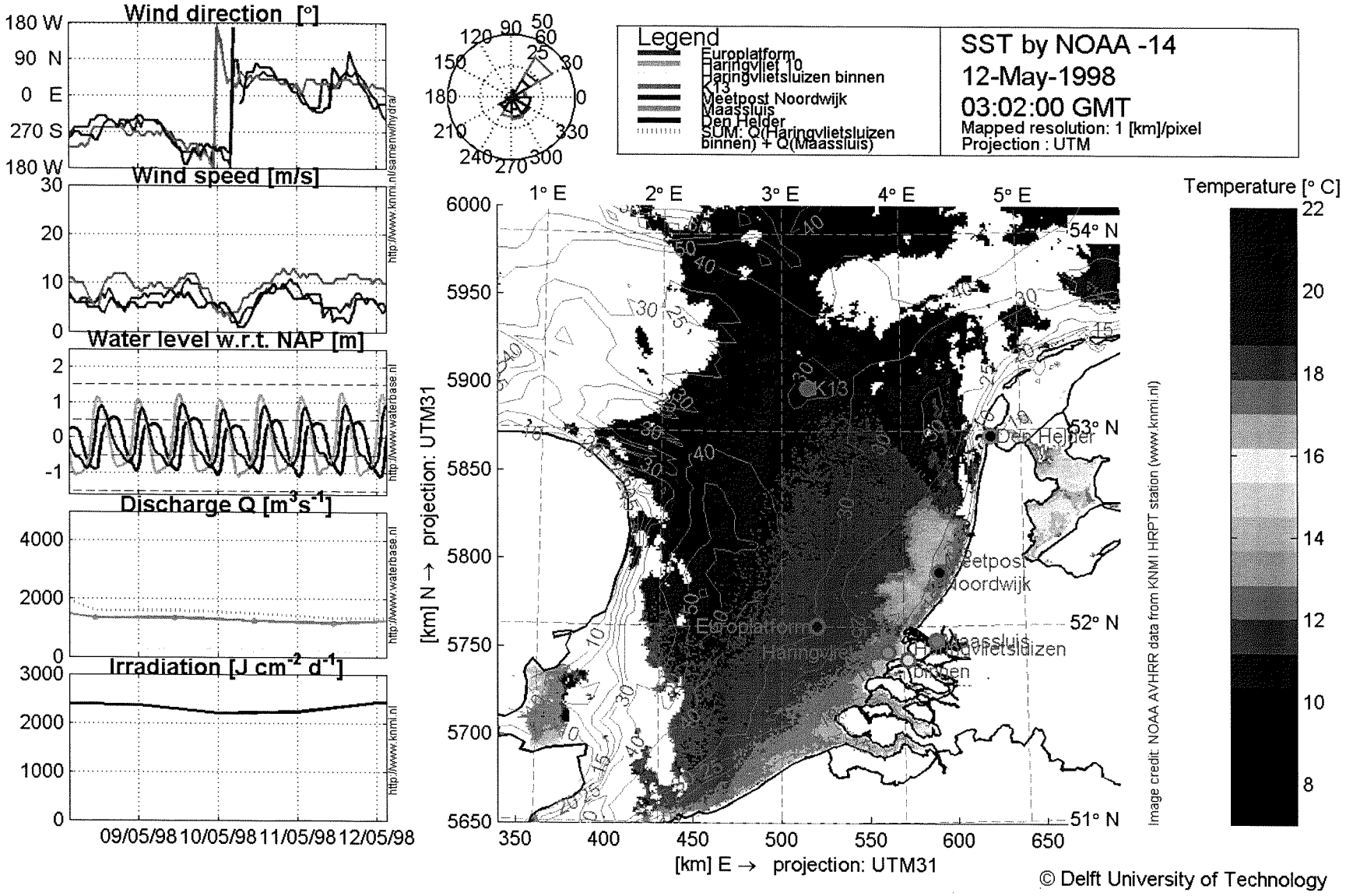
Wind direction [°]
180 W
90 N
0 E
270 S
180 W
Wind speed [m/s]
30
20
10
0
Water level w.r.t. NAP [m]
2
1
0
-1
Discharge Q [m3s-1]
4000
2000
0
Irradiation [J cm-2 d-1]
3000
2000
1000
0
09/05/98 10/05/98 11/05/98 12/05/98
http://www.knmi.nl/samenw/hydra/
http://www.waterbase.nl
http://www.knmi.nl
Legend
Europlatform
Haringvliet 10
Haringvlietsluizen binnen
K13
Meetpost Noordwijk
Maassluis
Den Helder
SUM: Q(Haringvlietsluizen binnen) + Q(Maassluis)
SST by NOAA -14
12-May-1998
03:02:00 GMT
Mapped resolution: 1 [km]/pixel
Projection : UTM
Temperature [° C]
22
20
18
16
14
12
10
8
1° E
2° E
3° E
4° E
5° E
54° N
53° N
52° N
51° N
6000
5950
5900
5850
5800
5750
5700
5650
[km] N → projection: UTM31
350
400
450
500
550
600
650
[km] E → projection: UTM31
K13
Den Helder
Meetpost Noordwijk
Europlatform
Maassluis
Haringvlietsluizen
Image credit: NOAA AVHRR data from KNMI HRPT station (www.knmi.nl)
© Delft University of Technology

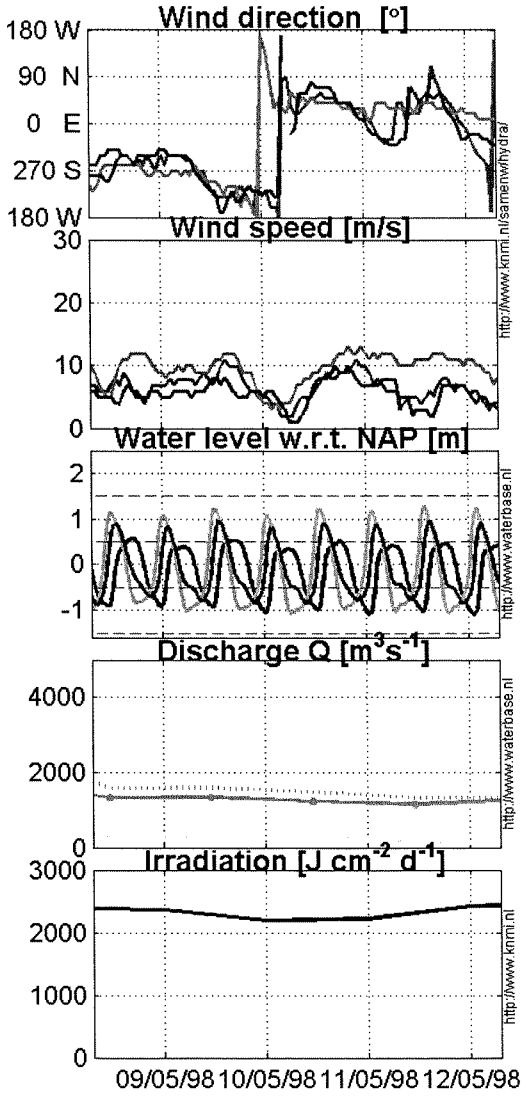

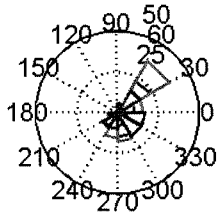

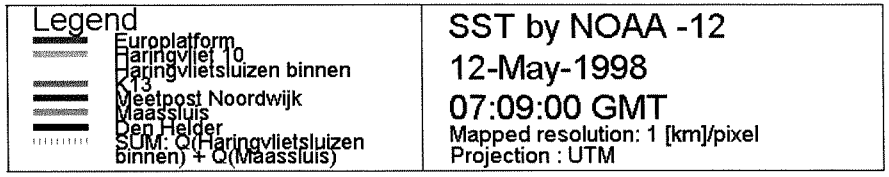

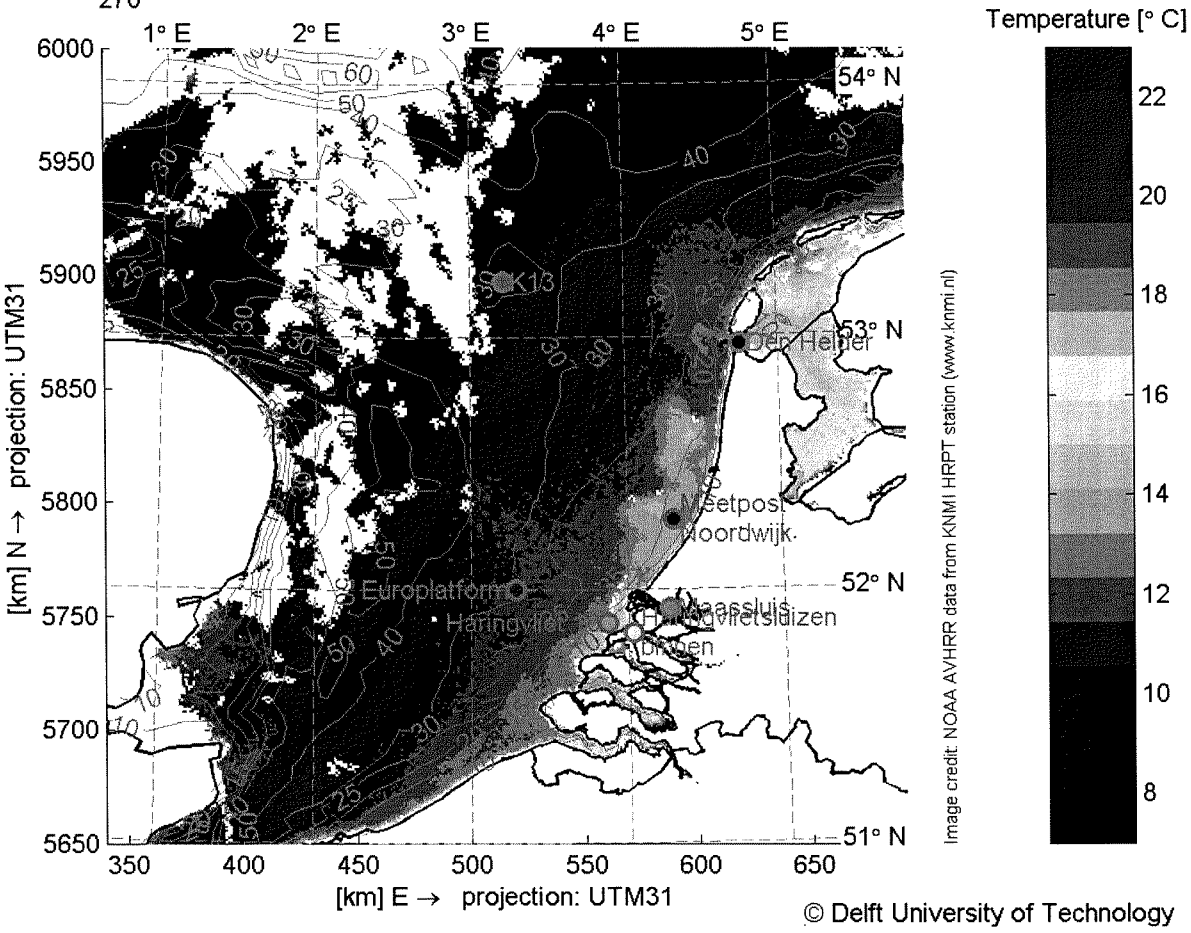

© Delft University of Technology

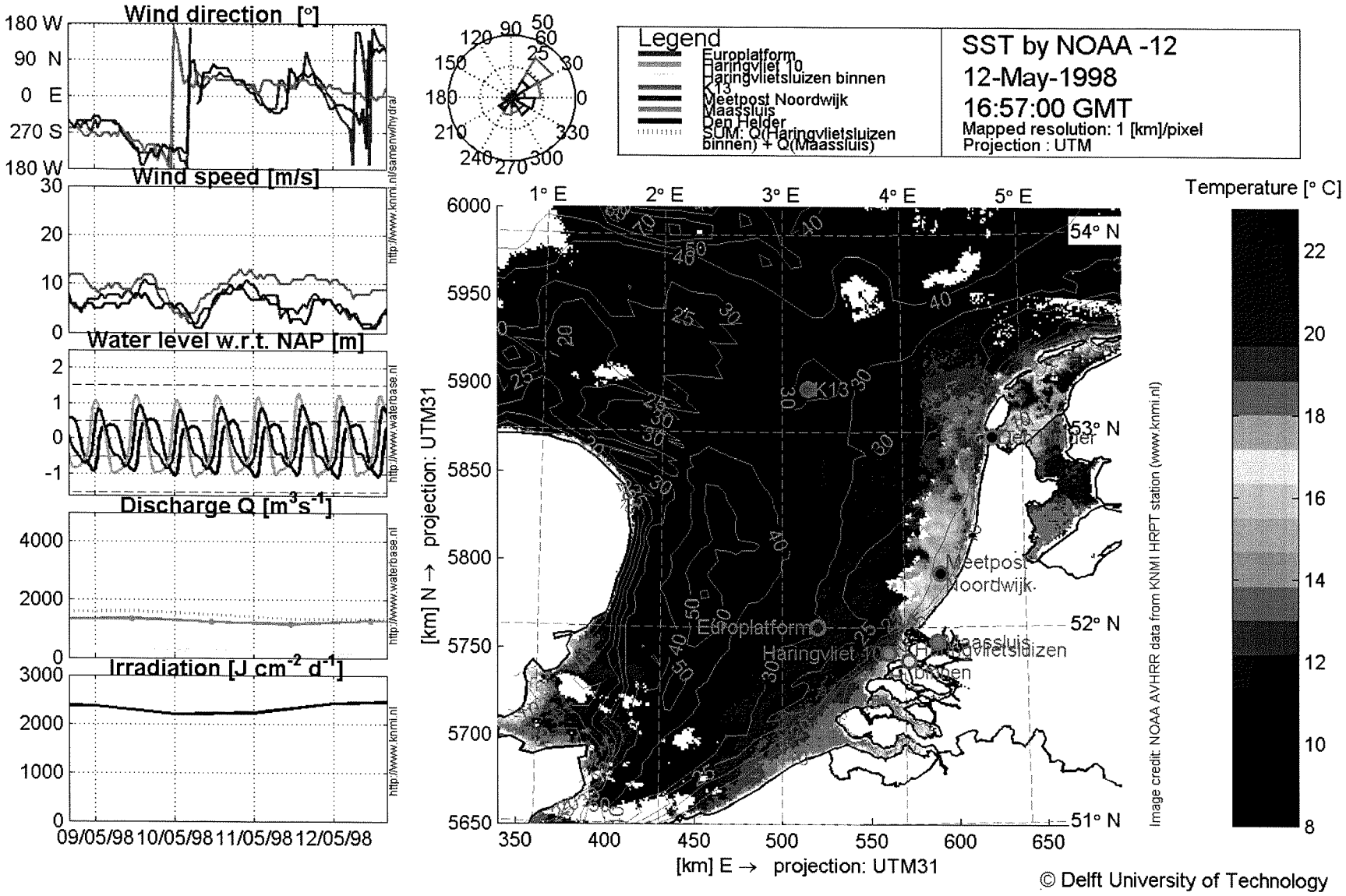
Wind direction [°]
180 W
90 N
0 E
270 S
180 W
Wind speed [m/s]
30
20
10
0
Water level w.r.t. NAP [m]
2
1
0
-1
Discharge Q [m3s-1]
4000
2000
0
Irradiation [J cm-2 d-1]
3000
2000
1000
0
09/05/98 10/05/98 11/05/98 12/05/98
http://www.knmi.nl/samenw/hydra/
http://www.waterbase.nl
http://www.knmi.nl
Legend
Europlatform
Haringvliet 10
Haringvlietsluizen binnen
K13
Meetpost Noordwijk
Maassluis
Den Helder
SUM: Q(Haringvlietsluizen binnen) + Q(Maassluis)
SST by NOAA -12
12-May-1998
16:57:00 GMT
Mapped resolution: 1 [km]/pixel
Projection : UTM
Temperature [° C]
22
20
18
16
14
12
10
8
1° E
2° E
3° E
4° E
5° E
54° N
53° N
52° N
51° N
6000
5950
5900
5850
5800
5750
5700
5650
[km] N → projection: UTM31
350
400
450
500
550
600
650
[km] E → projection: UTM31
K13
Meetpost Noordwijk
Europlatform
Haringvliet 10
Maassluis
Haringvlietsluizen binnen
Image credit: NOAA AVHRR data from KNMI HRPT station (www.knmi.nl)
© Delft University of Technology

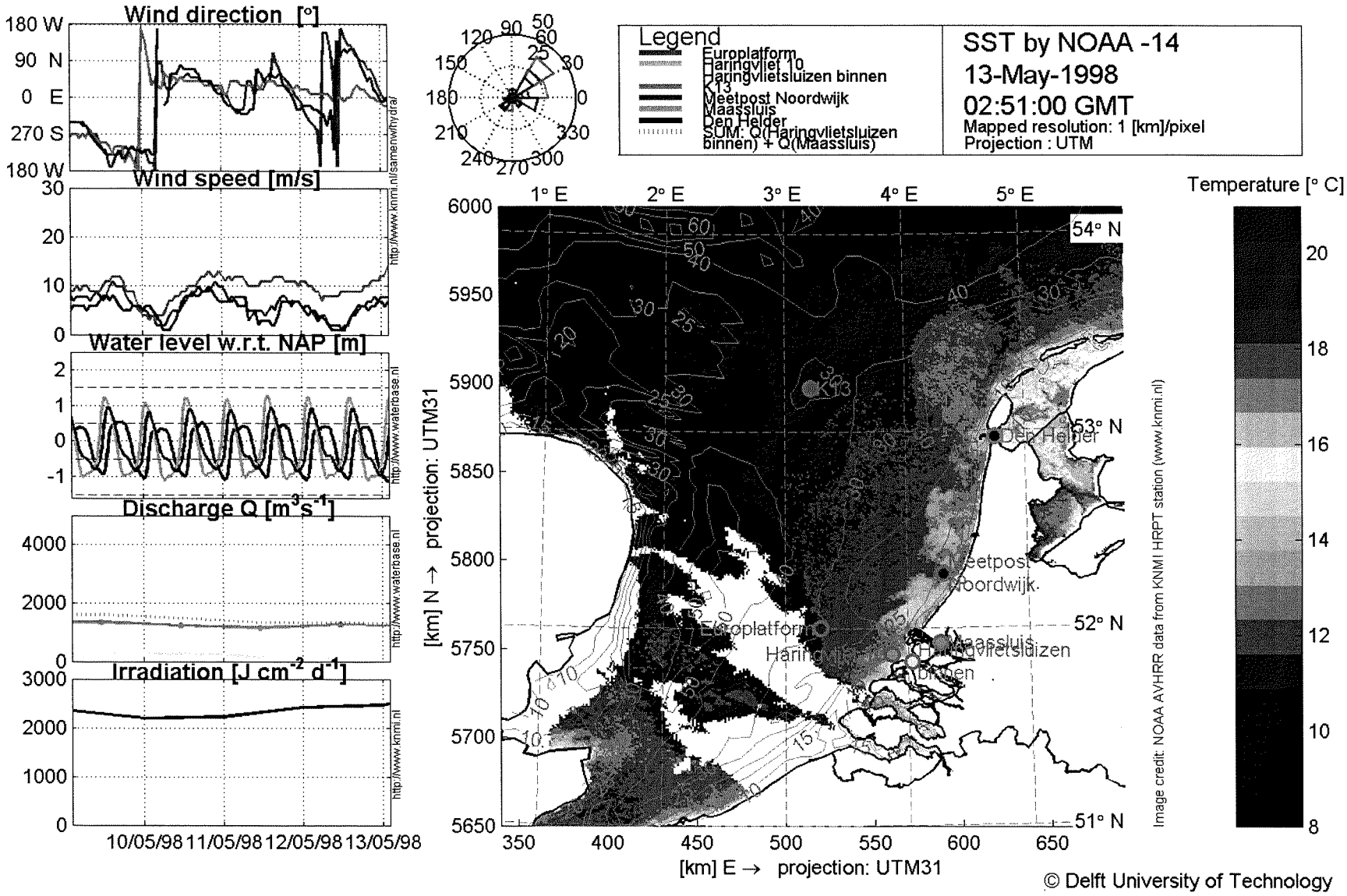
Wind direction [°]
180 W
90 N
0 E
270 S
180 W
Wind speed [m/s]
Water level w.r.t. NAP [m]
Discharge Q [m³s⁻¹]
Irradiation [J cm⁻² d⁻¹]
10/05/98 11/05/98 12/05/98 13/05/98
http://www.knmi.nl/samenw/hydra
http://www.waterbase.nl
http://www.knmi.nl
Legend
Europlatform
Haringvliet 10
Haringvlietsluizen binnen
K13
Meetpost Noordwijk
Maassluis
Den Helder
SUM: Q(Haringvlietsluizen binnen) + Q(Maassluis)
SST by NOAA -14
13-May-1998
02:51:00 GMT
Mapped resolution: 1 [km]/pixel
Projection : UTM
Temperature [° C]
1° E
2° E
3° E
4° E
5° E
54° N
53° N
52° N
51° N
[km] N → projection: UTM31
[km] E → projection: UTM31
Image credit: NOAA AVHRR data from KNMI HRPT station (www.knmi.nl)
© Delft University of Technology

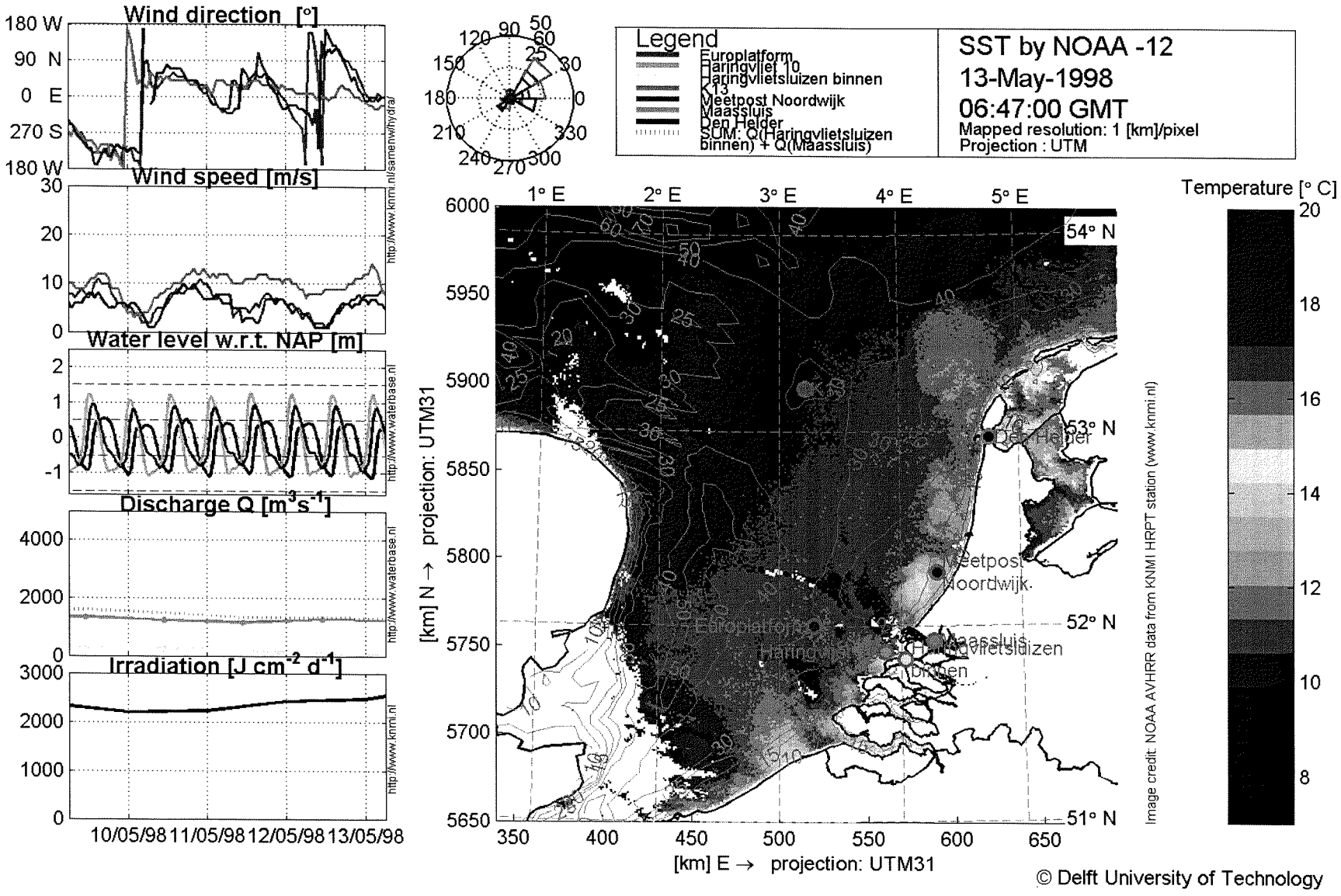
Wind direction [°]
180 W
90 N
0 E
270 S
180 W
Wind speed [m/s]
30
20
10
0
Water level w.r.t. NAP [m]
2
1
0
-1
Discharge Q [m3s-1]
4000
2000
0
Irradiation [J cm-2 d-1]
3000
2000
1000
0
10/05/98 11/05/98 12/05/98 13/05/98
http://www.knmi.nl/samenw/hydra
http://www.waterbase.nl
http://www.knmi.nl
Legend
Europlatform
Haringvliet 10
Haringvlietsluizen binnen
K13
Meetpost Noordwijk
Maassluis
Den Helder
SUM: Q(Haringvlietsluizen binnen) + Q(Maassluis)
SST by NOAA -12
13-May-1998
06:47:00 GMT
Mapped resolution: 1 [km]/pixel
Projection : UTM
Temperature [° C]
20
18
16
14
12
10
8
1° E
2° E
3° E
4° E
5° E
54° N
53° N
52° N
51° N
6000
5950
5900
5850
5800
5750
5700
5650
[km] N → projection: UTM31
350
400
450
500
550
600
650
[km] E → projection: UTM31
Den Helder
Meetpost Noordwijk
Europlatform
Maassluis
Haringvlietsluizen binnen
Image credit: NOAA AVHRR data from KNMI HRPT station (www.knmi.nl)
© Delft University of Technology

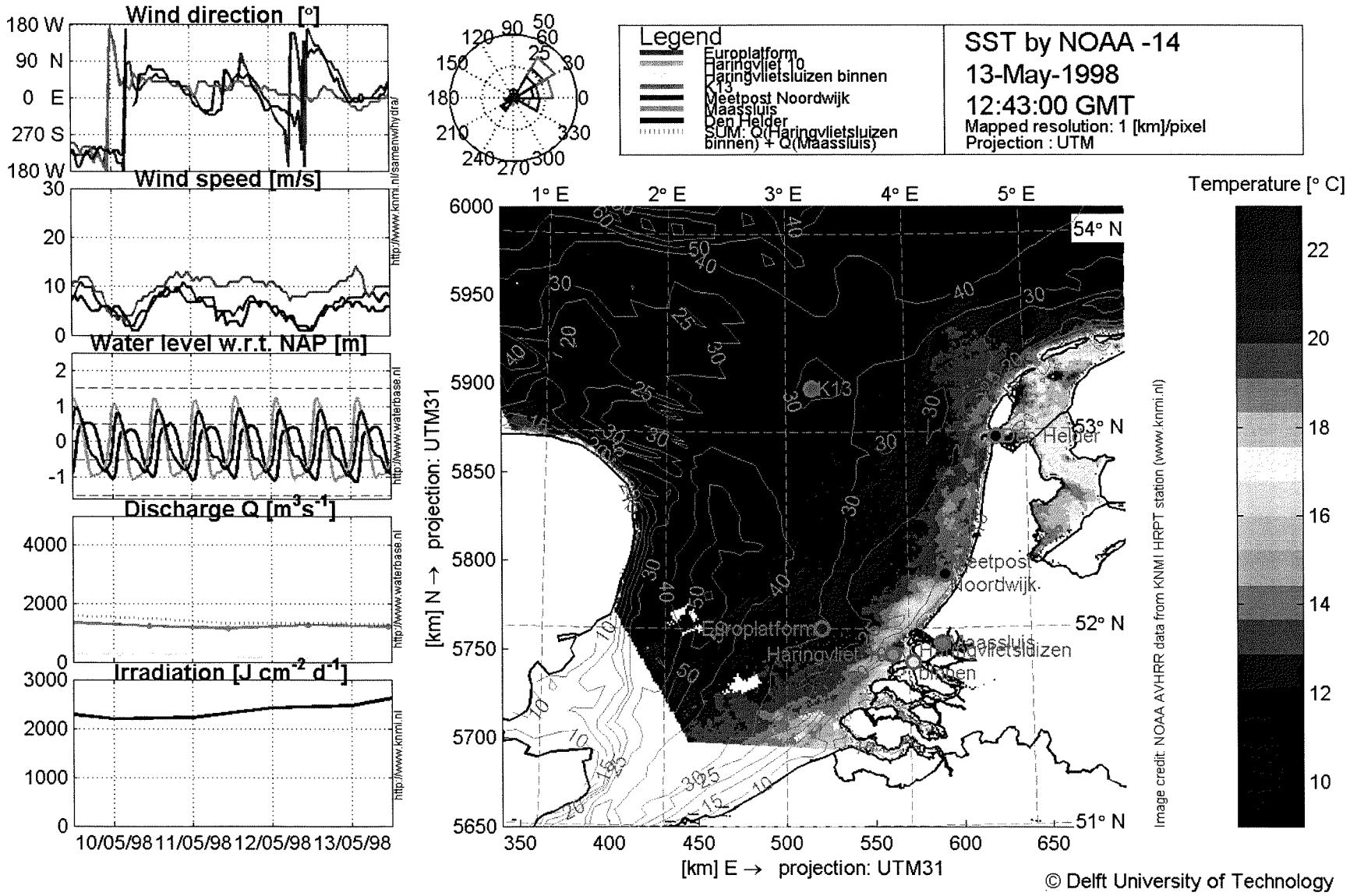
Wind direction [°]
180 W
90 N
0 E
270 S
180 W
Wind speed [m/s]
30
20
10
0
Water level w.r.t. NAP [m]
2
1
0
-1
Discharge Q [m³s⁻¹]
4000
2000
0
Irradiation [J cm⁻² d⁻¹]
3000
2000
1000
0
10/05/98 11/05/98 12/05/98 13/05/98
http://www.knmi.nl/samenwhydra/
http://www.waterbase.nl
http://www.waterbase.nl
http://www.waterbase.nl
http://www.knmi.nl
Legend
Europlatform
Haringvliet 10
Haringvlietsluizen binnen
K13
Meetpost Noordwijk
Maassluis
Den Helder
SUM: Q(Haringvlietsluizen binnen) + Q(Maassluis)
SST by NOAA -14
13-May-1998
12:43:00 GMT
Mapped resolution: 1 [km]/pixel
Projection : UTM
1° E
2° E
3° E
4° E
5° E
54° N
53° N
52° N
51° N
6000
5950
5900
5850
5800
5750
5700
5650
[km] N → projection: UTM31
350
400
450
500
550
600
650
[km] E → projection: UTM31
K13
Helder
Meetpost Noordwijk
Europlatform
Haringvliet
Maassluis
Haringvlietsluizen binnen
Image credit: NOAA AVHRR data from KNMI HRPT station (www.knmi.nl)
Temperature [° C]
22
20
18
16
14
12
10
© Delft University of Technology

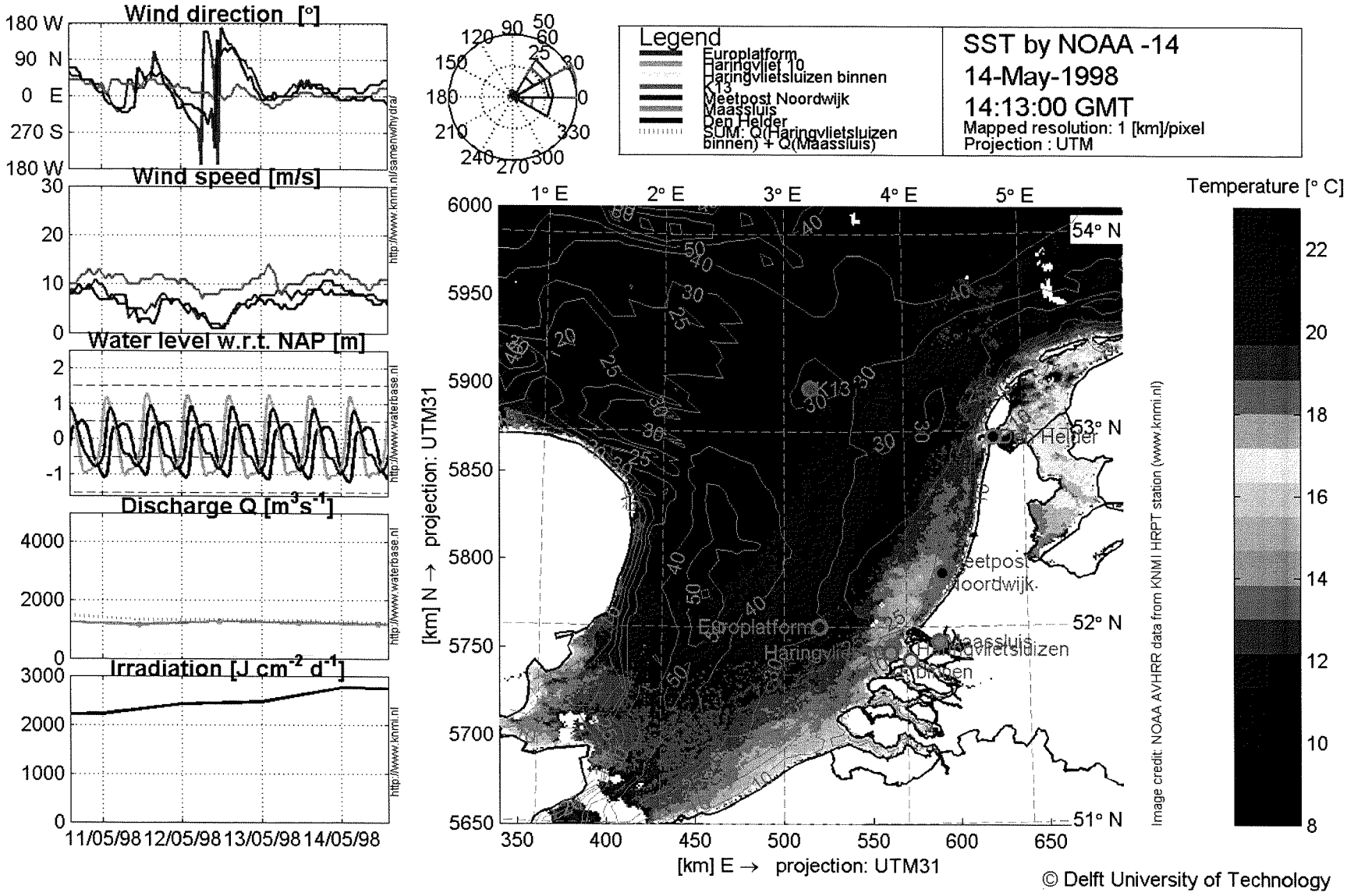
Wind direction [°]
180 W
90 N
0 E
270 S
180 W
Wind speed [m/s]
30
20
10
0
Water level w.r.t. NAP [m]
2
1
0
-1
Discharge Q [m3s-1]
4000
2000
0
Irradiation [J cm-2 d-1]
3000
2000
1000
0
11/05/98 12/05/98 13/05/98 14/05/98
http://www.knmi.nl/samenw/hydra/
http://www.waterbase.nl
http://www.knmi.nl
Legend
Europlatform
Haringvliet 10
Haringvlietsluizen binnen
K13
Meetpost Noordwijk
Maassluis
Den Helder
SUM: Q(Haringvlietsluizen binnen) + Q(Maassluis)
SST by NOAA -14
14-May-1998
14:13:00 GMT
Mapped resolution: 1 [km]/pixel
Projection : UTM
Temperature [° C]
22
20
18
16
14
12
10
8
1° E
2° E
3° E
4° E
5° E
54° N
53° N
52° N
51° N
6000
5950
5900
5850
5800
5750
5700
5650
[km] N → projection: UTM31
350
400
450
500
550
600
650
[km] E → projection: UTM31
Den Helder
Meetpost Noordwijk
Europlatform
Maassluis
Haringvlietsluizen
Image credit: NOAA AVHRR data from KNMI HRPT station (www.knmi.nl)
© Delft University of Technology

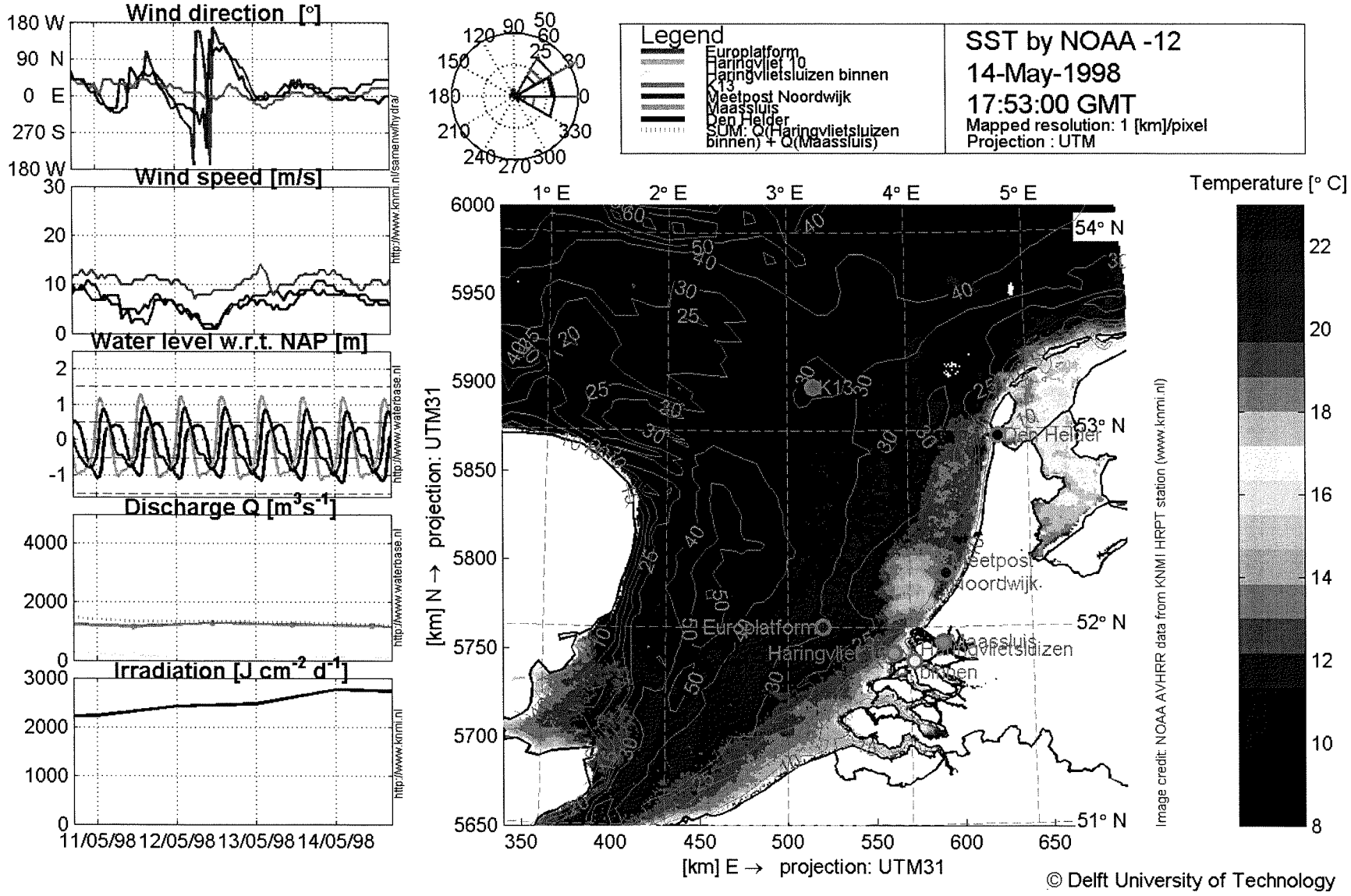
Wind direction [°]
180 W
90 N
0 E
270 S
180 W
Wind speed [m/s]
30
20
10
0
Water level w.r.t. NAP [m]
2
1
0
-1
Discharge Q [m³s⁻¹]
4000
2000
0
Irradiation [J cm⁻² d⁻¹]
3000
2000
1000
0
11/05/98 12/05/98 13/05/98 14/05/98
http://www.knmi.nl/samenwhydra/
http://www.waterbase.nl
http://www.knmi.nl
Legend
Europlatform
Haringvliet 10
Haringvlietsluizen binnen
K13
Meetpost Noordwijk
Maassluis
Den Helder
SUM: Q(Haringvlietsluizen binnen) + Q(Maassluis)
SST by NOAA -12
14-May-1998
17:53:00 GMT
Mapped resolution: 1 [km]/pixel
Projection : UTM
Temperature [° C]
22
20
18
16
14
12
10
8
1° E
2° E
3° E
4° E
5° E
54° N
53° N
52° N
51° N
6000
5950
5900
5850
5800
5750
5700
5650
[km] N → projection: UTM31
350
400
450
500
550
600
650
[km] E → projection: UTM31
K13
Den Helder
Meetpost Noordwijk
Europlatform
Haringvliet
Maassluis
Haringvlietsluizen binnen
Image credit: NOAA AVHRR data from KNMI HRPT station (www.knmi.nl)
© Delft University of Technology

Appendix 9

TIDAL PULSING

SST images for May together with water levels six hours prior to satellite pass:

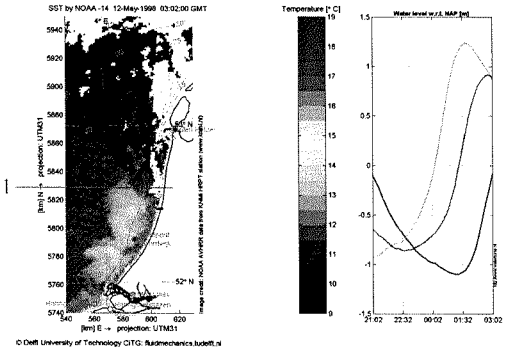

12-May 03:02

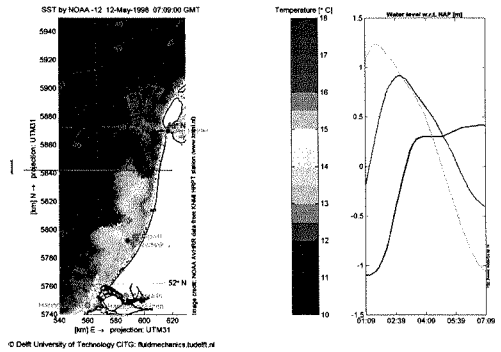

12-May 07:09

ΔT = 4:07; Δx = 14 km; v = 0.95 m s^{-1}

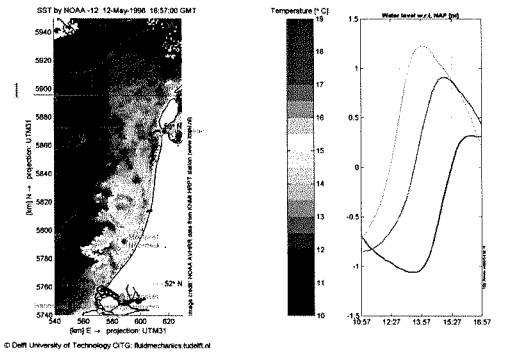

12-May 16:57

ΔT = 9:48; Δx = 53 km; v =1.5 m s^{-1}

ΔT= 9:54; Δx = 45 km;

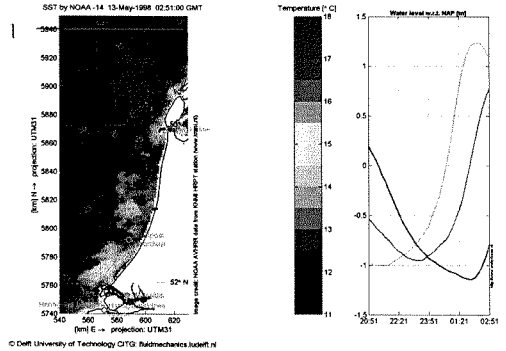

13-May 02:51

v = 1.26 m s^{-1}

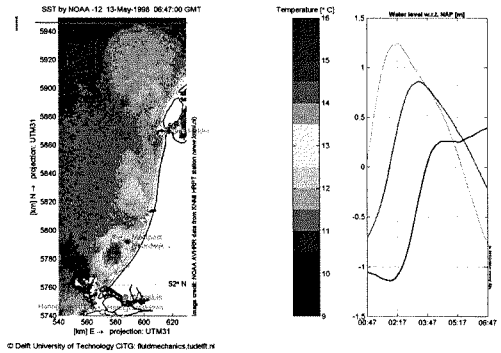

13-May 06:47

ΔT = 3:56; Δx = 6 km; v = 0.42 m s^{-1}

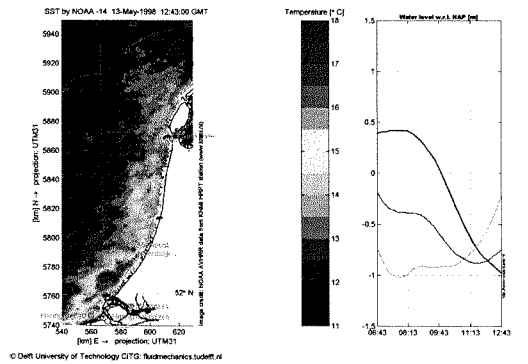

13-May 12:43

ΔT = 5:56

ΔT =1:30

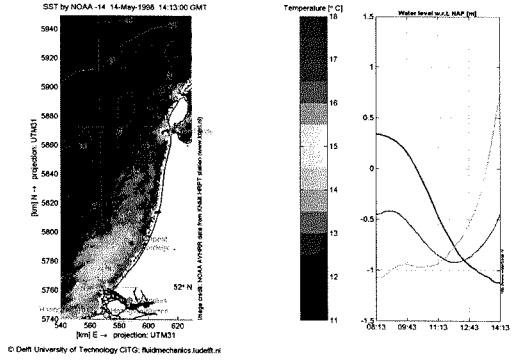

14-May 14:13

$\Delta T = 3{:}40$

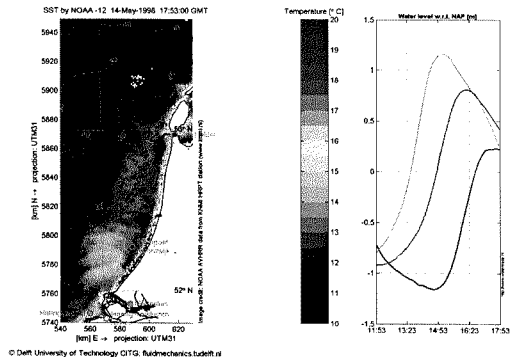

14-May 17:53
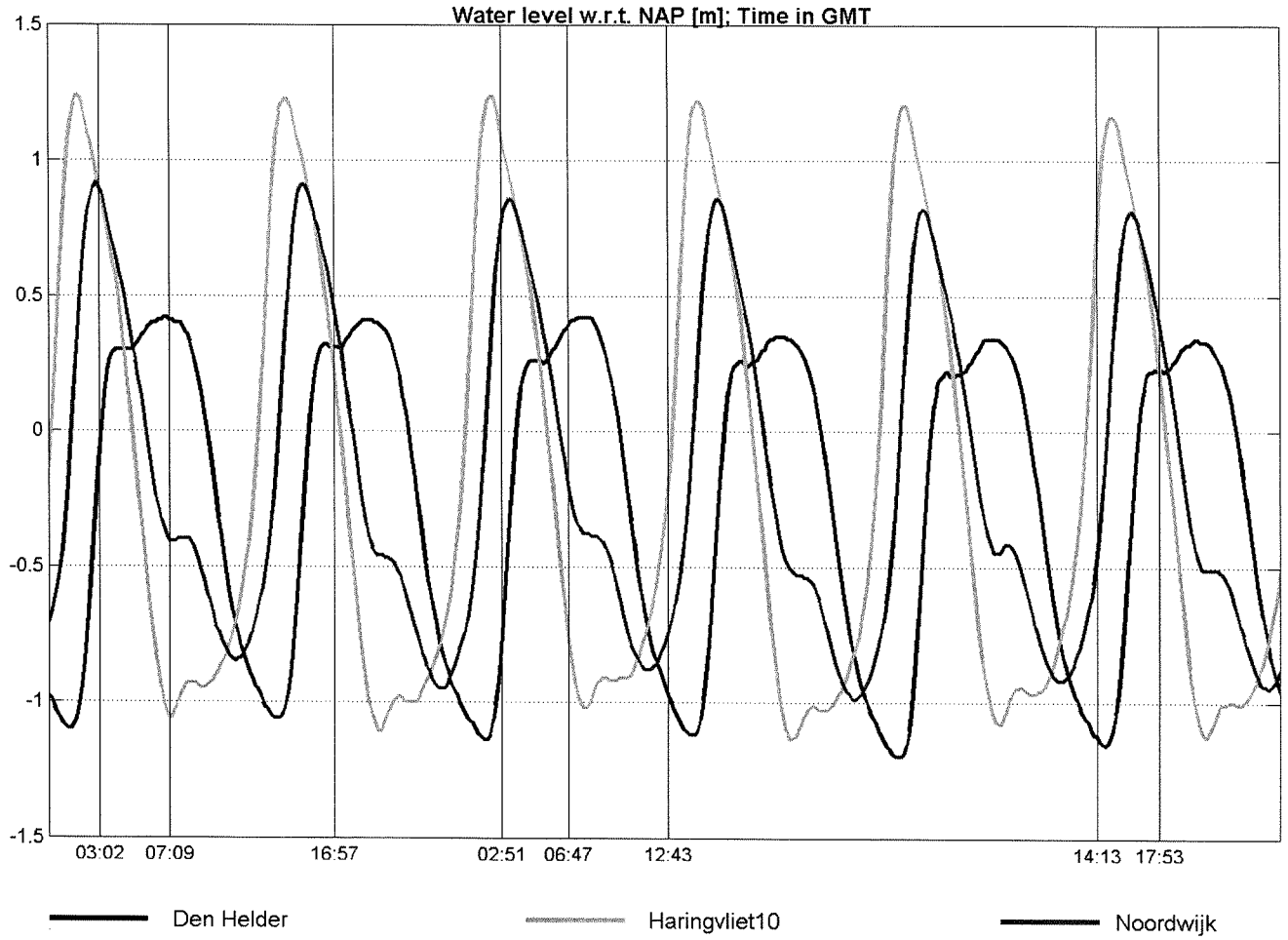
Time of satellite pass for May sequence with respect to water levels at three locations: